南京大學

研 究 生 毕 业 论 文

（申请博士学位）

论 文 题 目	不稳定核寿命计算及相对论重离子碰撞中ϕ介子产生
作 者 姓 名	张 小 平
学科、专业名称	物理学
研 究 方 向	理论核物理
指 导 教 师	任中洲 教授 (南京大学物理系) 许怒 研究员 (劳伦斯伯克利国家实验室)

二〇一〇年 五月 十四日

学　　　　　号:　DG0622059

论文答辩日期:　　　年　　月　　日

指　导　教　师:　　　　　　　　　　（签字）

A Dissertation for the Ph. D Degree

Lifetime Calculations for Unstable Nuclei and ϕ Meson Production at RHIC

Candidate: ZHANG Xiaoping
Co-Supervisors: Prof. REN Zhongzhou (Nanjing University)
Dr. XU Nu (Lawrence Berkeley National Laboratory)
Speciality: Physics

Department of Physics, Nanjing University
Nanjing, P. R. China

May, 2010

南京大学研究生毕业论文中文摘要首页用纸

毕业论文题目: 不稳定核寿命计算及相对论重离子碰撞中ϕ介子产生
物 理 专业 2006 级博士研究生 姓名：张小平
指导教师（姓名、职称）：任中洲 教授，许怒 研究员

摘 要

本文包含两部分研究内容，在第一部分我们系统研究了远离β稳定线核β衰变以及重核和超重核α衰变和自发裂变的新规律。第二部分主要阐述了通过ϕ介子产生研究Cronin效应、相对论重离子碰撞的初始条件以及夸克胶子等离子体的形成、衍化和输运特性。

我们首先系统研究了远离β稳定线核$\beta^{\pm}$衰变的新规律。远离稳定线核的$\beta^{\pm}$衰变寿命是全面理解天体重元素合成的先决条件之一，然而目前实验室里面还无法合成极端丰质子和丰中子的重原子核，因此这些远离稳定重核的$\beta^{\pm}$衰变寿命完全依赖理论计算。由于核多体问题的复杂性，微观模型中核$\beta^{\pm}$衰变跃迁矩阵元的计算精度受到一定限制。通过系统分析实验数据，我们发现远离稳定线核$\beta^{\pm}$衰变寿命与它的质子数/中子数或者衰变过程中发射电子/正电子的最大动能E_{m}之间存在指数关系。通过系统比较发现，这一新指数规律优于传统的Sargent定律。Sargent定律可从Fermi单能级β衰变理论近似导出，它认为$\beta^{\pm}$衰变寿命与E_{m}之间是幂级数关系，这只是反映了母核衰变到子核单个能级的情况。实际上，对于远离稳定线的核$\beta^{\pm}$衰变，由于衰变能较大，母核基态可以衰变到子核的一系列激发态，因此我们的指数规律可能反映了从母核衰变到子核多个能级的统计行为。这首次表明远离稳定线核$\beta^{\pm}$衰变寿命具有和核α衰变、结团放射性寿命类似的指数规律。虽然上述衰变过程是由不同相互作用所主导，但是在核环境中，核跃迁矩阵元和子核能级分布对不同种类的核衰变可能有相似影响，从而导致类似的指数规律。基于上述指数规律，引入合理的核结构效应，比如奇偶效应和壳效应，我们提出了一个新公式用于计算远离稳定线核$\beta^{\pm}$衰变寿命。我们利用新公式对原子核质量数A从9到238的所有735个远离稳定核$\beta^{\pm}$衰变寿命进行了系统计算。实验寿命与理论计算的符合程度与最好的微观计算模型相当甚至更优。这表明新公式能够较好地描述远离稳定核$\beta^{\pm}$衰变寿命。这些核的$\beta^{\pm}$衰变寿命跨越六个数量级，表明我们的计算公式是真实物理过程的一种合理近似。因此它可以用于预言远离稳定线核$\beta^{\pm}$衰变寿命，供将来实验和理论研究参考。

我们还研究了重核和超重核α衰变和自发裂变寿命。对于超重核基态和同质异能态寿命的准确预言是成功进行超重核合成与鉴别的先决条件之一。实验中合成的超重核一般都是处于激发态或者同质异能态。靠近可能的“超重核稳定岛”附近，可能会存在更

多同质异能态。实验研究发现，某些超重核的同质异能态与基态相比具有更长的寿命。关于同质异能态α衰变的系统计算在文献中还不多见。通过引入由高角动量导致的离心势垒，我们推广了有效液滴模型用于同时计算母核基态/同质异能态经过α衰变到子核基态/同质异能态的寿命。理论计算与实验数据符合较好。计算表明由于高角动量而引入的离心势垒是长寿命超重核同质异能态存在的主要原因。此外，我们还系统分析了长寿命线附近奇A重核和超重核自发裂变寿命。对于长寿命线附近质子数Z在92-106之间的奇A核，其自发裂变寿命与最大裂变能量之间具有指数规律。这一规律可能反映了自发裂变的隧穿特性。但是对于质子数大于等于108的奇A超重核，其自发裂变实验寿命系统地大于这一指数规律的期待值。这表明在可能存在的核质子壳层$Z = 114$附近，核对于自发裂变具有增强的稳定性。通过宏观微观模型对核自发裂变位垒进行的系统计算表明，在$Z = 114$附近，核自发裂变具有双峰位垒结构并且其位垒高度会有明显增加。这些理论计算结果可供将来实验研究参考。

在本文第二部分，我们通过ϕ介子产生研究了位于美国布鲁克海文实验室的相对论重离子对撞机（RHIC）上产生的一种新物质形态—由退禁闭的夸克胶子组成的等离子体(QGP)。通过氘核-金核对撞，我们可以研究极端高能量条件下的核物质性质，有利于我们理解金核-金核对撞过程的初始条件以及随后可能出现的QGP的性质。著名的Cronin效应—质子-核碰撞过程中高横向动量（p_T）区单位硬碰撞的粒子产额相对于质子-质子碰撞的增强— 就是在质子与核碰撞过程中发现的。Cronin效应虽然已经发现了三十多年，但是它的物理起源特别是不同粒子的产额增强幅度不一样这一难题一直没有得到较好解决。我们利用输运模型（AMPT）模拟了质心系能量为200GeV的氘核-金核对撞过程。研究发现，如果强子由弦碎裂产生，并且引入末态强子散射，大质量强子产额在中高横向动量区比小质量强子增强幅度更大。末态产生的大量低横向动量、低质量粒子与少量高横向动量、低质量粒子之间散射截面较大。由于末态强子散射，导致低质量粒子在高横向动量区产额减小。这种产额增强的粒子质量依赖性与2003年在RHIC氘核-金核对撞中反质子产额增强幅度大于π介子产额增强这一测量结果一致。进一步研究发现，如果没有引入末态强子散射，则在中高横向动量区各种强子的增强幅度没有明显差异，这与实验数据不符合。因此我们首次提出Cronin效应具有质量依赖，这种质量依赖的根源在于末态强子散射减少了低质量粒子在高横向动量区的产额。另外一种模型认为Cronin效应起源于碰撞以后夸克之间的重组形成强子，也能够解释氘核-金核对撞中质子和π介子的不同增强幅度，这种模型认为Cronin效应具有重子（3个价夸克）-介子（2个价夸克）依赖性。

为了进一步检验上述两种不同强子产生机制以及随后的末态强子散射效应，我们测量了质心系能量为200GeV的氘核-金核对撞中ϕ介子产额的横向动量，碰撞中心度以及快度依赖。通过分析STAR探测器上收集的实验数据，初步实验结果表明在中心氘核-金核对撞中，中间快度、中高横向动量区单位硬碰撞的ϕ介子产额比相应的质子-质子碰撞中的产额要大。这表明ϕ介子具有Cronin增强。在$1.2 < p_T < 4$ GeV/c区域，ϕ介子产

额的增强幅度略低于$\Lambda+\overline{\Lambda}$重子，大于$K_0^S$介子（$\sim$95%置信区间）。由于$\phi$介子质量稍低于$\Lambda$（$\overline{\Lambda}$）重子，比$K_0^S$介子质量大，这表明在RHIC能区Cronin效应可能具有质量依赖，这与我们之前的计算符合。同时，K_0^S介子，ϕ介子和$\Lambda+\overline{\Lambda}$重子产额的快度依赖也展现了类似的质量效应。这也与我们的计算结果定性符合。初步实验结果支持我们关于Cronin效应具有粒子质量依赖的计算及其理论解释，即这种质量依赖起源于末态强子散射。这同时也表明，计算中采用的弦脆裂强子化机制能够较好地描述质心系能量为200GeV的氘核-金核对撞中中高横动量区的强子产生。上述对于末态强子化机制和强子散射效应的研究对于今后进一步研究高能量核的初态动力学性质具有重要意义。

我们还测量了金核-金核对撞中产生的ϕ介子在横向动量空间相对于反应平面的各向异性分布（椭圆流）。在非对心碰撞中，初始相互作用体积是一个椭球形状，如果初期产生的高温高密系统具有很强的内在相互作用，在椭球的长轴和短轴将会建立不同的压力梯度，导致末态发射粒子在其动量空间出现各项异性的方位角分布。因此椭圆流测量可以反映对撞产生的火球是否达到初态热力学平衡，以及其随后的衍化过程和输运特性。理论计算表明，末态强子耗散效应和共振粒子强衰变对椭圆流参数v_2有一定影响。人们认为ϕ介子与非奇异强子散射截面比较小，末态强子散射对ϕ介子v_2的贡献较小，因此ϕ介子椭圆流能更好地反映系统初态衍化—可能的QGP形成—强子产生过程的性质。我们测量了不同碰撞对心度的金核-金核对撞事件中ϕ介子椭圆流参数。如果扣掉初始几何效应，测量的椭圆流集体展开强度在接近对心碰撞中更强。这与假设局域热力学平衡的理想流体动力学计算结果不一致，表明在偏心碰撞中系统没有达到局域热力学平衡或者末态强子耗散效应更大。在低横向动量区域，由于椭圆流（各项异性流）和系统径向展开流速的相互作用，理想流体力学预言了在相同横向动量的条件下低质量强子具有较大v_2，这称为v_2的质量顺序性。但是如果引入了末态强子耗散效应，由于不同强子散射截面不一样，相应的耗散效应也不一样，Hirano等人的计算表明这种质量顺序性可能会被破坏。我们比较了半对心碰撞中低横向动量区ϕ介子和质子的v_2，发现在横向动量小于1GeV/c时，测量到的ϕ介子v_2与质子v_2相当。在横向动量小于0.7GeV/c时，ϕ介子v_2甚至略大。由于ϕ介子质量比质子大9%左右，这表明理想流体模型预言的质量顺序性很可能被破坏了。这与Hirano等人利用理想流体力学加上末态强子散射机制的混合模型计算定性符合。上述测量与理论结果的比较可能说明ϕ介子确实具有较小的强子散射截面，同时末态强子散射效应对低横向动量区强子椭圆流具有一定影响。

在中间横向动量区，v_2开始偏离理想流体力学的计算结果，随横动量增加的趋势减缓，然后饱和。如果把v_2和p_T（m_T-m_0，横向动能）都除以强子中组分夸克数目n_q，重子和介子将符合同一条曲线。我们称之为组分夸克数目标度性（横向动能标度性）。这个组分夸克数目标度性本身，表明强子的v_2有组分夸克自由度。组分夸克重组合模型认为强子是由组分夸克重组产生的，它可以定性解释这个标度性。我们比较了$\phi(s\overline{s})$介子和$\Omega(sss)$重子的v_2，发现含有奇异价夸克的$\phi(s\overline{s})$介子和$\Omega(sss)$重子的v_2也满足组分夸克数目标度性，在夸克重组模型的框架下，表明退禁闭的奇异夸克也具有和轻味夸克类似

的集体行为。这给RHIC金核-金核对撞中的夸克退禁闭提供了一个强有力的证据。我们还比较了中间横向动量区轻味夸克组成的强子和奇异强子的组分夸克数目标度性和横向动能标度性，发现在$2.5 < p_T < 5$ GeV/c区域，同样的p_T/n_q或$(m_T - m_0)/n_q$，ϕ介子的v_2/n_q 比π介子的v_2/n_q要小，而与Λ重子的v_2/n_q相当。这一测量结果将会挑战简单的价夸克重组模型。Dusling等人引入了流体粘滞系数和强子种类依赖的弛豫时间效应的流体力学计算有望解释这一横向动能标度性。

今后通过与粘滞流体力学计算结果比较，我们有望通过ϕ介子v_2得到QGP的粘滞系数。随着全面覆盖的飞行时间探测器的安装和成功运行，我们可以测量由夸克胶子等离子体热辐射产生的双轻子对。这将使测量QGP的初始温度成为可能。同时，测量低质量矢量介子（ω、ρ、ϕ etc.）双轻子衰变道的不变质量分布，有望对RHIC上可能的QGP相变所导致的手征对称恢复以及质量起源给出解答。我们在STAR氘核-金核对撞中对$\phi \to e^+e^-$衰变道的首次测量为随后进一步研究打下了良好基础。

关键词：β衰变寿命、指数规律、α衰变和自发裂变寿命、有效液滴模型、宏观微观模型、超重核素、同质异能态、夸克胶子等离子体、相对论重离子碰撞、Cronin效应、ϕ介子、核修正因子、椭圆流、多相输运模型

南京大学研究生毕业论文英文摘要首页用纸

THESIS: Lifetime Calculations for Unstable Nuclei and ϕ Meson Production at RHIC

SPECIALIZATION: Physics

POSTGRADUATE: ZHANG Xiaoping

MENTOR: Prof. REN Zhongzhou, Senior Scientist XU Nu

Abstract

In the first part of this dissertation, we address the topic of half-lives of nuclear decay in extreme cases theoretically. First, we investigate the new decay law and new calculation method for β-decay half-lives of nuclei far from β-stable line, which is a prerequisite for better understanding of astrophysical nucleosynthesis process. A new exponential law is found between the half-life of $\beta^{\pm}$-decay and the nucleon number (Z, N) for proton-rich or neutron-rich nuclei. This new law implies the exponential dependence of nuclear $\beta^{\pm}$-decay half-lives on the maximum kinetic energy of the electron or positron emitted in the $\beta^{\pm}$-decay process. It may reflect the statistical behavior of multi-energy-level decay properties for the nucleus far from β-stable line, that is, from the ground state of parent nucleus to many excited energy levels of daughter nucleus. It is superior to the traditional Sargent law, a fifth power law between $\beta^{\pm}$-decay half-lives and decay energies, which can be approximately derived from single-level Fermi β-decay theory. Based on the new exponential law and including reasonable nuclear structure effects, new formulae are proposed to describe the $\beta^{\pm}$-decay half-lives of nuclei far from β-stable line. Experimental half-lives are well reproduced by the simple formulae. The agreement with experimental data is comparable with or even slightly better than the best microscopic model calculations for all available nuclei far from stability ranging from mass numbers $A = 9 - 238$ and with half-lives spanning 6 orders of magnitude (10^{-3}–10^{3} s). This formula can be used to predict the $\beta^{\pm}$-decay half-lives of the nuclei far from the β-stable line.

Next, α decay and spontaneous fission half-lives are systematically studied. Synthesis and identification of superheavy nucleus require precise prediction on its half-lives of decays from ground-states/isomeric-states of parent nucleus to ground-states/isomeric-states of daughter nucleus. By including the centrifugal potential barrier, we generalize the effective liquid drop model to describe the half-lives of α-transitions from ground-states to ground-states, from isomeric-states to ground-states, and from isomeric-states

to isomeric-states using unified model parameters. Good agreement is achieved between the experimental α-decay half-life and theoretical one. In addition, spontaneous fission half-lives of heavy and superheavy odd-mass nuclei are also systematically investigated. Available experimental data of spontaneous fission half-lives of odd-A nuclei with $Z = 92 - 110$ are well reproduced by an improved formula. A new exponential law is found between the spontaneous fission half-lives along the long-lifetime line and maximum Q values of the fission processes for odd-A nuclei with $Z = 92 - 106$. This exponential law may indicate the tunnelling property of spontaneous fission. An interesting result is that the experimental spontaneous fission half-lives are apparently larger than the anticipant values from the above exponential law for nuclei with $Z \geqslant 108$. This may be caused by enhanced shell effects for the nuclei approaching $Z = 114$. Subsequent macroscopic-microscopic (MM) model calculations for odd-A heavy and superheavy nuclei show that the apparent increase of the height of the fission barrier and the double-humped shape of the barrier for nuclei close to $Z = 114$ lead to longer spontaneous fission half-lives than expected values from the exponential law, thus indicate enhanced stability against spontaneous fission for odd-A nuclei approaching $Z = 114$.

In the second part of this dissertation, we focus on the experimental and theoretical studies on a new form of QCD matter called quark-gluon plasma (QGP) created in relativistic heavy ion collisions at Brookhaven National Laboratory through ϕ meson production. The initial conditions of nuclear collisions can be studied in d+Au like collisions. To extract the initial conditions, one has to understand the well known Cronin effect — hadron production enhancement at intermediate transverse momentum with respect to binary collision scaling — in d+Au collisions. Although the Cronin effect was discovered more than 30 years ago, its origin, especially the species dependence is not fully understood. To address this long-outstanding puzzle, both new theoretical insights and corresponding experimental measurements are presented.

In theoretical side, we studied the mechanism of hadron formation and subsequent hadronic interactions in d+Au collisions at center-of-mass energy $\sqrt{s_{NN}} = 200$ GeV. In a multiphase transport model with Lund string fragmentation for hadronization and the subsequent hadronic rescatterings included, we find particle mass dependence of central-to-peripheral nuclear modification factor R_{CP}. The AMPT calculation indicates the suppressions of low mass particles (pions and kaons) at large p_T during the final-state hadronic rescatterings, thus lead to the observed particle species dependence of R_{CP} in d+Au collisions at RHIC. Recently measured difference between R_{CP} of antiproton and that of pion at mid-rapidity in year 2003 d+Au collisions at RHIC can be understood in terms of this final-state hadronic rescatterings. This shows for the first time the importance of final state hadronic interactions in d+Au collisions, since none of the initial-state models would predict a species-dependent Cronin effect at present.

Our above theoretical findings are further tested with STAR year 2008 d+Au data. We have studied the transverse momentum, centrality and pseudo-rapidity dependence of ϕ meson production in d+Au collisions at $\sqrt{s_{NN}} = 200$ GeV. Enhanced production of intermediate-p_T ϕ meson — with respect to binary collision scaling — have been observed in d+Au 200 GeV (0-20%) central collisions at mid-rapidity ($|y| < 0.5$). The ϕ meson yield is observed to be higher in the gold beam direction (backward pseudo-rapidity) than the deuteron beam direction (forward pseudo-rapidity) of the collisions. Ratios of ϕ-meson yields in backward pseudo-rapidity to those in forward pseudo-rapidity increase with ϕ-meson transverse momenta for p_T below 5 GeV/c. Compared to the enhancement of other identified hadrons K_S^0 and $\Lambda + \overline{\Lambda}$, both nuclear modification factors and the pseudo-rapidity asymmetry likely show particle mass dependence for $1.2 < p_T < 4$ GeV/c. This preliminary result is consistent with our transport model (AMPT) calculation which employs the string model with soft and coherent interactions for hadronization and includes the final state hadronic rescatterings and resonance decays. This calculation suggests that final state hadronic interaction contributes to particle species dependence of Cronin effect at RHIC for the first time.

ϕ meson is a golden probe to study the QGP formation and evolution in the early stage and its transport properties like viscosity since it is little affected by the late stage hadronic rescatterings due to its presumably small hadronic interaction cross section. We presented the measurement of ϕ meson elliptic flow parameter v_2 in year 2007 Au+Au collisions at $\sqrt{s_{NN}} = 200$ GeV. The eccentricity scaled ϕ meson v_2 shows stronger flow strength in more central collisions. The number-of-quark (n_q) scaling has been evidenced with ϕ ($s\bar{s}$) and Ω (sss) at intermediate p_T ($2.5 < p_T < 5$ GeV/c). Within the framework of valence quark coalescence model, this is thought to be a strong evidence of the development of partonic collectivity at the early stage, thus indicates the QGP formation at RHIC. However, the number-of-quark scaled v_2 versus p_T/n_q or $(m_T - m_0)/n_q$ for ϕ meson is systematically smaller than those of pions and kaons, and follows the trend of scaled v_2 of Λ for $2.5 < p_T < 5$ GeV/c. This challenges the simple quark coalescence explanation of number-of-quark scaling. From recently developed viscous hydrodynamic model by Dusling *et al.* which employs species dependent relaxation time, the relatively smaller ϕ meson v_2/n_q versus $(m_T - m_0)/n_q$ may be qualitatively understood by its longer relaxation time and thus early decoupling from hydrodynamic evolution due to its presumably small hadronic cross section. The v_2 of ϕ mesons below $p_T = 1$ GeV/c seems to be consistent with that of proton, and even larger than that below $p_T = 0.7$

GeV/c. This observation contradicts the prediction of the mass ordering of v_2 from ideal hydrodynamic models, where heavier hadrons have smaller v_2 for a given p_T. This result supports the picture that the dynamics at late hadronic stage is described well by hadron cascade models and the ϕ has small hadronic cross section. Extending the low p_T reach will be crucial to see the violation of mass ordering more clearly and could be possible by using full Barrel Time-Of-Flight system installed in 2010 RHIC run at STAR.

With full coverage of barrel time-of-flight (TOF) system, the electron identification is greatly enhanced. It is feasible for direct measurement of di-lepton thermal radiation from QGP. In addition, the measurements of vector mesons ρ, ω and ϕ through electromagnetic decay channels can shed light on whether chiral symmetry that breaks in QCD vacuum is restored in the QGP, and furthermore indicate the origin of mass in nature. Our first $\phi \rightarrow e^+e^-$ measurement in STAR d+Au 2008 run is a good start toward this exciting direction.

Key words: β-decay half life, Exponential law, α-decay and spontaneous fission half life, Effective liquid drop model, Macroscopic-Microscopic model, Superheavy nuclei, Isomeric states, Quark gluon plasma, Relativistic heavy ion collisions, Cronin effect, ϕ meson, Nuclear modification factor, Pseudo-rapidity asymmetry, Elliptic flow, A multiphase transport model

Table of Contents i

Chapter I Introduction

1.1 Nuclear β-decay half-life calculation

1.1.1 Weak interaction

The discovery of nuclear radioactivity by Becquerel in 1896 has opened up the door of the secrets of strong and weak interactions, which are two of the four known basic interactions responsible for the evolution of our universe. Important progress has been made during the studies of nuclear β-decay and weak interaction within less than 1 century. The study on the energy conservation problem of β-decay leads to the prediction of a new particle neutrino by Pauli. Based on the possible existence of the neutrino, Fermi proposed the basic formulation of β-decay theory in 1934 [1,2]. In 1956−1957, Lee and Yang made an important contribution on the theory of β-decay which led to the full development of the theory of weak interactions. They suggested that the parity might not be conserved in a weak process like β-decay [3]. The hypothesis of the violation of parity conservation in weak interactions was immediately confirmed in an experiment completed by Wu *et al.* [4]. In 1958, the V-A theory of four-fermion interactions was founded by Feynman, Gell-Mann [5], Sudarshan and Marshak [6]. To the 1960s, Weinberg [7], Salam [8] and Glashow [9] established a unified theory of weak and electromagnetic interactions. The predicted intermediate bosons $W^{\pm}$ and Z^0 by the unified theory were found by two groups of CERN in 1983 [10–12]. The measured masses of these particles are consistent with predicted ones. The β-decay study has received renewed interest in past decades. Currently, numerous experiments have been carried out to search for neutrinoless double-β decay. The observation of neutrinoless double-β decay, in addition to confirming the Majorana nature of the neutrino, would give information on the absolute neutrino mass scale, and potentially also on the neutrino mass hierarchy and the Majorana phases appearing in the Pontecorvo – Maki – Nakagawa – Sakata (PMNS) matrix.

The weak interaction plays an important role in the evolution of our universe. For example, it has several crucial effects in the course of development of a star [13]. It initiates the gravitational collapse of the core of a massive star triggering a supernova explosion, plays a key role in neutronization of the core material via electron capture by free protons and by nuclei, and effects the formation of heavy elements above iron (including the so-called cosmo-chronometers which provide information about the age of the galaxy and of the universe) at the final stage of the supernova explosion [13]. The weak interaction also largely determines the mass of the core and thus the strength and fate of the shock wave formed by the supernova explosion.

Another example is the nucleosynthesis, which is the process of creating new atomic nuclei from pre-existing nucleons (protons and neutrons). It is thought that the primordial nucleons themselves were formed from the quark-gluon plasma from the Big Bang as it cooled below two trillion degrees. A few minutes afterward, starting with only protons and neutrons, nuclei up to lithium and beryllium (both with mass number 7) were formed, but only in relatively small amounts. Then the fusion process essentially shut down due to drops in temperature and density as the universe continued to expand. This first process of primordial nucleosynthesis may also be called nucleogenesis.

The subsequent nucleosynthesis of the heavier elements requires heavy stars and supernova explosions, at some point in time, to create. This theoretically happened as hydrogen and helium from the Big Bang (perhaps influenced by concentrations of dark matter), condensed into the first stars, perhaps 500 million years after the Big Bang. The elements created in stellar nucleosynthesis range in atomic numbers from six (carbon) to at least 98 (californium), which has been detected in spectra from supernovae. Syntheses of these heavier elements occurs either by nuclear fusion (including both rapid and slow multiple neutron captures) or by nuclear fission, sometimes followed by β decays.

In modern theory, there are a number of astrophysical processes which are believed to be responsible for nucleosynthesis in the universe. The majority of these occur within the hot matter inside stars. The successive nuclear fusion processes which occur inside stars are known as hydrogen burning (via the proton-proton chain or the CNO cycle), helium burning, carbon burning, neon burning, oxygen burning and silicon burning. These processes are able to create elements up to iron and nickel, the region of the isotopes having the highest binding energy per nucleon. Heavier elements can be assembled within stars by a slow neutron capture process known as the s process or in explosive environments, such as supernovae, by a number of processes. The more important nucleosynthesis processes responsible for heavier elements formation include the r process, which involves rapid neutron captures, the rp process, which involves rapid proton captures, and the p process (sometimes known as the gamma process), which involves photodisintegration of existing nuclei.

1.1.2 β-decays of nuclei far from stability

The β-decay properties of proton-rich and neutron-rich nuclei is a prerequisite for a better understanding of the nucleosynthesis process. The nucleosynthesis theory was put forward in more than five decades ago. Both the element distribution on the path of nucleosynthesis, and the resulting final distribution of stable elements are highly sensitive to the β-decay properties of the unstable nuclei involved in the process. There are about several thousands of nuclei between the β stability line and the proton or neutron drip line. Currently, most of these heavy nuclei cannot be produced in terrestrial laboratories and one has to rely on theoretical extrapolations for their β-decay properties.

Previous microscopic calculations of weak interaction rates have led to a better understanding of the nucleosynthesis process. However, all β-decay microscopic models which are used to calculate the nuclear half-life of β-decay come down to the calculations of transition matrix elements. Due to the inherent complexity of both weak interaction and strong interaction for atomic nuclei, it still remains for most cases a difficult and cumbersome task to calculate β-decay probabilities. In 1933, Sargent made an empirical study of β-decay half-lives and discovered a law which is consistent with the Fermi β-decay theory proposed one year later [14]. From then on, there exist few parametric models based on some aspects of real physical behavior prescribed to the complex quantum many-body system, such as the Kratz-Herrmann formula [15, 16] and the gross theory [17] proposed in about four decades ago.

1.1.3 Why studying new β decay law of nuclei far from stability?

Along with the development of many kinds of experimental technologies such as the application of accelerators, of detectors, and of radioactive nuclear beams [18], many nuclei far from the β-stable line were synthesized and their properties were studied. Up till now, the study of nuclear physics has been extended to nuclei near the proton and neutron drip lines. This also includes the resonance states outside the drip line [19]. Many new experimental phenomena of nuclei such as the neutron-skin [20], neutron-halo [21, 156], proton-halo [23, 24], and "the island of inversion" [25] were discovered. With the accumulation of more and more data of nuclear β-decays far from β-stable line, it is feasible to make an empirical investigation on nuclear β-decay half-lives far from stability. New physics may lie behind the simple law, which can help to clarify the underlying physics of a certain phenomenon in an approximate but simple and transparent way.

For nuclei close to β-stable line, the β-decay half-lives change dramatically. There are two reasons for this. First, the β^--decay energy is very small for nuclei close to β-stable line. The nuclear structure effects, such as the even-odd effects and the structure of excited energy level, cause the large fluctuations of β-decay energy. This affects the β-decay half-lives significantly. Second, the uncertainty on ground-state and low-lying excited energy level structure such as parity and angular momentum will make it difficult to determine the forbidden level of β-decays. However, for the nucleus far from the β-stable line, the β-decay energy is much larger than that of the nucleus close to the β-stable line. As a result, the influence of certain nuclear structure effects can be smooth according to Fermi theory of β-decay. Furthermore, the decay of parent nucleus can go to a series of excited energy levels of daughter nucleus. The total decay probabilities are the sum of the probabilities of parent nucleus decays to different energy levels of daughter nucleus. Therefore the ground state angular momentum and parity are not so important as those for nuclei close to β-stable line. As a result, there may exist some new rules of β-decay half-lives to manifest this "mean" effect for nuclei far from stability. In Chapter 2, I present the systematical study on new law and formula of $\beta^{\pm}$-decay half-lives for nuclear far from stability. In addition, a parameterized formula is proposed to calculate half-lives of allowed orbital electron-capture transitions for nuclei close to β-stable line.

1.2 α decays and spontaneous fissions of heavy and superheavy nuclei

1.2.1 Island of stability

The idea of the island of stability was first proposed by nobel prize winner Glenn T. Seaborg. The heaviest known naturally occurring element is uranium, with an atomic number 92. In 1941, G. T. Seaborg and his team at the University of California, Berkeley, synthesized the second element heavier than uranium by bombarding it with neutrons (the first transuranium element neptunium was discovered in 1940 by the team of E. McMillan) [26]. The new element with an atomic number 94 was named plutonium. Subsequently, Seaborg made significant extensions to the periodic table, predicting several more elements heavier than uranium. His team went on to synthesize a total of 10 so-called transuranium elements, and pushed the periodic table of elements up to atomic number 106 in 1974, which was eventually named seaborgium.

Since then, other scientists have taken on the challenge of making "superheavy" elements (with an atomic number of 104 or more qualifies as superheavy) [27–33]. This is more than for better understandings of nuclear structure where the relativistic effects begin to manifest themselves in superheavy nuclei. When Seaborg started his work on transuranium elements, the accepted theory of the nucleus was the "liquid drop model", developed by Niels Bohr and John Wheeler [34]. In this model, the nucleus is regarded as a drop of charged liquid whose surface tension counteracted the Coulomb repulsion of the protons within, keeping the nucleus stable. Subsequent developments of both experiment and theory have shown that the nucleus has "shell structure", so the idea of shell model was proposed [35, 36].

In shell model, protons and neutrons populate discrete energy levels, within the nucleus, which is similar to electrons exist in atomic nuclei based on Pauli exclusion principle. The "shell" structure is formed by the groups of quantum energy levels that are relatively close to each other. Energy levels from quantum states in two different shells will be separated by a relatively large energy gap. So when neutrons and protons completely fill the energy levels of a given shell in the nucleus, the binding energy per nucleon will reach a local maximum and thus that particular configuration will have a longer lifetime than nearby isotopes that do not have filled shells. A filled shell would have "magic numbers" of neutrons and protons. It is confirmed by experiments the existence of proposed proton "magic numbers" (2, 8, 20, 28, 50, 82) and neutron "magic numbers" (2, 8, 20, 28, 50, 82, 126). This model successfully explains why some heavyish elements are unstable, such as the highly radioactive polonium (atomic number 84), while their neighbours on the periodic table, such as lead (82), are not. This is because Pb isotopes with proton magic number thus relatively large binding energies, this leads to large α decay energies of Po isotopes to daughter Pb isotopes. As a result, the half-lives of Po isotopes are much smaller than those of Pb isotopes.

One prediction of the shell model is the existence of long-lived superheavy elements - the island of stability - among a sea of unstable elements. These elements should have magic numbers of protons and neutrons thus much stabler than the other unstable isotopes. According to the theory, one possible magic number of neutrons for spherical nuclei is 184, and some possible matching proton numbers are 114, 120 and 126, due to the modification in the theory to account for the effects of superheavy nuclei.

1.2.2 Synthesis and identification of superheavy nuclei

Scientists has been working on synthesis of superheavy elements over the past several decades [27]. In laboratory, the synthesis of superheavy nuclei involves bombarding certain heavy elements with a beam of lighter "naked" nuclei - atoms with their electrons stripped away - in the hope that they might fuse into a new element. The key is to use nuclei for the beam which have just the right number of protons to form the superheavy element you want. For example, element 118 was formed by fusing californium, which has 98 protons, and calcium, which has 20. It's an elaborate and laborious procedure. The beam has to have just the right amount of energy to encourage fusion with the target. If the nuclei have too little energy, electrostatic repulsion between the two atomic nuclei causes them to ricochet apart. Use too much energy and the resulting combined nucleus is overexcited and unstable. The probability of fusing a projectile particle with one of the target nuclei is extremely small. Experiments can last for months, and produce as little as one superheavy element per month.

Despite the difficulties, scientists have made wonderful progress taking advantage of improved experimental technology recently. In 1995-1996 at GSI of Germany, $Z = 110-112$ elements were synthesized [27]. In Japan, synthesis of element $Z = 113$ in the reaction $^{209}\mathrm{Bi}(^{70}\mathrm{Zn,n})^{278}113$ was reported in 2004 [31]. In Dubna of Russia, Oganessian's team along with colleagues at the Lawrence Livermore National Laboratory (LLNL) in California, has pioneered the synthesis of atoms heavier than $Z = 113$ [28–30]. So far, they have made elements with atomic numbers 113-118 — the heaviest made to date. In 2001 and 2004, Gan *et al.* at Institute of Modern Physics in China also synthesized two superheavy isotopes $^{259}\mathrm{Db}$ and $^{265}\mathrm{Bh}$ with $Z = 105$ and $Z = 107$, respectively [32, 33].

1.2.3 Why studying decay half-lives of superheavy nuclei?

Currently, all synthesized superheavy elements are proton-rich nuclei due to the relatively large ratio of proton number over neutron number of lighter nuclei which fuse into the superheavy nucleus. Due to quantum tunnelling effect, α decay and spontaneous fission are two main decay modes of the synthesized proton-rich superheavy nuclei. Scientists have accumulated experimental data on a series of α decay chains of known superheavy isotopes. If one heavier isotope emits α particle, it will be a new comer in the α decay chain. According to the reconstruction of whole α decay chain, one can get the information of the new heavier element, like proton number, neutron number, α decay energy and half-life. Most of known superheavy elements are identified in this way.

Accurate prediction from theoretical model of the α-decay and spontaneous half-lives is a prerequisite for an elaborate design of the experiment for synthesis and identification of superheavy elements. Since the half-lives of superheavy elements change dramatically by several orders of magnitudes, the corresponding half-life measurements require different experimental technology. This is especially important due to the very rare and expensive of the projectile and target material used in the synthesis of superheavy elements. In Chapter 3, I present our improved theoretical calculations on the α decay and spontaneous fission half-lives of superheavy nuclei.

1.3 Quantum chromodynamics and relativistic heavy ion collisions

1.3.1 Quantum chromodynamics and deconfinement

§1.3.1.1 Quantum chromodynamics

Quantum chromodynamics (QCD) is one part of the modern theory of particle physics called the Standard Model. It has been established since the 1970s [37] to describe strong interaction — a fundamental interaction between the quarks and gluons which make up hadrons (such as the proton, neutron or pion). Other parts of this Standard Model deal with weak and electromagnetic interactions, another two fundamental interactions. The theory of electrodynamics has been tested and found correct to a few parts in a trillion. The theory of weak interactions has been tested and found correct to a few parts in a thousand. Perturbative aspects of QCD have been tested to a few percent. In contrast, non-perturbative aspects of QCD have barely been tested.

QCD is a non-abelian gauge theory invariant under SU(3) and as a result the interaction is governed by massless spin 1 objects called “gluons”. Gluons couple only to objects that have “color”: quarks and gluons. There are three different charges (“colors”): red, green and blue, compared to only one charge (electric) in quantum electrodynamics (QED). There are eight different gluons, and the gluon exchange can change the color of a quark but not its flavor. For example, a red u-quark can become a blue u-quark via gluon exchange. Since gluons have color there are couplings involving 3 and 4 gluons, while in QED the 3 and 4 photon couplings are absent since the photon does not have an electric charge.

The renormalized QCD effective coupling constant $\alpha_s(\mu)$ is dependent on the renormalization scale, similar to that in QED (running coupling). The QED running coupling increases with energy scale, while the gluon self-interactions lead to a complete different behavior in QCD. $\alpha_s(\mu)$ can be written as:

$$\alpha_s(\mu) \equiv \frac{g_s^2(\mu)}{4\pi} \approx \frac{4\pi}{\beta_0 \ln(\mu^2/\Lambda_{QCD}^2)}, \tag{1.1}$$

where μ is momentum transfer scale, β_0 is a constant dependent on the number of quarks with mass less than μ and Λ_{QCD} is called the QCD scale. When $\beta_0 > 0$, this solution illustrates the asymptotic freedom property: $\alpha_s \longrightarrow 0$ as $\mu \rightarrow \propto$, which means QCD can be calculated perturbatively in high momentum transfer or short distance approach [38]. On the other hand, this solution also shows strong coupling at $\mu \sim \Lambda_{QCD}$, so QCD is non-perturbative in this case. α_s needs to be determined from experiment. The world averaged α_s at the fixed-reference with μ_0 equal to the mass of Z boson $M_{\rm Z}$ is $\alpha_s(M_{\rm Z}) = 0.1184 \pm 0.0007$ [39], and the QCD scale $\Lambda_{QCD} = 217^{+25}_{-23}$ MeV. Fig. 1.1 shows the measured α_s at the respective energy scale μ [39].

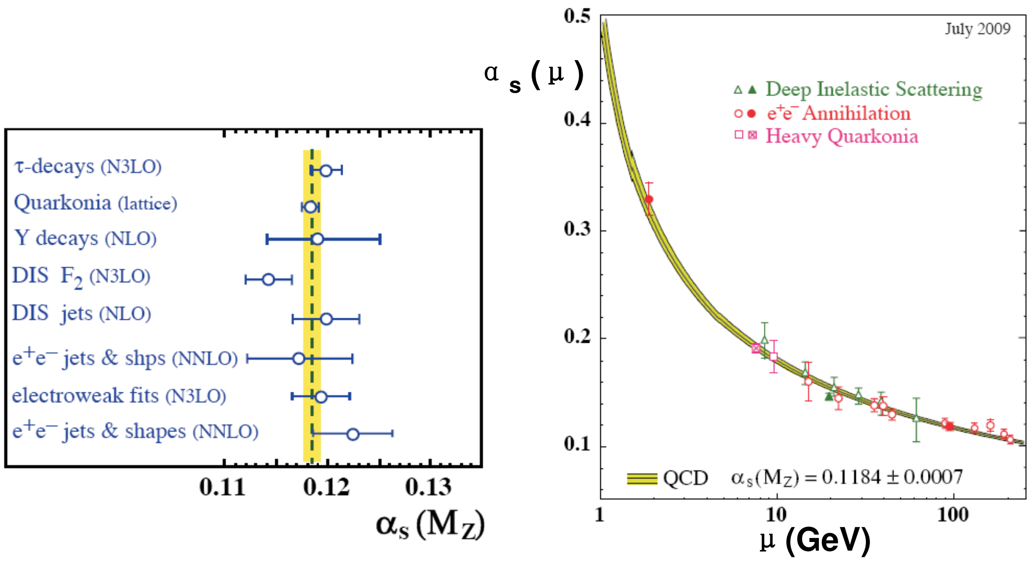

Figure 1.1: Left: Summary of measurements of $\alpha_s(M_{\rm Z})$, used as input for the world average value; Right: Summary of measurements of α_s as a function of the respective energy scale μ. Plots are from Ref. [39].

Due to the properties of coupling constants, the QCD are handled with different methods at different energy scales. The QCD can only be calculated perturbatively in high momentum transfer or short distance approach (pQCD). Although limited in scope, this approach has resulted in the most precise tests of QCD to date. At the strong coupling case, pQCD is irrelevant and some other methods are needed, such as Lattice QCD. The Lattice QCD uses a discrete set of space-time points (called the lattice) to reduce the analytically intractable path integrals of the continuum theory to a very difficult numerical computation which is then carried out on supercomputers. While it is a slow and resource-intensive approach, it has wide applicability, giving insight into parts of the theory inaccessible by other means. However, the numerical sign problem makes it difficult to use lattice methods to study QCD at high density and low temperature (e.g. nuclear matter or the interior of neutron stars).

§1.3.1.2 Quark confinement

Nowadays, all hadrons are found to be in color neutral states. Free quarks and/or colors have never been observed. People believe that quarks must be confined within hadrons to maintain the color neutral. Quark confinement in an SU(3) gauge theory can only be proved analytically for the 2D case of 1 space + 1 time. However, detailed numerical calculations show that even in 4D (3 space + time) quarks configured as mesons and baryons in color singlet states are confined.

Intuitively, confinement is due to the force-carrying gluons having color charge and self-coupling. In QED case, there is no self coupling between photons. As any two electrically-charged particles separate, the electric fields between them diminish quickly, allowing (for example) electrons to become unbound from atomic nuclei. However, as two quarks separate, the gluon fields form narrow tubes (or strings) of color charges, which tend to bring the quarks together as though they were some kind of rubber band. Because of this behavior, the color force experienced by the quarks in the direction to hold them together, remains constant, regardless of their distance from each other. The color force between quarks is large, even on a macroscopic scale, being on the order of $\sim$100,000 newtons. As discussed above, it is constant, and does not decrease with increasing distance after a certain point has been passed.

When two quarks become separated, as happens in particle accelerator collisions, at some point it is more energetically favorable for a new quark – antiquark pair to spontaneously appears out of the vacuum, than to allow the quarks to separate further. As a result of this, when quarks are produced in particle accelerators, instead of seeing the individual quarks in detectors, one can see “jets” of many color-neutral particles (mesons and baryons), clustered together. This process is called hadronization, fragmentation, or string breaking, and is one of the least understood processes in particle physics.

§1.3.1.3 QCD phase transition and quark-gluon plasma

Quarks are confined in hadrons at ordinary conditions with relatively low energy and particle number densities. If the media is so dense that several hadrons overlap, the 'other' color charges will screen the binding forces between the quarks of any given hadron. As a result, the constituents of the medium become deconfined, since screening suppresses the long-range confining potential

$$\sigma r \to \sigma r(\frac{1-e^{-\mu r}}{\mu r}), \tag{1.2}$$

in a form similar to the Debye screening of the Coulomb potential [40–42]. The screening mass μ is the inverse of the screening radius and increases with temperature, so that the range of the potential decreases, and eventually deconfinement sets in [40].

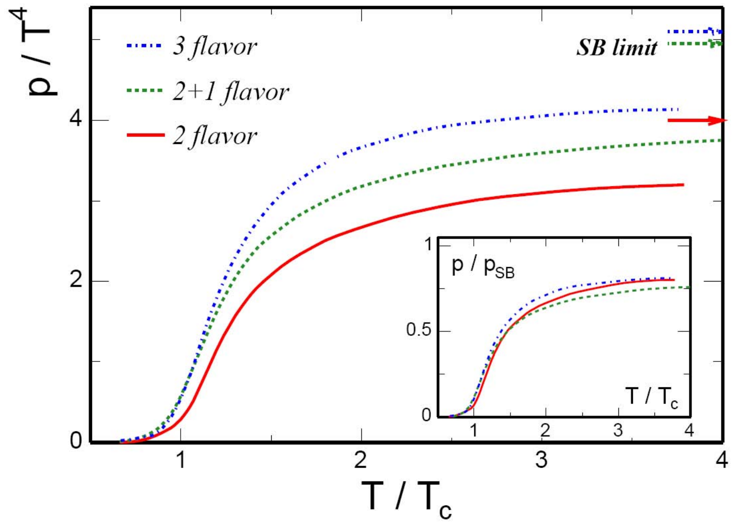

Figure 1.2: Lattice QCD calculation results for the pressure p divided by T^4 of strongly interacting matter as a function of temperature T. The arrows indicate the Stefan-Boltzmann limit for each case. The insert plot shows the ratio of p/p_{SB} as a function of T [43].

At enough high temperature and high energy density, the Lattice QCD predicted a phase transition from normal QCD (hadron) matter to a new form of matter, named Quark Gluon Plasma (QGP), with new color degrees of freedom (DOF). In this new phase, quarks and gluons are liberated from hadrons, and can move around in a larger distance rather than confined in hadrons, which is called deconfinement. Within the volume of QGP, the quarks and gluons will manifest themselves with color degrees of freedom, while outside this volume, it should still show color neutral. It is illustrated in

Fig. 1.2 the appearance of these color DOF by a sharp increase in pressure around the critical temperature of this phase transition. In Fig. 1.2, the arrows indicate the Stefan-Boltzmann limits, which are for the systems with massless, non-interacting quarks and gluons. The energy density divided by T^4 shows similarly sharp increasing trend around the critical temperature of this phase transition.

1.3.2 Ultrarelativistic heavy ion collisions

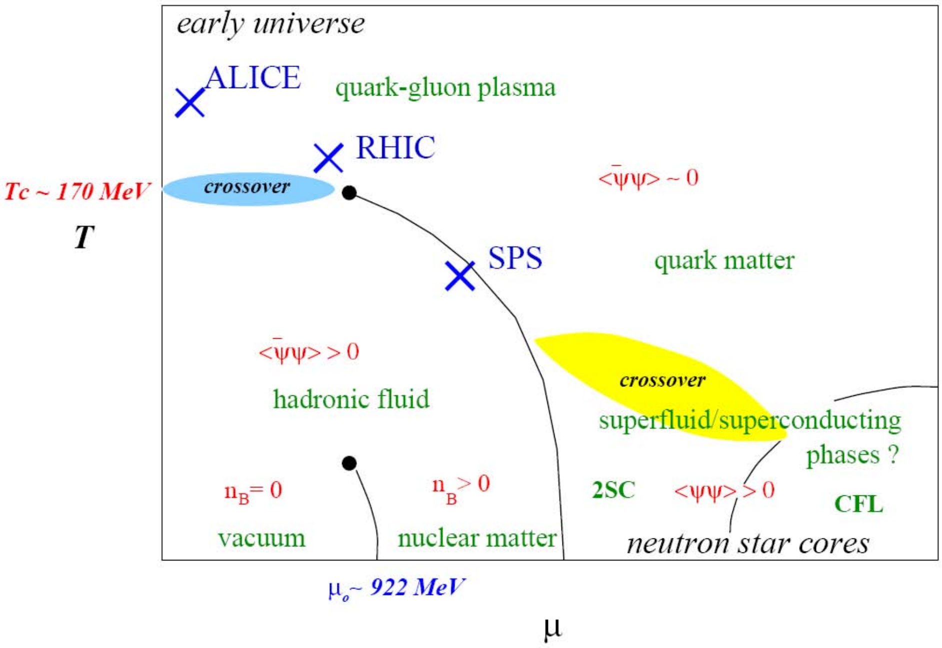

Figure 1.3: The contemporary view of the QCD phase diagram from Ref. [44]. SPS, RHIC and ALICE (LHC) are the names of relativistic heavy-ion collision experiments. 2SC and CFL refer to the diquark condensates [44].

One of the proposed QCD phase diagram (temperature versus baryon chemical potential) [44] is shown in Fig. 1.3. From the phase diagram, high temperature and low baryon chemical potential is one of the way to reach the QGP phase in experiment. Since 1970's, there are/were many experiments including BEVALAC at LBL, SIS at GSI, AGS at BNL, SPS at CERN, RHIC at BNL and the coming LHC at CERN with increasing center-of-mass energy (higher temperature) trying to discover and study the QGP phase.

The Relativistic Heavy Ion Collider (RHIC) at Brookhaven National Laboratory (BNL) is the first machine in the world capable of colliding heavy ions. RHIC collides two beams of gold ions head-on when they are traveling at nearly the speed of light. Because of Lorentz contraction (γ = 106.6 for 100 GeV/c^2 proton) in the moving direction of the ion, two nuclei can be represented as two thin disks in the laboratorial frame of reference. The two colliding nuclei pass through each other in a very short time about 0.13 fm/c. The question is how much energy is stored in this collision. From the fact that baryon number is conserved and the rapidity distribution is only slightly affected by rescatterings in the late stage of collisions, one can estimate the initial deposited energy by using the rapidity loss of net baryon number ($B - \overline{B}$) to study the energy loss of initial participant nucleons. It is estimated that $73 \pm 6^{+12}_{-26}$ GeV of the initial 100 GeV per participant is deposited and available for excitations from the measurements of BRAHMS Collaboration at RHIC [45].

§1.3.2.1 Initial condition of nuclear collisions

From theoretical calculations, the expected critical energy density for the QGP phase transition is $\varepsilon_c \sim 1$ GeV/fm^3. To measure the energy density, one can count up the energies in produced particles/matter at velocities/rapidities intermediate between those of the original incoming nuclei. In the Bjorken model [46], the produced "quanta" goes out with random velocities after a finite formation time and follow classical trajectories. Here the "quanta" formation time τ at mid-rapidity ($p_z \sim 0$) is estimated according to its transverse energy $m_T = \sqrt{p_T^2 + m_0^2}$, where p_T is transverse momentum and m_0 is the rest mass of the "quanta". From the PHENIX measurements [47] of the mean transverse energy of final state formed hadrons, one can approximately estimate the formation time $\tau \sim 0.35$ GeV/c according to the uncertainty principle $\tau \sim \hbar/m_T$. The initial Bjorken energy density [46] can be calculated using formula:

$$\varepsilon_{BJ} = \frac{1}{A_\perp \tau} \frac{dE_T}{dy}, \tag{1.3}$$

where $A_\perp$ is the area of nuclei transverse overlap region. The measured dE_T/dy from PHENIX Collaboration [47] indicates an initial energy density of ~ 15 GeV/fm^3 assuming $A_\perp = \pi R^2$ and $R \approx 1.2 A^{1/3}$ fm at central Au + Au collisions at RHIC. Here the assumption is that the number density of "quanta" does not go down with time (entropy conservation) and the transverse energy density dE_T/dy only goes down with time. Thus the initial energy density at RHIC is believed to be capable of QGP formation.

However, very little is known about the initial conditions. The first question is: how does the initial collision nucleus look like at extreme high energy, that is, what is the parton (quark/gluons) distribution in the energetic nucleus? This is especially important for the small x region (momentum fraction of the nucleon in the nucleus carried by the interacting parton). In high energy collisions, the multiplicity of produced hadrons as a function of the distance from the fragmentation region, is approximately independent of energy. That means the large x degrees of freedom do not change much (related to valence quarks). When the collision energies increase, the new physics is associated with the additional degrees of freedom at small rapidities ($p_z \sim 0$) in the center of mass frame (small-x degrees of freedom) since with higher energies we can probe the sea quarks and gluons which relate to small x [48]. That is, in the mid-rapidity region, the enhanced particle production is caused by more and more sea quarks and gluons which involves in the interactions.

At the initial time, the degrees of freedom are most energetic and therefore one has the best chance to understand them using weak coupling methods in QCD. In the Glauber model and pQCD framework, the nucleus-nucleus interaction are described in terms of interaction between the constituent nucleons with a given density distribution. The hard scatterings between nucleons will result in energetic partons (minijet). The produced minijet partons scatter with each other and/or fragment into hadrons according to empirical string fragmentation model. Small x partons are mainly sea quarks and gluons, the corresponding Q^2 are small, thus related to large wavelengths according to the uncertainty principle. Therefore it goes through more multiple scatterings compared to the large x parton with only small wavelength. As a result, the opacity of the nuclei is large for the small x partons. In this framework, the large p_T (related to large x) hadron yields in A+A collisions should scale with the number of binary nucleon-nucleon collisions in the absence of subsequent final state interactions after its production. Here the initial nuclear effects are pure geometrical effects related to the opacity of the nucleus for partons with different energy scale. The whole process can be modeled in a transport theory. However, the transport model can not describe the particle down to $\tau = 0$ since classical transport theory assumes we know a distribution function $f(p, x, t)$ [48], which is a simultaneous function of momenta and coordinates. At some early time $\tau = 0$, the initial state is quantum mechanical state, thus the distribution function $f(p, x, t)$ violates the uncertainty principle. Furthermore, since there is zero entropy of the initial quantum state and a finite one with distribution function $f(p, x, t)$, this is also related to the basic question: where does the entropy come from? [48]

Another description of the initial nuclear effects is Color Glass Condensate (CGC) [48]. The CGC states that the nucleus at extremely high energies is represented by a new form of hadronic matter, a dense condensate of gluons. These gluons can be packed until their phase space density is so high that interactions prevent more gluon occupation. This forces at increasingly high density the gluons to occupy higher momenta, and the coupling becomes weak. The density saturates at $\sim 1/\alpha_s \gg 1$, and is a condensate. The model describes genuine dynamical nuclear effect due to nonlinear gluon interactions. When the two colliding nuclei pass through each other, the "quantas" are produced from the induced classic color field which evolutes with time. At some time, the energy density becomes dilute, and the field equations should linearize in some gauge. One can then identify the "quanta" of the linearized fields in the standard way that one does in classical radiation theory of electrodynamics [48]. CGC is important because it has proposed a universal form of matter that describes the properties of all high-energy, strongly interacting particles. It should be tested with high energy experiment where the dynamical effects begin to play a role besides the geometrical effects as shown in the Glauber plus pQCD framework.

§1.3.2.2 Pre-equilibrium, thermalization and hydrodynamic evolution

From the above two different initial descriptions of nuclear initial parton distribution and the followed dynamics, the initially produced energetic partons and/or hadrons scatter with each other strongly due to very high "quanta" number density. The system may reach local thermal equilibrium, meanwhile the residual hadrons (if there are) melts down, and the quark-gluon plasma forms. If the system reaches thermal equilibrium, then the QGP evolution can be approximately described by perfect fluid hydrodynamics [46]. The hydrodynamical models need the equation of state (EOS) of QCD matter as an essential input, which can be obtained in time-consuming Lattice calculation or other methods, for example, Dyson-Schwinger approach [49, 50].

One important observable which is sensitive to this stage is elliptic flow. In non-central heavy-ion collisions, in the plane transverse to the beam direction, the initial overlap region is not a circle, but an ellipse. If there are no re-interactions the produced matter will free stream to the detector, thus the initial geometry will have no influence on the evolution, and the angular distribution of the final observed hadrons will also be azimuthally symmetric [51]. On the other hand, if there are strong rescatterings between the "quantas" which maintain local thermal equilibrium, the pressure gradients in the direction of short axis x of the ellipse (dP/dx) will be larger than that in its long axis y direction. An anisotropy in the coordinate space will develop, and ultimately translate to the anisotropy in the momentum space in the transverse plane. Experimentally, this momentum anisotropy (elliptic flow) is characterized by the second harmonic coefficient (v_2) of an azimuthal Fourier decomposition of the momentum distribution of final produced particles in the transverse plane, that is, the particle production with respect to the reaction plane can be written in a form of Fourier series,

$$E\frac{d^3N}{d^3p} = \frac{1}{2\pi}\frac{d^2N}{p_T dp_T dy}(1 + \sum_{n=1}^{\infty} 2v_n \cos[n(\varphi - \Psi_r)]), \tag{1.4}$$

where Ψ_r is the real reaction plane angle and φ is the particle's azimuthal angle. Experimentally one can approximately use the event plane to denote Ψ_r and the event plane can be determined by summing the flow vectors of all particles in the transverse plane [52]. The coefficient v_2 in the second order term of the expansion is the dominant part and is called the 2nd harmonic anisotropic flow parameter, or elliptic flow.

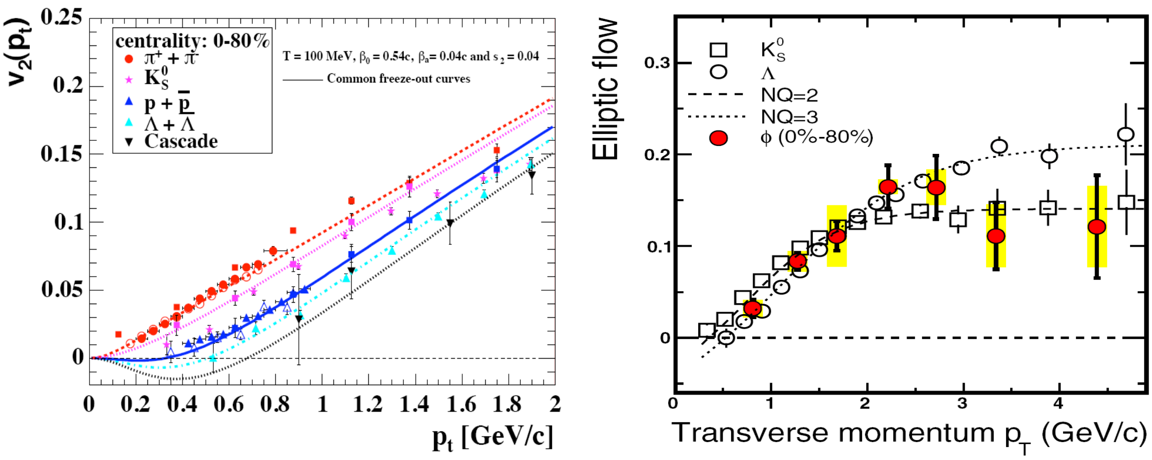

Figure 1.4: Left: Comparison of "minimum bias" $v_2(p_T)$ dependence on particle mass with hydrodynamic inspired blast-wave model fits. Figure is taken from [53]. Right: STAR results on minimum bias v_2 as a function of p_T for the ϕ meson, K^0_S, and $\Lambda + \overline{\Lambda}$. The dashed and dotted lines represent what is expected from coalescence for two- and three-quark particles. Figure is taken from [54].

Elliptic flow for identified particles have been extensively measured at RHIC, as shown in Fig. 1.4 [53]. In the left panel of Fig. 1.4, v_2 is plotted as a function of particle transverse momentum for pions, K^0_S, protons and antiprotons, $\Lambda + \overline{\Lambda}$ and Cascades. In this low p_T range ($p_T < 2$ GeV/c), v_2 is positive and increase with particle transverse momentum. This shows that the anisotropy in coordinate space at early time is transferred to the anisotropy in momentum space. When we compare the particle species dependence of v_2, there is larger v_2 for lower mass particles at the same p_T.

This phenomenon can be qualitatively understood by the interplay between radial flow and anisotropic flow [55]. The velocity of hadrons are affected by average radial expansion velocity, anisotropic velocity caused by different pressure gradient in x and y direction (the amplitude of modulation in radial expansion velocity as a function of the relative angle to the reaction plane), and thermal velocity, which depends on the temperature and the mass of the particle [55]. The velocity of a hadron in the reaction plane direction x is larger than that in perpendicular direction y. This pushes the particles in x direction to higher p_T, thus decreases more number of particles at low p_T in x direction than in y direction. As a result, the low v_2 at p_T is reduced. The radial flow effects are larger for particles with larger rest mass since $\triangle p_T = m_0 \triangle v_T$ increases with rest mass m_0. Therefore v_2 of the hadrons with larger masses are decreased more. This measured mass ordering of v_2 is consistent with hydrodynamic inspired blast-wave model fits which assume ideal relativistic fluid flow and negligible relaxation time compared to the time scale of the equilibrated system. The parameters in the blast-wave fits are a common set of four freeze-out parameters: the temperature, the mean radial flow velocity, the azimuthal dependence of the radial flow velocity and the source deformation [56]. The agreement may imply the local thermalization caused by strongly interactions and short mean free path within the matter is reached during the early stages of the collisions. However, more decisive measurements such as heavy quark flow is needed.

The advantage of this model fit is that it provides an accurate description of the system at freeze-out [53] and can be used to extract the freeze-out temperatures for different hadrons. However, to get a full understanding of the initial conditions, QGP transport properties like shear viscosity and the possible phase transition from the QGP to hadron gas, the full dynamic description with hydrodynamic evolution, QGP phase transition and the subsequent hadron cascade is needed, since the hadronic dissipation effect would contribute to the QGP viscosity to a large extent. This should also be studied in further experimental measurements on multi-strange hadrons v_2 which are not sensitive to late hadronic rescatterings and on heavy-quark elliptic flow since the heavy quarks are produced in the early stages.

In ideal hydrodynamics the mass ordering in v_2 persists up to large p_T, although less pronounced because the v_2 of different particles start to approach each other [53]. However, it is shown in the right panel of Fig. 1.4 that v_2 at intermediate p_T does not follow the mass ordering anymore. v_2 of heavier hadrons like ϕ meson is close to that of lighter hadron like K_S^0, while the heavier baryon has larger v_2. The baryon-meson grouping phenomenon has inspired the quark coalescence explanation on hadron production at intermediate p_T. The number-of-quark scaling [57] has been used to fit the observed v_2. This offers a strong evidence which is used to argue that the collectivity is developed at partonic level and there is deconfinement at RHIC. Besides the simple quark coalescence explanation which specializes at intermediate p_T, viscous hydrodynamic calculation by including species dependent relaxation time is trying to address this phenomenon with a more consistent way [51]. The details are discussed in the following section 1.3.4.3.

Another important observable which is sensitive to this stage is hard parton — medium interaction and energy loss. Since the energetic hard parton is mainly produced during the initial hard scattering, when it travels through the dense medium (contains a lot of "quantas"), it loses energy through collisional energy loss and medium-induced gluon radiation, the latter being the dominant mechanism in a QGP. If the initial interaction is very strong, then the high p_T hadrons produced from the hard partons fragmentation will be suppressed. In Glauber model + pQCD framework, the high p_T hadron yields should be scaled by number of binary collisions in the absence of parton-medium interactions. The ratio of the hadron yields in ion (A+B) collision and those in p+p collisions, scaled by the number of binary nucleon-nucleon collisions:

$$R_{\mathrm{AB}}(p_T) = \frac{d^2N_{\mathrm{AB}}/dp_Tdy}{T_{\mathrm{AB}}d^2\sigma^{\mathrm{pp}}/dp_Tdy}; \tag{1.5}$$

should reflect the strength of energetic parton and medium interactions. In Eq. (1.5), $T_{\mathrm{AB}} = N_{bin}/\sigma_{pp}^{inel}$ is the nuclear overlap geometry factor, calculated from a Glauber model [58]. In the absence of parton-medium interactions, the R_{AB} at high p_T should be consistent with unity.

The left panel of Fig. 1.5 shows the STAR measurements on R_{AB} as a function of transverse momentum in d+Au and Au+Au 200 GeV collisions at RHIC. One can see a strong suppression of high p_T hadrons in central Au+Au collisions, while in d+Au central (0-20%) collisions with cold nuclear matter, the suppression is not apparent. This large suppression is so surprising since the SPS Pb+Pb central-to-peripheral nuclear modification factor R_{CP} at $\sqrt{s_{NN}} = 17.3$ GeV has shown no significant suppression for p_T up to 5 GeV/c [60]. It offers evidence that the energetic partons strongly interact with the hot dense medium and lose energy, producing lots of soft particles instead of fragmenting into high p_T hadrons.

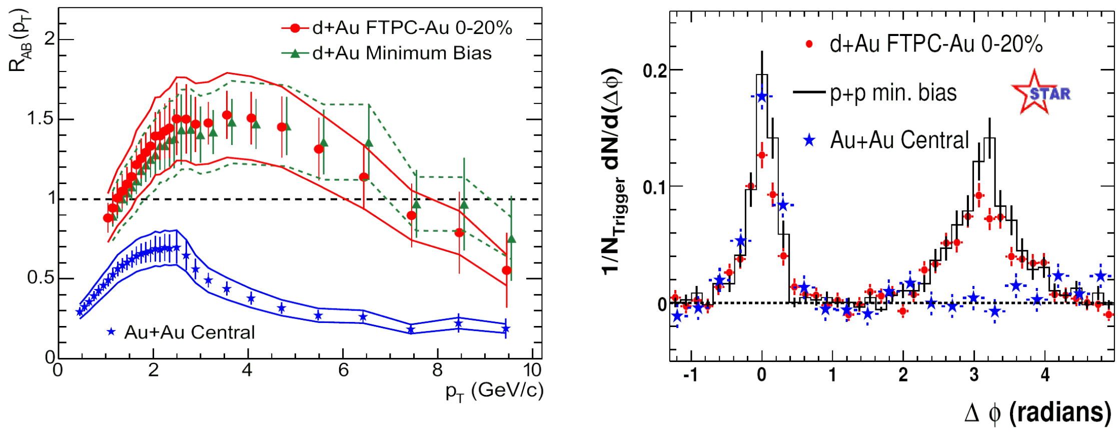

Figure 1.5: Left: STAR data on R_{AB} as a function of transverse momentum in d+Au and Au+Au 200 GeV collisions at RHIC. Right: Two particle azimuthal distributions in p+p, d+Au central and Au+Au central collisions at $\sqrt{s_{NN}}$ = 200 GeV. Figure is taken from Ref. [59].

The energy loss may have a path length dependence. The initial produced parton pairs should have opposite directions due to energy and momentum conservation. Thus if one measures the back-to-back azimuthal correlation of the high p_T hadrons, it will disappear due to strong rescatterings when the hard partons traverse through the medium. It is shown in the right panel of Fig. 1.5 that the azimuthal angle distribution of hadrons with $p_T^{associated} > 2$ GeV/c relative to a trigger hadrons with $p_T^{trigger} > 4$ GeV/c. A hadron pair produced from a single jet will generate an enhanced correlation at near side ($\triangle\phi \sim 0$), as observed for p+p, d+Au and Au+Au collisions, with similar correlation strengths, widths. The pair from the back-to-back jet correlation at ($\triangle\phi \sim \pi$) is only present in p+p and d+Au collisions while it almost completely disappears in central Au+Au collisions. This is consistent with the expectation of strong interactions between initially produced parton and the hot dense medium.

§1.3.2.3 Hadronization and later-stage hadronic interactions

The temperature of system will decrease with the continuous expansion of the system, the matter becomes more and more dilute and when it drops to critical temperature, the possible QGP phase is transformed to hadron resonance gas through a transition. The hadronization mechanism is not clear yet. In the hydrodynamic description, the freeze out happens at hyper-surface with parameterized space-time points. Assuming local thermalization, particle momentum distribution at the freeze-out hyper-surface follows the Cooper-Frye formula [61]. In the transport model, where no thermalization is assumed, the hadrons are formed from either string fragmentation or quark coalescence [62]. After the hadrons are formed, they scatter with each other inelastically and elastically. At some time, the chemical component of the hadrons doesn't change any more, then it is called as chemical freeze-out. After chemical freeze-out, the hadrons still scatter with each other elastically and their transverse momenta change. When the hadrons do not scatter with each other any more, it is called kinetic freeze-out.

The later stage hadronic interactions strongly depend on the hadronic cross sections. For multi-strange hadrons, their hadronic cross sections are thought to be small with other non-strange particles, therefore, they will freeze-out early from the system. The blast-wave fits on measured transverse momentum distribution of $\phi(s\bar{s})$ and $\Omega(sss)$ show that they freeze out early from the system with a relatively high temperature and small collective velocity [63]. As a result, they are thought to carry the information just around the hadron formation (at the time QGP transition to hadron gas). So they are ideal probes to illustrate the properties of the possible quark-gluon plasma created at RHIC.

1.3.3 Cronin effect and d+Au collisions at RHIC

As shown in section 1.3.2.2, The high p_T hadron suppression is a key measurement in Au+Au 200 GeV collisions at RHIC [59], since it is surprisingly large compared to that at SPS energy ($\sqrt{s_{NN}} = 17.3$ GeV) where no significant suppression of high-p_T hadron production is observed [60]. Two different theoretical frameworks: pQCD and CGC (shown in section 1.3.2.1) which are related to different initial conditions of relativistic nuclear collisions can describe this phenomenon. The pQCD calculations [64–68] shows that the energy loss of parton propagation in a dense medium induced by multiple scattering is proportional to the gluon density. Within this framework, RHIC data thus indicate an initial gluon density in central Au + Au collisions at the RHIC energies is much higher than that in a large cold nucleus. The CGC mechanism was recently proposed for the observed high-p_T hadron suppression in Au+Au collisions at RHIC based on the parton saturation in the initial energetic nucleus. The CGC model [69] also predicts a similar high-p_T suppression in p+A collisions at RHIC, in contrast to the predicted enhancement or ~ 1 (at mid-rapidity) by the multiple parton scattering model. Especially when approaching forward (deuteron beam direction) rapidity, the suppression will be more apparent. Thus the d+Au results will allow one to clarify the relative importance of initial and final state interactions at different transverse momenta and rapidities of the produced particles [69]. They are necessary for establishing a complete physical picture of heavy ion collisions at RHIC energies.

To start this section, a brief introduction on the p+A results (the well-known Cronin effect) at lower energy is presented in the following.

§1.3.3.1 Cronin effect

Cold nuclear matter effects are non-QGP effects. It forms baseline features of nuclear collisions. To announce the QGP formation at RHIC, it is quite important to disentangle the cold nuclear matter effect and QGP effect. For hard process, like high-p_T particle and J/ψ production, it is calculable in perturbative QCD. If there is no cold nuclear matter effect, the hard processes should have a linear A (atomic number) dependence of cross section in p+A like collisions, that is, $\sigma_{\mathrm{pA}} \sim \sigma_{\mathrm{pp}} A$, where σ_{pA} is the cross section in p+A collisions and σ_{pp} is the cross section in p+p collisions.

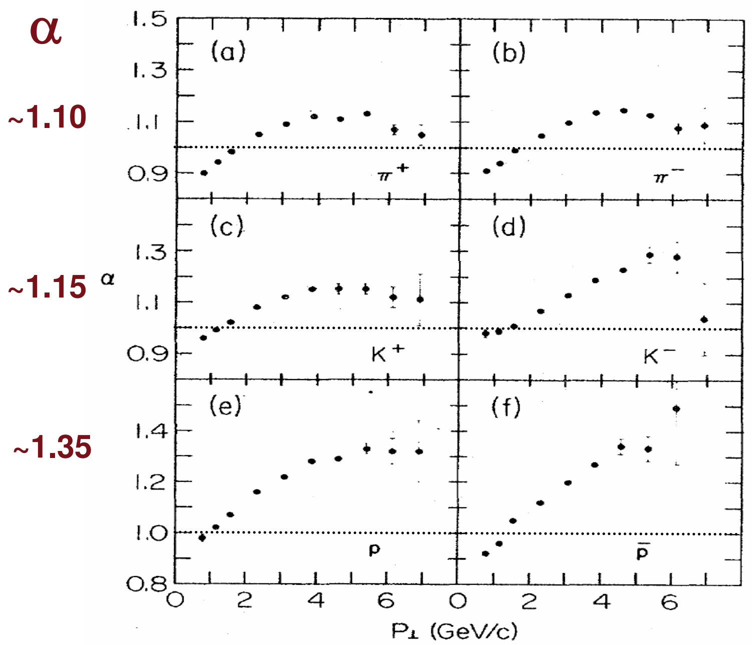

Figure 1.6: The power α of the A dependence of the invariant cross section versus p_T for the production of hadrons by 400-GeV protons; (a) π^+, (b) π^-, (c) K^+, (d) K^-, (e) p, and (f) $\bar{p}$. Figure is from [71].

It was first discovered by Cronin *et al.* [70, 71] that there is enhanced hadron production at large transverse momentum (p_T) with increasing target nucleus size in fixed-target proton-nucleus (p+A) collisions at center of mass energy $\sqrt{s_{NN}} = 27.4$ GeV. The invariant cross section of per nucleus is parameterized in the following form

$$\sigma(p_T, A) = \sigma(p_T, 1) A^{\alpha(p_T)}. \tag{1.6}$$

It is seen from Fig. 1.6 that α is significantly larger than 1 at large p_T, indicating that the cold nuclear matter has extra effect on particle production. In addition, the enhancement of proton is larger than that of kaon, and the kaon enhancement is larger than π. This shows a particle species dependence of the enhancements. Later experiment with higher center of mass energy $\sqrt{s_{NN}}$ = 38.8 GeV (800 GeV projectile protons on the fixed tungsten(W) and beryllium(Be) targets) shows similar effect [72].

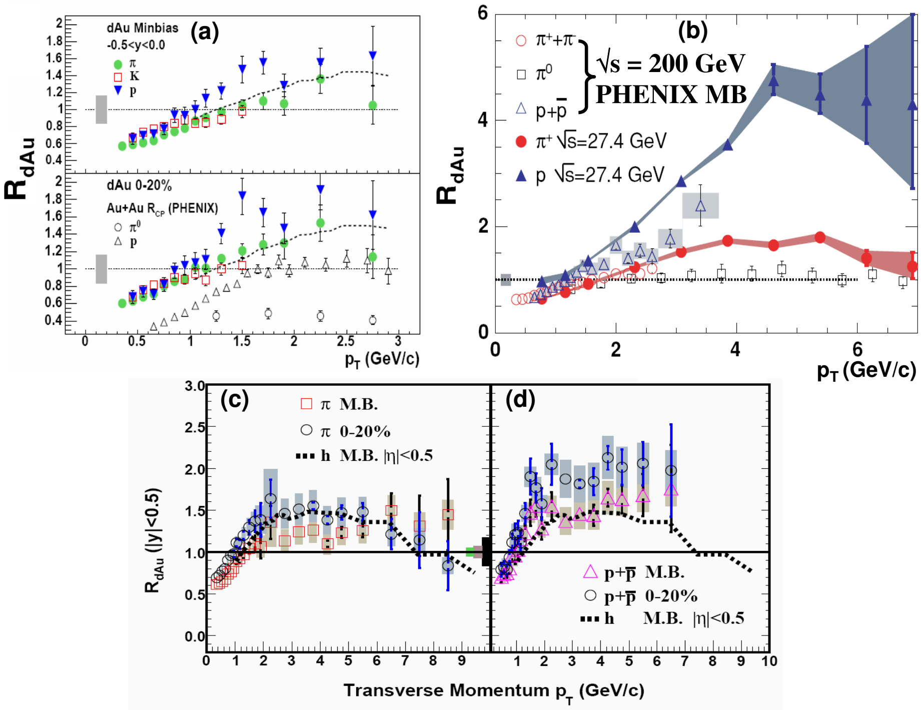

Figure 1.7: Nuclear modification factors for pions, protons and antiprotons from d+Au collisions at $\sqrt{s_{NN}}$ = 200 GeV: (a), (c), and (d) STAR results [73]; (b) PHENIX measurements [74]. Nuclear modification factors calculated from the per-beam nucleon cross sections which were reported for $\sqrt{s_{NN}}$ = 27.4 GeV p+A fixed target experiment are also presented in figure (b) for comparison [71].

§1.3.3.2 d+Au collisions at RHIC

In the later study, the "Cronin Effect" is explained by the broadening of the parton transverse momentum distribution at intermediate p_T due to multiple scatterings in p+A collisions as compared to those in p+p collisions. However, the origin of Cronin enhancement and its particle species dependence are not yet completely understood, and further experimental study is warranted in its own right [74]. Furthermore, in the search for the quark gluon plasma at the BNL Relativistic Heavy Ion Collider (RHIC), the Cronin effect is extremely important, as novel effects observed in central Au +

Au collisions require good control of the initial state conditions. As shown in previous section, at RHIC energies ($\sqrt{s_{NN}} = 200$ GeV), it was discovered that hadron production at high transverse momentum ($p_T > 2.5$ GeV/c) is strongly suppressed with respect to the binary scaling expectation in central Au + Au collisions [59] compared to nucleon-nucleon collisions. Such suppression may be interpreted as a consequence of the energy loss suffered by the hard-scattered partons as they propagate through the hot and dense medium. However, since the Cronin effect acts in the opposite direction, enhancing the hadron yields, it has to be taken into account when the parton energy loss is determined from the data.

The effects from the initial state are best studied by performing a control experiment in which no hot and dense matter is produced [74]. Deuteron+gold collisions at $\sqrt{s} = 200$ GeV serve this purpose. Since there is no hot and dense final state medium, the initial-state conditions become accessible to the experiment. In addition to Cronin enhancement, known initial state effects also include nuclear shadowing and gluon saturation [69].

Recent experimental data in d+Au collisions from RHIC have shown that similar effect exists at higher collision energy ($\sqrt{s} = 200$ GeV) [73, 74]. It is shown in Fig. 1.7 both STAR and PHENIX have measured that the nuclear modification factors R_{dAu} of protons and pions are larger than 1 at large p_T. Here R_{dAu} is the ratio between particle yields in d+Au collisions and those in p+p collisions scaled by number of binary collisions (see Eq. (1.5)). The p_T dependence of nuclear modification factor is also similar to that measured at low energy fixed target experiment. When comparing with $\sqrt{s_{NN}} = 27.4$ GeV fixed target experiment, in 200 GeV collisions the magnitude of the enhancement for pions at $p_T > 3$ GeV/c is smaller, as shown in Fig. 1.7(b).

It is interesting to discuss why there is larger enhancement at $\sqrt{s_{NN}} = 27.4$ GeV fixed target experiment than at RHIC. This energy dependence of the Cronin effect for pions has been interpreted as evidence for a different production mechanism for high-p_T hadrons at RHIC energies compared to lower energies [75]. In this model, high-p_T hadrons are produced incoherently on different nucleons at low energy, while in higher energy collisions the production amplitudes can interfere because the process of gluon radiation is long compared to the binary collision time. Coherent radiation from different nucleons is subject to Landau-Pomeranchuk suppression. However, the particle species dependence of Cronin effect is not predicted by this model.

§1.3.3.3 How to understand particle species dependence of Cronin effect?

Although the Cronin effect has been discovered for more than 30 years, it is not fully understood. One important unexplained question is the particle species dependence of Cronin effect. It is difficult because this is related to the basic question, that is, the mechanism of hadron production.

Parton p_T broadening due to initial-state multiple scatterings? The Cronin enhancement is usually attributed to parton transverse momentum broadening due to multiple initial-state soft [76] or semihard [77–80] scatterings. Such models typically do not predict the particle species dependence observed in the data, although they can reproduce the observed centrality dependence for pions very well by choosing appropriate parameters of parton transverse momentum broadening.

Hadronization from final-state parton coalescence in d+Au? Recently, Hwa and Yang [81] demonstrated the recombination of soft and shower partons in the final state could explain different enhancements of intermediate p_T protons and pions. This model predicts a larger enhancement for protons than for pions at $1 < p_T < 4$ GeV/c. It shows there is no distinction of the hadronization mechanism if hot or cold nuclear matter is produced. However, the inclusion of recombination from deconfined partons requires a high energy density in initial state, which may not be justified in d+Au collisions.

1.3.4 Why using ϕ meson to study heavy ion collisions?

§1.3.4.1 Unique properties of ϕ meson

ϕ meson is thought to have small hadronic cross sections with other non-strange particles. The effect of hadronic rescatterings on ϕ meson is thought to be small, thus it is a good probe for extracting the properties of QGP accurately. ϕ meson is also a heavy meson with mass close to proton or Λ. It is convenient to use ϕ meson for distinguishing meson-baryon effect or mass effect. ϕ ($s\bar{s}$) meson also provides important information on strangeness enhancement due to its hidden strangeness. In addition, it decays in both hadronic channels and di-leptonic channels. This is thought to be nice probe for possible chiral symmetry restoration in QGP.

From phenomenological analysis, it is suggested that the ϕ meson mean free path in hadronic media is large because of its small cross section of scattering with hadrons [82]. Many other calculations also indicate that the ϕ meson has small rescattering cross sections with hadronic matter [83, 84]. However, after including three- and four-vector meson vertices into their hidden local symmetry model, Alvarez-Ruso and Koch [85] found that the ϕ meson mean free path in nuclear media is smaller than that usually estimated. Ishikawa *et al.* [86] presented new data on near-threshold ϕ meson photoproduction on several nuclear targets. They found that the cross section between a ϕ meson and a nucleon, $\sigma_{\phi N}$, is equal to 35^{+17}_{-11} mb, which appears to be much larger than previous expectations, although the experimental uncertainty is very large [87]. Meanwhile, Sibirtsev *et al.* [88] presented a new analysis of existing ϕ photoproduction data and found $\sigma_{\phi N}$ ~10 mb. Thus, $\sigma_{\phi N}$ in heavy-ion collisions is still unclear. The measurement of ϕ production in heavy ion collisions will provide additional information on ϕ-hadron cross sections.

§1.3.4.2 Study particle species dependence of Cronin effect by ϕ meson production in d+Au collisions

To address the long-outstanding problem of the origin of Cronin effect, especially its particle species dependence, both experimental data and new theoretical insights are needed.

In theoretical side, after hadronization, the effect of final state hadronic rescatterings and resonance decays has not been studied yet. This is correlated with hadronization mechanism and hadron formation time. Besides the hadronization from coalescence, an alternate way for hadronization is string fragmentation [62, 89–92]. In this scenario, hadrons are formed from the decays of excited strings, which result from the recombination of energetic minijet partons and soft strings that produced from initial soft nucleon-nucleon interactions. After the hadronization, the followed rescatterings between formed hadrons or between formed hadrons and nucleon spectators should also be taken into account.

In the following section 6.1, quantitative study is performed on how the two different hadronization mechanisms (string fragmentation and parton coalescence) and the subsequent hadronic interactions would contribute to the nuclear modification factors in d+Au collisions at $\sqrt{s}$ = 200 GeV. A multiphase transport model (AMPT) [62, 92] with two versions: default (hadronization from Lund string fragmentation, mainly hadronic rescatterings in the final state, version 1.11) and string melting (hadronization from quark coalescence, version 2.11) are used to study the later-stage effect. The final state hadronic and/or partonic interactions are included in the calculations. Quark transverse momentum kick due to multiple scatterings are treated in the same way as in Ref. [91].

To have a clean test of final state interactions, we assume no extra quark intrinsic p_T broadening [80], and see how the final state interactions would contribute to the Cronin effect observed. We show for the first time that recent data on particle species dependence of central-to-peripheral nuclear modification factor R_{CP} at mid-rapidity in d+Au collisions at RHIC can be understood in terms of the hadronization from string fragmentation and the followed hadronic rescatterings in the final state.

In experimental side, it is relevant to systematically measure identified hadron production as a function of centrality. The dependence of the enhancement upon the thickness of the medium, or the number of collisions suffered by each participating nucleon, can help differentiate among the different scattering models, and the species dependence helps to separate initial from final state effects in d+Au collisions. ϕ meson is a good probe to distinguish the effect of final state hadronic rescatterings due to its presumably small cross sections with other non-strange particles. The effect of hadronic rescatterings on ϕ meson is thought to be small. Most of the ϕ mesons are directly produced from the collision process, the feed-down contribution from other hadrons to ϕ meson is less than $\sim 1\%$. ϕ meson is also a heavy meson with mass close to proton or Λ. It is convenient to use ϕ meson for distinguishing meson-baryon effect or mass effect. Last but not least, it is possible to access the soft sector of QCD by measuring the strangeness enhancement of ϕ-meson production in d+Au collisions by taking advantage of its hidden strangeness ($s\bar{s}$). Preliminary results of experimental measurements on ϕ-meson production in year 2008 (Run 8) d+Au collisions at STAR will be presented and discussed in section 6.2.

§1.3.4.3 Study QGP properties by ϕ meson elliptic flow in Au+Au collisions

STAR has published ϕ elliptic flow (v_2) measurements from year 2004 (Run 4) Au+Au 200 GeV collisions [54]. The results show that at intermediate p_T ($2< p_T <5$ GeV/c), v_2 of ϕ-mesons is consistent with number-of-quark scaling for mesons. The observations indicate the development of partonic collectivity in the hot dense medium created at RHIC.

For $p_T < 2$ GeV/c, a mass ordering of v_2 has been observed for identified charged hadrons [93–96], i.e., heavier hadrons show smaller magnitude of v_2 for a given p_T. The pattern of v_2 has been qualitatively consistent with the predictions of ideal hydrodynamic models [97–99]. Recent measurements of v_2 [100] and developments of hydrodynamic models [101–103] have indicated the importance of finite viscous effects in both early partonic and late hadronic stages in order to reproduce the magnitude as well as the p_T dependence of v_2. To extract the specific shear viscosity η/s of the QGP created at RHIC, proper accounting for effects from late hadronic viscosity is a prerequisite.

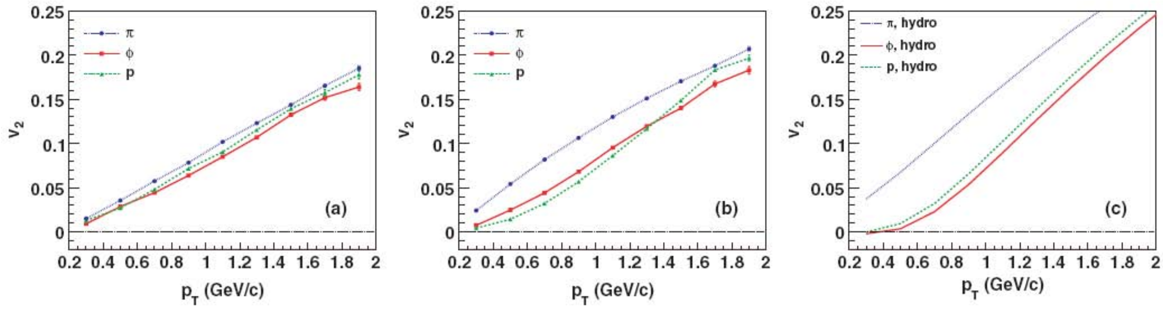

Figure 1.8: Transverse-momentum dependence of the elliptic flow v_2 for pions (blue dotted line with circle), protons (green dashed line and triangle), and ϕ mesons (red solid line and square), for Au+Au collisions at collision parameter $b = 7.2$ fm. (a) Before hadronic rescatterings. (b) After hadronic rescatterings. (c) Ideal hydrodynamics with $T_{th} = 100$ MeV. This figure is taken from Ref. [104].

Recently, Hirano *et al.* studied the dynamical origins of the observed mass ordering of $v_2(p_T)$ for identified hadrons, focusing on dissipative effects during the late hadronic stage by coupling the hydrodynamic model to a hadronic cascade [104]. Within their approach, they find that, at RHIC energies, much of the finally observed mass splitting is generated during the hadronic stage, due to buildup of additional radial flow. The ϕ meson, having a small interaction cross section, does not fully participate in this additional flow. As a result, it violates the mass-ordering pattern for $v_2(p_T)$ that is observed for other hadron species. They predict that ϕ meson v_2 at low p_T is larger instead of smaller due to mass ordering than that of proton, as shown in Fig. 1.8(b). The prediction of a violation of mass scaling of the differential elliptic flow $v_2(p_T)$ made in their calculation crucially depends on the reduced hadronic rescattering cross section for ϕ mesons and thus presents an important test of this widely accepted assumption. With a factor of about 5 higher statistics accumulated in year 2007 (Run 7) Au+Au 200 GeV run compared to that in Run 4, we test this possible violation predicted by Hirano *et al.* [104]. This is a first step toward the accurate extraction of η/s from ϕ meson v_2.

At intermediate p_T ($2.5 < p_T < 5$ GeV/c), it is found that v_2 from baryons and mesons, if scaled by their corresponding number of constituent quarks (n_q) and plotted against (p_T/n_q) or $(m_T - m_0)/n_q$, converges. This is the so called number of quark (n_q) or $m_T - m_0$ scaling. It is not expected from ideal hydrodynamic calculation. A simple quark coalescence model, which employs a different hadron formation mechanism, i.e., by combination of the thermal and/or shower quarks, will naturally result in the observed n_q scaling at intermediate p_T. The quark coalescence requires the de-confined matter with partonic degrees of freedom. As underlying quark flow is needed to explain the data, it provides evidence of the partonic collectivity in a phase where quarks and gluons are the relevant degrees of freedom. In this framework, ϕ meson v_2 is thought to be an important probe to detect the strange quark flow. With relatively large statistical uncertainties in Run 4, ϕ meson v_2 follows this n_q scaling [54]. Within the framework of quark coalescence model, this provides insights that the heavier s quark flows as the light u, d quarks.

Although the coalescence model can explain the observed n_q scaling reasonably, it assumes there is no dynamical gluons near the hadronization point. In principle, since the produced gluons dominate the parton distribution at early time, ϕ meson can be formed directly from gluon process, like $ggg \rightarrow \phi$, instead of $s + \overline{s} \rightarrow \phi$. This might cause the n_q scaling break for ϕ meson v_2. This is because in the ideal hydrodynamic case, the quark and gluon should have same v_2. If ϕ meson is formed from three gluons, then it may behave like a baryon.

Recently, the viscous hydrodynamic calculation shows that in the two-component (quarks and gluons) plasma with viscous corrections, due to shorter relaxation time of gluons, it will follow the ideal hydrodynamic evolution quicker than the quarks, thus the v_2 of gluons will be even larger than that of quarks [51]. Similar mechanism is used to describe the observed baryon-meson dependence. It is assumed that baryons relax to equilibrium 1.5 times faster than mesons, then the resulting viscous hydrodynamic calculation effortlessly reproduces the universal $m_T - m_0$ curve for $(m_T - m_0)/n_q$ below 1 GeV/c^2 (see Fig. 1.9). Physically what is happening is that in ideal hydrodynamics the baryons and mesons have approximately the same elliptic flow at intermediate p_T which is approximately described by a linear rise in m_T. The viscous correction then dictates that the baryons will follow this ideal trend 1.5 times farther than the mesons [51].

It is further speculated that the different relaxation time relates to the hadronic cross sections of baryons and mesons [51]. The baryons and mesons in the $p_T = 2 - 3$ GeV/c region are produced in the complex transition region where the energy density decreases from 1.2 GeV/fm^3 to 0.5 GeV/fm^3. In this range, the temperature decreases by only $\triangle T \simeq 20$ MeV. However, the hydrodynamic simulations evolve this complicated region for a significant period of time, $\tau \simeq 4$ fm/c $\leftrightarrow$ 6.5 fm/c, and the hadronic

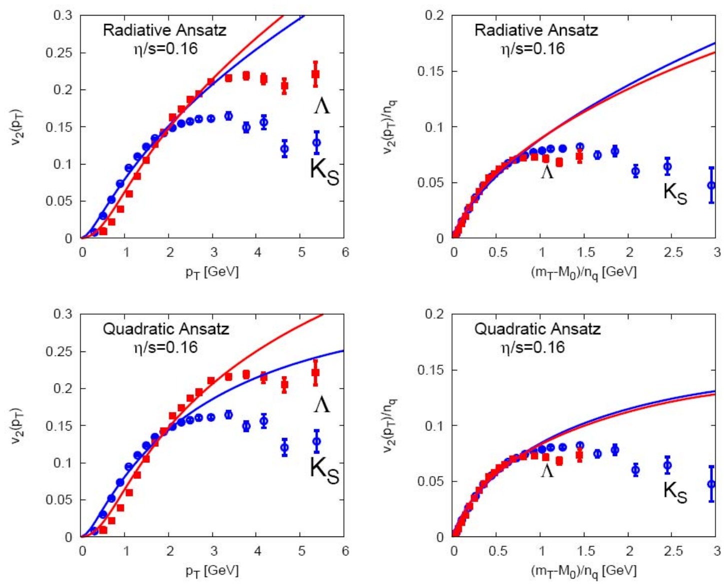

Figure 1.9: Plot from Ref. [51]. Viscous hydrodynamic calculation by a species dependent relaxation time of baryons and mesons [51]. Left: v_2 of K_S^0 and Λ. Right: $m_T - m_0$ scaling of v_2.

currents are built up over this time period. The interactions are probably quite inelastic and are not easily classified as hadronic or partonic in nature. The additive quark model was used to describe high energy total cross sections which are similarly inelastic [105]. It predicts the ratio of high energy nucleon-nucleon to pion-nucleon (as well as pion-nucleon to pion-pion) cross sections to be 3/2 in reasonable agreement with the experimental ratio [51]. This explanation looks promising since it provides a self-consistent explanation from viscous hydrodynamic calculation by a species dependent relaxation time. Considering the ϕ meson with a small presumably hadronic cross sections with other non-strange hadrons, from the cross-section argument, its relaxation time should be longer than other hadrons like pions and kaons. As a result, the ϕ meson v_2/n_q scaled by $(m_T - m_0)/n_q$ is expected to be smaller than those of pions and kaons. Therefore the study of $m_T - m_0$ scaling of ϕ meson would provide important constrain on present models. We can test the models by taking advantage of Run 7 data with a factor of ~ 5 higher statistics to get insights on the underlying physical process.

Chapter II New exponential law of β-decay half-lives of nuclei far from stability

In this chapter, we present the systematical study on new law and formula of β-decay half-lives for nuclear far from stability [106–108] and the parameterized formula to calculate half-lives of allowed orbital electron-capture transition. As discussed in section 1.1.3, the empirical study can help to understand the underlying physics of β-decay half-lives of nuclei far from β-stable line in an approximate but simple and transparent way. With the simple and accurate formula, it is also helpful for the calculations and predictions of β-decay half-lives of nuclei far from β-stable line, which is a prerequisite for a better understanding of the nucleosynthesis process.

In section 2.1, we propose an exponential law between $\beta^{\pm}$-decay half-lives and the neutron numbers of parent nuclei far from the β-stable line. The underlying physics of the exponential law is discussed in section 2.2. In sections 2.3 and 2.4, new formulae are proposed for calculating nuclear $\beta^{\pm}$-decay half-lives far from stability. The nuclear structure effects on $\beta^{\pm}$-decay half-lives are also discussed. In section 2.5, we suggest a parameterized formula to calculate half-lives of allowed orbital electron-capture transition. The summary of this chapter is given in section 2.6.

2.1 New exponential law between $\beta^{\pm}$-decay half-lives and neutron numbers

2.1.1 Common behavior of $\beta^{\pm}$-decay half-lives

There exists common character of $\beta^{\pm}$-decay half-lives. For nuclei close to the β-stable line, dramatic variations exist in nuclear $\beta^{\pm}$-decay half-lives. This is because the $\beta^{\pm}$-decay energy of the nuclei close to the β-stable line is very small, and the nuclear structure effects, such as the even-odd effects and the structure of excited energy level, cause the large fluctuations of $\beta^{\pm}$-decay energy (Q values). For small $\beta^{\pm}$-decay Q values, the $\beta^{\pm}$-decay half-lives are very sensitive to the $\beta^{\pm}$-decay energy. Therefore the $\beta^{\pm}$-decay half-lives often change dramatically along the isotopes close to β-stable line. For nuclei far from the β-stable line, the $\beta^{\pm}$-decay energy is much larger than that of the nuclei close to the β-stable line. As a result, the influence of certain nuclear structure

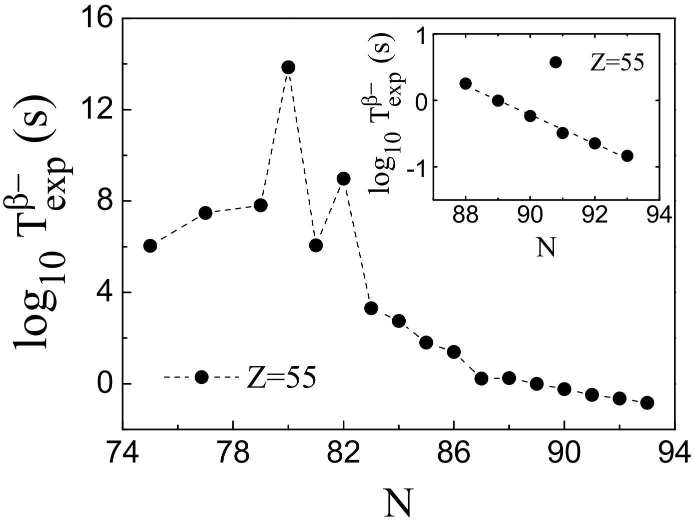

Figure 2.1: The large figure plots the β^--decay half-lives (in $\log_{10}$-scale) along Cs isotopic chain. The small figure in the inset shows the linear relationship between the logarithm of β^--decay half-life and the neutron number of Cs isotopes far from the β-stable line.

effects can be smooth according to Fermi theory of β-decay. For example, we make a rough estimation of the effect of the decay energy on $\beta^{\pm}$-decay half-life. For allowed β^--transition, the β^--decay half-life ($T^{\beta^-}_{1/2}$) is proportional to the reciprocal of the Fermi integral function $f(Z_\mathrm{d}, W_0)$ [109], which is written as

$$f(Z_\mathrm{d}, W_0) = \int_1^{W_0} F(Z_\mathrm{d}, W)(W^2-1)^{1/2}(W_0-W)^2 W \mathrm{d}W, \tag{2.1}$$

where Z_d is the proton number of the decay product, $F(Z_\mathrm{d}, W)$ is the factor of Coulomb correction, and W is the ratio between the total energy (including the rest energy) of the emitting electron and the rest mass of the electron. We assume that the factor of Coulomb correction is 1, and decay energy difference between two nuclei is 0.5 MeV. If the decay energy of one nuclide is 0.5 MeV, and that of the other is 1.0 Mev, the ratio $f(Z_\mathrm{d}, W_{\mathrm{latt.}})/f(Z_\mathrm{d}, W_{\mathrm{prev.}})$ is 15.2, where $f(Z_\mathrm{d}, W_{\mathrm{latt.}})$ is Fermi integral function of the latter nuclide and $f(Z_\mathrm{d}, W_{\mathrm{prev.}})$ is that of the previous nuclei. As a result, the β^--decay half-life of the previous nuclide will be larger than that of the latter by 14.2 times when the matrix element of the two nuclei is the same. In the same way, if the decay energy of one nuclide is 10.0 MeV, and that of the other is 10.5 MeV, the ratio between β^--decay half-life of the previous nuclide and that of the latter will be 1.28 according to the Sargent law [14]. Similar argument is valid for β^+ decay. This shows that the $\beta^{\pm}$-decay half-life of nuclide with large $\beta^{\pm}$-decay energy is less sensitive to the change of decay Q values than the nuclide with small $\beta^{\pm}$-decay energy for allowed $\beta^{\pm}$-transition. For nuclei far from the β-stable line, usually it is reasonable to assume that allowed $\beta^{\pm}$-transition exists because of the large β-decay energy and dense energy levels of daughter nuclei. Comparing with allowed transitions, the contributions from forbidden transitions are relatively small [13]. Therefore there may exist some rules of $\beta^{\pm}$-decay half-lives for nuclei far from the β-stable line because of the large $\beta^{\pm}$-decay energy. In Fig. 2.1 we plot the variation of β^--decay half-life with the neutron number of parent nuclei along Cs isotopic chain. It is seen from the large figure of Fig. 2.1 that there are large fluctuations of β^--decay half-lives of nuclei close to the β-stable line, whereas for nuclei far from the β-stable line ($N \geq 88$ for neutron-rich Cs isotopes), there is linear relationship between β^--decay half-life and the neutron number of parent nuclei. The linear relationship is clearly shown in the small figure of Fig. 2.1.

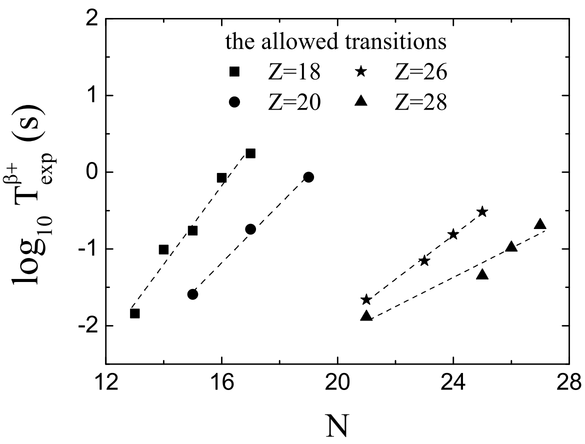

Figure 2.2: The experimental β^+-decay half-lives (in $\log_{10}$-scale) are plotted versus the neutron numbers of the parent nuclei with Z=18, 20, 26 and 28.

At first, we define the concept "far from the β-stable line" used in this chapter quantitively. All available nuclei with $\delta N > 5$ are included in our investigation. The parameter $\delta N = |N - N_{stable}|$ is defined to denote the nuclei far from the β-stable line. For the nuclei with even proton numbers, N_{stable} [110] is the maximum (for β^- decay) or minimum (for β^+ decay) neutron number of corresponding stable nuclei. For odd-Z nuclei, we set N_{stable} as the average of the two maximum (for β^- decay) or minimum (for β^+ decay) neutron numbers of two neighboring even-Z nuclei because the maximum (for β^- decay) or minimum (for β^+ decay) neutron number of stable odd-Z nuclei is often smaller (for β^- decay) or larger (for β^+ decay) than that of the neighboring stable even-Z nuclei. For nuclei with $Z \geq 83$, there does not exist stable nuclei according to our present knowledge. We obtain N_{stable} from the semi-empirical formula [111] for nuclei with $Z \geq 83$, which is written as

$$N_{stable} = A - \frac{A}{1.98 + 0.0155A^{2/3}}, \tag{2.2}$$

where A is nuclear mass number.

2.1.2 β^+ decays

Usually, one use the comparative half-lives other than the β^+-decay half-life to classify the order of β^+-decay in textbooks [2]. Although the β^+-decay half-lives approximately vary from 10^{-2}s to 10^{18}y for known nuclei, the comparative half-lives vary in a very narrow range. For example, the comparative half-lives (in $\log_{10}$-scale) of the super allowed transitions change from 2.9 to 3.7 for many nuclei [111].

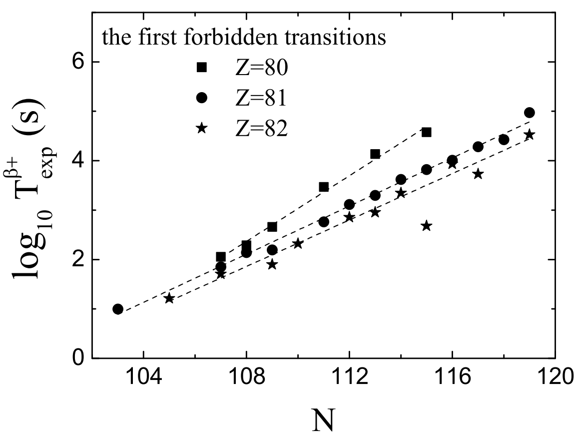

Figure 2.3: Same as in Fig. 2.2, but for the first forbidden β^+-decay of the nuclei with Z=80, 81 and 82.

Beyond the traditional method based on nuclear β-decays close to β-stable line, we directly analyze the relationship between the experimental β^+-decay half-lives (in $\log_{10}$-scale) and the neutron number of parent nuclei. At first, we investigate the β^+-decay half-lives of the nuclei near the closed shells, because there usually exist more experimental data of the half-lives of β^+-decay with a same order near the closed shells. All the experimental values (without special notation) of β^+-decay half-lives which are used in this thesis are taken from Nubase table of nuclear and decay properties by Audi *et al.* [112]. The β^+-decay in the Nubase table [112] contains two kinds of process: positron emission and orbital electron capture. The variations of the logarithms of β^+-decay half-lives along different isotopic chains near the closed shells are shown in Figs. 2.2−2.4. For a few isotopic chains, the available experimental data of β^+-decay with a same order is less than 3. In this case, we do not draw them in the figures. For example, the isotopic chains of K, Co, and Cd are not drawn in Figs. 2.2−2.4. A few points are missing in the figures because there is no experimental data for the β^+-decay of a few nuclei.

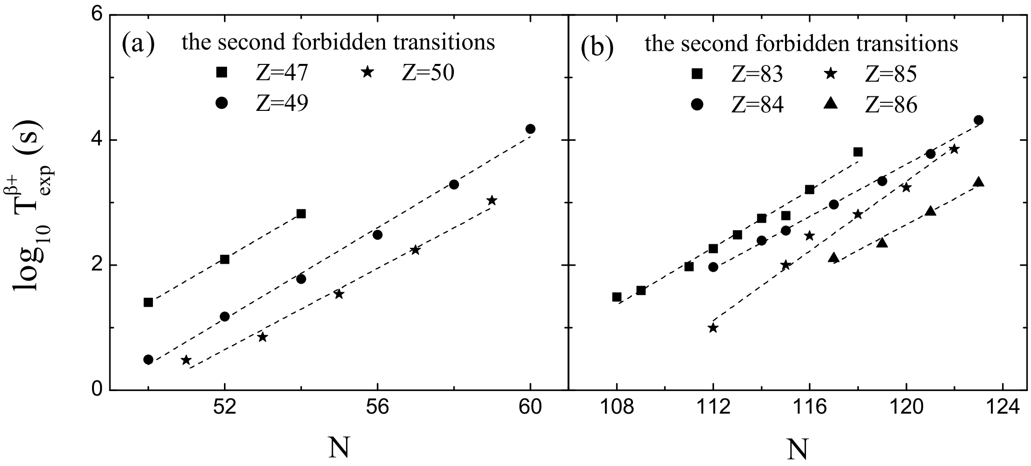

Figure 2.4: Same as in Fig. 2.2, but for the second forbidden β^+-decay of the nuclei with Z=47, 49, 50, 83, 84, 85 and 86. The β^+-decay half-life of ^{197}At is from reference [113].

From Figs. 2.2−2.4 we find that the logarithms of half-lives of β^+-decay with a same order approximately lie on a straight line along any isotopic chain near the proton closed shells (Z=20, 28, 50, 82). This linear relationship between the logarithm of half-life and the neutron number can be written as

$$\log_{10} T_{1/2} = aN + b, \tag{2.3}$$

where a and b are two constants to be determined and N is the neutron number of the nuclei on the isotopic chain. This equation shows an exponential law between the β^+-decay half-lives and the neutron number of parent nuclei. The dashed lines in Figs. 2.2−2.4 are plotted according to the linear fit of the experimental β^+-decay half-lives (in $\log_{10}$-scale). The standard deviation of the linear fit is defined as

$$\sigma = \sqrt{\frac{1}{K}\sum_{i=1}^{K}[\log_{10} T_{1/2}^{i}(\mathrm{exp}) - \log_{10} T_{1/2}^{i}(\mathrm{cal})]^2}. \tag{2.4}$$

Here, K is the number of experimental data of the nuclei with the same order of β^+-decay on an isotopic chain, $T_{1/2}^{i}(\mathrm{exp})$ and $T_{1/2}^{i}(\mathrm{cal})$ represent the experimental half-life value and the calculated one respectively.

Table 2.1: The values of parameters a, b and corresponding fitting errors in the linear fit of the experimental half-lives and the standard deviation σ of the linear fit.

order of β^+-decay	Z	a	b	σ
allowed	18	0.511 ± 0.051	-8.349 ± 0.767	0.125
	20	0.381 ± 0.025	-7.278 ± 0.423	0.040
	26	0.288 ± 0.013	-7.725 ± 0.309	0.028
	28	0.191 ± 0.032	-5.946 ± 0.801	0.104
first-forbidden	80	0.332 ± 0.015	-33.478 ± 1.674	0.085
	81	0.243 ± 0.006	-24.190 ± 0.650	0.087
	82	0.224 ± 0.021	-22.320 ± 2.388	0.264
second-forbidden	47	0.355 ± 0.006	-16.358 ± 0.299	0.009
	49	0.364 ± 0.013	-17.783 ± 0.707	0.088
	50	0.325 ± 0.023	-16.272 ± 1.249	0.111
	83	0.229 ± 0.011	-23.400 ± 1.290	0.093
	84	0.209 ± 0.006	-21.439 ± 0.655	0.046
	85	0.274 ± 0.018	-29.567 ± 2.124	0.119
	86	0.206 ± 0.022	-22.120 ± 2.607	0.069

All parameters a and b used in the calculation of the half-lives and the standard deviations σ of the linear fits are listed in Table 2.1. In Table 2.1 the first column denotes the order of β^+-decay. The second column shows the proton number of the isotopic chain. The values of parameters a, b and corresponding fitting errors in the calculation of the half-lives are listed in columns 3 and 4, respectively. The standard deviation of the isotopic chain is listed in the last column. It is seen from Table 2.1 that all standard deviations of the linear fits are rather small. For the allowed transitions of four isotopic chains near Z=20 and 28 closed shells, the standard deviations vary from 0.028 to 0.125. As to the first forbidden β^+-transitions, the standard deviations are 0.085 to 0.264 for the three isotopic chains near Z=82 closed shell. The linear fits for the second forbidden β^+-decays are also acceptable, in which the standard deviations vary from 0.009 to 0.119 for the seven isotopic chains near Z=50 and 82 closed shells. According to the above investigations, we can draw the conclusion that the logarithm of the half-life of β^+-decay with a same order linearly depends upon the neutron number of parent nuclei along any isotopic chain near the proton closed shells.

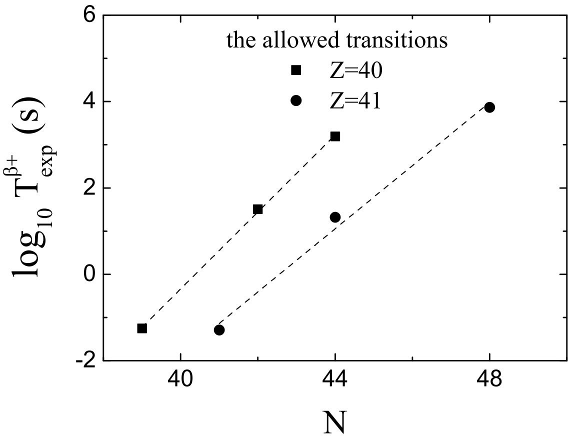

Figure 2.5: The linear relationship between the logarithms of experimental β^+-decay half-lives and the neutron number of parent nuclei with Z=40 and 41.

After the investigation of β^+-decay half-lives of the nuclei near the closed shells, we analyze the experimental data of the nuclei between the closed shells. The variations of the β^+-decay half-lives along different isotopic chains between the closed shells are shown in Figs. 2.5−2.6. In Fig. 2.5, we plot the logarithms of β^+-decay half-lives of the allowed transition versus the neutron number of parent nuclei along Zr and Nb isotopic chains. In Fig. 2.6, we draw the variation of the logarithm of β^+-decay half-life of the first forbidden transition with the neutron number of the parent nucleus along Gd, Tb, Dy, Ho, Cf, Es and Md isotopic chains.

It is seen from Figs. 2.5−2.6 that the experimental half-lives of β^+-decay with a same order lie approximately on a straight line along above isotopic chains from Z=40 to the transuranium region both for the allowed and first forbidden β^+-transitions of the nuclei between the closed shells. The linear fits for the nuclei between the closed shells are as good as that for the nuclei near the closed shells. This shows that the exponential law between the β^+-decay half-life and the neutron number of the parent nuclei is valid for both the nuclei near closed shells and the nuclei between the closed shells. Therefore, it can be concluded that the exponential law of β^+-decay half-lives is valid for all the isotopic chains. It is new and useful for scientists to analyze the experimental data and to predict the β^+-decay half-life of unknown nucleus. The physics behind this new exponential law is discussed in section 2.2.

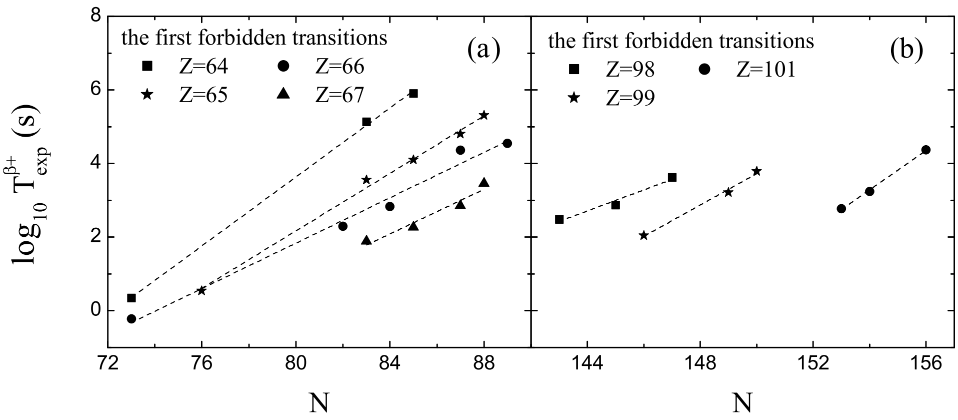

Figure 2.6: Same as in Fig. 2.5, but for the first forbidden β^+-decay of the nuclei with Z=64, 65, 66, 67, 98, 99 and 101. The β^+-decay half-lives of the nuclei with Z=100 are not drawn in the figure because the number of experimental data is less than 3. The order of β^+-decay of ^{248}Es is estimated according to Audi's table [112].

2.1.3 β^- decays

We now systematically investigate the relationship between the logarithm of experimental β^--decay half-life and the neutron number of parent nuclei. The experimental values (without special notation) of β^--decay half-lives used in this thesis are taken from Nubase table of nuclear and decay properties by Audi *et al.* [112]. The variations of the logarithms of β^--decay half-lives along different isotopic chains are shown in Fig. 2.7. From Fig. 2.7 we find that the logarithms of β^--decay half-lives lie approximately on a straight line along different isotopic chains. This linear relationship between the logarithm of β^--decay half-life and the neutron number is the same as Eq. (2.3), which shows an exponential law between β^--decay half-life and the neutron number of parent nuclei. The dashed lines in Fig. 2.7 are plotted according to the linear fit of available experimental β^--decay half-lives (in $\log_{10}$-scale). The standard deviation of the linear fit is defined in Eq. (2.4).

All parameters a and b used in the calculation of the β^--decay half-lives and the standard deviations σ of the linear fits are listed in Table 2.2. In Table 2.2, the first and fifth columns denote the proton number of the isotopic chain. It is seen from Table 2.2 that all standard deviations of the linear fits are small. The standard deviations vary from 0.029 to 0.181 for the linear fits of the experimental data of 22 isotopic chains from the region of light nuclei to the regions of the middle and heavy nuclei. This implies that

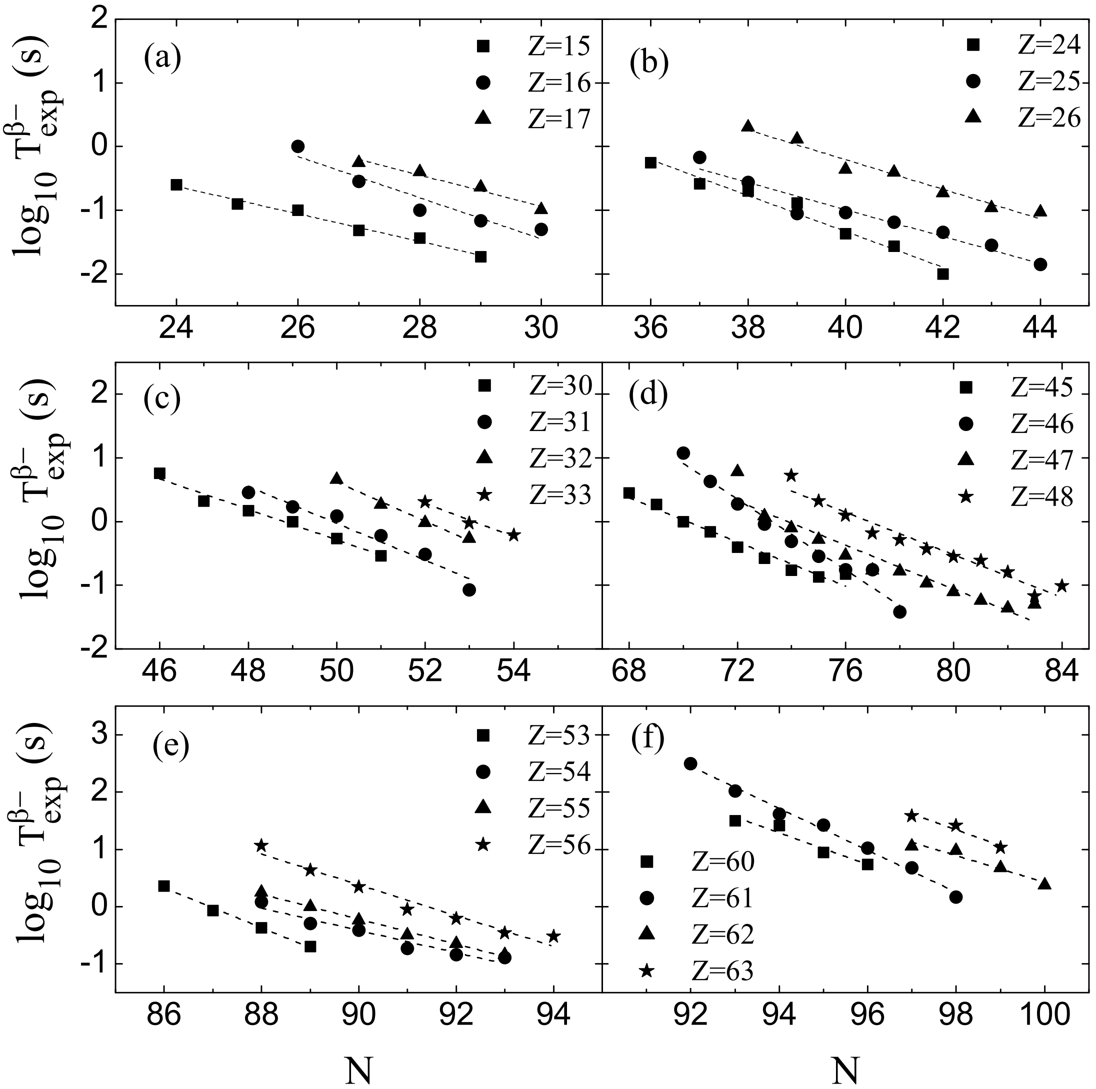

Figure 2.7: Experimental β^--decay half-lives (in $\log_{10}$-scale) are plotted versus neutron numbers of parent nuclei. The experimental β^--decay half-lives of $^{39-44}$P, $^{43-46}$S, $^{46-47}$Cl, $^{116-121}$Rh, and $^{119-124}$Pd are taken from [114,115]. The following nuclei $^{155-158}$Nd, $^{153-157}$Pm, ^{159}Sm, and $^{160-162}$Pm which are not very far from the β-stable line ($\delta N \leq 5$) are included in Fig. 2.7(f) because the number of available experimental data of β^--decay half-lives of nuclei far from the β-stable line is few for the isotopic chain with $Z \geq 60$.

Table 2.2: The values of parameters a, b and standard deviation σ in the linear fit of experimental β^--decay half-lives.

Z	a	b	σ	Z	a	b	σ
15	-0.216 ± 0.013	4.568 ± 0.458	0.046	46	-0.279 ± 0.019	20.425 ± 1.389	0.128
16	-0.323 ± 0.056	8.244 ± 1.567	0.137	47	-0.172 ± 0.017	12.719 ± 1.286	0.181
17	-0.247 ± 0.034	6.464 ± 0.972	0.054	48	-0.167 ± 0.013	12.864 ± 1.024	0.123
24	-0.281 ± 0.020	9.925 ± 0.781	0.089	53	-0.347 ± 0.018	30.195 ± 1.584	0.029
25	-0.211 ± 0.022	7.470 ± 0.885	0.122	54	-0.195 ± 0.025	17.095 ± 2.291	0.086
26	-0.232 ± 0.019	9.092 ± 0.790	0.086	55	-0.218 ± 0.009	19.416 ± 0.830	0.031
30	-0.239 ± 0.018	11.688 ± 0.887	0.062	56	-0.268 ± 0.024	24.508 ± 2.198	0.108
31	-0.290 ± 0.032	14.481 ± 1.616	0.109	60	-0.274 ± 0.049	27.084 ± 4.606	0.077
32	-0.306 ± 0.023	15.941 ± 1.192	0.037	61	-0.366 ± 0.016	36.149 ± 1.502	0.071
33	-0.260 ± 0.040	13.808 ± 2.143	0.033	62	-0.233 ± 0.039	23.702 ± 3.882	0.062
45	-0.174 ± 0.013	12.173 ± 0.948	0.090	63	-0.277 ± 0.065	28.509 ± 6.361	0.053

the linear relationship is a common rule of β^--decay half-lives for nuclei far from the β-stable line. In other words, it can be concluded that there exists the exponential law between β^--decay half-life of nuclei far from the β-stable line and the neutron number of parent nuclei along any isotopic chain.

It is noticed that the linear relationship between the logarithm of β^--decay half-life and the neutron number of parent nuclei far from stability is similar to that of β^+-decay half-life which has been discovered in the previous section. The linear relationship between the β^+-decay half-life and the neutron number is under the condition that the forbiddenness of the β^+-transition is the same, whereas the linear relationship of β^--decay half-life is valid for all isotopes far from the β-stable line. This shows the difference between β^+-decay and β^--decay half-lives. It is interesting to investigate the reason of this difference. It may be due to that the β^+-decay contains two kinds of process: positron emission and orbital electron capture, whereas the β^--decay contains only one kind of process, i.e. electron emission. It seems that β^+ decay is more sensitive to the forbiddenness of transition from ground state to ground state than β^- decay.

2.2 Physics behind the exponential law

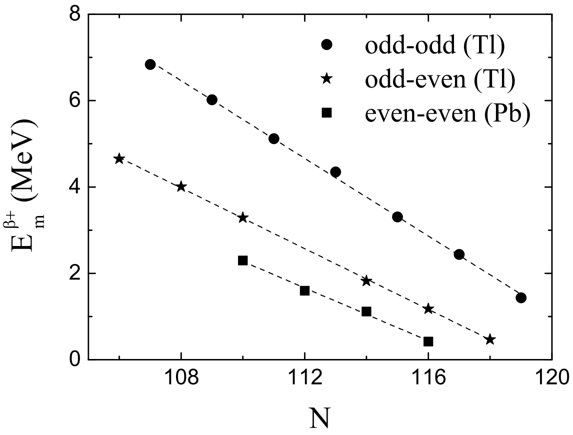

Figure 2.8: The linear relationship between the maximum kinetic energy $E_{\rm m}$ of the positron emitted in the first forbidden β^{+}-decay and the neutron number of the parent nucleus along Tl and Pb isotopic chains.

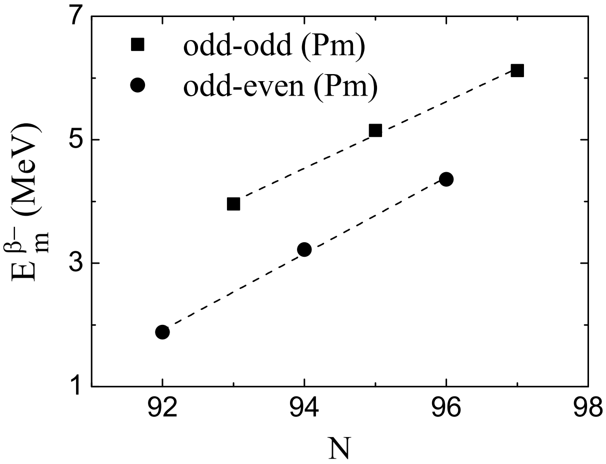

Figure 2.9: The variation of the maximum kinetic energy $E_{\rm m}$ of the electron emitted in the β^{-}-decay with the neutron number of parent nuclei along Pm isotopic chain.

It is interesting to investigate the physics behind the exponential law between $\beta^{\pm}$-decay half-life and the neutron number of parent nuclei. A linear relation between the the maximum kinetic energy $E_{\rm m}$ of the positron emitted in the β^{+}-decay process and the neutron number of the parent nucleus is found and drawn in Fig. 2.8. It is assumed that the rest mass of neutrino is zero. According to the mass-energy relation, $E_{\rm m}$ is calculated by

$$E_{\rm m} = (M_p - M_d - 2m_e)c^2, \tag{2.5}$$

where c is the speed of light in vacuum, M_p, M_d and m_e are the rest masses of the parent nucleus, the daughter nucleus and the electron respectively. All the mass values are taken from the AME2003 atomic mass table by Audi *et al.* [116]. It is seen clearly from Fig. 2.8 that the maximum kinetic energy of the positron emitted in the β^+-decay linearly depends on the neutron number along the Tl and Pb isotopes, i.e.

$$E_m = d_1 N + d_2, \tag{2.6}$$

where d_1 and d_2 are two constants to be determined.

For β^--decay, this linear relationship between the maximum kinetic energy $E_{\rm m}$ of the electron emitted in the β^--decay process and the neutron number of the parent nucleus is also valid. This is illustrated in Fig. 2.9.

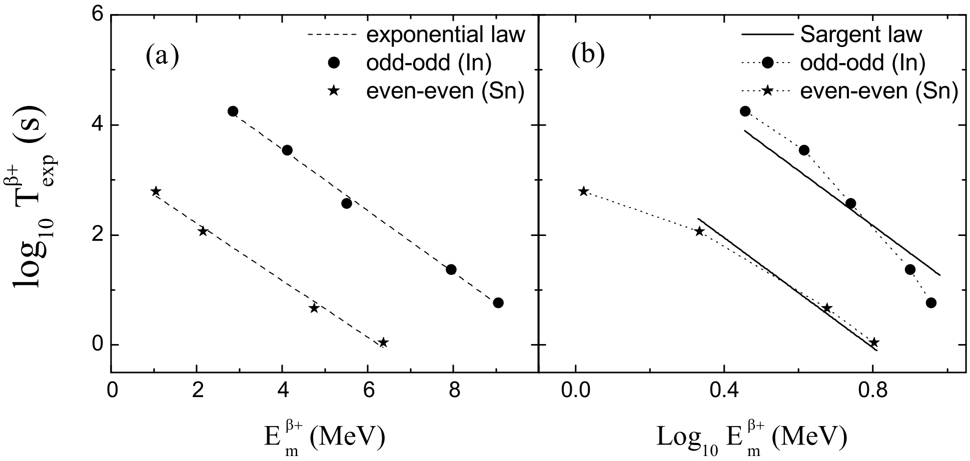

Figure 2.10: The logarithm of β^+-decay half-life is plotted versus the maximum kinetic energy ($E_{\rm m}$) of the positron emitted in the sixth forbidden β^+-decay (Fig. (2.10a)) and the logarithm of $E_{\rm m}$ (Fig. (2.10b)) for the nuclei near Z=50 closed shell, respectively. The dashed line in (Fig. (2.10a)) denotes our new exponential law and the solid line in (Fig. (2.10b)) is the Sargent law which is presumably valid in the range of large $E_{\rm m}$ for single energy-level β^+-decay.

We derive from Eq. (2.3) and Eq. (2.6) that there also exists a linear relationship between the logarithm of β^+-decay half-life and the maximum kinetic energy $E_{\rm m}$. This relation is drawn in Fig. (2.10a) and Fig. (2.11a). It is seen clearly from Fig. (2.10a) and Fig. (2.11a) that the experimental half-lives lie approximately on a straight line in the entire range of $E_{\rm m}$ for the In, Sn, Tl and Pb isotopes, i.e.

$$\log_{10} T_{1/2} = d_3 E_m + d_4, \tag{2.7}$$

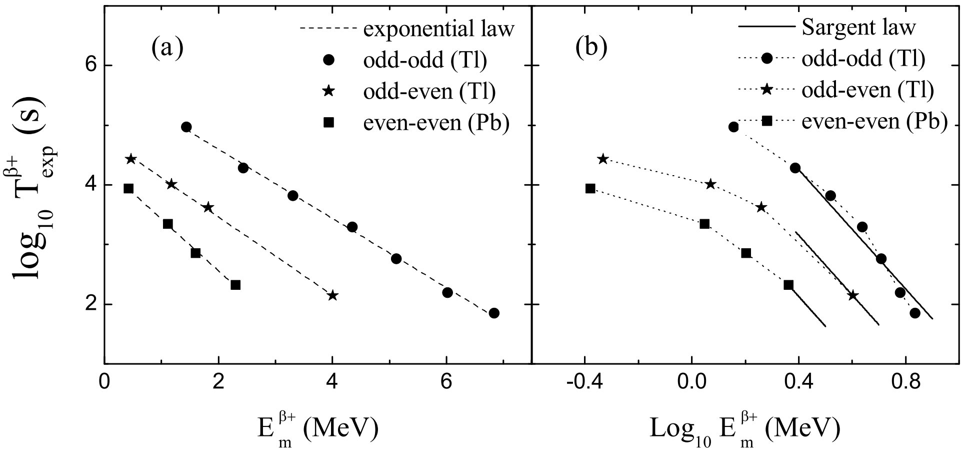

Figure 2.11: Same as in Fig. 2.10, but for the first forbidden β^+-decay of the nuclei near Z=82 closed shell. The dashed line in (Fig. (2.11a)) denotes our new exponential law and the solid line in (Fig. (2.11b)) is the Sargent law which is presumably valid in the range of large E_m for single energy-level β^+-decay.

where d_3 and d_4 are two constants to be determined. This equation shows an exponential law between the β^+-decay half-life and the maximum kinetic energy E_m for an isotopic chain.

Eq. (2.7) is also valid for β^--decays. This relation is drawn in Fig. 2.12(a) and Fig. 2.12(c). It is seen clearly from Fig. 2.12(a) and Fig. 2.12(c) that the logarithms of experimental β^--decay half-lives lie approximately on a straight line along E_m for the Pm and I isotopes. This shows an exponential law between β^--decay half-life and the maximum kinetic energy E_m for an isotopic chain.

It is well known that there is the Sargent law [14, 109, 117–119] between the β-decay half-life and the maximum kinetic energy E_m of the electron/positron for large E_m. This relationship was proposed before Fermi theory of β-decay. The Sargent law is a fifth-power law between β-decay half-life and the maximum kinetic energy E_m:

$$T_{1/2} \propto E_\mathrm{m}^{-5}. \tag{2.8}$$

When we compare Eq. (2.7) with Eq. (2.8), it seems that there is a contradiction between our new exponential law and the Sargent law. The Sargent law is a fifth-power law between β^--decay half-life and E_m, whereas our new relationship is an exponential law. It is interesting to make a comparison between our exponential law and the Sargent law.

The variation of the logarithm of β^+-decay half-life with $\log_{10} E_\mathrm{m}$ is drawn in Fig.

(2.10b) and Fig. (2.11b). It is seen from in Fig. (2.10b) and Fig. (2.11b) that the experimental data forms a curve because the Sargent law is not valid in the range of low energy. In the range of large $E_{\rm m}$, there roughly exists a linear relationship in Fig. (2.10b) and Fig. (2.11b), but the linear relationship in Fig. (2.10b) and Fig. (2.11b) is not so general as that in Fig. (2.10a) and Fig. (2.11a).

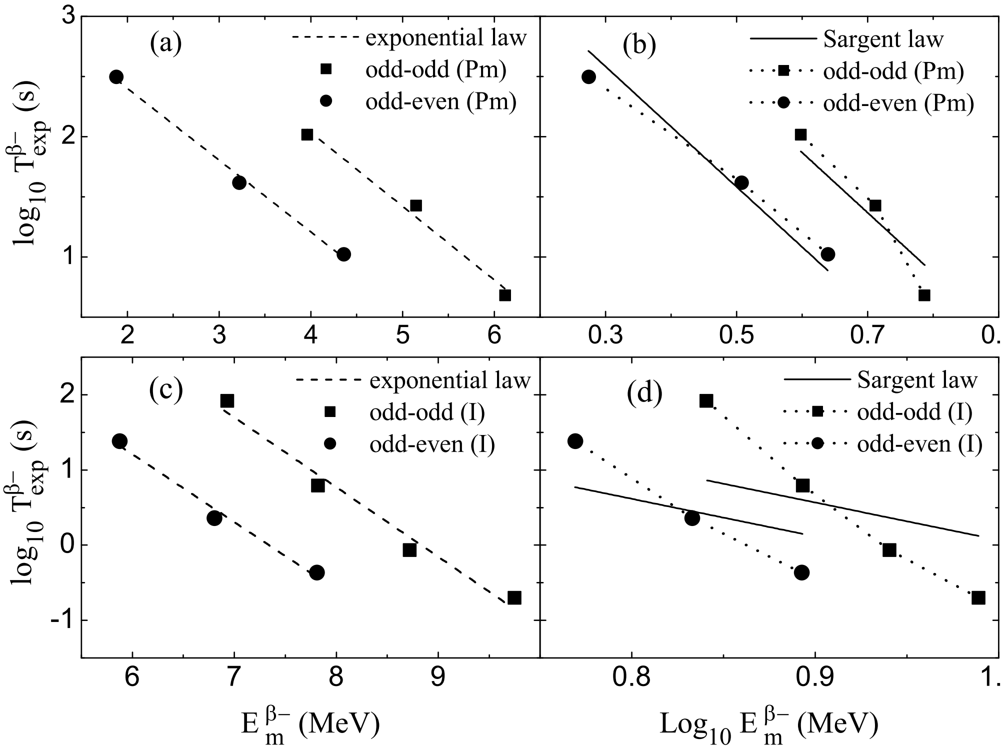

Figure 2.12: Logarithm of β^--decay half-life plotted versus the maximum kinetic energy $E_{\rm m}$ of the electron emitted in the β^- decay and logarithm of $E_{\rm m}$ for Pm and I isotopes. The dashed line denotes our new exponential law and the solid line denotes the Sargent law. The nuclei $^{136-138}$I which are not very far from the β-stable line ($\delta N \leq 5$) are included. The β^--decay energy is taken from atomic mass table [116].

In the case of β^--decay, the variation of the logarithm of β^--decay half-life with $\log_{10} E_{\rm m}$ is drawn in Fig. 2.12(b) and Fig. 2.12(d). It is seen from Fig. 2.12(b) and Fig. 2.12(d) that experimental β^--decay half-lives deviate from the Sargent law for the Pm and I isotopes. It implies that the exponential law is more appropriate for describing the β^--decay half-lives of nuclei far from stability than the Sargent law for Pm and I isotopes. According to the expression between the decay const λ and the half-life (i.e., $\lambda = \ln 2/T_{1/2}$) and using Eq. (2.7), we get the relationship between λ and $E_{\rm m}$:

$$\lambda = 0.693 \times 10^{-d_4} e^{-2.303 d_3 E_{\rm m}}. \tag{2.9}$$

We can expand the exponential term of Eq. (2.9) into the form of a power series:

$$\lambda = f_0[1 + f_1E_{\mathrm{m}} + \frac{(f_1E_{\mathrm{m}})^2}{2!} + \cdots + \frac{(f_1E_{\mathrm{m}})^5}{5!} + \cdots + \frac{(f_1E_{\mathrm{m}})^n}{n!} + \cdots], \tag{2.10}$$

where $f_0 = 0.693 \times 10^{-d_4}$ and $f_1 = -2.303d_3$. f_1 is positive because d_3 is negative according to Fig. 2.12(a) and Fig. 2.12(c). For example, d_3 is -0.5967 and f_1 is 1.374 for the odd-even isotopes of Pm. E_{m} is usually several MeV and the series in Eq. (2.10) is degressive after the term $(f_1E_{\mathrm{m}})^9/9!$. We can see from Eq. (2.10) that the Sargent law, which is described as $\lambda \propto E_{\mathrm{m}}^5$, can be regarded as the term $(f_1E_{\mathrm{m}})^5/5!$ in Eq. (2.10). Therefore the Sargent law can be considered as a special term of our new relationship.

Actually, the Sargent law can be approximately derived from Fermi theory of β-decay [109, 117–119], and the term E_{m}^5 relates to the calculation of the density of the final nuclear state. The derivation of the fifth-power law (Sargent law) is under the assumption that there is only the β^--transition from ground state to ground state. However, for many nuclei far from the β-stable line, the β^--transition from ground state to ground state is not the main decay channel because of large β-decay energy. For example, the branching ratios of the β^--transitions from ground states to ground states for ^{136}I, ^{138}I, and ^{153}Pm are about 3.0%, 32%, and 5% [126], respectively. According to Fermi theory of β-decay and assuming that the Coulomb correction is 1, the total β-decay const λ of the ground state of parent nucleus can be written as

$$\lambda = \sum_i p_i(E_{\mathrm{m}} - E_i)^5, \tag{2.11}$$

where E_i denotes the excited energy of ith energy level of daughter nucleus, and p_i denotes the product of const term and matrix elements of the transitions from the ground state of parent nucleus to the ith energy level of daughter nucleus. After we expand the term in Eq. (2.11), it is written as

$$\begin{aligned}\lambda = {} & (\sum_i p_i)E_{\mathrm{m}}^5 - 5(\sum_i p_iE_i)E_{\mathrm{m}}^4 + 10(\sum_i p_iE_i^2)E_{\mathrm{m}}^3 \\ & -10(\sum_i p_iE_i^3)E_{\mathrm{m}}^2 + 5(\sum_i p_iE_i^4)E_{\mathrm{m}} - \sum_i p_iE_i^5.\end{aligned} \tag{2.12}$$

When comparing Eq. (2.10) and Eq. (2.12), one can regard Eq. (2.12) as the low order term of Eq. (2.10). As a result, our exponential law is more general than Sargent law because it contains the contribution of β^--transitions from the ground state of parent nuclei to both ground state and excited states of daughter nucleus. Furthermore, the Coulomb correction for the nucleus with large proton number should be included. It is interesting to investigate this problem more deeply in the future. It is shown that there is common behavior for the half-lives of α-decay, β-decay, and cluster radioactivity although they are governed by different interactions such as strong, weak and electromagnetic interactions, that is, there is the exponential law between the decay half-life and the decay energy (or nucleon number) for nuclear α-decay, β-decay, and cluster radioactivity.

2.3 New formula for β^+-decay half-lives

2.3.1 Nuclei near the closed shells

Based on the linear relationship between the logarithm of β^+-decay half-life and the neutron number, we propose the following formula to describe the β^+-decay half-lives:

$$\log_{10} T_{1/2} = (c_1 Z + c_2)N + c_3 Z + c_4, \tag{2.13}$$

where $T_{1/2}$ is the half-life of β^+-decay (in second) and Z is the proton number of the parent nuclei. The values of parameters c_1, c_2, c_3 and c_4 are determined according to the available experimental data of the β^+-decay half-lives. This is an exponential relationship between the β^+-decay half-life and the nucleon number (Z, N). It is very similar to the cases of α-decay and of cluster radioactivity [120–122]. At first, we use the new formula (Eq. (2.13)) to calculate the half-lives of the first forbidden β^+-transition. Through a least-square fit to the available experimental data of 27 nuclei near Z=82 closed shell (see Table 2.3), we obtain a set of parameters of equation (3): $c_1 = -0.0378$; $c_2 = 3.3183$; $c_3 = 3.7962$ and $c_4 = -333.0918$.

The numerical results of Z=80−82 are given in Table 2.3 and in Fig. (2.13a). In Table 2.3 the first and second columns denote the proton number and the mass number of parent nuclei, respectively. The third and fourth columns are respectively experimental β^+-decay half-lives and calculated ones from Eq. (2.13). The ratio between calculated half-life and the experimental one is listed in column 5. The half-lives calculated by Möller *et al.* [123] are listed in the last column for the comparison. It is seen from columns 3−5 that the half-lives from the formula agree with the experimental ones well. The ratios (T_{cal}/T_{exp}) are close to 1 for many nuclei. Now we analyze the calculated error bar of the least-square fit. For a rough description, we can use the standard deviation σ or the average deviation Δ between the logarithms of the calculated and experimental β^+-decay half-lives to denote the calculating error bar. It has been suggested by Möller

Table 2.3: The calculated half-lives of the first forbidden β^+-transitions (Z=80−82) from the formula $\log_{10}(T_{1/2}^{\beta+}) = (c_1 Z + c_2)N + c_3 Z + c_4$ and the experimental ones. The half-lives of β^+-decays from Möller *et al.* [123] are also listed for the comparison.

Z	A	T_{exp}	T_{cal}	T_{cal}/T_{exp}	$T_{M\ddot{o}ller}$(s)
80	187	1.9 ± 0.3 m	2.1 m	$1.1^{+0.2}_{-0.1}$	>100
80	188	3.25 ± 0.15 m	4.08 m	1.26 ± 0.06	>100
80	189	7.6 ± 0.1 m	8.0 m	1.1 ± 0.1	>100
80	191	49 ± 10 m	31 m	$0.6^{+0.2}_{-0.1}$	>100
80	193	3.80 ± 0.15 h	2.01 h	0.53 ± 0.02	>100
80	195	10.53 ± 0.03 h	7.81 h	0.742 ± 0.002	>100
81	188	71 ± 2 s	70 s	$0.99^{+0.02}_{-0.03}$	>100
81	189	2.3 ± 0.2 m	2.1 m	$0.91^{+0.09}_{-0.07}$	>100
81	190	2.6 ± 0.3 m	3.8 m	1.5 ± 0.2	>100
81	192	9.6 ± 0.4 m	12.4 m	1.3 ± 0.1	>100
81	194	33.0 ± 0.5 m	40.4 m	$1.22^{+0.02}_{-0.01}$	>100
81	195	1.16 ± 0.05 h	1.22 h	$1.05^{+0.05}_{-0.04}$	>100
81	196	1.84 ± 0.03 h	2.20 h	1.20 ± 0.02	>100
81	197	2.84 ± 0.04 h	3.97 h	1.40 ± 0.02	>100
81	198	5.3 ± 0.5 h	7.2 h	$1.4^{+0.1}_{-0.2}$	>100
81	199	7.42 ± 0.08 h	12.92 h	1.74 ± 0.02	>100
81	200	26.1 ± 0.1 h	23.3 h	$0.893^{+0.003}_{-0.004}$	>100
82	187	$16.3^{+0.7}_{-0.6}$ s	14.5 s	$0.89^{+0.03}_{-0.04}$	22.5510
82	189	51^{+4}_{-3} s	40 s	0.78 ± 0.05	76.0592
82	191	1.33 ± 0.08 m	1.81 m	$1.36^{+0.09}_{-0.08}$	>100
82	192	3.5 ± 0.1 m	3.0 m	$0.86^{+0.02}_{-0.03}$	>100
82	194	12.0 ± 0.5 m	8.2 m	$0.68^{+0.03}_{-0.02}$	>100
82	196	37 ± 3 m	22 m	$0.59^{+0.06}_{-0.04}$	>100
82	197	8 ± 2 m	37 m	$4.6^{+1.6}_{-0.9}$	>100
82	198	2.4 ± 0.1 h	1.0 h	$0.42^{+0.01}_{-0.02}$	>100
82	199	90 ± 10 m	101 m	$1.1^{+0.2}_{-0.1}$	>100
82	201	9.33 ± 0.03 h	4.64 h	$0.497^{+0.002}_{-0.001}$	>100

Table 2.4: The calculated half-lives of the second forbidden β^+-transitions (Z=83−88) from the formula $\log_{10}(T_{1/2}^{\beta+}) = (c_1Z + c_2)N + c_3Z + c_4$ and the experimental ones. The half-lives calculated by Möller *et al.* [123] are also listed for the comparison.

Z	A	T_{exp}	T_{cal}	T_{cal}/T_{exp}	$T_{Möller}$(s)
83	191	$30.8^{+32.2}_{-10.8}$ s	23.0 s	0.7 ± 0.4	17.5409
83	192	$39.3^{+3.5}_{-3.1}$ s	39.7 s	$1.01^{+0.09}_{-0.08}$	38.2102
83	194	95 ± 3 s	118 s	1.2 ± 0.1	>100
83	196	5.1 ± 0.2 m	5.9 m	1.2 ± 0.1	>100
83	197	9.3 ± 0.5 m	10.2 m	1.1 ± 0.1	>100
83	198	10.3 ± 0.3 m	17.5 m	1.70 ± 0.05	>100
83	199	27 ± 1 m	30 m	1.1 ± 0.1	>100
83	201	108 ± 3 m	90 m	0.83 ± 0.02	>100
84	196	$92.7^{+475.3}_{-43.2}$ s	62.1 s	0.7 ± 0.6	39.5079
84	198	$4.12^{+0.27}_{-0.25}$ m	3.08 m	0.75 ± 0.05	79.6837
84	199	$5.92^{+0.20}_{-0.19}$ m	5.32 m	0.90 ± 0.03	90.7183
84	201	$15.5^{+0.3}_{-0.2}$ m	15.8 m	$1.02^{+0.01}_{-0.02}$	>100
84	203	36.7 ± 0.5 m	47.1 m	$1.28^{+0.02}_{-0.01}$	>100
84	205	1.66 ± 0.02 h	2.34 h	1.41 ± 0.02	>100
84	207	5.80 ± 0.02 h	6.97 h	1.20 ± 0.01	>100
85	197	$9.9\ ^{+4.7}_{-2.4}$ s [113]	18.9 s	1.9 ± 0.6	5.6305
85	200	$100.5^{+18.7}_{-14.2}$ s	96.8 s	1.0 ± 0.2	38.8078
85	201	293^{+107}_{-65} s	167 s	$0.6^{+0.3}_{-0.2}$	>100
85	203	$10.7^{+0.8}_{-0.7}$ m	8.3 m	$0.78^{+0.05}_{-0.06}$	>100
85	205	29.1 ± 1.2 m	24.6 m	$0.85^{+0.03}_{-0.04}$	>100
85	207	1.97 ± 0.07 h	1.22 h	0.62 ± 0.02	>100
86	203	$127.9^{+54.5}_{-31.6}$ s	87.2 s	0.7 ± 0.2	10.4064
86	205	$3.6^{+0.4}_{-0.3}$ m	4.3 m	1.2 ± 0.1	>100
86	207	$11.71^{+0.68}_{-0.64}$ m	12.84 m	1.10 ± 0.06	>100
86	209	$34.3^{+2.1}_{-1.9}$ m	38.2 m	$1.11^{+0.07}_{-0.06}$	>100
87	207	$296.0^{+200.7}_{-86.0}$ s	135.3 s	0.5 ± 0.2	8.1408
87	209	$454.5^{+174.3}_{-99.5}$ s	401.6 s	$0.9^{+0.2}_{-0.3}$	>100
88	207	13 ± 2 s	24 s	$1.8^{+0.4}_{-0.2}$	8.1326
88	209	46 ± 2 s	71 s	1.5 ± 0.1	25.7711

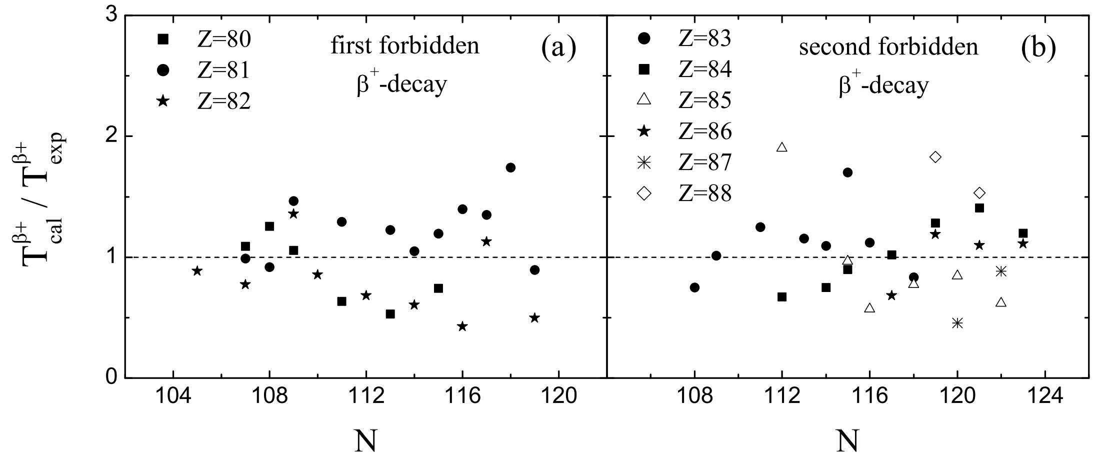

Figure 2.13: The ratios $T^{\beta+}_{\rm cal}/T^{\beta+}_{\rm exp}$ between calculated half-lives (from Eq. (2.13)) and experimental ones of the first and second forbidden β^+-decays (Fig. (2.13a) and Fig. (2.13b)) for parent nuclei with Z=80−88. ^{197}Pb with a ratio of 4.6 is not included for the convenience of plotting.

et al. that the quantity $\log_{10}(T_{cal}/T_{exp})$ is better than the quantity $(T_{cal}-T_{exp})$ to denote the deviation of calculated half-life due to the very large range of the variation of β^+-decay half-life [123]. The standard deviation for the 27 nuclei of Table 2.3 is $\sigma = 0.20$. The average deviation is defined as

$$\Delta = \frac{1}{K}\sum_{i=1}^{K} |\log_{10} T^i_{cal} - \log_{10} T^i_{exp}|. \tag{2.14}$$

For the β^+-decay half-lives of the 27 nuclei in Table 2.3, the average deviation is 0.15. This means that the average ratio between the theoretical half-life and the experimental one is a factor of 1.4. This is very good agreement between calculated β^+-decay half-life and experimental one. There is an abnormal deviation with the ratio 4.6 for ^{197}Pb. It seems to us that the half-life of ^{197}Pb is obviously smaller than that of the neighboring nuclei. It will be interesting to investigate the reason of this phenomenon both experimentally and theoretically. It is also seen from Fig. (2.13a) that the ratios between calculated half-lives and experimental ones for many nuclei lie between two values 0.5 and 1.5. When we compare our results with those calculated by Möller *et al.* [123], we find that the two results are comparable. The formalism which is used by Möller *et al.* to calculate Gamow-Teller β-strength functions involves adding pairing and Gamow-Teller residual interactions to the folded-Yukawa-single-particle Hamiltonian and solving the resulting Schrödinger equation in the quasi-particle random-phase approximation (QRPA) [123]. Here our calculation by the formula is very simple and convenient. It should be pointed out that this formula does not work very well for few nuclei very close to the β-stable line. This is because the kinetic energy of the positron emitted in the β^+-decay of the nuclei very close to the β-stable line is usually very small and the Coulomb correction is rather large. Therefore the experimental half-life of few nuclei very close to the β-stable line will be larger than the estimated half-life from Eq. (2.13) when the kinetic energy of the positron is very small. Möller *et al.* has the similar opinion with us on the deviation of long-lived nuclei [123]. They think that the calculations of half-lives are more reliable for nuclei far from stability than those close to β-stable nuclei [123]. They limit the comparison between calculated half-lives and experimental ones of the nuclei with β-decay half-lives shorter than 1000 s [123].

Table 2.5: Predicted half-lives of the first forbidden β^+-transitions from the formula $\log_{10}(T_{1/2}^{\beta+}) = (c_1Z+c_2)N+c_3Z+c_4$ (Z=80−82). The nucleus with the superscript (a sign of star, $*$) denotes that the order of the β^+-decay is estimated according to the angular momentum and parity given by Audi *et al.* [112].

Z	A	T_{cal}(s)	$T_{Möller}$(s)	Z	A	T_{cal}(s)	$T_{Möller}$(s)
80	171*	0.0024	0.1902	81	187	38.85	28.2596
80	173*	0.0094	0.2396	81	191	412.48	>100
80	175*	0.037	0.6988	81	193*	1344.00	>100
80	177*	0.14	1.6066	82	181*	0.70	0.3728
80	190	948.86	>100	82	182*	1.17	1.3770
80	192	3679.59	>100	82	183*	1.93	3.8985
81	179*	0.34	0.6911	82	184*	3.19	3.4661
81	181*	1.12	1.5255	82	185*	5.28	9.2031
81	182*	2.03	3.8800	82	186	8.74	10.0292
81	183*	3.66	3.6526	82	188	23.92	26.2945
81	184*	6.61	9.6011	82	190	65.49	96.8300
81	185*	11.92	8.9556	82	193*	296.69	>100
81	186	21.52	29.5706	82	195*	812.27	>100

After we calculate the first forbidden β^+-decay half-lives by this formula, now we use it to calculate the half-lives of the second forbidden β^+-decay. Through a least-square fit to the available experimental half-lives of 29 nuclei near Z=82 closed shell (see Table 2.4), we obtain a set of parameters as below: $c_1 = -0.0002$; $c_2 = 0.2537$; $c_3 = -0.4950$ and $c_4 = 16.8402$. The standard deviation of the fit for 29 nuclei (Z=83−88) is $\sigma = 0.15$ and the average deviation is $\Delta = 0.12$.

The numerical results are given in Table 2.4 and in Fig. (2.13b). The meaning of all columns in Table 2.4 is the same as those in Table 2.3. It is seen from columns 3−5 of Table 2.4 that the formula reproduces the experimental data well. The ratios T_{cal}/T_{exp} of all nuclei are between two values 0.5 and 2 for second forbidden β^+-decay of the nuclei with Z=83−88. The comparisons between our calculated half-lives and the results of Möller *et al.* [123] show again that the formula is reliable. It can also be seen from Fig. (2.13b) that the ratios (T_{cal}/T_{exp}) are close to 1 for many nuclei. In other words, the good agreement between calculated half-lives and experimental ones shows that the formula of β^+-decay half-lives has a firm basis in physics. Important physics is included in the formula. Therefore it is reliable to use the above two sets of values to predict the half-lives of the first and second forbidden β^+-decays of the emitters near Z=82 closed shell.

In Tables 2.5 and 2.6 we use the formula to predict the half-lives of the first and second forbidden β^+-decays of the nuclei near Z=82 closed shell. The calculated β^+-decay half-lives are listed in the third and seventh columns of Tables 2.5 and 2.6 where Table 2.6 is for the first forbidden β^+-decay and Table 2.6 is for the second forbidden β^+-decay. The corresponding results calculated by Möller *et al.* [123] are also listed in the fourth and last columns for comparison. It is seen from Tables 2.5 and 2.6 that many predicted results from the formula (Eq. (2.13)) are comparable with those calculated by Möller *et al.* [123] within a few times.

We now discuss the origin of the new formula for β^+-decay half-lives. From the new linear relationship between the logarithms of β^+-decay half-lives and the neutron number of parent nuclei along an isotopic chain, we get Eq. (2.3). For different isotopic chains, the parameters a and b in Eq. (2.3) are the function of the proton number Z. Therefore we replace the parameters a and b by the functions $a(Z)$ and $b(Z)$ in Eq. (2.3). Then we assume that both the functions $a(Z)$ and $b(Z)$ are linear functions of

Table 2.6: Predicted half-lives of the second forbidden β^{+}-transitions from the formula $\log_{10}(T_{1/2}^{\beta+}) = (c_1 Z + c_2)N + c_3 Z + c_4$ (Z=83−88). The nucleus with the superscript (a sign of star, $*$) denotes that the order of the β^{+}-decay is estimated according to the angular momentum and parity given by Audi *et al.* [112].

Z	A	T_{cal}(s)	$T_{Möller}$(s)	Z	A	T_{cal}(s)	$T_{Möller}$(s)
83	184*	0.50	0.8099	85	199	56.10	51.5309
83	185*	0.87	0.8835	85	202	287.81	73.1807
83	186	1.50	2.0916	86	196*	1.93	2.5256
83	187*	2.59	2.3738	86	197*	3.32	3.0374
83	188*	4.47	5.3884	86	198	5.73	4.5468
83	189	7.72	5.9501	86	199*	9.88	4.1937
83	190	13.33	14.2261	86	200	17.03	6.3188
83	193	68.58	55.1928	86	201	29.36	7.4289
83	195*	204.36	>100	86	202	50.61	45.9578
84	188*	0.79	1.0369	87	200*	3.00	1.1869
84	189*	1.36	0.5182	87	201	5.17	1.8796
84	190	2.35	1.5836	87	202	8.91	1.8093
84	191*	4.06	1.4769	87	203*	15.35	2.6678
84	192	7.00	6.1282	87	204	26.44	2.2906
84	193*	12.09	6.4327	87	205	45.56	5.5758
84	194	20.85	23.4324	87	206	78.51	5.9714
84	195*	35.98	14.3612	88	202	1.57	1.9605
84	197	107.13	27.3832	88	203*	2.70	2.3119
85	193*	2.13	2.4858	88	204	4.65	3.5742
85	194*	3.68	3.6588	88	205	8.01	3.0422
85	196*	10.94	5.1830	88	206	13.80	9.8328
85	198	32.53	6.0437	88	211	209.17	33.6425

the proton number Z, i.e.

$$
\begin{aligned}
a(Z) &= c_1 Z + c_2, \\
b(Z) &= c_3 Z + c_4,
\end{aligned}
\tag{2.15}
$$

where c_1, c_2, c_3 and c_4 are four constants to be determined. At last, we substitute the expressions of $a(Z)$ and $b(Z)$ for the parameters a and b in Eq. (2.3) and get the new formula (Eq. (2.13)) for β^+-decay half-lives.

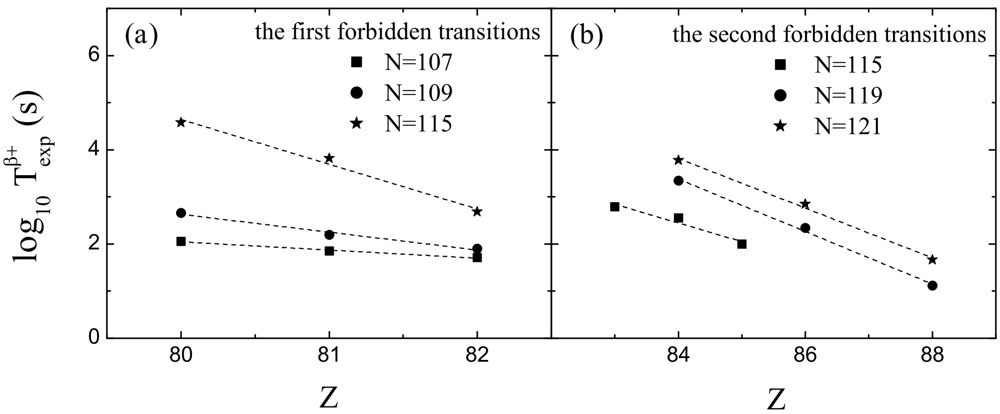

Figure 2.14: The variation of experimental β^+-decay half-lives (in $\log_{10}$-scale) with proton number for isotonic chains with N=107, 109, 115, 119 and 121. Fig. (2.14a) is for the first forbidden transitions and Fig. (2.14b) is for the second forbidden ones.

We can also derive from the formula (Eq. (2.13)) that the logarithm of β^+-decay half-life depends linearly on the proton number along any isotonic chain. The relationship between the β^+-decay half-lives (in $\log_{10}$-scale) and the proton numbers is drawn in Figs. (2.14a) and (2.14b) where the x axis is proton number and the y axis is experimental β^+-decay half-life (in $\log_{10}$-scale). It is seen clearly from Figs. (2.14a) and (2.14b) that the experimental half-lives of both the first and second forbidden transitions lie approximately on a straight line for isotonic chains. This shows again that the formula is reliable for describing the β^+-decay half-lives.

2.3.2 Generalization of the formula to all nuclei far from stability

In previous section, it is demonstrated that the new formula (Eq. (2.13)) works very well for describing the first and second forbidden β^+-decays of the nuclei far from stability near the $Z = 82$ closed shell. Now we generalize this formula to include the allowed β^+-transition and to include all available experimental data of nuclei far from

Table 2.7: The comparison of the two sets of parameters [(a) without even-odd effects; (b) with even-odd effects] used in the least-square fit of experimental half-lives of the allowed β^+-transition, the first and second forbidden β^+-transitions by the formula (Eq. (2.13)). The standard deviation σ of each set of parameters is also listed. The word "order" in the first column denotes the order of the β^+-decay from ground state to ground state.

(a)	even-odd effect not included				
order	c_1	c_2	c_3	c_4	σ
allowed	-0.00157	0.3829	-0.3080	-0.7489	0.70
first	-0.00125	0.3923	-0.4105	3.8172	0.36
second	-0.00161	0.3925	-0.3214	-0.2701	0.39

(b)	even-odd effect included						
order	c_1	c_2	c_3	c_4			σ
				e-o, o-e	o-o	e-e	
allowed	-0.00179	0.4233	-0.3405	-0.6443	-1.7089	-0.2132	0.47
first	-0.00127	0.3992	-0.4183	3.8215	3.7969	4.0364	0.35
second	-0.00162	0.3980	-0.3286	-0.1618	-0.4854	0.0267	0.35

the β-stable line. In our calculation, all available nuclei with $\delta N > 5$ is included, where $\delta N = N_{stable} - N$, denotes the nuclei far from the β-stable line, as defined in section 2.1.1.

First, we use the formula (Eq. (2.13)) to calculate the half-lives of the allowed β^+-transition of all available data of nuclei far from the β-stable line. All experimental values (without special notation) of β^+-decay half-lives used in this part are taken from the Nubase table of nuclear and decay properties by Audi *et al.* [112]. The β^+-decay in the Nubase table [112] contains two kinds of process: positron emission and orbital electron capture. Through a least-square fit to the available experimental data of 138 nuclei with allowed β^+-decay, we obtain a set of parameters of Eq. (2.13) (see Table 2.7(a)): $c_1 = -0.00157$, $c_2 = 0.3829$, $c_3 = -0.3080$, and $c_4 = -0.7489$. The standard deviation of the least-square fit is defined the same as Eq. (2.4). For the 138 nuclei with allowed β^+ transitions, the standard deviation is 0.70 (see Table 2.7(a)).

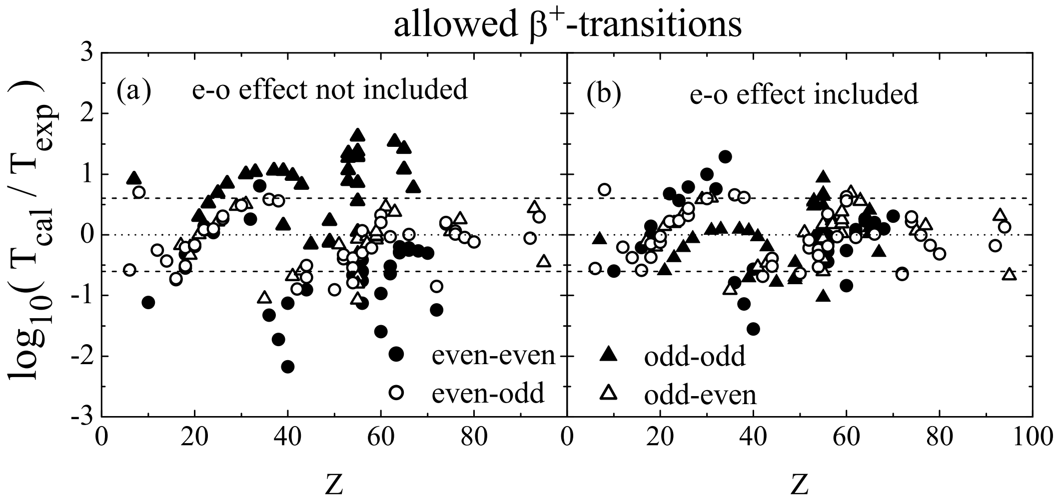

Figure 2.15: The ratio $T_{\rm cal}/T_{\rm exp}$ (in $\log_{10}$ scale) between calculated and experimental half-lives of allowed β^+-decay plotted vs proton numbers of the parent nuclei. Deviation by a factor of 4 between theory and experiment is represented by broken lines. The figure shows the results for the two sets of parameters (without e-o effects and with e-o effects) for 138 nuclei with allowed β^+-transitions from ground states to ground states.

The logarithms of ratios between calculated and the experimental half-lives of allowed β^+ decays are plotted versus the proton numbers of the parent nuclei in Fig. (2.15a). It is seen from Fig. (2.15a) that the deviations between theoretical and experimental results are within a few times for many nuclei. This denotes that the formula is valid for crudely describing β^+-decay half-lives of allowed β^+-transitions. When focusing on the results shown in Fig. (2.15a), we find that large deviations mainly concentrate on the odd-odd nuclei and the even-even nuclei, while the deviations are small for the even-odd nuclei and the odd-even nuclei. For the odd-odd nuclei, the calculated β^+-decay half-lives are generally larger than the experimental ones, whereas for the even-even nuclei, most of the calculated results are smaller than the experimental ones. This is because the β^+-decay energy of the odd-odd nucleus is averagely larger than that of the even-even nucleus due to the pairing energy effects. Therefore the even-odd (e-o) effects should be included for the allowed β^+-transitions. As a simple treatment of the even-odd effects, we use different values of c_4 for even-even, odd-odd, and odd-A nuclei, respectively. c_4 is adopted the same value for the even-odd and odd-even nuclei because of proton-neutron symmetry (the differences of β^+-decay energy are not obvious for the even-odd and odd-even nuclei).

By taking into account the e-o effects and through a least-square fit to 138 nuclei with allowed β^+ decay, we obtain a new set of parameters of Eq. (2.13) (see Table

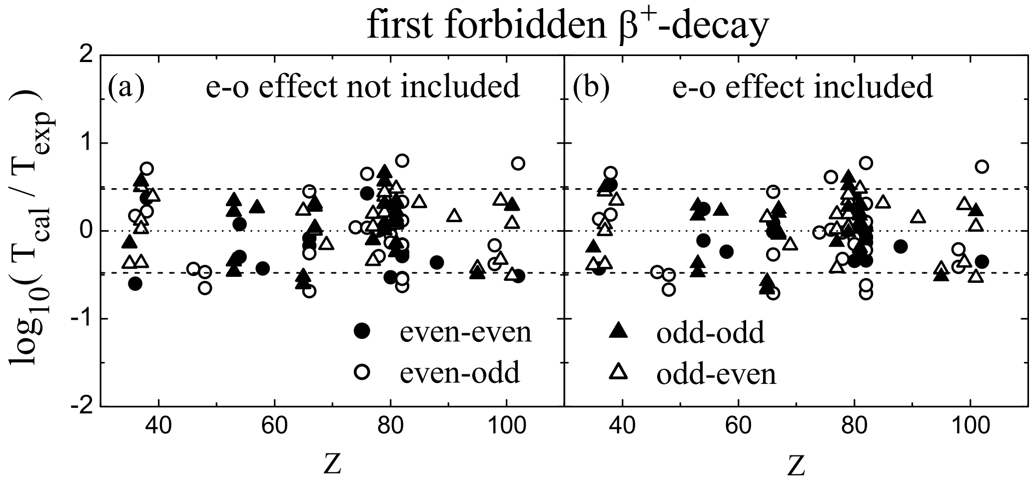

Figure 2.16: Same as in Fig. 2.15, but for 102 nuclei with the first forbidden β^{+}-decays from ground states to ground states. Deviation by a factor of 3 between theory and experiment is represented by broken lines.

2.7(b)): $c_1 = -0.00179$, $c_2 = 0.4233$, $c_3 = -0.3405$, $c_4^{\rm eo,oe} = -0.6443$, $c_4^{\rm oo} = -1.7089$, and $c_4^{\rm ee} = -0.2132$, where $c_4^{\rm eo,oe}$ is the value of c_4 for even-odd or odd-even nuclei, and $c_4^{\rm oo}$ and $c_4^{\rm ee}$ are the values of c_4 for odd-odd and even-even nuclei, respectively. The standard deviation is 0.47 for the 138 nuclei with allowed β^{+} transitions. The ratio (in log-scale) between calculated and experimental β^{+}-decay half-life is plotted versus proton number of parent nucleus in Fig. (2.15b). It is seen from Fig. (2.15b) that the deviations between $T_{cal.}$ and $T_{exp.}$ are within a factor of four for most nuclei. The average deviation is a factor of 2.3, although the β^{+}-decay half-lives vary in a wide range from 10^{-3} s to 10^{6} s. This shows that the formula can give a reliable description of the β^{+}-decay half-lives of all available nuclei (with the allowed β^{+}-transitions from ground states to ground states) far from the β-stable line by taking into account the e-o effects. In addition, it should be pointed out that the formula can also give acceptable description of the β^{+}-decay half-lives for some nuclei close to the β-stable line. The average deviation between calculated and experimental β^{+}-decay half-lives of the nuclei close to the β-stable line is relatively larger than that of the nuclei far from stability [123]. In this case, these nuclei are included in the calculation.

After we calculate the half-lives of allowed β^{+}-transitions by this formula (Eq. (2.13)), we now use it to calculate the β^{+}-decay half-lives of all available nuclei far from the β-stable line with the first and second forbidden β^{+}-transitions from ground states to ground states. The two sets of parameters without e-o effects and with e-o effects, and the standard deviation σ of each set of parameters are listed in Table 2.7. It is

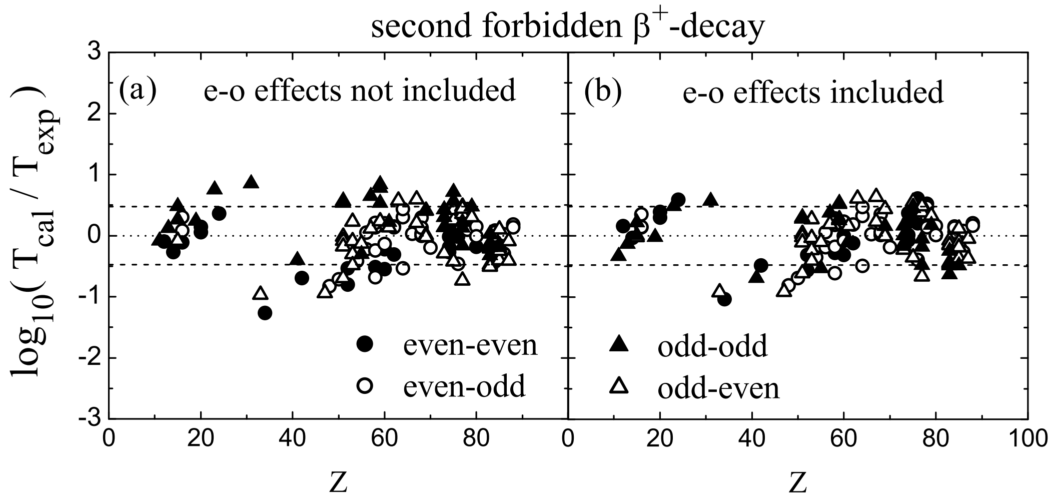

Figure 2.17: Same as in Fig. 2.15, but for 144 nuclei with the second forbidden β^+-decays from ground states to ground states. Deviation by a factor of 3 between theory and experiment is represented by broken lines.

seen from Table 2.7 that the standard deviations of both two sets of parameters (e-o effects not included and included) for the nuclei with the first and second forbidden β^+ decays are smaller than the corresponding standard deviations for the nuclei with allowed transitions. When the e-o effects are not included, the standard deviations are respectively 0.36 and 0.39 for the first and second forbidden β^+ decays, whereas both standard deviations of the two kinds of forbidden transitions decrease to 0.35 after taking into account the e-o effects. It is also seen from Figs. (2.16a), (2.16b), (2.17a), and (2.17b) that the deviations between calculated and experimental half-lives of both the first and second forbidden β^+ decays of most nuclei are within a factor of 3 using both sets of parameters with e-o effects and without e-o effects. This is good agreement between theoretical and experimental β^+-decay half-lives with a simple formula. In the calculation, there are large changes of nucleon numbers ($A = 20 - 257$) and large changes of β^+-decay half-lives (10^{-3}–10^6 s). The comparison between calculated results and experimental ones shows that the formula with both the two sets of parameters (e-o effects not included and included) can give good descriptions of the half-lives of the first and second forbidden β^+-transitions of all available nuclei far from β-stable line. It should be pointed out that the experimental β^+-decay half-life of ^{84}Mo is taken from the result of measurement by Kienle *et al.* [124]. The β^+-decay half-life of ^{84}Mo in the Nubase table is 3.8 ± 0.9 ms [112], while it is $3.7^{+1.0}_{-0.7}$ s from the result of measurement by Kienle *et al.* [124]. There may be a printing error on the β^+-decay half-life of ^{84}Mo in the Nubase table because the value of β^+-decay half-life of ^{84}Mo in the Nubase table is cited from the result of measurement by Kienle *et al.* [124]. The calculated β^+-decay half-life of ^{84}Mo from the formula (with e-o effects) is 1.2 s, which deviates from the experimental data measured by Kienle *et al.* [124] by a factor of 3.

All above results show that the formula of β^+-decay half-lives is valid for both nuclei with allowed β^+-transitions and nuclei with the first and second forbidden β^+ transitions from ground states to ground states. Different orders of β^+ decays can be described in a unified formula with different sets of parameters. This denotes that the formula of β^+-decay half-lives has a firm basis in physics. Important physics is included in the formula. The analytical formula is not only simple, but also practical to experimentalists for estimating β^+-decay half-lives of nuclei conveniently. A typical example is the Viola-Seaborg formula [120,121] and Geiger-Nuttall law, which are widely used in the calculation of α-decay half-lives [120,121,125]. Therefore it is reliable to use the formula to analyze the experimental data and to predict the β^+-decay half-lives of nuclei far from the β-stable line. The input quantities are proton number and neutron number of parent nucleus. It is easy to get the β^+-decay half-lives of nuclei from this formula.

In Table 2.8 we use the formula to predict the half-lives of the allowed β^+-transitions of the nuclei far from the β-stable line with $Z = 50 - 70$. The e-o effects is included in the calculation. The calculated β^+-decay half-lives are listed in the third and seventh columns of Table 2.8. The corresponding results calculated by Möller *et al.* [123] are listed in the fourth and last columns for comparison. It is seen from Table 2.8 that many predicted results from the formula (Eq. (2.13)) are comparable with those calculated by Möller *et al.* [123] within a factor of a few.

2.3.3 Even-odd effects on β^+-decay half-lives

We now discuss the e-o effects on β^+-decay half-lives. For the allowed β^+-decay, the calculated β^+-decay half-lives by this formula is greatly improved by taking into account the e-o effects (σ decreases from 0.70 to 0.47). The differences between $c_4^{\rm ee}$ and $c_4^{\rm oo}$ are close to 1.5 (see Table 2.7). This shows that the β^+-decay half-lives of even-even nuclei are averagely larger than those of the odd-odd nuclei by about 30 times for allowed β^+-transitions. Therefore the e-o effect is very apparent for the allowed β^+-transitions. Whereas for the first and second forbidden β^+ decays, the improvement on the calculated results is not so apparent as the allowed β^+-transition after taking into the e-o effects (σ decreases from 0.36 to 0.35 and from 0.39 to 0.35, respectively

Table 2.8: Predicted half-lives of the allowed β^+-transitions from the formula $\log_{10}(T_{1/2}^{\beta+}) = (c_1 Z + c_2)N + c_3 Z + c_4$ ($Z = 50 - 70$) by taking into account the e-o effects. Nuclei marked with an asterisk denote that the order of the β^+ decay is estimated according to the angular momentum and parity given by Audi *et al.* [112]. The β^+-decay half-lives calculated by Möller *et al.* [123] are also listed for the comparison.

Z	A	$T_{cal.}$(s)	$T_{\text{Möller}}$(s)	Z	A	$T_{cal.}$(s)	$T_{\text{Möller}}$(s)
50	99*	0.049	0.0418	55	113*	0.29	0.4321
51	103*	0.18	0.0917	59	123*	0.40	0.6794
51	105	0.83	0.3175	59	127*	7.40	4.0607
51	107*	3.83	1.3605	60	125*	0.29	0.4186
51	109*	17.65	9.4043	60	127*	1.23	0.9949
52	105*	0.14	0.3675	60	129*	5.28	5.1610
52	107*	0.65	0.8994	60	131*	22.63	23.7632
52	109*	2.97	3.0620	61	127*	0.21	0.3316
52	111*	13.57	37.2692	61	129*	0.88	0.7857
53	108*	0.020	0.1350	61	131*	3.74	2.1035
53	109	0.50	0.3380	62	131*	0.62	0.7476
53	110*	0.092	0.5278	62	138*	258.30	>100
53	111*	2.28	0.9116	63	131*	0.10	0.1474
53	112*	0.42	1.5971	63	137*	7.65	4.9741
53	113*	10.35	2.8818	64	139*	5.24	5.8943
53	115*	46.97	9.3350	65	139*	0.87	1.1528
54	110*	0.49	0.6187	66	147*	39.87	4.3337
54	111*	0.39	0.8058	67	141	0.098	0.2712
54	112*	2.21	2.0679	68	143*	0.066	0.2673
54	113*	1.74	2.1606	69	150	0.12	0.4486
54	115*	7.83	7.5922	70	150	0.62	0.5318
55	112*	0.012	0.2298				

for the first and second forbidden β^+ decays). The differences between $c_4^{\rm ee}$ and $c_4^{\rm oo}$ are 0.24 and 0.51, respectively for the first and second forbidden β^+ decays (see Table 2.7). This denotes that the β^+-decay half-lives of the even-even nuclei are averagely larger than those of the odd-odd nuclei by 0.7 and 2.2 times for the first and second forbidden β^+-transitions, respectively. Therefore the e-o effects on the half-lives of the first and second forbidden β^+-transitions are much less apparent than those on the half-lives of allowed β^+-transitions.

It is interesting to analyze the reason which causes the difference of the e-o effects on the half-lives of allowed and of forbidden β^+-transitions. It is known that there are β^+-transitions from the ground states of parent nuclei to excited levels of daughter nuclei. For allowed β^+-decay, the branching ratio of the β^+-transition from ground state to ground state is relatively larger than that of the β^+-transition from ground state to excited state for many nuclei because the decay energy of β^+-transition from ground state to ground state is the largest and many β^+-transitions from ground state to excited states are forbidden transitions. For example, the branching ratios of the β^+-transitions from ground states to ground states for ^{124}Cs, ^{125}Cs, and ^{126}Cs are 58%, 54%, and 56.4% [126], respectively. For most nuclei close to the β-stable line, the branching ratios of the β^+-transitions from ground states to ground states are close to 100%, such as ^{130}Cs and ^{131}Cs, with the branching ratios 94.5% and 100% [126], respectively. The available energy of the β^+-transition (from ground state to ground state) of the even-even nuclei is smaller than that of the corresponding odd-odd nuclei because of the effects of pairing energy. As a result, the β^+-decay half-lives of the even-even nuclei are larger than that of the corresponding odd-odd nuclei. Therefore, the e-o effects are apparent for the nuclei with mainly allowed β^+-transitions from ground state to ground state.

For the forbidden β^+-transitions, the β^+-transitions from ground states to ground states are not the main decay channel for many nuclei because there usually exists the allowed β^+-transition from ground state to the excited energy level of daughter nuclei. For example, the branching ratios of the β^+-transitions from ground states to ground states for ^{200}Tl, ^{190}Pb, ^{192}Pb, and ^{194}Pb are 5.8%, 0.5%, 0.5%, and 0.8% [126], respectively. For the β^+-transition from ground state to excited state, the Q-value of the decay can be written as

$$
\begin{aligned}
Q_{oo}^{e.x.} &= Q_{oo}^{g.s.} - E_{ee}^{e.x.}, \qquad \text{for odd-odd nuclei,} \\
Q_{ee}^{e.x.} &= Q_{ee}^{g.s.} - E_{oo}^{e.x.}, \qquad \text{for even-even nuclei,} \qquad (2.16)
\end{aligned}
$$

where $Q^{e.x.}$ and $Q^{g.s.}$ is the Q-value of the β^{+}-transition from ground state to exited state and of the β^{+}-transition from ground state to ground state, respectively. $E^{e.x.}$ is the excited energy of the daughter nuclei. The excited energy of even-even nuclei is often larger than that of the odd-odd nuclei, that is, $E_{ee}^{e.x.} > E_{oo}^{e.x.}$. Although $Q_{oo}^{g.s.}$ is larger than $Q_{ee}^{g.s.}$ due to the effect of pairing energy, $E_{ee}^{e.x.}$ is larger than $E_{oo}^{e.x.}$. As a result, the difference between $Q_{oo}^{e.x.}$ and $Q_{ee}^{e.x.}$ decreases. In other words, the difference between the excited energy of even-even nuclei and that of the odd-odd nuclei partially offsets the effect of pairing energy for forbidden β^{+}-transitions. Therefore the e-o effects on the half-lives of the forbidden β^{+}-transitions are less apparent than those on the half-lives of the allowed β^{+}-transitions.

2.4 New formula for β^{-}-decay half-lives

2.4.1 New formula for β^{-}-decay half-lives of nuclei far from stable stability

Since the half-lives of β^{-} decay and β^{+} decay obey a similar exponential law for nuclei far from β-stability, we use the same formula which is justified for the β^{+}-decay half-lives to describe the β^{-}-decay half-lives. The formula is written as

$$\log_{10} T_{1/2} = (c_1 Z + c_2)N + c_3 Z + c_4, \tag{2.17}$$

where $T_{1/2}$ is the half-life of β^{-}-decay (in seconds) and Z is the proton number of parent nuclei. The values of parameters c_1, c_2, c_3 and c_4 are determined according to all available experimental data of β^{-}-decay half-lives of nuclei far from the β-stable line ($\delta N > 5$). Through a least-square fit to all available experimental data of 351 nuclei far from the β-stable line, we obtain a set of parameters of Eq. (2.17): $c_1 = 2.65 \times 10^{-4}$, $c_2 = -0.2275$, $c_3 = 0.3652$, and $c_4 = -0.8852$. The standard deviation σ and average deviation Δ between the logarithms of the calculated and experimental β^{-}-decay half-lives are used to denote the reliability of the formula. The standard deviation for the 351 nuclei is 0.44 (a factor of 2.8). The average deviation which is written as

$$\Delta = \frac{1}{K}\sum_{i=1}^{K} |\log_{10} T_{\mathrm{cal}}^{i} - \log_{10} T_{\mathrm{exp}}^{i}| \tag{2.18}$$

is 0.35 (a factor of 2.2). It is seen from Figs. (2.18a) and (2.18b) that experimental β^{-}-decay half-lives of nuclei far from β-stable line are reproduced reasonably by this simple formula [Eq. (2.17)] with four parameters.

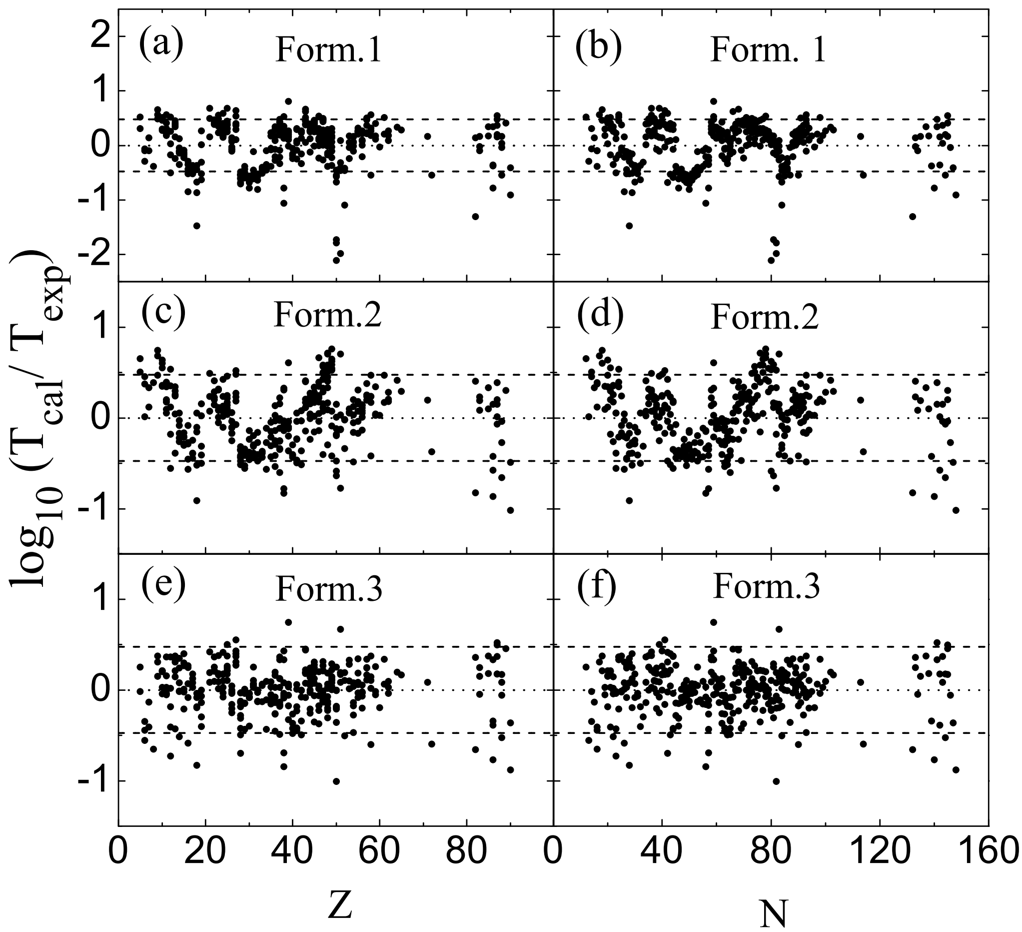

Figure 2.18: The ratios $T_{\rm cal}/T_{\rm exp}$ (in $\log_{10}$-scale) between calculated and experimental β^--decay half-lives plotted versus proton and neutron numbers of parent nuclei. Deviation by a factor of 3 between theory and experiment is represented by broken lines. The figure shows three sets of numerical results: Eq. (2.17) (Form.1), Eq. (2.21) (Form.2), and Eq. (2.22) (Form.3).

When we focus on Figs. (2.18a) and (2.18b), we find that the calculated β^--decay half-lives are systematically smaller than the experimental ones for nuclei near the proton "magic numbers" ($Z = 20, 28, 50, 82$) or the neutron "magic numbers" ($N = 28, 50, 82, 126$). This indicates that the nuclei near the proton or neutron shells are stabler than other nuclei despite they are far from the β-stable line. The shell effects still strongly influence β^--decay half-lives of nuclei far from stability. For example, near the "magic cross" at ^{132}Sn, the experimental β^--decay half-lives are underestimated by about 2 orders of magnitudes from Eq. (2.17). The simple formula [Eq. (2.17)] only reflects the average trends of the change of β^--decay half-lives for nuclei far from stability. Therefore the shell corrections which is caused by the quantum effect should be included.

The details of the shell effects on β^--decay half-lives will be discussed in section 2.4.2. Here we take into account the shell effects empirically. It is seen from Figs. (2.18a) and (2.18b) that the closer the nuclei to the proton or neutron "magic-number" regions, the larger deviations exist between calculated β^--decay half-lives and experimental ones. There seems to exist a correlation between β^--decay half-lives and the fine details in the systematics of the ground masses of nuclei. A simple way of exhibiting this correlation is to include the deviations between experimental ground state masses and theoretical ones from the smooth liquid drop model ($\Delta M = M_{\rm exp} - M_{\rm the}$, in units of MeV/$c^2$) in Eq. (2.17). The function of shell correction is empirically written as

$$shell(Z, N, \Delta M, Q_{\beta^-}) = c_5 \frac{\Delta M c^2}{Q_{\beta^-} + c_6 ZN}, \tag{2.19}$$

where Q_{β^-} is the Q values of β^--decay (in units of MeV), and c_5 and c_6 are two constants to be determined. The denominator of Eq. (2.19) demonstrates the hindrance factor caused by ΔM. In our calculations, the experimental ground state mass $M_{\rm exp}$ are taken from the 2003 atomic mass table by Audi *et al.* [116]. The semiempirical mass surface $M_{\rm the}$ is $M_{\rm the} = ZM(^1H) + NM(n) - B/c^2$, where $M(^1H)$ and $M(n)$ are experimental masses of hydrogen and neutron, respectively. B is the binding energy from the liquid drop model [127]:

$$B = 15.73A - 17.77A^{2/3} - 0.70905\frac{Z^2}{A^{1/3}} - (26.46A - 17.70A^{2/3})I^2, \tag{2.20}$$

where $I = (N - Z)/A$ is the *charge-asymmetry parameter* of the given nucleus [127].

After including the shell effects, we have the following formula

$$\log_{10} T_{1/2} = (c_1 Z + c_2)N + c_3 Z + c_4 + c_5 \frac{\Delta M c^2}{Q_{\beta^-} + c_6 ZN} \tag{2.21}$$

to describe the β^--decay half-lives. According to a least square fit to available experimental data, we obtain a set of parameters of Eq. (2.21): $c_1 = 3.77 \times 10^{-4}$, $c_2 = -0.2990$, $c_3 = 0.4629$, $c_4 = -0.5230$, $c_5 = -1.0222$, and $c_6 = 1.16 \times 10^{-3}$. The standard deviation σ for the 351 nuclei is 0.34 (a factor of 2.19), and the average deviation Δ is 0.28 (a factor of 1.91).

In order to use the formula to calculate β^--decay half-lives of nuclei with unknown masses, we consider another form to describe the shell effects. The Gaussian function is used to characterize the shell effects of a single "magic number" region and the effects of "magic cross" region near ^{132}Sn on β^--decay half-lives. The functions of shell corrections and β^--decay half-lives are written as

$$\begin{aligned} shell(Z,N) &= c_5[e^{-(N-29)^2/15} + e^{-(N-50)^2/37} + e^{-(N-85)^2/9} \\ &\quad + e^{-(N-131)^2/3}] + c_6 e^{-[(Z-51.5)^2+(N-80.5)^2]/1.9}, \\ \log_{10} T_{1/2} &= (c_1 Z + c_2)N + c_3 Z + c_4 + shell(Z,N). \end{aligned} \tag{2.22}$$

The particular values used in the Gaussian functions of Eq. (2.22) are empirically determined according to detailed analysis of Figs. (2.18a) and (2.18b). The chosen centers of Gauss functions are close to the "magic number" region and sometimes it slightly deviates from the "magic number" because of the dramatic changes of the β^--decay half-lives and energy level structures of daughter nuclei close to the "magic number" and "magic cross" regions. For example, to describe the $Z = 50$ and $N = 82$ "magic cross" region, we use the term $c_6 e^{-[(Z-51.5)^2+(N-80.5)^2]/1.9}$ plus the term $c_5 e^{-(N-85)^2/9}$. The sum of the two terms makes shell correction on $N = 80$ bigger than that on $N = 82$ for Sn isotopic chain. This reason is that ^{130}Sn is relatively closer to β^--stable line than ^{132}Sn. According to our analysis in section 2.1.1, the β^--decay half-life of the nuclide close to β-stable line is more sensitive to nuclear structure effects than that of the nuclide far from the β-stable line. As a result, the shell correction on β^--decay half-life of ^{130}Sn is relatively larger than that of ^{132}Sn. And the choice of the particular value of sigma used for Gauss function is based on the width of influenced nuclear region by corresponding "magic number". For example, we can see from Fig. 2.18(b) that the influencing region of $N = 50$ closed shell are approximately from $N = 44$ to $N = 56$, therefore we choose the term $c_5 e^{-(N-50)^2/37}$ (sigma is close to 6) to describe the shell correction of $N = 50$ closed shell.

The parameters of Eq. (2.22) are obtained through a least-square fit to the experimental data: $c_1 = 3.37 \times 10^{-4}$, $c_2 = -0.2558$, $c_3 = 0.4028$, $c_4 = -1.0100$, $c_5 = 0.9039$, and $c_6 = 7.7139$. The standard deviation σ is 0.27 (a factor of 1.86), and the average deviation Δ is 0.21 (a factor of 1.62). The ratio (in $\log_{10}$-scale) between calculated half-life and experimental one is plotted versus proton number (left panel) and neutron number (right panel) of parent nucleus in Fig. 2.18. It is seen from Figs. (2.18c), (2.18d), (2.18e), and (2.18f) that the ratios between calculated β^--decay half-lives and experimental ones are within a factor of 3 for most nuclei, indicating good agreement with the experimental data. Form.3 reproduces experimental data better than Form.2. It reproduces 261 (74.4%) nuclei of all available experimental data of 351 nuclei within

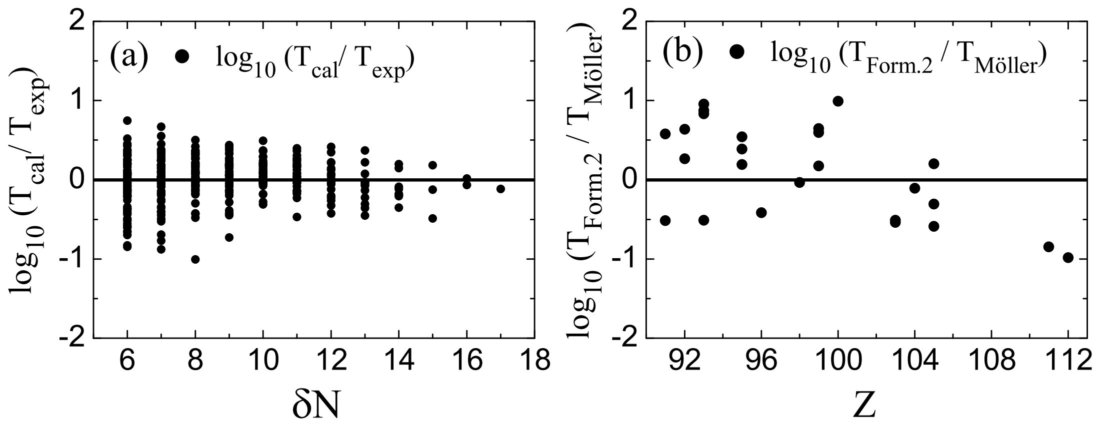

Figure 2.19: (a): Variations of the ratios ($T_{\mathrm{cal}}/T_{\mathrm{exp}}$, in $\log_{10}$-scale) between calculated β^--decay half-lives from Form.3 [Eq. (2.22)] and experimental ones with δN (distance from the β-stable line). (b): The comparison between predicted β^--decay half-lives from Form.2 [Eq. (2.21)] and those calculated by Möller *et al.* [123]. In our calculation, the experimental masses and Q values of β^--decays are replaced by the calculated values by Möller *et al.* [123]. The plotted nuclei are taken from Table 2.10.

a factor of 2, and 324 (92.3%) nuclei within a factor of 3. The calculated results from Form.3 [Eq. (2.22)] is comparable to those calculated from the microscopic model. For example, the calculation using pn-QRPA model by Nabi *et al.* [13] reproduces 82.2% of all experimentally known β^--decay half-lives shorter than one minute within a factor of 2, and 90.8% within a factor of 3 in the mass range $A = 40 - 100$. In addition, the large changes of nucleon number (A=17−238) and large changes of β^--decay half-lives (10^{-3}−10^3 s) in our calculation demand that the formula has a firm basis in physics. It may reflect the statistical behavior of nuclear β^--decay half-lives due to the fact that the β^--decays occur between the ground state of parent nucleus to multi-energy levels of daughter nucleus for nuclei far from β-stable line. Therefore, we can draw the conclusion that the formula is valid for describing β^--decay half-lives of nuclei far from the β-stable line.

Before we use Form.3 [Eq. (2.22)] to predict the β^--decay half-lives, we want to check the predictive power of this simple formula for nuclei far from the β-stale line. In Fig. 2.19(a) we plot the variation of the logarithm of the ratio ($T_{\mathrm{cal}}/T_{\mathrm{exp}}$) between calculated β^--decay half-life from Form.3 and experimental one with δN (the distance from the β-stable line). It is seen from Fig. 2.19(a) that there are general trends of

Table 2.9: Comparisons between the calculated β^--decay half-lives from Form.2 and Form.3 and experimental ones of nuclei close to the β-stable line ($\delta N \leq 5$) with $T_{\mathbf{exp}}^{\beta-} < 1$ hour and $Z > 90$.

Z	A	$T_{\rm exp}$	$T_{\rm Form.2}$	$T_{\rm Form.3}$
91	235	24.44 ± 0.11 min	32.72 min	28.02 min
91	236	9.1 ± 0.1 min	17.2 min	16.7 min
91	237	8.7 ± 0.2 min	9.6 min	9.9 min
91	238	2.27 ± 0.09 min	5.12 min	5.92 min
92	239	23.45 ± 0.02 min	18.43 min	16.77 min
92	242	16.8 ± 0.5 min	3.1 min	3.5 min
93	241	13.9 ± 0.2 min	33.5 min	28.3 min
93	242	2.2 ± 0.2 min	17.4 min	16.9 min
93	243	1.85 ± 0.15 min	9.63 min	10.08 min
93	244	2.29 ± 0.16 min	5.06 min	6.01 min
95	246	39 ± 3 min	58 min	49 min
95	247	23.0 ± 1.3 min	32.8 min	29.0 min
96	251	16.8 ± 0.2 min	17.2 min	17.6 min
97	251	55.6 ± 1.1 min	110.6 min	84.0 min
99	256	25.4 ± 2.4 min	187.3 min	146.7 min

decrease of the deviation between theory and experiment along with the increase of δN. The ratios ($T_{\rm cal}/T_{\rm exp}$) are within a factor of 3 when $\delta N \geq 10$. This indicates that Form.3 is reliable for predicting the β^--decay half-lives of nuclei quite far from the β-stable line. Furthermore, the calculation with Form.3 [Eq. (2.22)] is very simple and it is convenient to physicists for analyzing the experimental data.

Similarly, to display the usefulness of Form.2 [Eq. (2.21)] in the region of the nuclear chart where there are very little experimental data. For example, the experimental masses and β^--decay Q vales are unknown. In Fig. 2.19(b) we make the comparisons between predicted β^--decay half-lives from Form.2 [Eq. (2.21)] and those calculated by Möller *et al.* [123] for heavy nuclei with $Z > 90$. In our calculation, the experimental masses and Q values of β^--decays are replaced by the calculated values by Möller *et al.* [123]. The plotted nuclei are taken from Table 2.10. It is seen from Fig. 2.19(b) that the ratios between our predicted results and those calculated by Möller *et al.* [123] are within a factor of 10. This shows the reliability of Form. 2 [Eq. (2.21)] in predicting the β^--decay half-lives of unknown nuclei far from stability.

Moreover, to demonstrate the extrapolability of the formula, we calculate the β^--decay half-lives from Form.2 and Form.3 for nuclei not far from the β-stable line ($\delta N \leq 5$) and with $Z > 90$. The comparisons between calculated β^--decay half-lives and experimental ones are shown in Table 2.9. We limit the comparisons to nuclei with experimental β^--decay half-lives shorter than 1 hour. Our limitation is similar to that made by Möller *et al.* [123] for the comparisons between theoretical β^--decay half-lives and experimental data. This is due to that the formula is valid for nuclei far from the β-stable line and the calculations of β^--decay half-lives are more reliable for nuclei far from stability than those close to β-stable line [13,123]. In Table 2.9 the first and second columns denote the proton and mass number of parent nuclei, respectively. The third column is the experimental β^--decay half-lives. The numerical results from Eq. (2.21) (Form.2) and from Eq. (2.22) (Form.3) are given in column 4 and column 5, respectively. It is seen from Table 2.9 that calculated β^--decay half-lives agree with experimental ones reasonably. The ratios ($T_{\rm cal}/T_{\rm exp}$) are within a factor of a few. Although the fitting parameters of the formula are obtained for the nuclei with $Z \leq 90$ and $\delta N > 5$ (there is no available experimental data of β^--decay half-lives of nuclei with $\delta N > 5$ and $Z > 90$ at present), the extrapolation to the nuclei with $Z > 90$ and $T^{\beta-}_{\rm exp} < 1$ hour is also valid according to the above analysis.

Table 2.10: Predicted β^--decay half-lives from Form.3 [Eq. (2.22)] for heavy nuclei with $Z > 90$. The β^--decay half-lives calculated by Möller *et al.* [123] are listed for comparison.

Z	A	$T_{\rm Form.3}$(s)	$T_{\rm Möller}$(s)	Z	A	$T_{\rm Form.3}$(s)	$T_{\rm Möller}$(s)
91	240	125.89	22.4422	102	274	97.80	>100
91	241	74.96	>100	102	275	58.74	>100
91	242	44.64	81.9792	102	276	35.28	>100
92	241	357.27	70.9913	103	277	102.07	>100
92	243	126.88	>100	103	278	61.35	78.0285
92	244	75.61	>100	103	279	36.88	40.7871
92	245	45.06	14.0344	104	280	106.87	>100

(Continued on next page)

Table 2.10 – continued from previous page

Z	A	$T_{\text{Form.3}}$(s)	$T_{\text{Möller}}$(s)	Z	A	$T_{\text{Form.3}}$(s)	$T_{\text{Möller}}$(s)
93	245	215.09	22.1105	104	281	64.28	30.8755
93	246	128.28	9.3281	104	282	38.67	>100
93	247	76.51	6.5868	105	283	112.23	28.5362
93	248	45.63	73.6410	105	284	67.56	49.5192
94	249	130.10	>100	105	285	40.67	52.3822
94	250	77.65	>100	106	286	118.24	>100
94	251	46.35	>100	106	287	71.23	>100
95	252	132.36	21.1622	106	288	42.91	>100
95	253	79.06	16.5794	107	289	124.95	>100
95	254	47.23	13.6702	107	290	75.33	>100
96	255	135.07	>100	107	291	45.42	>100
96	256	80.75	>100	108	293	79.92	>100
96	257	48.27	59.3366	108	294	48.22	>100
97	258	138.27	>100	108	295	29.10	>100
97	259	82.72	>100	109	296	85.05	>100
97	260	49.49	>100	109	297	51.36	>100
98	261	141.98	>100	109	298	31.01	>100
98	262	85.01	>100	110	299	90.79	>100
98	263	50.90	24.0113	110	300	54.87	>100
99	264	146.25	18.9654	110	301	33.16	>100
99	265	87.63	27.0286	111	302	97.22	>100
99	266	52.51	4.5650	111	303	58.80	>100
100	267	151.11	7.4366	111	304	35.56	>100
100	268	90.61	>100	111	305	21.51	25.0499
100	269	54.34	>100	112	305	104.42	>100
101	270	156.62	>100	112	306	63.20	>100
101	271	93.99	>100	112	307	38.25	>100
101	272	56.41	>100	112	308	23.15	37.9761

In Table 2.10 we use Form.3 [Eq. (2.22)] to predict the β^--decay half-lives of heavy and superheavy nuclei with proton number $Z = 91 - 112$. The calculated β^--decay half-lives are listed in the third and seventh columns of Table 2.10. The corresponding results calculated by Möller *et al.* [123] are listed in the fourth and last columns for comparison. It is seen from Table 2.10 that many predicted results from Form.3 are comparable with those calculated by Möller *et al.* [123] within a factor of a few.

2.4.2 Shell effects on β^--decay half-lives

Nuclear decay data provides the original and credible information of nuclear structure. It is an important topic to explore the relationship between nuclear decays and the effects of nuclear structure in nuclear physics. In this section, we focus on the shell effects on β^--decay half-lives and discuss the relation between nuclear β^--decay half-lives and the major shell or subshell closures.

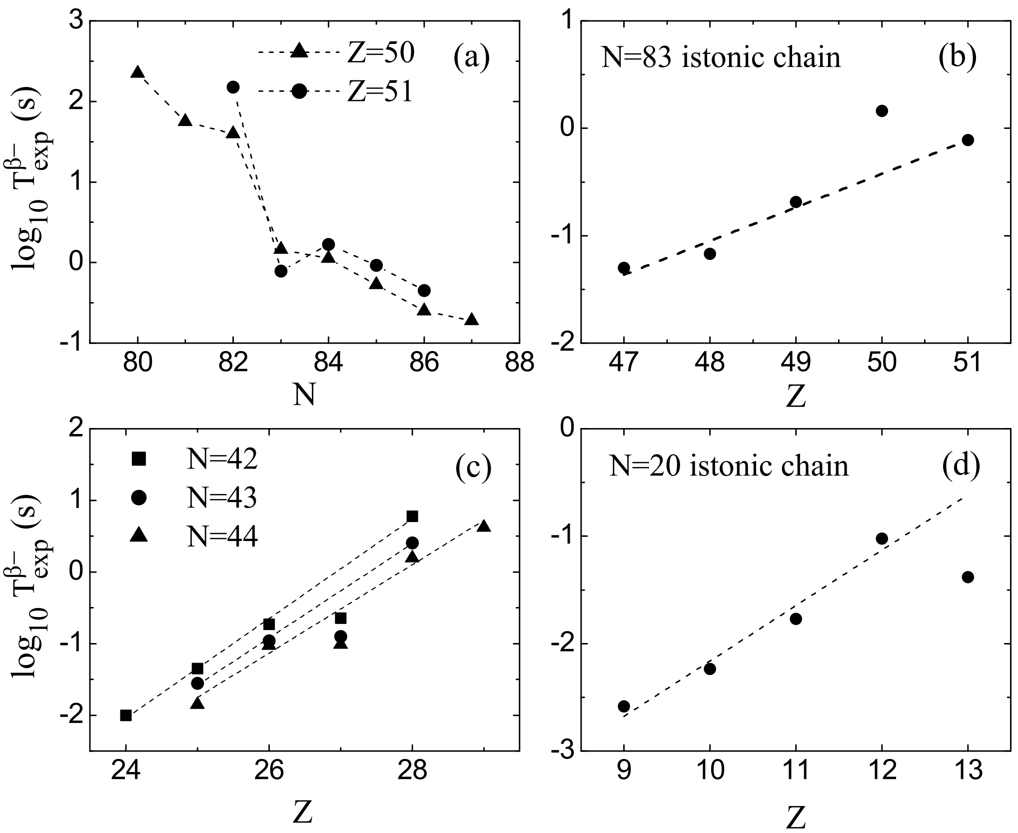

Figure 2.20: The experimental β^--decay half-lives (in $\log_{10}$-scale) along different isotopic or isotonic chains near $N = 82$, $Z = 50$, $Z = 28$, and $N = 20$ closed shells.

We plot the logarithms of experimental β^--decay half-lives along different isotopic chains near $N = 82$, $Z = 50$, $Z = 28$, and $N = 20$ closed shells in Fig. 2.20. All available nuclei far from the β-stable line are included. It is seen from Fig. 2.20(a) that there are large deviations from the linear relationship at the neutron numbers $N = 82$ and 83 for Sn ($Z = 50$) and Sb ($Z = 51$) isotopic chains. At the neutron number $N = 82$, the experimental β^--decay half-lives are much larger than the anticipant values from the linear relationship, whereas the experimental β^--decay half-lives are smaller than the anticipant values at $N = 83$. This deviation from the linear relationship suggests that there exist shell effects on the β^--decay half-lives at $N = 82$. The big split of the energy levels at $N = 82$ closed shell increases the β^--decay energy largely at $N = 83$. This makes the β^--decay half-lives of the nuclei with $N = 83$ systematically smaller than the anticipant value from the linear relationship. In Fig. 2.20(b), we can see an abnormal increase of β^--decay half-lives at $Z = 50$ on $N = 83$ isotonic chain. This clearly shows the enhanced stability of $Z = 50$ closed shell at $N = 83$. The β^--decay half-lives of the other nuclei ($Z = 47, 48, 49, 51$) on $N = 83$ isotonic chain approximately form a straight line and this is consistent with the prediction from Eq. (2.17) for an isotonic chain.

For nuclei near the $Z = 28$ closed shells, there also exist shell effects on β^--decay half-lives. It is interesting to see from Fig. 2.20(c) that experimental β^--decay half-lives are systematically lower than the predicted values from the exponential law at $Z = 27$ and $N = 42 - 44$. This may show that β^--decay prefers to fill the quasi-proton hole and to form proton closed shell. Therefore the β^--decay half-lives of nuclei with $Z_{\rm m} - 1$ are smaller than anticipant values from the exponential law, where $Z_{\rm m}$ is the proton "magic number".

We can also see from Fig. 2.20(d) the abnormal deviation from the exponential law at $Z = 13$ on $N = 20$ isotonic chain. It is similar to the case of $Z = 27$ on $N = 42 - 44$ isotonic chain. The parent nuclei ${}^{33}_{20}\mathrm{Al}_{13}$ has 20 neutrons and 13 protons, and the daughter nuclei has 19 neutrons and 14 protons. The abnormal decrease of the β^--decay half-life of ${}^{33}_{20}\mathrm{Al}_{13}$ can not be explained by the shell effects of $N = 20$ closed shell (the neutron number changes from 20 to 19 in β^--decay). This may show that $Z = 14$ is a subshell closure at $N = 20$. The β^--decay seems to prefer to form major shell or subshell closures, therefore the β^--decay half-life of ${}^{33}_{20}\mathrm{Al}_{13}$ is smaller than the anticipant value. The recent results obtained by measurements of the other properties of nuclei, such as the 2^+ excited energy level of ${}^{34}\mathrm{Si}$, also have suggested that $Z = 14$ is a subshell closure at $N = 20$ [128,129]. This shows the feasibility of obtaining information of the major shell or subshell closures of the nuclei far from the β-stable line according to the systematical study of β^--decay half-lives.

2.5 Parameterized formula for half-lives of allowed orbital electron-capture transitions of nuclei close to β-stable line

According to the orbital angular momentum of leptons in the β-decay process, scientists theoretically grouped the β-decay into "allowed", "first forbidden", "second forbidden", etc. [2, 130]. If the effect of nuclear matrix element is small enough, there will exist several separated peaks in the distribution of logarithms of comparative half-lives ($\log_{10} fT_{1/2}$) values. However, the practical situation is more complicate. There exists a continuous distribution of nuclear comparative half-lives and extra small $fT_{1/2}$ values (superallowed transitions) due to nuclear structure effects on the β-decay matrix elements [2, 130]. β-decay matrix element reflects the overlap of nuclear multiparticle wave functions and provides clear and direct information about nuclear structure because of the simple form of associated operator. In particular, study of nuclear matrix elements can yield information about multiparticle structure of nuclear wave function [131, 132].

Up till now, the calculation of nuclear matrix element came down to many kinds of sophisticated microscopic models [13, 123, 133–142] due to the complexity of nuclear many-body problem. These microscopic models reproduce experimental data of nuclei not too close to β-stable line very well. However, for nuclei close to β-stability, there exists relatively large deviation between theory and experimental data. And usually it is hard to obtain a "visual" knowledge of nuclear matrix element in a simple and transparent way. Besides these sophisticated numerical approaches, the early analytical study on nuclear matrix elements can be traced back to 1950s. Talmi *et al.* performed calculation in the framework of single particle shell model [131, 143]. According to the single particle shell model, there exist major shell (quantum number n) or angular momentum (quantum number l) forbiddenness on nuclear matrix elements [131, 143]. This strong forbidden rule on nuclear matrix element did not work well for heavy nuclei because there still exists allowed (even superallowed) transitions between heavy nuclei although the nucleons undergo the transformation lie in different nl orbit, for example, the orbital electron capture (EC) of ^{163}Ho is superallowed transition [144]. It is a challenge for theoretician to establish an analytical and accurate description of matrix elements for nuclei close to β-stale line and for heavy nuclei in a simple and transparent way [16,17,106,108]. Accurate calculation of EC-decay rates is especially helpful to experimental physicists for designing experiments to identify the synthesized superheavy nuclei approaching the superheavy stable island [27–29] according to their decay properties.

Our newly proposed exponential law (Sec. 2.1.2) and empirical formulae (Sec. 2.3) for β^+-decay half-lives of nuclei far from the β-stable line [106] reproduces β^+-decay half-lives of nuclei far from the β-stable line well. However, it does not work well for nuclei close to β-stable line. For proton-rich nuclei close to β-stable line, orbital electron capture (EC) dominates the β^+-decay process (including e^+-emission and EC process), so does for superheavy nuclei [28, 29]. In this section, we focus on half-lives of allowed EC transitions of nuclei close to β-stable line to seek possible hindrance of angular momentum on the capture rates according to systematical analysis of experimental data. Then we propose a simple and relatively accurate parameterized formula to calculate the half-lives of allowed EC transitions of nuclei close to β-stable line. The formula is also used to calculate and to predict allowed EC-decay half-lives of U and transuranic nuclei.

2.5.1 Parameterized formula for nuclear matrix element

Under natural units, the electron-capture transition probability per unit time from all atomic shells is [133]

$$\lambda = \frac{G_\beta^2}{2\pi^3}\sum_x n_x C_x F_x. \tag{2.23}$$

Here, the rest mass of electron (m_e) is set to be unity, G_β is the fundamental weak coupling constant, n_x is the relative occupation number for partially filled shells (n_x =1 for closed shells), C_x contains nuclear matrix elements, and the summation extends over all atomic subshells x from which electrons can be captured. The function F_x , which corresponds to the integrated Fermi function of orbital electron capture, is given by [133]

$$F_x = \frac{\pi}{2} q_x^2 \beta_x^2 B_x, \tag{2.24}$$

where q_x is the neutrino energy (neglecting the atomic recoil energy, in unit of $m_e c^2$), β_x is the Coulomb amplitude of the bound-state electron radial wave function, and B_x is the associated electron exchange and overlap correction.

For allowed transition, the captures from the subshells K, L_1, L_2, M_1, M_2, N_1, $N_2 \cdots$ predominate, and the transition probability becomes [133]

$$\lambda = \frac{G_\beta^2}{4\pi^2}|M|^2[n_K q_K^2 \beta_K^2 B_K + n_{L_1} q_{L_1}^2 \beta_{L_1}^2 B_{L_1} + n_{L_2} q_{L_2}^2 \beta_{L_2}^2 B_{L_2} + \cdots], \tag{2.25}$$

where M is nuclear matrix elements, and $G_\beta^2|M|^2$ can be written as

$$G_\beta^2|M|^2 = G_F^2|M_F|^2 + G_{GT}^2|M_{GT}|^2, \tag{2.26}$$

where M_F and M_{GT} are respectively nuclear matrix elements of Fermi transition and Gamow-Teller transition, and G_F and G_{GT} are Fermi and G-T coupling constants, respectively. M_F and M_{GT} can be expressed by nuclear wave function in initial state ψ_i and in final state ψ_f, that is [131, 143],

$$M_F = \int \psi_f^* \psi_i, \quad \text{and } M_{GT} = \int \psi_f^* \vec{\sigma} \psi_i, \tag{2.27}$$

where $\vec{\sigma}$ is spin operator.

The spin operator $\vec{\sigma}$ operates on the spin coordinates only [131, 143]. Therefore Gamow-Teller transition matrix element M_{GT} mainly describes the overlap between nuclear initial state (parent nuclei) and final state (daughter nuclei). This is similar to the Fermi transition matrix element M_F. In other words, the more similar between nuclear wave function of parent nuclei and that of daughter nuclei, the larger the absolute value of nuclear matrix element. In the approximation of single particle shell model, the Fermi interaction contributes to allowed EC transition only if a proton in the nlj-orbit is transformed into a neutron in the same orbit. For these case $M_F = 1$, otherwise $M_F = 0$. For Gamow-Teller transition, only if a proton in the nlj_i-orbit is transformed into a neutron in the nlj_f-orbit where $|j_i - j_f|$ =0 or 1, M_{GT} is not equal to zero, otherwise $M_{GT} = 0$.

According to the single particle shell model, there exists major shell (quantum number n) or angular momentum (quantum number l) forbiddenness on nuclear matrix elements. For heavy nuclei, the nucleons undergo the transformation lie in different nl orbits. However, there still exist allowed (even superallowed) transitions between heavy nuclei, for example, the electron capture of ^{163}Ho is superallowed transition. Therefore a "sharp" forbidden rule only reflects some aspects of nuclear matrix elements. Considering that the nucleus is a many-body system, the many-body effects may weaken the "sharp" forbiddenness of major shell or angular momentum on nuclear matrix elements and make the hindrance continuous.

Here we assume that the overlap of ψ_i and ψ_f are mainly determined by the states of particle which undergoes the transformation from a proton to a neutron. Above states of corresponding proton and neutron are determined by their boundary conditions and different Hamiltonian according to solving the Schrodinger equations. The main differences in the radial Hamiltonian of corresponding proton and neutron are the Coulomb potential energy V_c, the centrifugal potential energy V_l, and the spin-orbit coupling energy V_{ls} because the proton is charged while the neutron not, and the single particle angular momentum of corresponding proton or neutron may be different. On one hand, along with the increase of proton number Z, the Coulomb energy differences between the proton and neutron which undergo the transformation become larger. On the other hand, the bigger differences in the angular momentum of corresponding proton or neutron, the larger differences of their corresponding centrifugal potential energy V_l since V_l is proportional to $l(l+1)$. The differences of the radial Hamiltonian of corresponding proton and neutron which undergoes transformation may affect nuclear matrix element.

Besides the different radial Hamiltonian of the proton and neutron which undergo transformation, the angular momentum of corresponding particle seems more important because the angular momentum directly determines the angular distribution of wave function and then affects the overlap of wave function. Different orbital angular momentums of corresponding proton and neutron which undergo transformation probably yield different overlap of wave functions. According to above analysis, we propose possible correlations between nuclear matrix element and the angular momentums of corresponding states (j_p and j_d) which undergo transformation, and between nuclear matrix element and the proton number Z of parent nucleus. Hence we empirically write the logarithm of the absolute value of matrix element of allowed EC-transition in the function of Z, j_p and j_d, that is,

$$\log_{10}|M| = c_1 Z + c_2\sqrt{j_p(j_p+1)j_d(j_d+1)} + c_3 + h_F + h_S, \tag{2.28}$$

where c_1, c_2, and c_3 are three parameters to be determined according to available experimental data, and h_F and h_S are correction factors to be determined below. Considering the differences of nuclear matrix elements between Gamow-Teller transition and Fermi transition, we introduce a correction factor h_F for pure fermi transition ($0^+ \longrightarrow 0^+$). For mixed Gamow-Teller and Fermi transitions, the decay constants λ_M is proportional to $(G_F^2|M_F|^2 + G_{GT}^2|M_{GT}|^2)$. However, for pure Fermi transition, the decay const λ_F is proportional to $G_F^2|M_F|^2$. The ratio between decay const of pure Fermi transition and mixed Gamow-Teller and Fermi transitions is given by

$$\frac{\lambda_F}{\lambda_M} = \frac{G_F^2|M_F|^2}{G_F^2|M_F|^2 + G_{GT}^2|M_{GT}|^2}, \tag{2.29}$$

Then we derive the expression of h_F as

$$h_F = \frac{1}{2}\log_{10}\frac{\lambda_F}{\lambda_M} \tag{2.30}$$

for $0^+ \longrightarrow 0^+$ transition. The value h_F is approximately obtained according to neutron β-decay. In neutron β-decay, $|M_F|^2$=1, and $|M_{GT}|^2$=3. According to Eq. (2.30), we obtain h_F to be -0.3803 by using $|G_{GT}/G_F| = 1.2599$ [139]. In addition, it is known from the experiment that the comparative half-life of superallowed transition is averagely smaller than that of the allowed transition by 1−2 magnitude order. Therefore the logarithm of absolute value of the matrix element of superallowed transition is correspondingly larger than that of the allowed transition by 0.5−1. Here we choose h_S to be 0.600 to describe the correction on matrix element of superallowed transition.

2.5.2 Numerical results and discussions

For most of the nuclei close to β-stable line, the decay Q value is small, and the allowed EC transition from ground state to ground state is the main decay channel. This is because the available energy of transition from ground state to ground state is the largest, and the transition rate is very sensitive to the available energy in the case of small Q value. In addition, owing to the small decay Q value, there are few possible decay channels, most of which are forbidden transitions. Therefore we assume that the transitions to the excited states of daughter nuclei are negligible for allowed ground-state-to-ground-state EC transitions of nuclei close to β-stable line, and we only calculate the allowed ground-state-to-ground-state transition rates.

Table 2.11: Comparison between experimental allowed EC-decay half-lives and calculated ones from the formula [Eqs. (2.25) and (2.28)]. The brackets in columns 3 and 4 denote that the spin and/or parity are uncertain.

Nucleus	Q(MeV)	J_p^π	J_d^π	$T_\mathrm{exp}^\mathrm{EC}$	$T_\mathrm{cal}^\mathrm{EC}$	$T_\mathrm{cal}^\mathrm{EC}/T_\mathrm{exp}^\mathrm{EC}$
^{7}Be	0.862	1.5^-	1.5^-	53.22 ± 0.06 d	107.03 d	2.01
^{37}Ar	0.814	1.5^+	1.5^+	35.04 ± 0.04 d	20.14 d	0.57
^{49}V	0.602	3.5^-	3.5^-	330 ± 15 d	153.22 d	0.46
^{51}Cr	0.753	3.5^-	3.5^-	27.7025 ± 0.0024 d	86.11 d	3.11
^{55}Fe	0.231	1.5^-	2.5^-	2.737 ± 0.011 y	0.34 y	0.12
^{67}Ga	1.001	1.5^-	2.5^-	3.2612 ± 0.0006 d	3.78 d	1.16
^{70}Ga	0.655	1^+	0^+	$3.58^{+0.61}_{-0.46}$ d	3.20 d	0.89

(Continued on next page)

Table 2.11 – continued from previous page

Nucleus	Q(MeV)	$J_{\rm p}^{\pi}$	$J_{\rm d}^{\pi}$	$T_{\rm exp}^{\rm EC}$	$T_{\rm cal}^{\rm EC}$	$T_{\rm cal}^{\rm EC}/T_{\rm exp}^{\rm EC}$
^{68}Ge	0.106	0^+	1^+	270.95 ± 0.16 d	129.18 d	0.48
^{71}Ge	0.233	0.5^-	1.5^-	11.43 ± 0.03 d	32.87 d	2.88
^{81}Kr^m	0.471	0.5^-	1.5^-	$6.1^{+1.2}_{-0.8}$ d	5.38 d	0.88
^{82}Sr	0.180	0^+	1^+	25.36 ± 0.03 d	25.51 d	1.01
^{87}Sr^m	0.106	0.5^-	1.5^-	39^{+14}_{-8} d	111.82 d	2.87
^{100}Tc	0.168	1^+	0^+	10^{+10}_{-3} d	21.03 d	2.10
^{110}Ag	0.888	1^+	0^+	$2.28^{+0.59}_{-0.40}$ h	11.23 h	4.93
^{116}In	0.469	1^+	0^+	$17.0^{+6.1}_{-3.6}$ h [145]	36.88 h	2.17
^{118}Te	0.278	0^+	1^+	6.00 ± 0.02 d	3.93 d	0.65
^{119}Xe	4.972	$2.5^{(+)}$	2.5^+	28^{+11}_{-6} m	60.91 m	2.18
^{122}Xe	0.725	0^+	1^+	20.1 ± 0.1 h	10.72 h	0.53
^{131}Cs	0.355	2.5^+	1.5^+	9.689 ± 0.016 d	5.33 d	0.55
^{128}Ba	0.529	0^+	1^+	2.43 ± 0.05 d	0.76 d	0.31
^{134}Ce	0.383	0^+	1^+	3.16 ± 0.04 d	1.36 d	0.43
^{140}Nd	0.443	0^+	1^+	3.37 ± 0.02 d	0.88 d	0.26
^{163}Ho	0.00257	3.5^-	2.5^-	4.570 ± 0.025 ky	2.78 ky	0.61
^{164}Ho	0.986	1^+	0^+	48^{+6}_{-5} m	151.86 m	3.16
^{165}Er	0.377	2.5^-	3.5^-	10.36 ± 0.04 h	9.96 h	0.96
^{164}Tm	4.062	1^+	0^+	3.3 ± 0.2 m	7.34 m	2.23
^{164}Yb	0.865	0^+	1^+	75.8 ± 1.7 m	167.74 m	2.21
^{170}Hf	1.056	0^+	0^+	16.01 ± 0.13 h	9.39 h	0.59
^{179}Ta	0.106	3.5^+	4.5^+	1.82 ± 0.03 y	2.05 y	1.12
^{180}Ta	0.852	1^+	0^+	$9.48^{+0.35}_{-0.33}$ h	2.42 h	0.26
^{178}W	0.091	0^+	1^+	21.6 ± 0.3 d	37.66 d	1.74
^{181}W	0.188	4.5^+	3.5^+	121.2 ± 0.2 d	117.81 d	0.97
^{229}Pa	0.312	(2.5^+)	2.5^+	1.50 ± 0.05 d	1.97 d	1.31
^{234}Pu	0.394	0^+	(0^+)	9.4 ± 0.1 h	26.34 h	2.80
^{244}Am^m	0.164	1^+	0^+	$50.0^{+3.9}_{-3.6}$ d	22.14 d	0.44

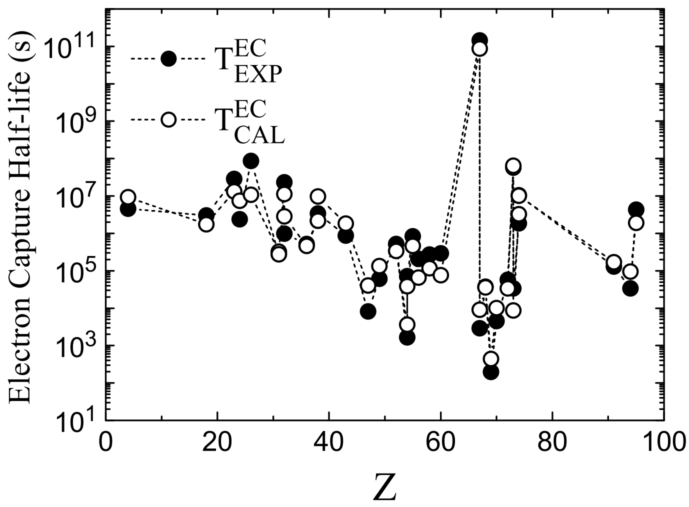

Figure 2.21: Experimental half-lives of allowed EC transitions (filled circle, in $\log_{10}$-scale) and calculated ones (open circle) from the new formula of nuclear matrix element [Eq. (2.28)] are plotted versus the proton number of parent nucleus close to β-stable valley.

We substitute the parameterized formula of matrix element [Eq. (2.28)] into Eq. (2.25) to calculate the half-lives of allowed EC transitions. Squared amplitudes of bound-state electron radial wave function β_x^2, the associated electron exchange and overlap correction B_x and the binding energy for the x*th* atomic subshell are taken from Ref. [133] and Ref. [146]. The weak coupling constant G_β is 1.415×10^{-62} J·m^3 from Ref. [139]. Through a least square fit of available experimental half-lives of allowed EC transitions ($\triangle\pi = +1, \triangle J = 0, \pm 1$) in the Nubase Table by Audi *et al.* [112], we obtain a set of parameters of Eq. (2.28): $c_1 = -4.22 \times 10^{-3}$; $c_2 = -3.88 \times 10^{-2}$; $c_3 = -0.3143$. The average deviation of the least-square fit is 0.31 for 35 nuclei. This means that the average ratio between theoretical half-life and experimental one is 2.0. In Table 2.11 we list the half-lives of parent nuclei with allowed EC transitions ($\triangle\pi = +1, \triangle J = 0, \pm 1$). The experimental data ($T_{\rm exp}^{\rm EC}$) are taken from the 2003 Nubase Table [112]. Also shown in Table 2.11 are the Q values of orbital electron capture and the angular momentums and parities of parent and daughter nuclei. We present in the last two columns of Table 2.11 the calculated values of half-lives ($T_{\rm cal}^{\rm EC}$) of allowed EC transitions from Eq. (2.28) and Eq. (2.25) and the ratios between calculated half-lives and experimental ones.

It is seen from the last three columns of Table 2.11 that this simple formula reproduces experimental values of half-lives of allowed EC transitions well. The agreement between calculated value and experimental data is within a factor of 2−4 for most of the nuclei. The largest deviation from experimental data occurs at ^{55}Fe, with a factor of about 8. Considering that accurate β-decay half-life calculation is more difficult for nuclei close to β-stable line than nuclei far from stability, and the ratios between calculated ones and experimental ones of some nuclei close to β-stability reach $10^2 - 10^3$ in the microscopic model calculation [123, 134], our simple formula works well for nuclei close to β-stable line. It is also seen from Fig. 2.21 that the calculated values follow the trends of variations of experimental half-lives of allowed EC transitions, even for nuclei with very long half-lives ($\sim 10^{11}$ s).

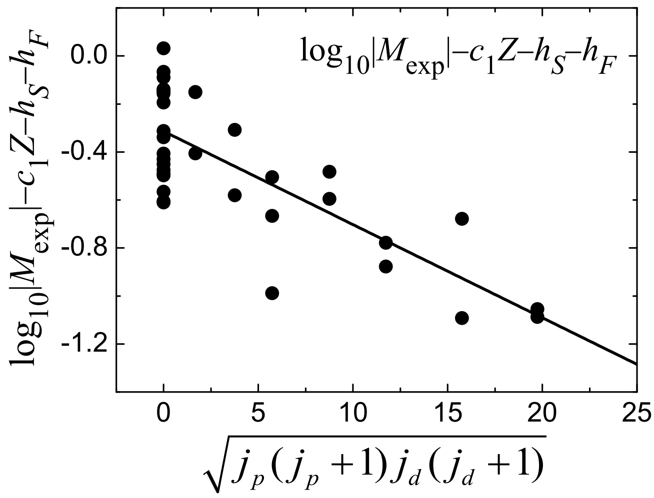

Figure 2.22: Variation of experimental nuclear matrix element of allowed EC transition ($\log_{10}|M_{\text{exp}}| - c_1Z - h_F - h_S$) with angular momentum of parent and daughter nuclei ($\sqrt{j_p(j_p+1)j_d(j_d+1)}\ \hbar^2$).

The good agreement between calculated half-lives and experimental ones shows that the formula of allowed EC-decay half-lives has a firm basis in physics. By taking into account the hindrance of angular momentum on nuclear matrix elements, important physics is included in the formula. The parameterized formula is not only simple, but also practical to experimentalists for estimating EC-decay half-lives of nuclei conveniently. A typical example is the Viola-Seaborg formula [120, 121] and Geiger-Nuttall law, which are widely used in the calculation of α-decay half-lives [120, 121, 125]. It is plotted in Fig. 2.22 the variation of experimental nuclear matrix element of allowed EC transition ($\log_{10}|M_{\text{exp}}| - c_1Z - h_F - h_S$) with angular momentum of parent and daughter nuclei ($\sqrt{j_p(j_p+1)j_d(j_d+1)}\ \hbar^2$). We can see clearly from Fig. 2.22 that experimental dots scatter around a descendent straight line, which shows the hindrance of angular momentum on nuclear matrix elements of allowed EC transition.

The hindrance of angular momentum on nuclear matrix elements seems similar to unfavored α-decay. The starting point of microscopic theory of α-decay is the basic quantum mechanical expression of perturbation rate [2]

$$\lambda = \frac{2\pi}{\hbar}|H_{\rm if}|^2 \frac{{\rm d}n}{{\rm d}E}, \tag{2.31}$$

where $H_{\rm if}$ is the transition perturbation matrix element and ${\rm d}n/{\rm d}E$ is the density of final states. The favored α-decay is S-state decay with a zero orbital angular momentum of the relative movement between α particle and daughter nuclei. However, in unfavored α-decay, there exists non-zero orbital angular momentum. The wave function of non-zero orbital angular momentum is different from S-state wave function and may cause hindrance on the matrix element of α-decay. It is shown that there exists similar behavior for the half-lives of orbital electron capture and α-decay although they are governed by different interactions, that is, the angular hindrance on transition matrix elements due to the overlap of wave function of initial state and final state.

2.5.3 Orbital electron capture of uranium and transuranic nuclei

α-decay, β^+-decay, and spontaneous fission are main decay modes of proton-rich heavy and superheavy nuclei. Up till now, α-decay and spontaneous fission are observed in most of synthesized superheavy nuclei. For the nuclei approaching β-stable line, the competition of orbital electron capture (EC) with α-decay and spontaneous fission becomes larger than that of the nuclei far from β-stability [28, 29]. Therefore it is necessary to study the orbital electron-capture rates of heavy and superheavy nuclei. This is especially helpful to experimental physicists for designing experiments to identify the synthesized superheavy nuclei approaching the superheavy stable island [27–29] according to their decay properties. We use the new formula [Eq. (2.28)] to calculate the half-lives of allowed EC transitions of U and transuranic nuclei. For U and transuranic nuclei, orbital electron capture dominates the β^+-decay process (including e^+-emission and EC process) in the region of low decay energy because the ratio $(\lambda_K/\lambda_{e^+})$ between orbital electron K-capture rate and positron emission is approximately proportion to Z^3. If $Q < 6$ MeV and $Z > 90$, the ratio λ_K/λ_{e^+} is larger than 10. The decay Q values are smaller than 6 MeV for most of known β^+-decay of U and transuranic nuclei. Therefore we approximately replace the experimental half-life of electron capture by that of β^+-decay in the Nubase Table [112] when we compare calculated results with experimental ones. Squared amplitudes of bound-state electron radial wave functions

Table 2.12: Calculated half-lives of allowed EC transitions of U and transuranic nuclei from the formula and the experimental β^+-decay half-lives. The β^+-decay half-lives calculated by Möller *et al.* [123] are also listed for comparison. Nuclei marked with a bracket or an asterisk respectively denote that the corresponding value is uncertain or estimated in Nubase Table [112]. The electron capture of odd-odd nucleus is assumed to be allowed transition if its angular momentum and parity is unknown. The angular momentum and parity of ^{263}Db is assumed to be 2.5$^+$.

Nucleus	Q(MeV)	J_p^π	J_d^π	$T_\mathrm{exp}^{\beta^+}$	$T_\mathrm{cal}^\mathrm{EC}$	$T_\mathrm{Möller}^{\beta^+}$(s)
^{229}U	1.313	(1.5$^+$)	(2.5$^+$)	72.5 ± 3.8 m	52.4 m	>100
^{228}Np	4.475*	–	0$^+$	102^{+16}_{-13} s	82 s	44.4974
^{231}Np	1.823	(2.5)$^{(+*)}$	(2.5)$^{(+*)}$	49.8 ± 0.7 m	42.0 m	>100
^{233}Np	1.030	(2.5$^+$)	2.5$^+$	36.2 ± 0.1 m	143.2 m	>100
^{234}Np	1.809	(0$^+$)	0$^+$	4.4 ± 0.1 d	0.036 d	>100
^{231}Pu	2.655	1.5$^+*$	(2.5)$^{(+*)}$	$9.9^{+1.2}_{-1.1}$ m	10.5 m	>100
^{233}Pu	2.100	2.5$^+*$	(2.5$^+$)	20.9 ± 0.4 m	29.3 m	>100
^{235}Pu	1.139	(2.5$^+$)	2.5$^+$	25.3 ± 0.5 m	108.0 m	>100
^{234}Am	4.180*	–	0$^+$	2.32 ± 0.08 m	1.39 m	>100
^{237}Am	1.477*	2.5$^{(-)}$	3.5$^-$	73.0 ± 1.0 m	99.1 m	>100
^{238}Am	2.255	1$^+$	0$^+$	98 ± 2 m	5 m	>100
^{239}Am	0.411	(2.5)$^-$	3.5$^-$	11.9 ± 0.1 h	31.8 h	>100
^{239}Cm	1.798*	(3.5$^-$)	(2.5)$^-$	$2.9 \pm X$ h	1.0 h	>100
^{238}Bk	4.890*	–	0$^+$	2.40 ± 0.08 m	0.88 m	16.8646
^{247}Es	2.473*	3.5$^+*$	3.5$^+*$	4.9 ± 0.3 m	53.0 m	>100
^{248}Es	3.060*	0$^+*$	0$^+$	27 ± 5 m	12 m	>100
^{249}Es	1.309*	3.5$^+$	2.5$^+$	102.2 ± 0.6 m	100.3 m	>100
^{248}Fm	1.606*	0$^+$	0$^+*$	$8.6^{+X}_{-4.7}$ m	42.7 m	>100
^{248}Md	5.244*	–	0$^+$	9^{+6}_{-4} s	35 s	32.4924
^{250}Md	4.566*	–	0$^+$	56^{+9}_{-8} s	47 s	22.0647
^{254}Lr	5.126*	–	0$^+$	54^{+69}_{-26} s	32 s	17.9787
^{256}Lr	4.046*	–	0$^+$	$3.0^{+7.0}_{-1.4}$ m	0.9 m	38.6044
^{260}Lr	2.670*	–	0$^+$	12^{+11}_{-5} m [146]	2 m	>100
^{256}Db	6.484*	–	0$^+$	$5.3^{+4.3}_{-2.2}$ s	17.4 s	22.8816
^{258}Db	5.350*	–	0$^+$	$12.5^{+5.1}_{-3.4}$ s	25.8 s	59.1114
^{263}Db	2.270*	2.5$^+$	1.5$^+*$	$7.0^{+4.9}_{-3.1}$ m	7.1 m	>100

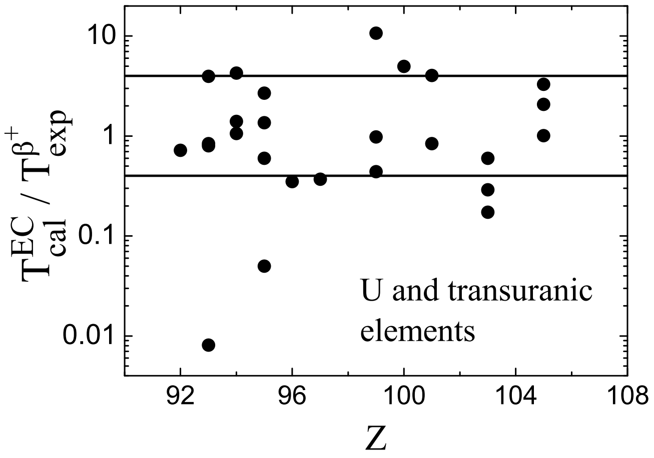

Figure 2.23: Ratios between calculated EC-decay half-lives and experiment half-lives of allowed β^+-transitions for U and transuranic nuclei ($Z \geq 92$).

β_x^2 and associated electron exchange and overlap correction B_x for $Z > 102$, and the atomic-electron binding energy for $Z > 104$ are extrapolated from polynomial fit of present atomic data [133, 146].

We present in Table 2.12 the calculated allowed EC-decay half-lives and experimental half-lives of allowed β^+-transitions. The decay Q-values and angular momentums of parent nuclei and daughter nuclei are also listed for reference. For a few odd-odd nuclei, the electron capture of parent nucleus is assumed to be allowed transition if its angular momentum and parity is unknown. In addition, the β^+-decay half-lives calculated by Möller *et al.* [123] are also listed for comparison. It is seen from columns 5 and 6 that the half-lives from the formula [Eqs. (2.25) and (2.28)] agree with experimental ones well for most of the nuclei. For the electron capture of ^{234}Np, large deviation exists between theory and experimental data. There may be two reasons for this large deviation. One is the uncertainty of the angular momentum and parity of ^{234}Np. The other one is that the orbital electron capture of ^{234}Np is pure Fermi transition ($0^+ \longrightarrow 0^+$) if the angular momentum and parity of parent nucleus is 0^+. It will be interesting to investigate the reason of this phenomenon both experimentally and theoretically. When we compare our results with those calculated by Möller *et al.* [123], we find that the two results are comparable. The formalism which is used by Möller *et al.* to calculate Gamow-Teller β-strength functions involves adding pairing and Gamow-Teller residual interactions to the folded-Yukawa-single-particle Hamiltonian and solving the resulting Schrödinger equation in the quasi-particle random-phase approximation (QRPA) [123].

Table 2.13: Predicted allowed EC-decay half-lives of transuranic nuclei ($Z = 93-110$) from the formula [Eqs. (2.25) and (2.28)]. The nucleus marked with an asterisk denotes that the electron capture is assumed to be allowed transition.

Nucleus	Q(MeV)	$T^{\rm EC}_{\rm cal}$(s)	$T^{\beta^+}_{\rm Möller}$(s)	Nucleus	Q(MeV)	$T^{\rm EC}_{\rm cal}$(s)	$T^{\beta^+}_{\rm Möller}$(s)
^{229}Np	2.569	716.1	50.4503	^{258}Lr*	3.360	77.2	>100
^{230}Np*	3.625	126.4	51.1309	^{259}Lr	1.740	25678.8	>100
^{230}Pu*	1.694	578.6	>100	^{262}Lr*	2.170	192.6	>100
^{232}Am*	5.034	56.9	53.0344	^{259}Rf	2.550	4366.5	>100
^{236}Am*	3.277	137.1	>100	^{260}Db*	4.530	36.3	>100
^{234}Cm*	2.194	1664.3	43.0442	^{262}Db*	3.880	50.0	68.9873
^{236}Cm*	1.710	501.9	>100	^{266}Sg*	0.960	944.2	>100
^{238}Cm	0.980	1680.7	>100	^{264}Bh*	5.290	23.0	10.9886
^{236}Bk*	5.510	41.6	51.7802	^{266}Bh*	4.550	31.4	>100
^{237}Bk	3.820	717.3	82.1114	^{268}Bh*	3.870	43.8	>100
^{240}Bk*	3.945	82.4	>100	^{270}Bh*	3.060	71.4	>100
^{239}Cf	3.860	657.8	5.6134	^{272}Bh*	2.680	94.2	>100
^{240}Cf*	2.360	224.0	53.5514	^{270}Hs*	0.970	810.4	>100
^{240}Es*	6.170	29.0	8.0654	^{272}Hs*	0.950	850.3	>100
^{242}Es*	5.630	35.0	16.5718	^{270}Mt*	5.590	17.9	19.1827
^{244}Es*	4.551	54.0	>100	^{272}Mt*	4.360	29.8	>100
^{247}Fm	2.970	990.6	57.7479	^{274}Mt*	4.060	34.5	>100
^{246}Md*	6.140	25.6	13.0075	^{276}Mt*	3.760	40.5	>100
^{252}Md*	3.813	67.9	>100	^{278}Mt*	2.100	137.6	>100
^{252}Lr*	5.959	23.8	2.1073	^{276}Ds*	1.750	190.2	>100
^{257}Lr	2.499	4871.5	84.1337	^{278}Ds*	1.540	251.4	>100

Here our calculation by the parameterized formula is very simple and convenient. We can also see from Fig. 2.23 that the ratios between calculated half-lives of electron capture and experiment half-lives of allowed β^+-transitions for U and transuranic nuclei are within a few times ($T_{\rm cal}^{\rm EC}/T_{\rm exp}^{\beta+} = 0.4-3$) for most of the nuclei. This demonstrates that the formula is valid for describing the half-lives of allowed EC transitions of U and transuranic nuclei. Therefore it is reliable to use the formula to predict the half-lives of allowed EC transitions of these nuclei.

In recent years, the study of decay properties of nuclei neighboring doubly magic nucleus ^{270}Hs is a hot point [147]. We predict the half-lives of orbital electron capture close to this region. The predicted EC-decay half-lives for nuclei with $Z = 93-110$ are listed in the third and seventh columns of Table 2.13. The nucleus marked with an asterisk denotes that the order of β^+-decay is assumed to be allowed. The Q-values are calculated from the evaluation of Nubase Table [112]. The corresponding β^+-decay half-lives calculated by Möller et al. [123] are also listed in the fourth and last columns for comparison. It is seen from Table 2.13 that the calculated allowed EC-decay half-lives for many nuclei neighboring ^{270}Hs are between 10 s and 10^3 s. For certain nuclei, the calculated allowed EC-decay branching ratios can reach about 10−40%, for example, ^{262}Db and ^{266}Bh. It is interesting for physicists to investigate the EC-decay in the superheavy region both experimentally and theoretically.

2.6 Summary of this chapter

In summary, we systematically investigate the experimental data of $\beta^\pm$-decay half-lives for both light nuclei and heavy nuclei far from β-stable line. A new exponential law is found between the half-life of $\beta^\pm$-decay and the nucleon number (Z, N) for proton-rich or neutron-rich nuclei. This new law implies the exponential dependence of nuclear $\beta^\pm$-decay half-lives on the maximum kinetic energy of the electron or positron emitted in the $\beta^\pm$-decay process. It reflects the statistical properties of multi-energy-level decay behavior for nucleus far from β-stable line, that is, from the ground state of parent nucleus to many excited energy levels of daughter nucleus. This is superior to the Sargent law, a fifth power law between $\beta^\pm$-decay half-lives and decay energies, which can be approximately derived from single-level Fermi theory of β-decay.

Based on the new exponential law and including reasonable nuclear structure effects, new formulae are proposed to describe the $\beta^\pm$-decay half-lives of nuclei far from β-stable line. Experimental half-lives are well reproduced by the simple formulae. The agreement with experimental data is comparable or even slightly better than the best microscopic model calculations for 735 nuclei ranging from $A = 9 - 238$ and with half-lives spanning 6 orders of magnitude (10^{-3}–10^{3} s). This shows that the formula have a firm basis in physics. It can be used to predict the $\beta^{\pm}$-decay half-lives of the nuclei far from the β-stable line.

Interesting nuclear structure effects on β-decay half-lives manifest beyond the "mean" behavior part of the simple formula (after systematical analysis, the part of nuclear structure effects is also included in our formula). For example, it is noticed that the even-odd effects on the β^{+}-decay half-lives of the first and second forbidden β^{+} decays are much less apparent than those of the allowed β^{+}-transition. This is a new phenomenon and it demonstrates that the allowed β^{+}-transitions are more sensitive to nuclear even-odd effect than the forbidden β^{+}-transitions. It is also found that the shell or subshell effect will strongly affect β^{-}-decay half-lives even for nuclei far from β-stable line. The additional correlation between the major shell or subshell closures and β^{-}-decay half-lives is obtained according to systematic investigation of nuclear β^{-}-decay half-lives. This correlation provides the feasibility of obtaining information of the major shell or subshell closures of the nuclei far from the β-stable line according to the exponential law.

Besides the above study for nuclei far from stability, the half-life of allowed orbital electron-capture (EC) transition of the nucleus close to β-stable line is also systematically studied. We have found the hindrance of angular momentum of parent and daughter nuclei on half-life of allowed orbital electron-capture (EC) transition. The hindrance of angular momentum is related to the overlap between multi-particle wave functions of parent and daughter nuclei. A new parameterized formula including the effect of angular momentum hindrance is proposed to calculate the half-life of allowed EC transition of the nucleus close to β-stable line. Experimental half-lives of allowed EC transitions of nuclei close to β-stable line are well reproduced by this formula. In addition, the formula is also proved to be valid for calculating allowed EC-decay half-lives of U and transuranic nuclei. It is useful to experimental physicists for designing experiments to identify the synthesized long-lived superheavy nuclei approaching the superheavy stable island according to their decay properties and analyzing experimental data.

Chapter III α decays and spontaneous fissions of heavy and superheavy nuclei

3.1 α decay half-lives of ground and isomeric states calculated in a unified theoretical framework

The quantum theory of α-decay was established in 1928 by Gamow according to tunnelling through a potential barrier [148]. From then on, various models [149–158] are developed to study the favored α decays occurring between the ground states of nuclei. For a long time the theoretical research on α decay concentrated on the transitions from ground-states to ground-states and the model of the decay was built based on the data of nuclei in ground states. It is known that there are isomers in nuclei and some isomers have α-decays. The first isomer ^{234}Pa^m was found as early as 1921 in the ^{234}Th β^- decay [111]. Along with the recent development of experimental technology, many new isomers have been discovered and have formed the island of isomerism near the proton or neutron shells. α transitions from isomeric states to ground states or to isomeric states are found from many nuclei. Very recently, it is reported from the α-decay data of ^{270}Ds and ^{271}Ds that there are isomeric states in ^{270}Ds and ^{271}Ds [27,159]. α decay from the isomeric state of ^{270}Ds was observed with a half-life of $6.0^{+8.2}_{-2.2}ms$ that is significantly longer than the half-life $100^{+140}_{-40}\mu s$ of the corresponding ground state [159, 160]. Configuration-constrained calculations of potential-energy surfaces in even-even superheavy nuclei demonstrated that there existed enhanced stability of superheay nuclei due to high-spin isomerism [160].

Although many α-decays from isomers are observed experimentally, theoretical studies on them are rare. Up to now, there are few systematic theoretical calculations on the α-decay half-lives of isomers as far as we know. This may be due to the fact that the isomers found long time ago are not α-emitters. It is not clear whether α-decay models of the ground states are valid for α-decays of isomers. Therefore a systematical research on the α-decay half-lives of isomeric-states is necessary. It can help us to check the validity of the ground-state α-decay model for the decays of isomeric-states, to calculate the α-decay half-lives of isomeric states and to predict some long-lived superheavy elements.

The effective liquid drop model was established in 1993 by Gonçalves and Duarte for describing the α decay and cluster radioactivity in a unified framework [161, 162]. Systematic calculation on α transitions from ground states to ground states using different combinations of mass transfer descriptions and inertia coefficients showed its validity in reproducing the experimental data [163]. As a fission-like model, it has been extended to deal with proton emission and cold fission process. Here we generalize it to calculate the α-decay half-lives of isomeric states.

The aim of this part is to extend the effective liquid drop model to calculate the α transitions from isomeric-states to ground-states and from isomeric-states to isomeric-states [125, 164]. Comparisons between the experimental data and calculated half-lives have been performed for the α decays occurring between the ground states of even-even heavy and superheavy nuclei (Z≥100), for the favored α decays of isomeric-states near Z=82 shell and for the α decays of isomers in heavy nuclei (Z≥99). In this part, we introduce the effective liquid drop model in section 3.1.1. The calculations of α-decay half-lives and comparisons with experimental data are presented in sections 3.1.2, 3.1.3, and 3.1.4. A summary of this part is given in section 3.1.5.

3.1.1 The effective liquid drop model

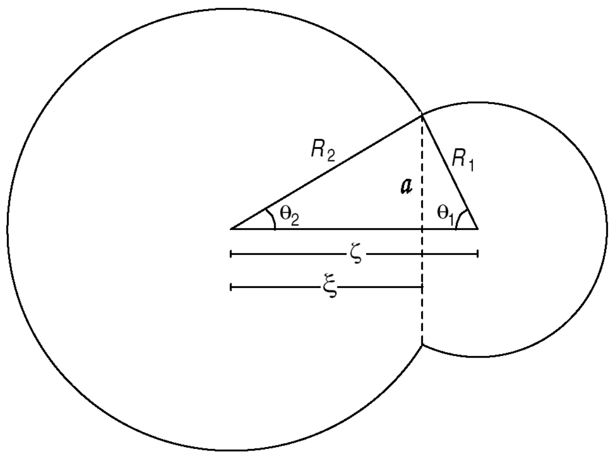

Figure 3.1: Schematic representation of the dinuclear decaying system. The daughter nucleus and the emitted (smaller) fragment have radius R_2 and R_1, respectively, and the distance between the geometrical centers of the fragments is denoted by ζ. The variable ξ represents the distance between the center of the heavier fragment and the circular sharp neck of radius a.

In the effective liquid drop model, α decay process is assumed as a super asymmetric fission. The dinuclear shape (see Fig. 3.1) is described as two intersecting spheres.

Four independent collective coordinates imported to determine the configuration of the nascent fragments are as follows: the radii of each spherical fragment, R_1 and R_2, respectively for the α particle and daughter nucleus; the distance between their geometric centers, ζ; and the height of the larger spherical segment, ξ. Three constraints are introduced to reduce the spherical four-dimensional problem to the equivalent one-dimensional one [162]. The incompressibility of nuclear matter demands that the total volume of the dinuclear system is constant, i.e.

$$2(R_1^3 + R_2^3) + 3[R_1^2(\zeta - \xi) + R_2^2\xi] - [(\zeta - \xi)^3 + \xi^3] = 4R_{\rm p}^3, \tag{3.1}$$

where $R_{\rm p}$ is the radius of the parent nucleus.

To keep the two spherical segments in contact, it is necessary to establish a geometric constraint,

$$R_1^2 - (\zeta - \xi)^2 = R_2^2 - \xi^2. \tag{3.2}$$

In the constant mass asymmetry shape description (CMAS), the volume of each fragment is set to be constant, and in terms of the lighter fragment the volume conservation gives

$$2R_1^3 + 3R_1^2(\zeta - \xi) - (\zeta - \xi)^3 - 4\bar{R}_1^3 = 0, \tag{3.3}$$

where $\bar{R}_1$ is the final radius of the α fragment.

There are three important contributions to the potential energy of the dinuclear shape: the Coulomb energy, effective surface energy and the centrifugal potential energy [162]. The effective, one-dimensional total potential energy is given by

$$V = V_{\rm c} + V_{\rm s} + V_l. \tag{3.4}$$

Coulomb contribution $V_{\rm c}$ is determined by using an analytical solution of Poisson's equation for a uniform charge distribution system [165]. Gonçalves *et al.* [161] defined a effective surface tension $\sigma_{\rm eff}$ to calculate the effective surface potential of a nuclear liquid. $\sigma_{\rm eff}$ is defined as a function of the the proton numbers of the parent ($Z_{\rm p}$), emitted (Z_1), and daughter (Z_2) nucleus, reads

$$\sigma_{\rm eff} = \frac{1}{4\pi(R_{\rm p}^2 - \bar{R}_1^2 - \bar{R}_2^2)}[Q - \frac{3}{20\pi\varepsilon_0}e^2(\frac{Z_{\rm p}^2}{R_{\rm p}} - \frac{Z_1^2}{\bar{R}_1} - \frac{Z_2^2}{\bar{R}_2})], \tag{3.5}$$

where $\bar{R}_2$ is the final radius of the daughter fragment. The Q value which denotes the energy released in the α decay process is taken from the 2003 atomic mass evaluation by Audi *et al.* [112, 116]. Therefore, the effective surface energy can be calculated as

$$V_{\rm s} = \sigma_{\rm eff}(S_1 + S_2), \tag{3.6}$$

where S_1 and S_2 are the surface areas of each spherical segment.

The centrifugal potential energy after the scission point reads

$$V_l = \frac{\hbar^2}{2\bar{\mu}}\frac{l(l+1)}{\zeta^2}, \tag{3.7}$$

Where l is the angular momentum of α particle, $\bar{\mu} = M_1M_2/(M_1 + M_2)$ is the reduced mass of two separated nuclei and $M_{\rm i}$ ($\rm i = 1, 2$) represents their atomic masses.

The effective mass before scission point is described by effective inertia coefficient [162] and given by the following equation

$$\mu_{\rm eff} = \bar{\mu}\alpha^2, \tag{3.8}$$

with

$$\begin{aligned}\alpha = 1 + \frac{\pi}{v_1}[R_1^2 - (\zeta - \xi)^2][R_1\frac{{\rm d}R_1}{{\rm d}\zeta} - (\zeta - \xi)(1 - \frac{{\rm d}\xi}{{\rm d}\zeta})] \\ + \frac{\pi}{v_2}(R_2^2 - \xi^2)(R_2\frac{{\rm d}R_2}{{\rm d}\zeta} - \xi\frac{{\rm d}\xi}{{\rm d}\zeta}).\end{aligned} \tag{3.9}$$

The penetrability factor is calculated by

$$\Gamma = \exp[-\frac{2}{\hbar}\int_{\zeta_0}^{\zeta_c}\sqrt{2\mu[V(\zeta) - Q]}\,{\rm d}\zeta], \tag{3.10}$$

where ζ_0 and ζ_c are the inner and outer classical turning points. Finally, the half-life is calculated as

$$\tau = \frac{\ln 2}{\lambda_0\Gamma}, \tag{3.11}$$

where λ_0 (with the dimension $\rm s^{-1}$) is a parameter associated with the time scale of α particle preformation and the surface oscillation characteristic time of the parent nucleus [162]. λ_0 together with the radius parameter, r_0, is determined in order to obtain the best agreement with experimental data [162].

3.1.2 α decays between the ground states of nuclei

Tavares and co-workers have calculated the favored α transitions from ground-states to ground-states in a wide region of nuclei and have reproduced the experimental data well [163]. Here we test this model for heavy nuclei (Z$\geq$ 82) before the calculation of α-decays of isomers. In the calculation, we choose the same model parameters ($r_0 = 1.13$,

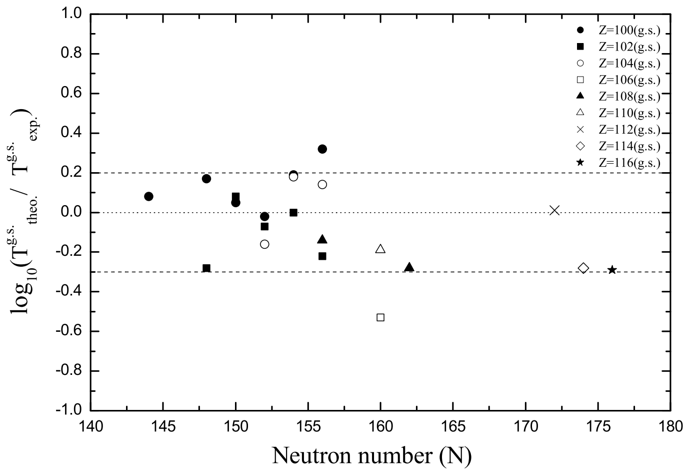

Figure 3.2: The ratio $T^{\text{g.s.}}_{\text{theo.}}/T^{\text{g.s.}}_{\text{exp.}}$ (in $\log_{10}$-scale) between theoretical α-decay half-life and experimental one is plotted versus neutron number of the parent nucleus. Deviation by a factor of 0.5 and 1.5 is represented by two broken lines respectively. The figure shows the results of α decays occurring between the ground-states of even-even heavy nuclei.

$\lambda_0 = 1.8 \times 10^{22}$ s^{-1}) for the combination of constant mass asymmetry description and effective inertia coefficient, as Tavares *et al.* did in reference [163]. The calculated α-decay half-lives agree with experimental data well. As an example, we list the calculated half-lives of the even-even heavy and superheavy nuclei in table 3.1. In table 3.1, the first and second columns mark the proton number and mass number of the parent nucleus, respectively. The α decay energy, experimental half-lives and theoretical ones are given in columns 3, 4 and 5. The ratio between theoretical half-life and experimental one is listed in the last column.

The parent nuclei given in table 3.1 belong to recently observed α decays. It is seen from table 3.1 that theoretical half-lives are close to experimental ones, within a factor of 2−3. It is seen clearly from Fig. 3.2 that the ratio ($T_{\text{cal}}/T_{\text{exp}}$) lies between two broken lines 0.5 and 1.5. There is a little bigger deviation for the two nuclei ^{256}Fm and ^{266}Sg, with the factors of 2 and 3 respectively. It is interesting to see (in Fig. 3.3) that α-decay half-lives of the nuclei with the neutron number N=152 are longer than those of the neighboring ones, while α-decay half-lives of the nuclei with the neutron number N=154 are shorter than those of the neighboring ones. This phenomenon demonstrates that there are subshell effects for the neutron number N=152. From Fig. 3.3 we can also see the good agreement between calculated values and experimental data.

Table 3.1: Comparisons between calculated and experimental half-lives of α decays occurring between the ground states of even-even heavy nuclei (Z≥100).

Z	A	$Q_\alpha^{\text{g.s.}}$(MeV)	$T_{\text{exp}}^{\text{g.s.}}$(s)	$T_{\text{cal}}^{\text{g.s.}}$(s)	$T_{\text{cal}}^{\text{g.s.}}$(s)/$T_{\text{exp}}^{\text{g.s.}}$(s)
100	244	8.56	0.83	1.00	1.20
100	248	8.00	38.7	57.5	1.49
100	250	7.56	$<2.0\times10^3$	2.3×10^3	>1.15
100	252	7.15	9.1×10^4	8.6×10^4	0.95
100	254	7.31	1.2×10^4	1.8×10^4	1.50
100	256	7.03	1.2×10^5	2.4×10^5	2.00
102	250	8.96	0.50[a]	0.27	0.54
102	252	8.55	3.64	4.42	1.21
102	254	8.23	56.7	48.4	0.85
102	256	8.58	2.91	2.91	1.00
102	258	8.15	120.0	72.9	0.61
104	256	8.93	2.02	1.41	0.70
104	258	9.25	0.092	0.14	1.52
104	260	8.90	1.05	1.44	1.37
106	260	9.92	9.5×10^{-3}	9.4×10^{-3}	0.99
106	266	8.76[b]	61.8	18.2	0.30
108	264	10.59	1.1×10^{-3}	7.7×10^{-4}	0.70
108	270	9.30	3.60[c]	1.89	0.53
110	270	11.20	1.6×10^{-4}	1.0×10^{-4}	0.63
112	284	9.30	31.0	31.8	1.03
114	288	9.97	2.80	1.49	0.53
116	292	10.71	0.12	0.062	0.52

[a] Value from reference [162]; [b] from reference [166]; [c] from reference [167].

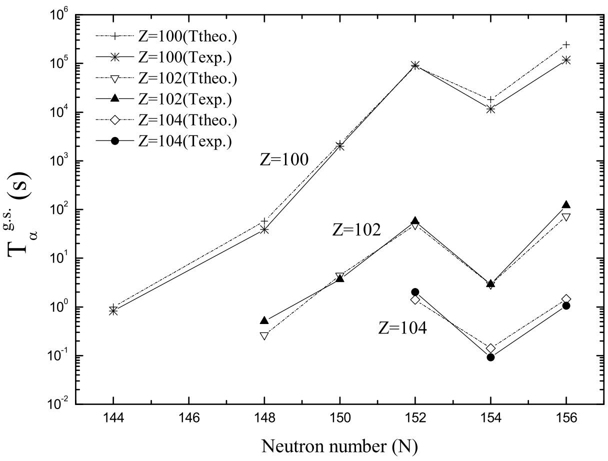

Figure 3.3: The comparisons between theoretical and experimental half-lives of α transitions from ground-states to ground-states are plotted versus the neutron numbers of the parent nuclei with Z=100, 102 and 104.

3.1.3 α decays of isomeric-states

There are large γ-transitions or β decay rates or high internal conversion coefficients in the early discovered isomers. α decay was only observed individually. The experimental development of radioactive beams and of new detector technology has made it possible to investigate the α decays of isomers. α decays are found in more than 100 first-excited isomers so far, ranging from medium-mass nuclei to the newly discovered superheavy nuclei such as $^{270}\mathrm{Ds}^m$ and $^{271}\mathrm{Ds}^m$, but systematic theoretical research on α decays of the isomeric states is rare. Can the present α-decay model which is based on the ground states of the nuclei be applied to the isomeric states? Are there any differences between the two kinds of α decays?

We make some analyses on the α decays of isomeric states. Firstly, the α-decay energy of isomeric-state is larger than that of the corresponding ground-state. Secondly, the orbital angular momentum of α particle is large sometimes, so the contribution of centrifugal potential to the decay half-life should be taken into account in the calculation. At last, the deformation of the isomeric-state is usually larger than the corresponding ground-state. Although the effective liquid drop model has been developed under the approximation of spherical fragments, the effect of deformation has been partially taken into account in the height of the barrier, through the Q-value of the decay and the effective separation of fragments at contact, which is dictated by the nuclear radius parameter, r_0 [168]. Because the effective surface tension σ_{eff} is a function of the decay energy and the penetrability factor Γ strongly depends on Q values, the relatively large

α-decay energy of isomeric state will affect the final theoretical half-life.

Table 3.2: Comparisons between calculated and experimental favored α-decay half-lives of isomeric states (Z=81-87).

Decay	J_i^π	J_f^π	$Q_\alpha^{i.s.}$(MeV)	$T_{exp}^{i.s.}$(s)	$T_{cal}^{i.s.}$(s)
$^{177}Tl^m \rightarrow ^4He+^{173}Au^m$	5.5−	5.5−	7.66	4.69×10^{-4}	3.02×10^{-4}
$^{185}Pb^m \rightarrow ^4He+^{181}Hg^p$	6.5+	6.5+	6.55	8.14	3.26
$^{187}Pb^m \rightarrow ^4He+^{183}Hg^p$	6.5+	6.5+[a]	6.21	152.5	70.9
$^{191}Pb^m \rightarrow ^4He+^{187}Hg^m$	6.5+	6.5+	5.40	6.54×10^{5}	3.46×10^{5}
$^{185}Bi^m \rightarrow ^4He+^{181}Tl$	0.5+	0.5+[a]	8.23	3.27×10^{-4}	2.89×10^{-5}
$^{186}Bi^m \rightarrow ^4He+^{182}Tl^p$	10−	10−	7.42	9.80×10^{-3}	7.05×10^{-3}
$^{191}Bi^m \rightarrow ^4He+^{187}Tl$	0.5+	0.5+	7.02	0.17	0.12
$^{193}Bi^m \rightarrow ^4He+^{189}Tl$	0.5+	0.5+	6.61	3.56	3.53
$^{195}Bi^m \rightarrow ^4He+^{191}Tl$	0.5+	0.5+	6.23	264	112
$^{195}Po^m \rightarrow ^4He+^{191}Pb^m$	6.5+[a]	6.5+	6.84	2.13	1.24
$^{197}Po^m \rightarrow ^4He+^{193}Pb^m$	6.5+	6.5+	6.52	30.7	20.3
$^{199}Po^m \rightarrow ^4He+^{195}Pb^m$	6.5+	6.5+	6.18	1.04×10^{3}	4.50×10^{2}
$^{201}Po^m \rightarrow ^4He+^{197}Pb^m$	6.5+	6.5+	5.90	1.84×10^{4}	7.42×10^{3}
$^{194}At^m \rightarrow ^4He+^{190}Bi^m$	10−[a]	10−	7.35	0.25	0.059
$^{197}At^m \rightarrow ^4He+^{193}Bi^m$	0.5+	0.5+	6.85	3.70	3.07
$^{198}At^m \rightarrow ^4He+^{194}Bi^n$	10−	10−	7.00	<1.16	0.82
$^{202}At^m \rightarrow ^4He+^{198}Bi^m$	7+	7+	6.26	2.09×10^{3}	5.54×10^{2}
$^{197}Rn^m \rightarrow ^4He+^{193}Po^m$	6.5+	6.5+	7.51	0.021	0.039
$^{200}Fr^m \rightarrow ^4He+^{196}At^m$	10−[a]	10−[a]	7.70	0.65	0.021

[a] Values estimated from systematic trends in reference [112].

In the favored α decay, the angular momentums and parities of the parent and daughter nucleus do not change. As a result, the orbital angular momentum of the relative movement between α particle and daughter nucleus is zero. We apply the model to this kind of relatively simple α decay near Z=82 shell at first. In our calculation, model parameters are chosen the same as we have done for the α transitions from ground states to ground states, namely, $r_0 = 1.13$, $\lambda_0 = 1.8 \times 10^{22}$ s^{-1}. We calculate the favored α-decay half-lives of all the isomeric-states (first excited isomers) near Z=82 shell (Z=81−87) and list the numerical results and experimental data in Table 3.2.

In Table 3.2, the first column marks the decays from parent nuclei to daughter ones. The second and third columns (J_{i}^{π} and J_{f}^{π}) are the spins and parities of the parent nuclei and daughter nuclei. The decay energy is listed in column 4. Experimental half-lives and theoretical ones are given in columns 5−6.

It is seen from Table 3.2 that theoretical half-lives are in reasonable agreement with experimental ones for α transitions from isomeric-states to both ground-states and isomeric-states. For most of the nuclei, the ratios between experimental half-lives and theoretical ones are just a few times. There are relatively large deviations between calculated results and experimental data for the two nuclei $^{185}\mathrm{Bi}^{m}$ and $^{200}\mathrm{Fr}^{m}$. One possible reason is the uncertainty of the spins and parities of daughter nuclei and/or parent nuclei. For example, the change of L_{α} from 0 to $5\hbar$ will lead to the increase of the half-life of $^{200}\mathrm{Fr}^{m}$ by a factor of 12.2. Because of the large angular momentums of parent nuclei and/or the daughter nuclei, the angular momentum transitions (L_{α}) of some decays can be very large. It can be seen clearly from Fig. 3.4 that the experimental data is reproduced well by this model. Therefore the effective liquid drop model is valid for favored α transitions from isomeric-states to other-states.

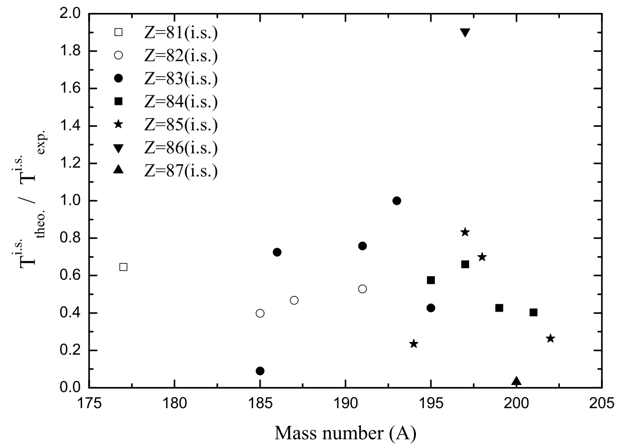

Figure 3.4: The ratio $T_{\mathrm{theo.}}^{\mathrm{i.s.}}/T_{\mathrm{exp.}}^{\mathrm{i.s.}}$ between theoretical and experimental favored α-decay half-life of isomeric-state is plotted versus mass number of the parent nucleus (Z=81-87).

Before ending this section, we would like to discuss the possible residual correlation which is beyond the present calculations of the effective liquid drop model. It is concluded from the previous discussion that the theoretical half-lives from this model agree with experimental ones within a factor of a few times for favored transitions ($\Delta L = 0$, $\Delta\pi = +1$). However, the quadrupole deformation of the daughter nucleus leads to the existence of a lowly excited rotational band based on the ground state. For well-deformed even-even nuclei, the first excited state is 2^+ state and its excited energy is very low. The branching ratios of α-transitions to the first 2^+ state of daughter nuclei are usually between 15% and 30% [169, 170] for the actinide nuclei. In our calculations, we have omitted the contribution from the α-decay to the first excited 2^+ state ($\Delta L = 2$, $\Delta\pi = +1$) because we only include the favored transitions ($\Delta L = 0$, $\Delta\pi = +1$). For well-deformed daughter nuclei, this can lead to a variation of the calculated half-life within a range of 30%. This means that the residual correlation between the ratio $T_{\rm cal}/T_{\rm exp}$ and the quadrupole deformation of the daughter nuclei is approximately less than 30% for well deformed daughter nuclei. On the daughter nuclei with less deformation the influence could be much less than 30%. For α-decays, if the ratio $T_{\rm cal}/T_{\rm exp}$ is within a factor of two (200%) or three (300%), one can say that good agreement is reached. Therefore a change of calculated half-life within 30% does not affect our conclusion.

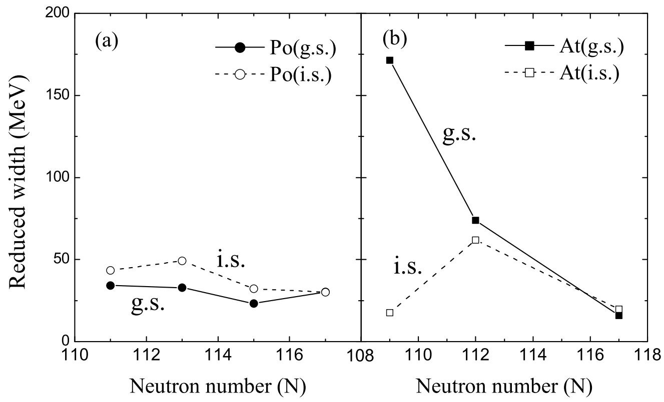

Figure 3.5: The comparisons between the reduced widths of favored α transitions from ground states and those of the isomeric states along Po (part (a)) and At (part (b)) isotopic chains are plotted versus the neutron numbers of the parent nuclei.

At present all models of α-decay is an effective model based on different generalizations of the Gamow's tunnelling effect. For an isotopic chain, it is interesting to analyze the variation of reduced width [171] which is defined as the ratio between experimental decay width and theoretical penetrability (Equation (3.10)). Because the reduced width is essentially a nuclear structure factor and is also model-dependent, it is interesting to compare the reduced widths of α-transitions from the ground states and from the isomeric states if both of them are favored transitions. On α-decays of isotopic chains there are very few complete chains which have both favored transitions from ground states and from isomeric states [112,116]. In Fig. 3.5, we draw the variation of reduced widths for α-decays from the ground states and from the isomeric states of Po and At chains. Some data are missing in above chains because there is no data on α-decay from ground state or there is no data on α-decay from isomeric state (i.e. the half-lives of α-decays do not exist at the same time for both the ground state and the isomeric state). It is seen from Fig. 3.5 that the ratio between the reduced width of the ground state and that of the isomeric state is less than two times for the Po isotopic chain. For the At chain, the reduced widths from isomeric decay and ground-state decay are close for two nuclei but the ratio between the reduced width of ^{194}At and that of ^{194}At^{m} (N=109) is anomalously large (approximately 9 times). On the At chain there are the large uncertainties of spin and parity of both ground state and isomeric state [112, 116]. We carried out the calculations of α-decay half-lives based on the estimated values of spin and parity by Audi *et al.* [112,116]. One possible explanation for the large difference of α-decays from ^{194}At and from ^{194}At^{m} is the uncertainty of the spin and parity of ^{194}At and ^{194}At^{m} [112, 116]. We consider that one of them should be an unfavored transition of α decay. It will be very interesting to measure the spin and parity of ^{194}At and ^{194}At^{m} experimentally and to test this view in future. In a word, it is concluded from Fig. 3.5 that the differences of the reduced widths are not large for favored transitions from the isomeric states and from the ground states. However, the difference of reduced widths can be relatively large if one of them is a favored transition ($\Delta\pi = +1$, $\Delta L = 0$) and another is an unfavored transition (especially for the case of $\Delta\pi = -1$ and large ΔL).

It is well-known that the logarithm of the α-decay width linearly depends upon the Sommerfeld parameter along any isotopic chain within a major shell. The Sommerfeld parameter η is defined as $\eta = 2Z_2e^2/\hbar v$ [172], where v is the velocity of α-particle, $v = \sqrt{2E/\mu}$. This is also called as the Geiger-Nuttall law in α-decay. Its generalization is the Viola-Seaborg formula [120]. This can be approximately derived based on the Gamow's tunnelling effect of the Coulomb barrier [120, 173]. This derivation is usually independent of the details of the attractive nuclear potential [120]. This relationship is mainly from the Gamow penetrating factor [120, 173]. It is shown in Fig. 3.6(a) that there is a linear relationship between the decay width and the Sommerfeld parameter. There are slight deviations on the linear relationship for some nuclei near N=152 because of the subshell effect.

There can be the residual correlation between the reduced width and the Sommer-

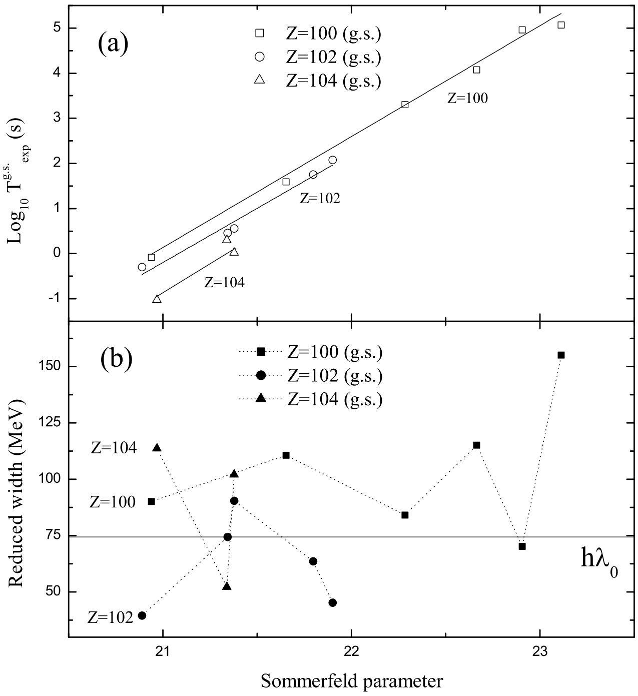

Figure 3.6: The experimental half-lives (in $\log_{10}$-scale) (part (a)) and the reduced width (part (b)) of α transitions from ground states are plotted versus the Sommerfeld parameter. All values of reduced widths in Fig. 3.6(b) are approximately within two times of the average value ($\approx 74-75$ MeV.)

feld parameter. It seems to us that the relationship between the reduced width and the Sommerfeld parameter may be very complicated because the reduced width is sensitive to nuclear structure and is also model-dependent. In order to see the residual correlation in the effective liquid model we have plotted the variation of the reduced width with the Sommerfeld parameter in Fig. 3.6(b). It is seen from Fig. 3.6(b) that many points lie near the line of the model parameter $h\lambda_0 = 74.442$ MeV (i.e. $T_{\rm cal}$=$T_{\rm exp}$). The distributions of the points are scattered in Fig. 3.6(b). Although the points of reduced widths are scattered in Fig. 3.6(b), all values of reduced widths are approximately within two times of the average value ($\approx 74-75$ MeV). This is also why the effective liquid model can reproduce the experimental half-lives of favored α decays within a few times.

3.1.4 α-decay half-lives of heavy and superheavy isomers

According to Audi's atomic mass table [112, 116], there are 28 first-excited isomers, 30 third-excited isomers and 2 fourth-excited isomers in the heavy and superheavy region of proton number Z$\geq$ 100. It is interesting to note that the second-excited isomers for Z$\geq$ 100 have not been observed to date [112, 116]. All the isomers in this area may

Table 3.3: Comparisons between calculated and experimental half-life values for the α-decays of heavy and superheavy isomers (Z≥99).

Decay	J_{i}^{π}	J_{f}^{π}	L_α	$Q_\alpha^{\mathrm{i.s.}}$(MeV)	$T_{\mathrm{exp}}^{\mathrm{i.s.}}$(s)	$T_{\mathrm{cal}}^{\mathrm{i.s.}}$(s)
$^{254}Es^m \rightarrow {}^4He + {}^{250}Bk$	2+	2−	1	6.70	4.42×10^{7}	3.08×10^{6}
$^{247}Md^m \rightarrow {}^4He + {}^{243}Es^p$	3.5+	3.5+	0	8.56	1.12	2.02
$^{249}Md^m \rightarrow {}^4He + {}^{245}Es^q$	0.5−	0.5−	0	8.21	1.90	26.60
$^{253}Lr^m \rightarrow {}^4He + {}^{249}Md^m$	0.5−	0.5−	0	8.86	1.67	1.08
$^{255}Rf^m \rightarrow {}^4He + {}^{251}No^m$	2.5+[a]	4.5−[a]	3	8.86	1.00	5.89
$^{257}Rf^m \rightarrow {}^4He + {}^{253}No$	5.5−	4.5−[a]	2	9.16	3.90	0.44
$^{265}Hs^m \rightarrow {}^4He + {}^{261}Sg$	1.5+[a]	3.5+[a]	2	10.89	—	2.18×10^{-4}
$^{265}Hs^m \rightarrow {}^4He + {}^{261}Sg^q$	1.5+[a]	1.5+	0	10.73	—	3.34×10^{-4}
$^{270}Ds^m \rightarrow {}^4He + {}^{266}Hs$	11−?	0+	11	12.33	6×10^{-3}	2.53×10^{-3}
$^{271}Ds^m \rightarrow {}^4He + {}^{267}Hs$	4.5+[a]	1.5+[a]	4	10.90	1.30×10^{-3}	1.98×10^{-3}

[a] Values estimated from systematic trends in reference [112].

form a new island of isomerism before the shell closure. α decays have been found in more than 28 isomers in the region. This is because most of the synthesized superheavy nuclei are proton-rich. As a result, large branching ratios of α decay and β^+ decay are observed in these isomers.

We extend the model which has been proved efficient for the favored α-decays of both the ground-states and isomer-states to calculate the α-decay half-lives of heavy and superheavy isomers. For the unfavored α-decays of isomeric-states, we take into account the effect of centrifugal potential barrier in the calculation. Numerical results and experimental data are listed in Table 3.3. L_α is the angular momentum of α particle.

We list all the isomers of nuclei with $Z \geq 99$ in Table 3.3 where the α-decay half-lives, spins and parities are taken from the 2003 mass table [112]. When we see Table 3.3, we find that there is also reasonable agreement between the theoretical values and the experimental data. The agreement is acceptable both for a new mass range and for unfavored decay where no adjustment on the parameter is made, considering the large experimental error bar due to the difficulty of measurements. The spins and parities of many parent nuclei and/or daughter nuclei are derived from systematic trends in reference [112]. As it is discussed in section 3.1.3, the influence of L_α on the α-decay

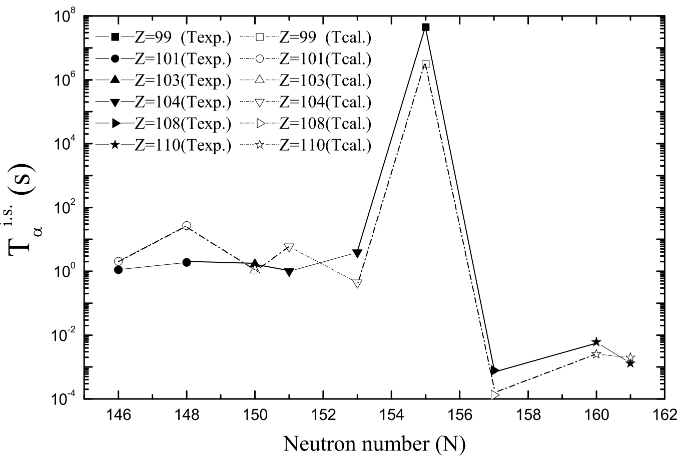

Figure 3.7: The comparisons between theoretical and experimental α-decay half-lives of heavy and superheavy isomers are plotted versus the neutron numbers of the parent nuclei with Z=99−110.

half-life is rather large. For $^{270}\mathrm{Ds}^m$, the spin and parity estimated in Audi's atomic mass table is 10^- [112]. But α-decay from the 10^- state ($^{270}\mathrm{Ds}^m$) to the 0^+ state ($^{266}\mathrm{Hs}$) is forbidden according to the selection rule of angular momentum and parity. We consider that possible configuration for $^{270}\mathrm{Ds}^m$ is the two-quasineutron state with $J^\pi = 11^-$ $(\nu\frac{13}{2}^- \bigotimes \nu\frac{9}{2}^+)$. In our calculation, we choose $L_\alpha = 11\hbar$ for the decay of $^{270}\mathrm{Ds}^m$. It coincides with the value $L_\alpha = 10 \pm 2\hbar$ estimated by Hofmann *et al.* [159]. The calculated half-life of $^{270}\mathrm{Ds}^m$ is close to the experimental one within a factor of 2.5. In a word, the effective liquid drop model reproduces the experimental α-decay half-lives of heavy and superheavy isomers well. This can be clearly seen from Fig. 3.7. In Fig. 3.7 we can also find the island of isomerism in the region of Z=99−110, N=146−161.

3.1.5 Summary of α decay half-lives calculation

In summary, the effective liquid drop model is generalized to describe the half-lives of α-transitions from ground-states to ground-states, from isomeric-states to ground-states, and from isomeric-states to isomeric-states using unified model parameters. Firstly, we test the model by calculating the half-lives of α-decays occurring between the ground states of even-even heavy and superheavy nuclei. Theoretical half-lives agree with experimental ones, within a factor of 2−3. Then we extend this model to calculate the favored α-decay half-lives of isomeric-states near proton shell Z=82. Good agreement is achieved between the experimental data and theoretical ones without any adjustment on the model parameters. Finally we generalize this model to calculate the

α-decays of isomers in superheavy region by taking into account the effect of centrifugal potential barrier for the unfavored α decays. The agreement between calculated half-lives of isomers and experimental data is acceptable for superheavy region. In a word, α-decay half-lives of both ground-states and isomeric-states can be calculated in a unified theoretical framework by the effective liquid drop model.

3.2 Spontaneous fission of odd-mass nuclei approaching $Z = 114$

For spontaneous fission of heavy nucleus in the ground state it is a pure quantum tunnelling effect. It is widely accepted that the barrier of spontaneous fission is mainly controlled by the Coulomb interaction (the strong interaction plays a partial role) [174–176]. This is similar to the barriers of proton emission, α decay, and cluster radioactivity. For the above three nuclear decay processes, which are governed by strong interaction and Coulomb interaction, there are simple laws between the decay half-lives and decay Q-values [106, 120, 122, 177]. For example, the Geiger-Nuttall law and Viola-Seaborg formula, the formulae of proton emission and cluster radioactivity show exponential relations between half-lives and decay Q-values of the corresponding decay processes [120, 122, 177, 178]. Therefore it is interesting to investigate the relationship between the half-life and Q-value of spontaneous fission. The formula of spontaneous fission half-life based on tunnelling effect and repulsive Coulomb barrier is proposed by Xu *et al.* [179, 180]. In this part, we improve the formula proposed by Xu *et al.*. [179, 180] by introducing the shell effects of parent and daughter nuclei to reproduce the recent data of spontaneous fission half-lives of odd-A nuclei with $Z \geqslant 108$. The relationship between the spontaneous fission half-lives and Q values will be investigated to obtain the analogous rule as the Geiger-Nuttall law.

Besides the above empirical investigations on spontaneous fission half-lives, the fission barriers were extensively studied both experimentally and theoretically [28, 29, 112, 123, 162, 181–188]. This is because the spontaneous fission half-lives of heavy nuclei are determined by the fission barriers. And the probability of superheavy nucleus formation in a heavy-ion fusion reaction is directly connected to the height of its fission barrier [181]. In addition, the shape of fission barrier is also connected to the spontaneous fission isomer. Theoretical studies on spontaneous fission barriers of even-even nuclei were performed by some nuclear structure models [123, 162, 181–184]. However, there are rare calculations of spontaneous fission barriers of odd-A nuclei. In this part, we systematically calculate the fission barrier of odd-A nuclei from $Z = 94 - 114$ by the macroscopic-microscopic (MM) model [25, 184, 189–191] and compare the calculated results with the present experiments [28, 29, 112, 185–188] to obtain information of nuclear shell effects at $Z = 114$ and get information of superheavy stable island.

This part is organized in the following way. In section 3.2.1, we propose an improved formula and a new exponential law for spontaneous fission half-life of odd-mass nucleus. In section 3.2.2, we systematically calculate the fission barriers of odd-mass nuclei ($Z = 94 - 114$) and discuss the shell effects on the spontaneous fission barriers and half-lives of odd-A nuclei approaching $Z = 114$. A summary of this part is given in section 3.2.3.

3.2.1 Formula for spontaneous fission half-life of odd-mass nucleus

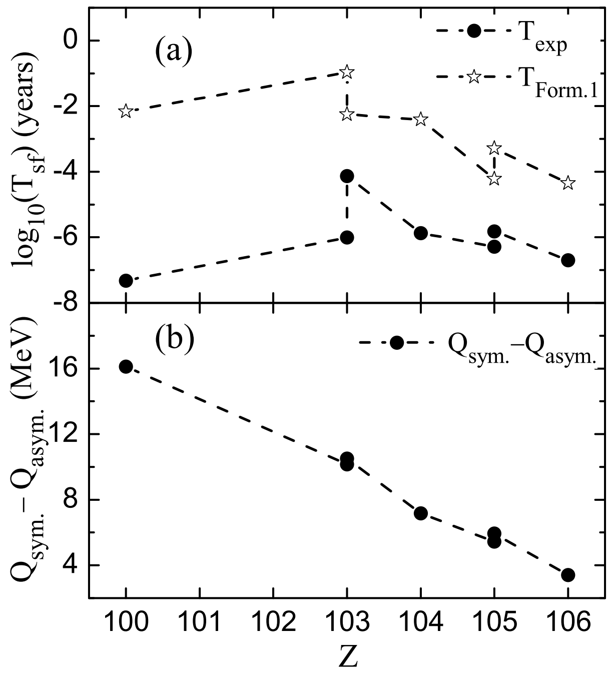

Figure 3.8: (a) Experimental spontaneous fission half-life and calculated one from Eq. (3.12) (proposed by Xu *et al.* [179, 180]) for nucleus with symmetric spontaneous fission; (b) The differences between the maximum Q values of symmetric and asymmetric mass distributions. The mass number of heavy fragment in the asymmetric mass distribution is approximately set to be 140.

Based on the quantum tunnelling effect and the empirical rule of $N = Z + 52$ long life-time line, Xu *et al.* [179, 180] proposed a new formula of spontaneous fission half-lives. It is written as

$$\log_{10}(T_{1/2}/\mathrm{yr}) = 21.08 + c_1\frac{Z-92}{A} + c_2\frac{(Z-92)^2}{A} + c_2\frac{(Z-92)^3}{A} + c_4\frac{Z-92}{A}(N-Z-52)^2, \tag{3.12}$$

where $c_1 = -548.825021$, $c_2 = -5.359139$, $c_3 = 0.767379$, and $c_4 = -4.282220$. The above formula [Eq. (3.12)] reproduces spontaneous fission half-lives of even-even nuclei very well. However, we find that there exists some systematical behavior of the deviations after detailed analyses of recent experimental data. At first, Eq. (3.12) overestimates the half-lives of symmetric spontaneous fission. It is seen from Fig. 3.8(a) that experimental half-lives of symmetric fissions are systematically shorter than the calculated values from Eq. (3.12). The reason is that the Q value of symmetric fission is larger than that of the asymmetric fission for a given nucleus. It is seen from Fig. 3.8(b) that there is a positive correlation between the deviations and the differences of the Q values of symmetric and asymmetric fissions. Secondly, the formula with the parent parameters is not valid for odd-A nuclei with $A \geqslant 271$ and $Z \geqslant 106$. This is shown in Table 3.4. The first and sixth columns of Table 3.4 denote nuclides. The second and seventh, third and eighth columns are the logarithms of experimental spontaneous fission half-lives [27–29, 112, 179, 185–188] and of the calculated ones from Eq. (3.12), respectively. It is seen from Table 3.4 that the calculated spontaneous fission half-lives of ^{271}Sg, ^{277}Hs, ^{279}Ds, ^{281}Ds, and ^{283}112 are much smaller than experimental ones. This implies that the empirical rule of $N = Z + 52$ long lifetime line is not valid for heavier odd-A nuclei with $Z > 106$. The possible shell effect at $Z = 114$ should be considered.

Based on above analyses, we propose the following improved formula

$$\log_{10}(T_{1/2}/\mathrm{yr}) = 21.08 + c_1\frac{Z-92}{A} + c_2\frac{(Z-92)^2}{A} + c_2\frac{(Z-92)^3}{A} + c_4\frac{Z-92}{A}|(N-Z-52)(N-Z-62)(Z-114)| + c_5(Q_{\mathrm{sym}} - Q_{\mathrm{asym}}) \tag{3.13}$$

to describe the spontaneous fission half-lives. The term $c_5(Q_{\mathrm{sym}} - Q_{\mathrm{asym}})$ is the correction of half-life for spontaneous symmetric fission. Q_{sym} and Q_{asym} denote the Q values (in MeV) of symmetric and asymmetric fissions, respectively. The mass number of heavy fragment in the asymmetric mass distribution is approximately set to be 140. The term $c_4\frac{Z-92}{A}|(N-Z-52)(N-Z-62)(Z-114)|$ denotes the correction of the long-lifetime line and the shell effect at $Z = 114$. According to a least-square fit of the available odd-A nuclei, we obtain a set of parameters: $c_1 = -573.0374$, $c_2 = 6.2674$, $c_3 = 0.1466$,

$c_4 = -0.1522$, and $c_5 = -0.5718$. The standard deviation is 1.52, and average deviation is 1.09.

Table 3.4: Logarithms of spontaneous fission half-lives (in years) calculated by the three formulae [Eqs. (3.12), (3.13) and (3.14)] .

Nucleus	$T_{\rm exp}$	$T_{\rm Eq.(3.12)}$	$T_{\rm Eq.(3.13)}$	$T_{\rm Eq.(3.14)}$	Nucleus	$T_{\rm exp}$	$T_{\rm Eq.(3.12)}$	$T_{\rm Eq.(3.13)}$	$T_{\rm Eq.(3.14)}$
^{235}U	19.00	21.08	21.08	18.72	^{259}Lr	−6.01	−0.97	−6.02	–
^{239}Pu	15.90	16.39	16.11	15.65	^{261}Lr	−4.13	−2.25	−6.91	−1.02
^{241}Am	14.08	14.08	13.80	13.98	^{253}Rf	−11.82	−12.71	−10.12	–
^{243}Am	14.30	14.14	13.93	13.83	^{255}Rf	−7.04	−7.61	−6.73	–
^{243}Cm	11.74	11.82	11.60	12.39	^{259}Rf	−5.88	−2.41	−5.89	–
^{245}Cm	12.15	11.90	11.77	12.24	^{267}Rf	−3.83	−10.94	−1.78	−3.63
^{249}Bk	9.26	9.13	9.19	10.30	^{255}Db	−6.60	−14.54	−11.03	–
^{237}Cf	−6.18	−6.05	−6.58	–	^{257}Db	−6.60	−9.06	−7.73	–
^{249}Cf	10.90	7.64	7.78	8.76	^{263}Db	−5.82	−3.29	−5.99	–
^{253}Es	5.80	4.83	5.31	6.38	^{267}Db	−3.86	−7.93	−3.31	−4.82
^{255}Es	3.41	3.08	5.18	–	^{263}Sg	−6.70	−4.35	−5.88	–
^{255}Fm	4.00	2.85	3.57	4.20	^{271}Sg	−4.92	−14.22	−5.92	−6.57
^{257}Fm	2.12	0.86	3.44	–	^{277}Hs	−4.12	−24.26	−4.53	–
^{259}Fm	−7.32	−2.16	−5.38	–	^{279}Ds	−8.15	−18.05	−6.37	–
^{245}Md	−10.54	−11.31	−9.89	–	^{281}Ds	−6.52	−26.55	−5.71	–
^{247}Md	−8.20	−6.06	−5.89	–	^{283}112	$\geqslant -5.92^a$	−18.42	−6.87	–

[a] Value from reference [29].

The numerical results are given in Table 3.4. The results calculated by the improved formula [Eq. (3.13)] are listed in columns 4 and 9. It can be seen from columns 4 and 9 that the half-lives from the improved formula agree with the experimental values well. Compared with Eq. (3.12), the improved formula can reproduce the half-lives of odd-A nuclei with symmetric fission and nuclei with $Z \geqslant 106$ well. The average deviation between the experimental data and the calculated values is about one order of magnitude. This demonstrates that Eq. (3.13) is valid for describing spontaneous fission half-lives of heavy and superheavy odd-A nuclei. We note that there is a relatively large deviation for ^{255}Db, with about 4.5 orders of magnitude. It seems to us that the half-life of ^{255}Db is obviously larger than the calculated value. This may be caused by the strong blocking effect of unpaired nucleon in ^{255}Db. It will be interesting to investigate the reason of this deviation both experimentally and theoretically.

Because the process of spontaneous fission of heavy nucleus in the ground state is a pure quantum tunnelling effect, it is interesting to investigate the relationship between the half-life and Q-value of spontaneous fission. The Q-value depends on the different combinations of charge number and mass number of two fission fragments. In Fig. 3.9, we plot the spontaneous fission half-life of heavy odd-A nucleus versus the maximum Q value of corresponding spontaneous fission process. It is seen from Fig. 3.9 that the spontaneous fission half-lives (in $\log_{10}$-scale) of relatively long-lived odd-A nuclei from $Z = 92$ to 106 form a straight line. However, experimental spontaneous fission half-lives are apparently larger than the expected values from the exponential relationship for nuclei with $Z \geqslant 108$. For example, the spontaneous fission half-life of $^{283}112$ is at least 7 orders of magnitude larger than the anticipant value from the exponential relationship. According to the calculation of macroscopic-microscopic model [123, 190], $Z = 114$ and $N = 184$ is the center of superheavy stable island. Therefore it is possible that the deviation from the exponential relationship for the odd-A nucleus approaching $Z = 114$ is caused by the strong shell effect. This is similar to the abnormal deviation of α-decay half-life from the Geiger-Nuttall law when the parent nucleus is close to the shell closure. Detailed discussions of the shell effects on spontaneous fission barriers of odd-A nuclei approaching $Z = 114$ will be presented in Sec. 3.2.2.

The linear relationship between the logarithms of spontaneous fission half-lives of odd-A nuclei along the long-lived line and the maximum Q values (in MeV) can be written as

$$\log_{10}(T_{1/2}/\mathrm{yr}) = c_1 Q_{\mathrm{max}} + c_2, \tag{3.14}$$

where $c_1 = -0.2788$, and $c_2 = 74.0839$. The standard deviation for the 14 nuclei along the long-lived line is 1.20, and average deviation is 0.84, which means the average deviation of the calculated results from experimental data is a factor of 6.9. The numerical results calculated by Eq. (3.14) are listed in columns 5 and 10 of Table 3.4. We can see from Table 3.4 that Eq. (3.14) works a little better than Eq. (3.13) for long-lived nuclei with $Z \leqslant 106$. The good agreement between theory and experiment shows that Eq. (3.14) has a firm basis in physics.

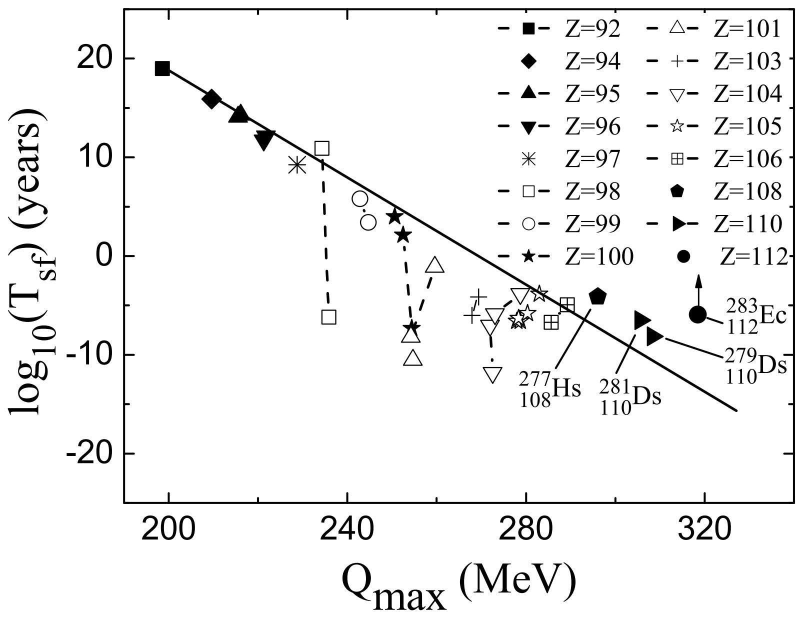

Figure 3.9: Variation of experimental spontaneous fission half-life with the maximum Q value of the fission process.

3.2.2 Systematics of fission barriers of odd-mass nuclei approaching $Z = 114$

In section. 3.2.1, the systematical relationship between spontaneous fission half-life and the maximum Q value of corresponding spontaneous fission process, and the apparent deviations of spontaneous fission half-lives of nuclei with $Z \geqslant 108$ from the exponential relationship [Eq. (3.14)] imply systematical variations of fission barriers. In this section, we mainly discuss the systematics of fission barriers of heavy and superheavy odd-A nuclei approaching $Z = 114$ in the framework of macroscopic-microscopic (MM) model [25, 184, 189–191]. The fission barrier depends on the way in which the intrinsic energy of the nucleus changes as its shape varies [181]. At the scission point, the intrinsic energy of the nucleus undergoes an important variation when its spherically symmetrical configuration turns into a strongly deformed configuration of two nuclei in contact. Under the framework of MM model, the fission barrier can be separated into two parts: a macroscopic collective component, which denotes the averaged variation of the Coulomb and nuclear energy, and a microscopic component, which is a function of a change in the shell structure of the deformed nuclear system. The macroscopic component of the fission barrier (usually calculated within the framework of the liquid drop model) declines rapidly along with the increasing atomic number because the increase of Coulomb energy (proportional to $Z^2/A^{1/3}$) is much rapider than that of the surface energy (proportional to $A^{2/3}$). For $Z > 105$, the simple liquid drop model predicts fission barriers of less than 1 MeV, which suggests that the fission properties and existence itself of those nuclei depend mainly on shell effects [181].

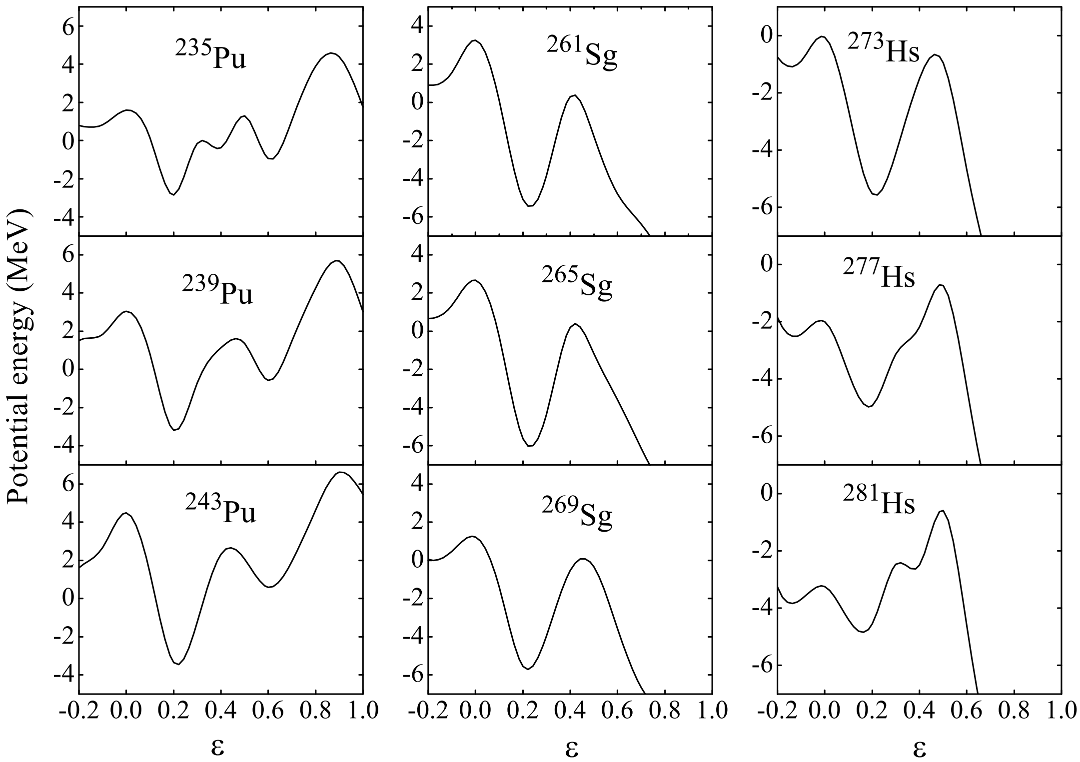

Figure 3.10: Total energy minimized with respect to ε_4 for each ε as function of ε for Pu, Sg, and Hs isotopic chains.

Since the MM model is a well-known model, here we do not present the details but only give the main results. Details of MM model calculation can be seen in Refs [25, 184, 189–191]. In this section, we use the macroscopic-microscopic model with Nilsson potential to calculate the fission barriers of heavy and superheavy odd-A nuclei. The Nilsson parameters used are the standard parameters [189]. The pairing energy is calculated by BCS method. We only include quadrupole deformation ε_2, hexadecapole deformation ε_4, and neglect other multipole deformations. We don't include the octupole deformation because available data of spontaneous fission half-lives clearly show that the conservation of parity should be kept to describe spontaneous fission where a quantum tunnelling effect happens [156].

We plot the calculated fission barriers of heavy and superheavy odd-A nuclei with $Z = 94-114$ in Figs. 3.10 and 3.11. The barrier is obtained as a function of deformation

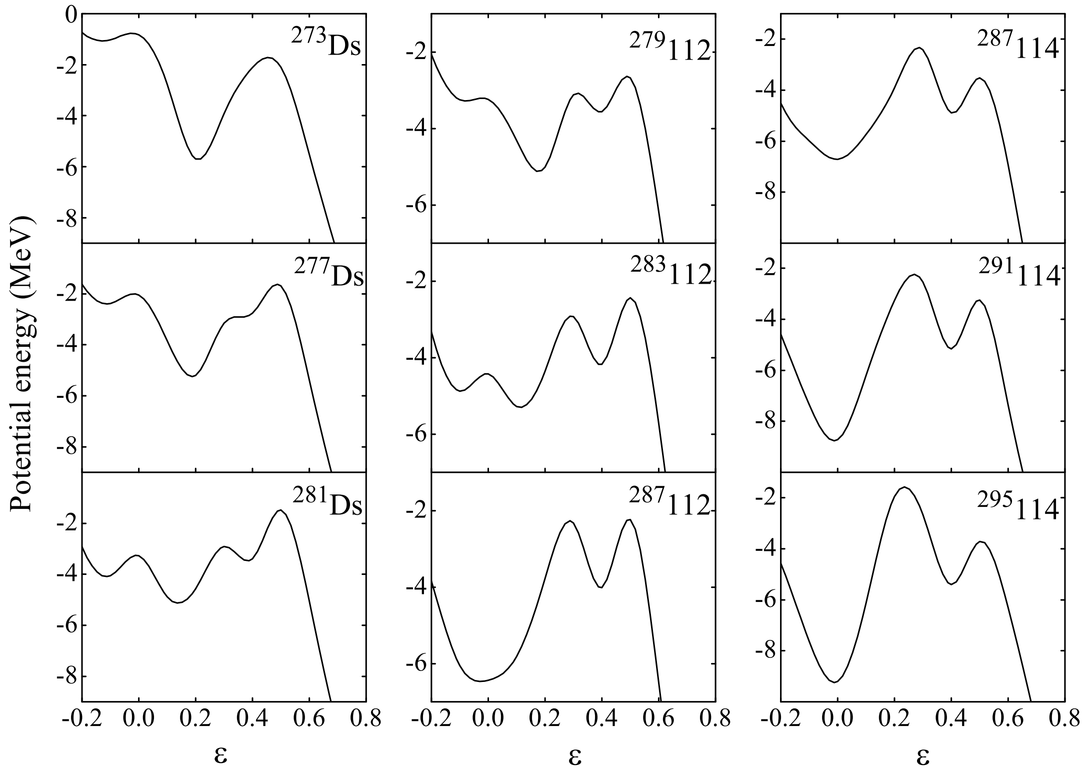

Figure 3.11: Same as Fig. 3.10 for isotopes of Z =110, 112, and 114.

parameter ε with minimization of energy with respect to ε_4 at each point. This type of plot represents a cut through the two-dimensional topographical map in the (ε, ε_4) plane along the potential energy minimum path with the energy projected onto the ε axis. For nuclei with $Z = 92-98$, there exist double-humped or three-humped barriers. Note that spontaneous fission half-life of a heavy nucleus depends not only on the height of the fission barrier but also on its shape [181]. It is seen from Fig. 3.10 that the barriers are relatively high for Pu isotopes, and the double-humped or three-humped shapes apparently widen the barriers. So are the barriers of neighboring nuclei ($Z = 92-98$), which cause relatively long spontaneous fission half-lives of nuclei in this region. For nuclei with $Z = 99-106$, the double-humped shapes of barriers gradually disappear and there are mainly single-humped barriers, which causes relatively short spontaneous fission half-lives. This is probably caused by the small shell correction on fission barrier. Another reason is that the shell effect of daughter nucleus ($Z_d \approx 50$) makes the decay energy relatively large and the symmetric fissions are the main fission modes for some nuclei in this region. For example, there exist bimodal spontaneous fission of ^{259}Lr [27]. According to the systematics of fission mass-yield distributions [27], symmetrical fission is probably the main decay mode of ^{261}Lr, which makes the spontaneous fission half-lives of ^{261}Lr shorter than the anticipant values from the exponential relationship [Eq. (3.14)] by about 3 orders of magnitude.

When we focus on the fission barrier of nuclei with $Z \geqslant 108$ in Figs. 3.10 and 3.11, we find the appearances of double-humped barriers of some Hs and Ds isotopes. For example, the barrier of ^{273}Hs is single-humped. Along with the increase of neutron number, the barrier of ^{277}Hs is widened and that of ^{281}Hs is double-humped, which make the spontaneous fission half-lives relatively long. The situation is similar for Ds isotopes. For $Z = 112$ and $Z = 114$ isotopes, the double-humped shapes of barriers are very apparent. Especially, the heights of the barriers of $^{287}112$, $^{291}114$ and $^{295}114$ are relatively high. For example, the barrier height of $^{295}114$ is above 7.5 MeV. This will make the spontaneous fission half-life of $^{295}114$ much longer than other superheavy isotopes shown in Fig. 3.11. The apparent increase of spontaneous fission half-life of $^{283}112$ may be viewed as a sign of longer spontaneous fission half-lives of nuclei approaching the predicted center ($Z = 114$ and $N = 184$) of superheavy stable island by the MM model.

3.2.3 Summary on spontaneous fissions of odd-mass nuclei

In this part, we systematically investigate the experimental data of spontaneous fission half-lives of heavy and superheavy odd-mass nuclei. Available data of spontaneous fission half-lives of odd-A nuclei with $Z = 92 - 110$ are well reproduced by an improved formula [Eq. (3.13)], with the average deviation from experimental data about one order of magnitude. A new exponential law [Eq. (3.14)] is found between the spontaneous fission half-lives along the long lifetime line and maximum Q values of the fission processes for odd-A nuclei with $Z = 92 - 106$. This may reflect the tunnelling property of spontaneous fission. An interesting result is that the experimental spontaneous fission half-lives are apparently larger than the anticipant values from the above exponential law for nuclei with $Z \geqslant 108$. This may be caused by enhanced shell effects for the nuclei approaching $Z = 114$. Systematical calculation of fission barrier is performed for odd-A heavy and superheavy nuclei by the macroscopic-microscopic (MM) model. The analyses of experimental spontaneous fission half-life and the corresponding calculated fission barrier suggest that both the height and shape of the barrier determine the spontaneous fission half-life. The apparent increase of the height of the fission barrier and the double-humped shape of the barrier for nuclei close to $Z = 114$ make the spontaneous fission half-lives much longer than the expected values from the exponential law [Eq. (3.14)], which means enhanced stability against spontaneous fission for odd-A nuclei approaching $Z = 114$. We suggest the experimental physicists to measure the spontaneous fission half-lives of $Z = 114$ isotopes to get more information of possible shell effect at $Z = 114$.

Chapter IV Experimental set-up for relativistic heavy ion collisions

4.1 RHIC accelerator

The Relativistic Heavy Ion Collider (RHIC) at Brookhaven National Laboratory (BNL) is designed to accelerate and collide heavy ions and polarized protons with high luminosity, allowing physicist to explore the strong interaction through many extensive and intensive measurements [192]. It was started to construct during 1991 and began to operate in 2000, following 10 years development and continuing construction. It is the first facility to collide heavy ion beams and the top center-of-mass collision energy is 200 GeV per nucleon pair, which is more than 10 times larger than the highest energy reached at previous fixed target experiment. The purpose of this extraordinary new accelerator is to seek out and explore new extremely high energy density and high temperature forms of matter and thus continue the centuries-old quest to understand the nature and origins of matter at its most basic level [192]. RHIC is also delivering polarized proton beams up to center-of-mass energy 500 GeV/c to carry on vigorous spin scientific program. The luminosity achieved now is actually much higher than the original design. The store-averaged luminosity reached now are 12×10^{26} cm^{-2}s^{-1} for Au+Au collisions, 2.3×10^{31} cm^{-2}s^{-1} for p+p collisions and 1.3×10^{29} cm^{-2}s^{-1} for d+Au collisions.

The complete RHIC facility is a complex set of accelerators interconnected by beam transfer lines [192]. Formation of bunches occurs prior to injection. The existing accelerator complex at BNL consisting of Tandem Van de Graaff accelerator, a Linear Proton Accelerator, the Booster Synchrotron ring, and the Alternative Gradient Synchrotron (AGS), serves as the injector for RHIC ring.

Figure 4.1 shows the sequence of steps in the chain of accelerators for particles. The particle passes through several stages of boosters before it reaches the RHIC storage ring. The first stage for ions is the Tandem Van de Graaff accelerator, while for protons, the 200 MeV linear accelerator (Linac) is used. As an example, gold (Au) nuclei with charge $Q = -1e$ are produced by the Pulsed Sputter Ion Source. They are then accelerated by Tandem Van de Graaff and some of their electrons are knocked off by stripping foils. Au nuclei leaving the Tandem Van de Graaff have an energy of about 1 MeV per nucleon and

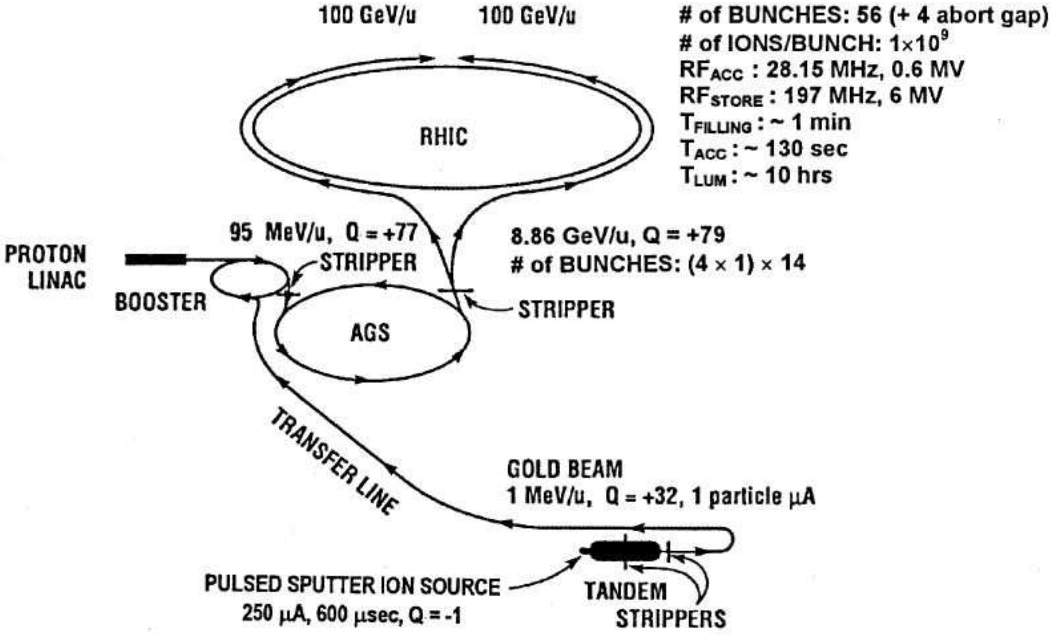

Figure 4.1: The RHIC complex for Au collisions [192].

have an approximate average electric charge $Q = +32e$ (32 electrons stripped from the Au atom). The selected $Q = +32e$ particles are then accelerated to 95 MeV per nucleon by the Booster Synchrotron. At the exit of the Booster Synchrotron the nuclei pass through another stripping foil and Au nuclei with $Q = +77e$ are selected for injection into the Alternating Gradient Synchrontron (AGS). In the AGS they finally reach 8.86 GeV per nucleon and after passing through a final stripping foil, fully stripped $Q = +79e$ Au nuclei are injected into the RHIC storage ring over the AGS-To-RHIC Transfer Line (ATR) sitting at the 6 o' clock position. In proton beam operations, protons are injected from Linac to the Booster Synchrotron and then accelerated and stored in the AGS and RHIC.

The RHIC consists of two quasi-circular concentric accelerator/storage rings on a common horizontal plane. Rings are oriented to intersect with one another at six locations along their 3.8 km circumference. Four of them are equipped with detectors. They are two large experiments STAR (6 o'clock) and PHENIX (8 o'clock) and two smaller ones PHOBOS (10 o'clock) and BRAHMS (2 o'clock), respectively.

In RHIC, ions reach their top energy and can be stored up to 10 hours. Since the first physics running in year 2000, RHIC has successfully run (polarized) p+p, Cu+Cu and Au+Au collisions at several beam energies and also d+Au collisions at $\sqrt{s_{NN}} = 200$ GeV.

4.2 STAR experiment

4.2.1 Overview

The Solenoidal Tracker at RHIC (STAR) specializes in tracking the thousands of particles produced simultaneously by each ion collision at RHIC. Weighing 1200 tons and as large as a house, STAR is a massive detector. It is used to search for the behavior of strongly interacting matter at high energy density and to search for signatures of QGP formation as well as the QCD phase diagram. It has an azimuthal symmetric acceptance and covers large range around mid-rapidity. STAR can measure many observables simultaneously to study signatures of a possible QGP phase transition and to understand the space-time evolution of the collision process in ultra-relativistic heavy ion collisions. The goal is to obtain a fundamental understanding of the microscopic structure of these hadronic interactions at high energy densities. In order to accomplish this, STAR was designed primarily for measurements of hadron production over a large solid angle, featuring detector systems for high precision tracking, momentum analysis, and particle identification at the mid-rapidity. The large acceptance of STAR makes it particularly well suited for event-by-event characterizations of heavy ion collisions and for the detection of hadron jets.

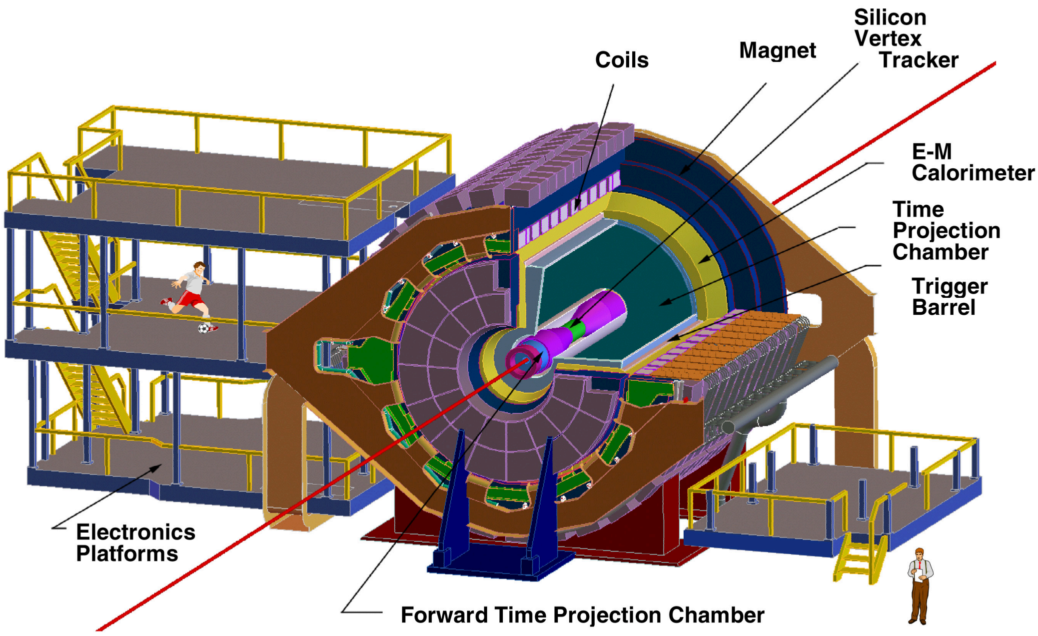

Figure 4.2: Layout of the STAR detector with cutaway showing the inner components.

As shown in Figs. 4.2 and 4.3, STAR consists of several subsystems and a main tracker - the Time Projection Chamber (TPC) located in a homogenous solenoidal analyzing magnet. From the beam pipe outward, at mid-rapidity the STAR detector system consists of the Silicon Vertex Tracker (SVT), Silicon Strip Detector (SSD), Time Projection Chamber (TPC), Central Trigger Barrel (CTB) and/or Time of Flight detector(TOF), Barrel Electro-Magnetic Calorimeter (BEMC), and the magnet system. At forward rapidity are the Forward Time Projection Chamber (FTPC), Endcap Electro-Magnetic Calorimeter (EEMC), Photon Multiplicity Detector (PMD), Forward Meson Spectrometer (FMS), Forward Hadron Calorimeter (FHC), Beam-Beam Counters (BBC), and Zero-Degree Calorimeter (ZDC). Details about these detectors can be found in Ref. [193].

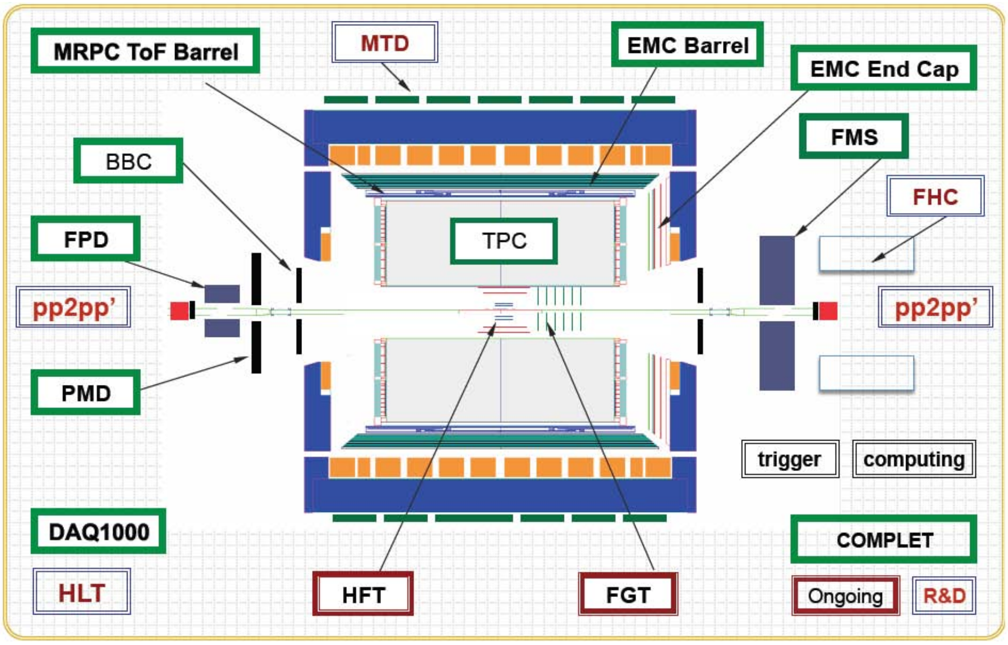

Figure 4.3: Cutaway side view of the STAR detector in year 2008 run and future upgrades.

Magnet The STAR magnet is cylindrical in design with a length of 6.85 m and has inner and outer diameters of 5.27 m and 7.32 m, respectively. It generates a field along the length of the cylinder having a maximum of $|B_z| = 0.5$ T. It allows the tracking detectors to measure the helical trajectory of charged particles to get their momenta. To date, the STAR magnet has been run in full field, reversed full field and half filed configurations.

Tracker The Time Projection Chamber is the main tracker of STAR, it covers the pseudo-rapidity $|\eta| < 1.8$ and 2π in azimuthal. The details of TPC detector will be discussed in the next section (sec. 4.2.2). There are inner detectors Silicon Vertex Tracker (SVT) and Silicon Strip Detector (SSD) close to the beam pipe, which provides additional high precision space points on tracks so that they improve the position resolution and allow us to reconstruct the secondary vertex of weak decay particles. The Inner tracker is helpful for secondary vertices reconstruction but contribute to considerable material budget which produces lots of photonic background to the electron related analysis. The SVT and SSD has been taken out in RHIC year 2008 run for this reason. To extend the tracking to the forward region, a radial-drift TPC (FTPC) is installed covering $2.5 < |\eta| < 4$ also with complete azimuthal coverage and symmetry [193]. To improve the precision of the tracking at the forward region, a Forward GEM Tracker (FGT) based on triple GEM technology is proposed and in preparation [194]. To provide more precise secondary vertices for heavy flavor (mostly c quark and b quark) measurements, STAR is proposing to build a new silicon vertex detector Heavy Flavor Tracker (HFT) [195, 196]. This detector will have two layers of pixels with limited materials located at mean radius of 1.5 cm and 5 cm from the beam axis and will be combined with the SSD to fill the gap between the innermost silicon detectors and the TPC.

Trigger detector The STAR trigger system is a 10 MHz pipelined system which is based on input from fast detectors to control the event selection for the much slower tracking detectors. The fast detectors that provide input to the trigger system are a central trigger barrel (CTB) at $|\eta| < 1$, zero-degree calorimeters (ZDC) located in the forward direction at $\theta < 2$ mrad and Beam-Beam Counter (BBC). The CTB surrounds the outer cylinder of the TPC, and triggers on the flux of charged-particles in the mid-rapidity region. Now it is replaced by the Barrel TOF system. The ZDCs are used for determining the energy in the neutral particles remaining in the froward directions. The BBC consists of a hexagonal scintillator array structure at 3.5 m from the nominal interaction point. It is the main device to make the relative luminosity measurement and to provide a trigger to distinguish polarized $p+p$ events from beam related background events by means of timing measurements. Some other detectors are used for special triggers, e.g. pseudo Vertex Position Detectors (pVPDs) or upgraded pVPDs (upVPD) are used for TOF triggered events (this will be discussed in the following section 4.2.3), and BEMC is used to trigger on events with high transverse momentum (p_T) particles etc.

Electro-Magnetic Calorimeter The STAR Barrel Electro-Magnetic Calorimeter (BEMC) located outside of the TPC covers $|\eta| < 1$ with complete azimuthal symmetry [197]. The Endcap Electro-Magnetic Calorimeter (EEMC) provides coverage for $1 < \eta \leq 2$, over the full azimuthal range, supplementing the BEMC [198]. This system allows measurements of the transverse energy of events, and trigger on and measure high transverse momentum photons, electrons, and electromagnetically decaying hadrons.

Time-Of-Flight System The STAR Time-Of-Flight (TOF) [199–201] is based on Multigap Resistive Plate Chamber (MRPC) technique. It locates between TPC and BEMC, covers $|\eta| < 1$ and full azimuthal angle, has < 80 ps intrinsic timing resolution and $> 95\%$ detecting efficiency for particles with $p_T > 0.5$ GeV/c. The TOF provides very good particle identification at moderate momentum range, extends π/K separation from 0.7 GeV/c to 1.6 GeV/c and proton/(π,K) separation from 1.1 GeV/c to 3 GeV/c. Combining with TPC, it also provide electron identification at $p_T > 0.2$ GeV/c. This will enables the di-electron measurements in STAR. About 3/4 coverage of this detector was installed and worked very well in RHIC year 2009 run. Now it is completed installation and taking data in RHIC year 2010 run. The trigger system of the TOF detector is the two upgraded Pseudo Vertex Position Detectors (upVPD), each staying 5.7 m away from the TPC center along the beam line. They provide the starting timing information for TOF detectors and pseudo vertex position at the beam direction of each event. Details of TOF geometry and calibration are discussed in the following section 4.2.3.

4.2.2 Time Projection Chamber

The TPC is the primary tracking device of the STAR detector [202]. It records the tracks of particles, measures their momenta, and identifies the particles by measuring their ionization energy losses (dE/dx). Consisting of a 4.2 m long cylinder with 4.0 m in diameter, it is the largest single TPC in the world. The cylinder is concentric with the beam pipe, and the inner and outer radii of the active volume are 0.5 m and 2.0 m, respectively. It can measure charged particles within momentum $0.15 < p_T < 30$ GeV/c for magnetic field $|B_z| = 0.5$ T (0.075 GeV/c low limit for magnetic field 0.25 T). The TPC covers the full region of azimuth ($0 < \phi < 2\pi$) and the pseudurapidity range of $|\eta| < 2$ for inner radius and $|\eta| < 1$ for outer radius. Fig. 4.4 shows the TPC structure schematically.

The TPC is divided into two parts by the central membrane. It is typically held at 28 kV high voltage. A chain of 183 resistors and equipotential rings along the inner and outer field cage create a uniform drift filed ($\sim$135 V/cm) from the central membrane to the ground planes where anode wires and pad planes are organized into 12 sectors for each sub-volume of the TPC. The working gas of the TPC is two gas mixture . P10 (Ar 90% + CH4 10%) regulated at 2 mbar above the atmospheric pressure. The electron

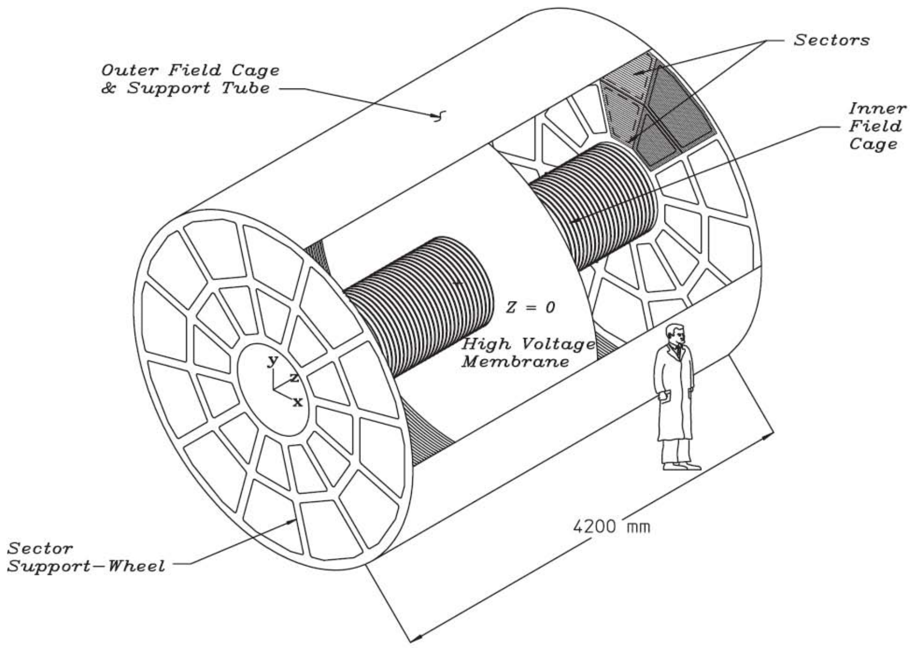

Figure 4.4: The STAR TPC surrounds a beam-beam interaction region at RHIC. The collisions take place near the center of the TPC [202].

drift velocity in P10 is relatively fast, ∼5.45 cm/μs at 130 V/cm drift field. The gas mixture must satisfy multiple requirements and the gas gains are ∼3770 and ∼1230 for the inner and outer sectors working at normal anode voltages (1170 V for inner and 1390 V for outer), respectively. Each readout plane is instrumented with a thin Multi-Wire Proportional Chamber (MWPC) together with a pad chamber readout. Each pad plane is also divided into inner and outer sub-sectors, while the inner sub-sector is designed to handle high track density near collision vertex. A total of 136,608 readout pads provide (x, y) coordinate information, while z coordinate is provided by 512 time buckets and the drift velocity. Typical position resolution is ∼0.5-1.0 mm.

When charged particles traverse the TPC, they liberate the electrons from the TPC gas due to the ionization energy loss (dE/dx). These electrons are drifted towards the end cap planes of the TPC. There the signal induced on a readout pad is amplified and integrated by a circuit containing a pre-amplifier and a shaper. Then it is digitalized and then transmitted over a set of optical fibers to STAR Data AcQuisition system (DAQ).

The TPC reconstruction process begins by the 3D coordinate space points finding. This step results in a collection of points reported in global Cartesian coordinates. The Timing Projection chamber Tracker (TPT) algorithm is then used to reconstruct tracks by helical trajectory fit. The resulted track collection from the TPC is combined with any other available tracking detector reconstruction results and then refit by application of a Kalman filter routine − a complete and robust statistical treatment. The primary collision vertex is then reconstructed from these global tracks and a refit on these tracks with the distance of closest approach (dca) less the 3 cm is preformed by a constrained Kalman fit that forces the track to originate from the primary vertex. The primary vertex resolution is $\sim 350\ \mu$m with more than 1000 tracks. The refitted results are stored as primary tracks collection in the container. The reconstruction efficiency including the detector acceptance for primary tracks depends on the particle type, track quality cuts, p_T, track multiplicity etc. The typical value for the primary pions with number of fit points $N_{fit} > 24$ and $|\eta| < 0.7$, $dca < 3.0$ cm is approximately constant at $p_T > 0.4$ GeV/c: $>\sim 90\%$ for Au + Au peripheral collisions and $\sim 80\%$ for central collisions, respectively.

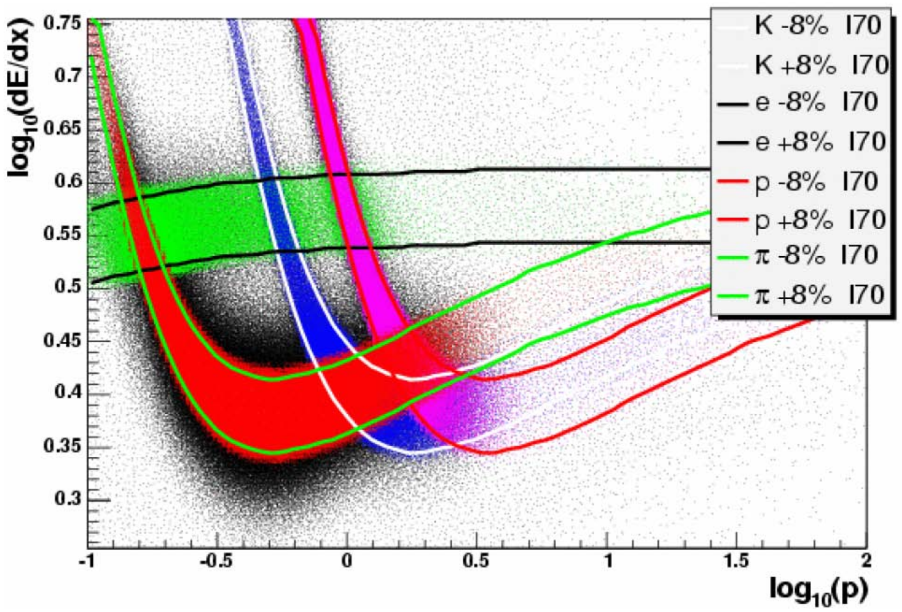

Figure 4.5: Distribution of $\log_{10}(dE/dx)$ as a function of $\log_{10}(p)$ for electrons, pions, kaons and protons. The units of dE/dx and momentum are keV/cm and GeV/c, respectively. The color bands denote within $\pm 1\sigma$ dE/dx resolution [203].

The TPC can identify particles by the dE/dx of charged particles traversing the TPC gas. The mean rate of dE/dx is given by the Bethe-Bloch Eq. (4.1) [204]:

$$-\frac{dE}{dx} = Kz^2\frac{Z}{A}\frac{1}{\beta^2}\left(\frac{1}{2}\ln\frac{2m_ec^2\beta^2\gamma^2T_{max}}{I^2} - \beta^2 - \frac{\delta}{2}\right). \tag{4.1}$$

The meaning of each symbol can be referred to Ref. [204]. Different types of particles (different rest masses) with the same momentum have different kinematic variables

$\beta(\gamma)$, which may result in distinguishable dE/dx. Figure 4.5 shows the measured dE/dx distribution. The typical resolution of dE/dx in Au + Au collisions is $\sim$ 8%, which makes the π/K separation up to p $\sim$ 0.6 GeV/c and proton/meson separation up to p $\sim$ 1.1 GeV/c.

The TPC is originally designed to identify particles at low momentum, but the separation of dE/dx of particles at relativistic rising region also allows people to identify particles at high momentum ($p > 3$ GeV/c) [199, 205, 206]. This method is especially more powerful for high momentum electron, which is much more difficult to be identified at low momentum. The e/π(e/K) separation is approximately $3\sigma(5\sigma)$ at $p_T = 3$ GeV/c and $2\sigma(3.5\sigma)$ at $p_T = 10$ GeV/c [206].

4.2.3 Time-Of-Flight detector and its calibration

STAR has performed the upgrade of full barrel Time-Of-Flight (TOF) detector based on the Multigap Resistive Plate Chamber (MRPC) technology since the year 2009 run (run 9). The timing electronics is based on CERN's HPTDC chip. In run 9, 86 out of 120 trays (72% coverage) worked very well in physical data taking. With stable running, TOF participated in nearly all runs. Only 2 channels out of 16512 were dead. In Run 10, all trays are fully installed with 2π azimuthal coverage. Currently 119 trays works very well. One tray is out due to a HV problem.

Fig. 4.6 shows the installed tray distribution in Run 9. Each tray covers 6 degree in azimuthal direction (ϕ) around the TPC. The uninstalled position of the west side is at the place of TPC supporting structure.

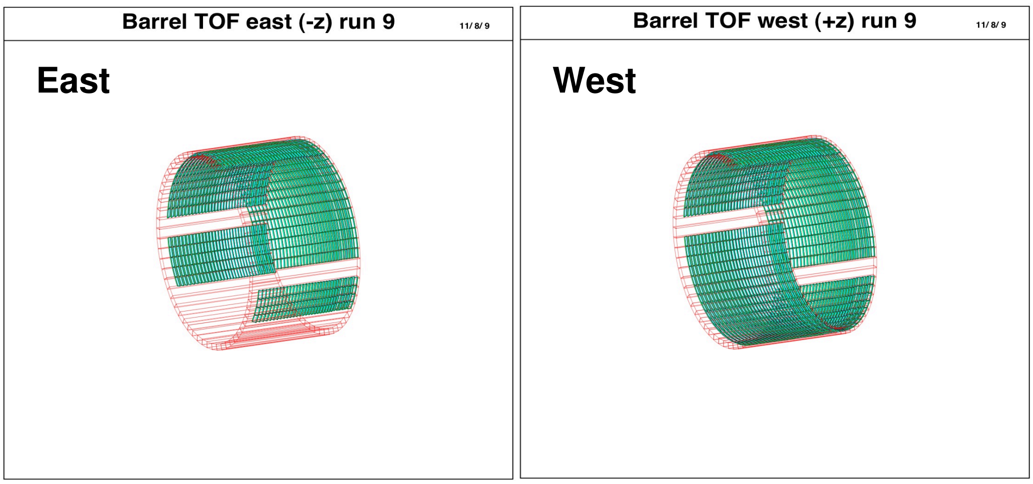

Figure 4.6: TOF trays distribution in Run 9. Filled (unfilled) strips show installed (uninstalled) trays.

There are 32 MRPC modules each tray, placed along beam (Z) direction. In each module, there are 6 read-out strips (called as pad/cell/channel) on each module along azimuthal (ϕ) direction. The detailed geometry and the definition of local coordinate system on each pad are shown in Fig. 4.7.

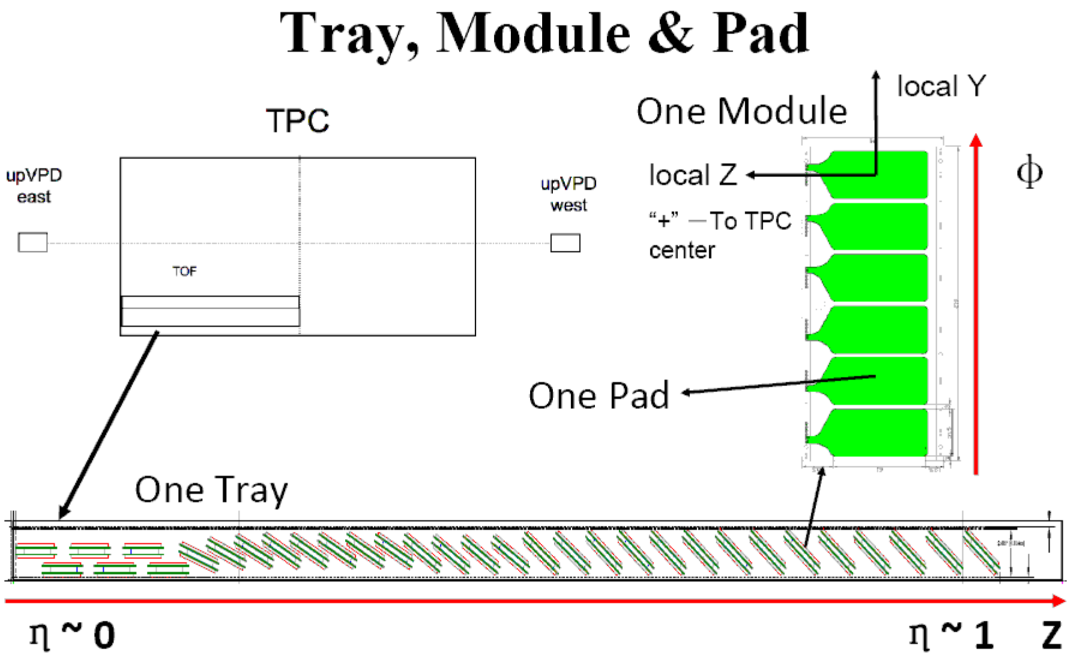

Figure 4.7: Geometry of trays, modules and pads.

As introduced in section 4.2.1, TOF system consists of TOF trays and VPD. The TOF trays provide the stop time of each track. The VPD provides the common start time of the event. The VPD can also provide the independent Z component of the vertex. But all of these rely on proper calibration. The timing resolution for each VPD or TOF tray channel is on ns level before any calibration. The improvement from calibration is about an order of magnitude. The calibration has three steps in general: TDC integral non-linearity calibration which is already applied before producing chain for calibration; VPD calibration; TOF trays calibration [207].

Integral Nonlinearity (INL) and calibration in TDIG board channel In STAR TOF system, TDIG boards are used to read out the time information from MRPC through TINO boards. About 1000 TDIG boards will be used for entire STAR-TOF system. Each TDIG board has 3 HPTDC chips with 8 read-out channels. At STAR-TOF, the TDC data system acquires data into all TDC bins, for the following reasons, the bin width of each HPTDC bins are not even.

- A. The HPTDC uses tapped delay line architecture to perform its time-sampling function. The 40MHz input clock is multiplied on chip to 320MHz. This 3.125ns clock signal is fed through a 32-tap delay locked loop (DLL). The unequal bin widths in the DLL will cause the differential nonlinearity in HPTDC.

- B. The DLL tap intervals are further subdivided by a 4-tap resistor-capacitor (RC) delay network. The unequal bin widths in the RC tapped delay lines is another source of differential nonlinearity in HPTDC.
- C. Noise coupling from the logic clock network (40MHz) within the chip into the sampling clock network (320MHz) also contributes to the differential nonlinearity in HPTDC.

The RC nonlinearity is periodic over 4 bins, the DLL nonlinearity is periodic over 32 bins, and the clock feedthrough nonlinearity is periodic over 1024 bins (25ns). In all cases, these effects are deterministic and periodic for a given chip. Once the DLL and RC parameters are fixed, the clock noise coupling will dominate. A standard technique for statistical bin width measurement is so called code density test: a pulse generator inputs a uniformly random distribution (with respect to HPTDC clock) into 2 HPTDC channels, if all TDC bins were the same width, then the probability of a pulse arriving in any bin would be the same as that of any other bin. Given enough statistics, the bin value variations are a direct measure of bin width variation. In the TDIG calibration setup at Rice University, one uses a so called cable delay test, which uses the similar data acquisition condition as STAR-TOF, to perform the Integral Nonlinearity calibration. After calibration, the INL parameters for all boards are saved and uploaded to offline database. The average time resolution per electronic channel is about 14ps.

VPD calibration The main calibration for the VPD is the slewing correction for each channel. The VPD has 19 channels on the east side and 19 channels on the west side. For each VPD hit, the *tdc* and *tot* are recorded. The *tdc* is the time when the leading edge of the pulse goes up over the threshold. The *tot* is the duration of the pulse stay over the threshold. It is correlated with the amplitude of the pulse. The slewing correction is done by removing the correlation of *tdc* and *tot*, on east side and west side separately. Since the *tdc*s are not absolute time but random event-by-event, we have to find a reference time for each channel. In the same event, all of the fired hits should have the same time. So for each hit, we can use the average time of all of the rest fired channels on the same side as a reference time. To ensure good reference time resolution, we require at least two hits to be used. That means only event which has at least 3 hits on the east and/or west side can be used for VPD calibration.

After the slewing correction (usually several iterations to correct the residual correlation), we get the corrected timing of east VPD and west VPD. For each side, the timing difference between different channels on the same side should have been shifted to zero, but the absolute time is floating. The absolute start time of the event does not make sense. But the timing difference between east and west VPD are directly correlated with z component of vertex (Vz) and should not be floating. To correct this, after applying the phase difference between east VPD and west VPD, we shift the mean value of the distribution of Vz(VPD)-Vz(TPC) to zero. Then the start time of the event can be calculated.

TOF tray calibration Once the VPD calibration has been done, one can start the TOF tray calibration. As mentioned before, the VPD provide the start time of each event T_{start}, the TOF hit provide the stop time of each track. The difference of these two is the time of flight (*tof*) of the associated track. To calibrate the TOF channels, we have to know what the *tof* should be. We usually select a pure pion sample at low momentum (p). From the momentum and mass, we can get the velocity of the track, we can also get the track length by projecting the helix onto TOF, then we know the time of flight (*tof*) expected. Our task is to shift the tof - tof_{expected} to zero, and remove any dependence. The TOF tray calibration is more complicate than the VPD calibration, it consists of 3 parts: 1) T_0 correction; 2) slewing correction; 3) hit position correction.

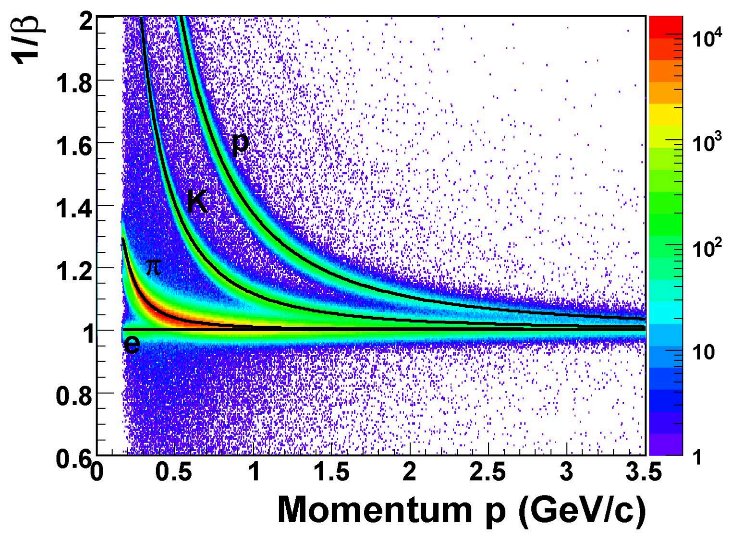

Figure 4.8: $1/\beta$ vs. momentum (p) from Run 9 200 GeV p + p collisions. Here $\beta = v/c$, where v is the speed of a particle.

Once the pure pion sample has been selected, we can start the so called T_0 correction. This correction is due to the different cable lengths and signal transition

Table 4.1: TOF system performance in different runs.

Operating condition			Timing Resolution (ps)		
			Vpd	Overall	TOFr
Run 3	200GeV d+Au		85	120	85
	200GeV p+p		140	160	80
Run 4	62GeV Au+Au		55	105	89
	200GeV Au+Au	Full-field	27	86	82
		Half-field	20	82	80
Run 5	200GeV Cu+Cu (ToT)		50	92	75
	62GeV Cu+Cu (ToT)		82	125	94
Run 8	200GeV d+Au (ToT)		N/A	N/A	N/A
	200GeV p+p (ToT)		83	112	75
Run 9	500GeV p+p		85	115	78
	200GeV p+p		81	110	74
Run 10	200GeV Au+Au (Preliminary)		28	87	82

time for different read-out channels. This can be simply done by shifting the mean value of the distribution of tof - tof_{expected} to zero channel by channel. The TOF tray use the same electronics as the VPD, the slewing correction is quit similar. The difference is now we use the T_{start} as the reference time, fit the correlation between $tdc - T_{\text{start}} - tof_{\text{expected}} = tof' - tof_{\text{expected}}$ and tot, here the tof' is the tof after the T_0 correction. In addition, as shown in figure 4.7, the signal is read out from one end of the stripes. Different hit position on the read-out strips result in different transition time. That means the tof is correlated with the distance between the hit position and the read-out end along the stripe which is designed as Z direction. The correction method is the same as that of slewing correction, just replace the tot by the Z. These 3 steps are correlated, so we need several iterations. Detailed documentation on TOF software can be found in [208].

Table 4.1 lists the calibrated timing resolution results for TOFr system since Run III (year 2003). The results show that the intrinsic timing resolution of TOF was around 75 ps and this performance was quite stable since run 5.

Fig. 4.8 shows the hadron identification capability of TOFr system in 200 GeV p+p collisions in Run 9. The performance of TOFr satisfies STAR TOF system upgrade requirements. Besides the bands of electron, pion, kaon and proton, one can also see the deuteron band.

Chapter V ϕ meson measurements in Run 7 Au+Au and Run 8 d+Au collisions at STAR

In this chapter the methods used to select events and measure the ϕ meson production through its decay channels $\phi \to K^+K^-$ and $\phi \to e^+e^-$ in the available data samples are presented. Here the $\phi \to e^+e^-$ signal is firstly reconstructed in STAR using Run 8 d+Au data by taking advantage of less inner material budget due to the removal of the inner tracker SVT and SSD. The event mixing technique which is used to measure ϕ meson and other resonances has been developed in the STAR experiment and many details can be found in Eugene Yamamoto's [209] and Jinguo Ma's [210] Ph.D. theses and recent papers [211–213] and presentations [214, 215]. We start this chapter by describing the data sets that are used in the analysis, followed by description of the detailed analysis procedure. We will describe the methods that are used to calculate the ϕ meson transverse momentum distribution, and the elliptic flow v_2 parameter.

5.1 Data sets and trigger

The data sets used in the measurement were taken by the STAR detector during the year 2007 and year 2008 RHIC run for Au + Au and d + Au collisions at $\sqrt{s_{NN}} = 200$ GeV. The typical luminosity or cross-section of the beam-beam collision per second achieved at RHIC is much higher (on the level of several orders of magnitudes) than the event recording rates of slow tracking detectors, such as the STAR TPC. The slow STAR detector subsystems only operate at event rates lower than 100 Hz (before TPX upgrade). The actual interaction rates are in the order of 1 MHz for p+p collisions and 100 KHz for Au+Au collisions [203]. There is room for the fast detectors to select (or trigger on) interesting events for the slow detector to read out. In this analysis, only "minimum bias" (MinBias) triggered data are used. Table 5.1 lists all data sets and event selections used in this analysis. The number of usable events is the final number of events after these selections.

The d + Au minimum bias trigger (VPD-ZDCE) required at least one beam-rapidity neutron in the ZDC in the Au beam outgoing direction, which is assigned negative pseudorapidity (η). In addition, there is an online VPD Z vertex cut at $|V_z| < 30$ cm and so some loss of efficiency and trigger bias from worsening resolution in peripheral

Table 5.1: Data sets from Run 7 and Run 8 used in this analysis

Data Set	Decay channel	Centrality Selection	Vertex Z Cut	Usable Events (M)
MinBias d + Au	$\phi \rightarrow K^+K^-$	0-20%	$\lvert V_z\rvert < 30$ cm	$\sim$ 7.3M events
MinBias d + Au	$\phi \rightarrow e^+e^-$	N/A	$\lvert V_z\rvert < 30$ cm	$\sim$33M events
MinBias Au + Au	$\phi \rightarrow K^+K^-$	0-80%	$\lvert V_z\rvert < 30$ cm	$\sim$64.7M events

events. The is because the VPD vertex Z calculation needs at least 1 hit in the east and 1 hit in the west. For peripheral events, the multiplicity of VPD hits is quite low, thus many of them will be rejected by the trigger. This will bring difficulties to the centrality selection, which will be discussed later.

The Au + Au minimum bias trigger requires a coincidence between the two ZDCs in different sides of the detectors (with large rapidity gap). It additionally requires an online VPD vertex Z cut within 5 cm of the TPC center. The tighter online cut on VPD vertex Z in Au+Au system is due to the better vertex Z resolution from VPD because of increased multiplicity in Au+Au system. This cut also causes the trigger bias in peripheral events.

The online cut on the vertex Z is set to only record events around the center of the TPC when the detector is taking data. A cut on the offline vertex Z from TPC is applied to avoid bias of this online vertex cut and also to select events around the center of the TPC, since the online vertex cut is determined by VPD and it is not calibrated. The offline calibrated TPC vertex has a much better resolution.

5.2 Centrality selection

In d+Au collisions centralities are selected based on the charged particle multiplicity measured in the East Forward Time Projection Chamber (EFTPC). The reason to use the FTPC multiplicity instead of the TPC mid-rapidity multiplicity for centrality selection is to avoid auto-correlation between centrality and the measurements of charged particles in the TPC. In run 8, the FTPC data need to be studied carefully because it had a number of readout boards (RDO) out, which changed over time, and it also had serious pile-up effect (two or more collisions regarded as one event) due to the higher coincidence rate [216].

After extensive tests it has been found that to get a stable charged particle mul-

Table 5.2: Applied cuts to get stable charged particle multiplicity distribution in east FTPC for centrality determination in Run 8 d+Au collisions.

Event cuts	Track cuts
$\lvert V_z\rvert < 30$ cm	$-3.8 < \eta \leq -2.8$
nBEMCmatch ≥ 1	$6 \leq$ nHitsFit ≤ 11
nFTPCErefMult > 0	$p_T < 3$ GeV/c
	$dca < 2$ cm

tiplicity distribution (M_{FTPCE}) from east FTPC versus the beam luminosity, we need to use the cuts listed in Table 5.2. Here nBEMCmatch means the number of tracks used in the vertex finding matches with BEMC hits, this is used for rejecting pile-up effects due to the high luminosity in d+Au collisions. nFTPCErefMult is the number of uncorrected charged particles measured from east FTPC. We also cut on the distance of closest approach ($dca < 2$ cm) of the track to the event vertex to make sure the particles are from collision vertex. nHitsFit is number of hits used to fit the track using the helix model. More hits used in the fit, the corresponding track momentum and dca resolution will be higher.

To take into account the effect of dead FTPC readout boards, three run periods are separated to reflect the FTPC acceptance. Due to the trigger inefficiency along V_z, the V_z dependent biases in multiplicity distribution require a re-weighting correction to be applied as a function of V_z in 2 cm bins for each run period. In addition, the vertex finder only finds vertex with at least 5 TPC tracks, as a result there are significantly biases in peripheral events. The final number of participants and number of binary collisions in peripheral events are under study. In this analysis, only the 0-20% central d+Au collisions are used in the $\phi \rightarrow K^+K^-$ spectra analysis. For run numbers from 8340015 to 9008109, the cut is $M_{\text{FTPCE}} > 10$. For run numbers from 9009007 to 9020089, the cut is $M_{\text{FTPCE}} > 10$. For run number > 9021001, the cut is $M_{\text{FTPCE}} > 8$. For details of the centrality definition, see the document here [216].

For Run 7 Au+Au 200 GeV centrality selection, the inclusion of inner tracking in this production rendered previous $refmult$ definition which was based on primary track a poor method to determine centrality [217]. There is a dependence on the primary vertex position for the reconstruction efficiency in the $\lvert V_z\rvert < 30$ cm region. The dependence was generally absent for TPC only tracking used in many of the previous productions, and is undesirable since it requires the centrality cuts to change as a function of V_z. Another variable is proposed called $gRefMult$ which counts global tracks under the following conditions: $|\eta| < 0.5$, $dca < 3$ and $nHitsFit \geq 10$. After extensive tests, $gRefMult$'s reconstruction efficiency was determined to be stable as function of V_z and running time. Subsequent fit with a MC Glauber soft+hard simulation to the high end of the $grefmult$ distribution results in the centrality cuts which are listed in Table 5.3.

Table 5.3: Centrality selection in Run 7 Au+Au 200 GeV collisions using $gRefMult$.

Centrality	$gRefMult$	Centrality	$gRefMult$	Centrality	$gRefMult$
0 - 5%	≥485	20 - 30%	≥178	50 - 60%	≥39
5 - 10%	≥399	30 - 40%	≥114	60 - 70%	≥21
10 - 20%	≥269	40 - 50%	≥69	70 - 80%	≥10

The remaining issues are biases on multiplicity distribution introduced by the main online VPD trigger setup [217]. The biases come from two sources. Firstly, over the full range in V_z, the VPD is more efficient at triggering on central events relative to peripheral. This leads to a general deficit in peripheral events for a given data sample. The second comes from a centrality dependence of the VPD's online V_z resolution which is worse for peripheral events relative to central due to lower multiplicity in peripheral events. Since the trigger-setup insisted events fall within the inner tracking acceptance, i.e., with an online cut of $|V_z(\text{VPD})| < 5$ cm, the resolution issue means that events at the higher "real" primary vertex Z (PVz, from TPC tracking, much better resolution) are more likely to be peripheral whereas the events at lower PVz are more likely to be central. This is shown in Figs. 5.1(a) and 5.1(c).

The V_z dependent biases in multiplicity distribution require a re-weighting correction to be applied for the analysis. For our analysis with a "signal" summed up over a range of $gRefMult$, events at PVz$\sim$0 will have their peripheral contribution scaled up in order to restore the unbiased case via the correction. The opposite will be true for events at higher |PVz| where the peripheral contribution will be scaled down - again to restore the unbiased case. The correction has to be applied as a function of PVz in 2 cm bins for acceptance reasons. The typical weight factor is shown in Figs. 5.1(b) and 5.1(d). Detailed documentation on Run 7 Au+Au 200 GeV centrality selection can be found here [217].

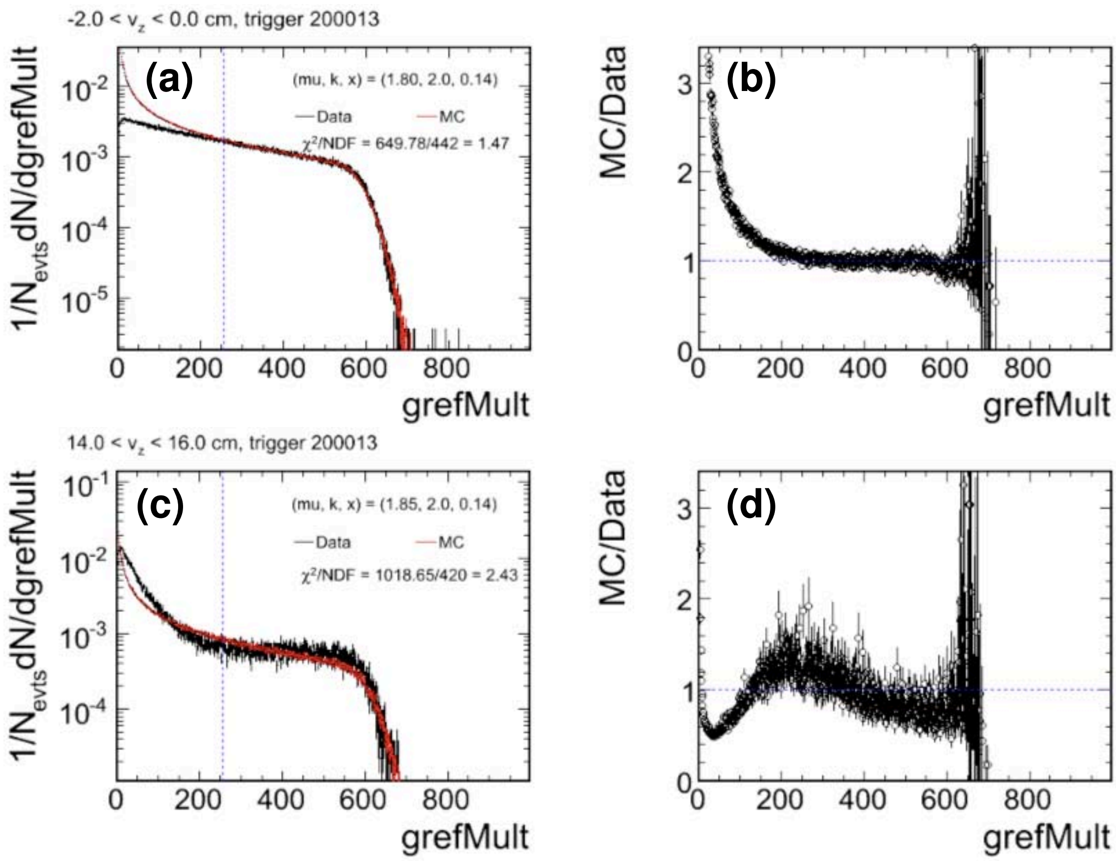

Figure 5.1: (a): $gRefmult$ distribution and Glauber MC simulation for $-2 < \mathrm{PVz} < 0$ cm. (b): The ratio of Glauber MC simulation versus data as the $gRefmult$ weight. (c): same as (a), but for $14 < \mathrm{PVz} < 16$ cm. (d): same as (b), but for $14 < \mathrm{PVz} < 16$ cm.

Fig. 5.2 shows the $gRefmult$ distribution before and after re-weighting. After re-weighting for different PVz bins, the $gRefmult$ distribution matches with the expectation from Glauber MC simulation.

5.3 $\phi \to K^+K^-$ reconstruction

TPC is the main detector in STAR for tracking and identifying charged particles as discussed in section 4.2.2. To reconstruct ϕ with good mass resolution and signal to background ratio from its K^+K^- decay channel, both excellent tracking and kaon identification are needed.

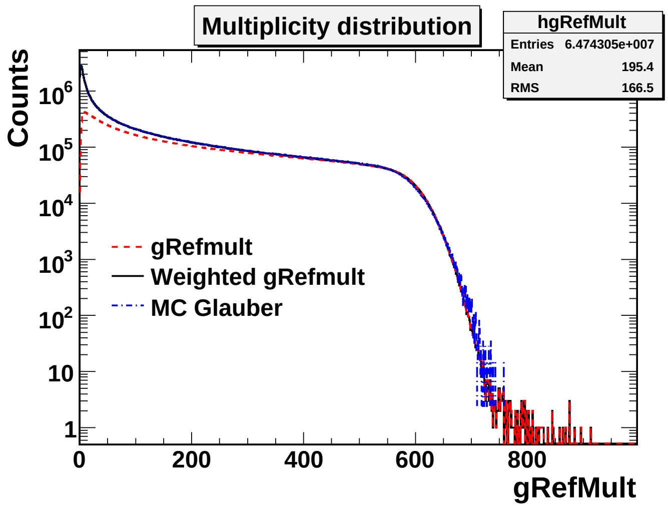

Figure 5.2: Un-weighted and weighted $gRefmult$ distribution and Glauber MC simulation for |PVz| < 30 cm. After re-weighting, the $gRefmult$ distribution overlaps with Glauber MC expectation.

5.3.1 Kaon track selection

Table 5.4 lists some track quality cuts for ensuring that we get the good tracks. The flag of a track is used to record the status of the track fitting at the stage of track reconstruction. It is required to be greater than 0 to avoid tracks with bad fitting and smaller than 1000 to reject tracks from post crossing the central membrane of TPC.

Table 5.4: List of cuts for selecting good kaon candidates.

Primary Track	Yes ($dca < 3$ cm)
Track Fitting Flag	0 < flag < 1000
Track Number of Hit Points	nHits $\geq$ 15
Track Hit Points to Maximum Points Ratio	nHits/nMax > 0.52
Track Pseudo-Rapidity	$\lvert\eta\rvert < 1.0$
Track Momentum	$0.15 < p < 12.0$ GeV/c
Track Transverse Momentum	$0.15 < p_T < 12.0$ GeV/c
Track PID by dE/dx	$-2.0 < n\sigma_{\rm kaon} < 2.0$
χ^2 of the primary track fit (in d+Au)	$\chi^2 < 6$

The lifetime of ϕ meson is so small ($c\tau \sim 46.3$ fm, here τ is ϕ-meson lifetime in vacuum, $\phi \rightarrow K^+K^-$ branching ratio 49.2%.) that it decays very close to the event primary vertex, thus we are interested in kaons originating from the primary vertex. A primary charged track includes the event primary vertex into the track fitting to get good momentum resolution, as discussed in section 4.2.2. Furthermore, the distance of closet approach (*dca*) to the event primary vertex of its associated global track is required to be smaller than certain value to reject 1) tracks from different collisions which mostly have different primary vertexes, 2) tracks decayed from weak decay particles with long lifetime like K_S^0, Λ, Ξ, Ω, etc., 3) tracks scattered by beam pipe, and so on [203]. In principle, the kaons decayed from ϕ meson should have $dca \sim 0$ cm. However, since the silicon detectors (inner trackers) are not included in Run 8 d+Au collisions and the first TPC measured points are at least 50 cm away from the event primary vertex, the resolution of *dca* is on the order of centimeter, depending on p_T and primary vertex resolution. Therefore, we require that the kaon candidate with $dca < 3$ cm. In Run 7 Au+Au collisions, the inner trackers (SVT and SSD) were included in the tracking, and the *dca* resolution was improved, but the inner trackers only participated in parts of the runs and it changed with time, so we still cut $dca < 3$ cm to avoid the complication.

To ensure good momentum resolution, number of TPC hits used in tracking is required to ≥ 15 (45 in maximum). The ratio of the number of TPC hits used in tracking to the maximum possible number of hit points was required to be greater than 52% to avoid split tracks where a real track is reconstructed in two or more segments. Charged tracks within a pseudo-rapidity window $|\eta| < 1.0$ are selected to be well within the TPC coverage. Tracks with transverse momenta and momenta less than 0.15 GeV/c were not used as their combined acceptance and efficiency becomes very small. In d+Au collisions, to reject the tracks from pile-up events, we require the χ^2 of the primary track fit less than 6. If the track is from pile-up event, then the χ^2 of this primary track fit by including the current primary vertex will be poor. The validity of this cut is justified by the stability of the mean number of primary tracks per event versus beam luminosity.

Charged tracks in the TPC are identified by their ionization energy loss dE/dx in the TPC gas. The energy loss is calculated at each hit point and the mean is calculated after truncating the highest 30%. Figure 5.3 shows the mean ionization energy loss ($< dE/dx >$) of charged tracks measured by the TPC v.s. the momentum of the track. Different bands around the expected mean dE/dx from Bichsel formula correspond to different particle species as indicated in Fig. 5.3. The electron band crosses with the pion bands, kaon bands and proton bands in different momentum regions. Through the $< dE/dx >$ measurement, kaons and pions can be separated by the TPC up to the momentum of about 0.6 GeV/c. And protons can be separated from kaons and pions up to the momentum of about 1.1 GeV/c.

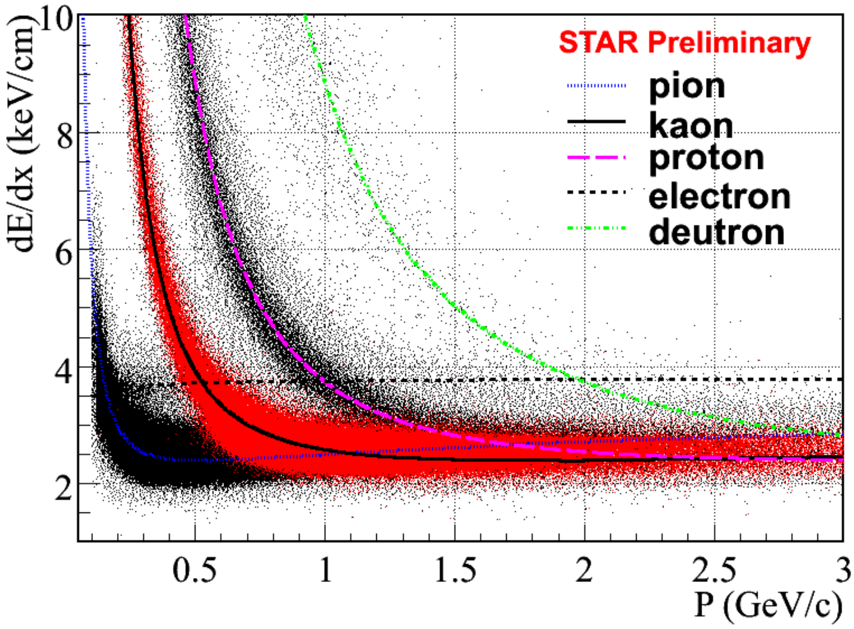

Figure 5.3: Measured $< dE/dx >$ in Run 8 d+Au 200 GeV collisions versus momenta of reconstructed tracks in the TPC.

The red dots in the Fig. 5.3 are kaon candidates by a 2σ cut on $< dE/dx >$. For the ϕ meson analysis, a cut $-2.0 < n\sigma_{\mathrm{kaon}} < 2.0$ is applied to select the kaon candidates. As we can see from the figure, the kaon sample is contaminated by electrons around $p \sim 0.5$ GeV/c, pions at $p > 0.6$ GeV/c and protons at $p > 1.1$ GeV/c. After the kaon sample selection, the K^+ and K^- are separated by their different charges measured by TPC.

5.3.2 Event mixing and raw yield extraction

The ϕ meson signal is generated by pairing all K^+K^- tracks from the same event that pass the selection criteria and by then calculating the invariant mass (m_{inv}) for all possible K^+K^- pairs. As random combinations of K^+K^- pairs are dominant in this process, the resulting same-event invariant mass distribution contains the ϕ meson signal on top of a large combinatorial background. An event-mixing technique [209, 211, 218, 219] is applied to calculate the shape of the combinatorial background, where the invariant mass is calculated by pairing two kaons from two different events with same primary vertex and multiplicity bins (mixed-event). Ideally, since it combines two different events, the mixed-event distribution contains everything except the real same-event correlations. The STAR TPC has symmetric coverage around the center of the collision region. However, variations in the acceptance occur since the collision vertex position may change considerably event-by-event. This variation in the collision vertex position gives rise to a non-statistical variation in the single particle phase-space acceptance which would lead to a mismatch between the mixed-event and same-event invariant mass distributions [211]. This mismatch would prevent the proper extraction of the ϕ meson signal. By sorting events according to their primary vertex V_z position and performing event-mixing only among events in the same V_z bin, the mismatching effect is minimized. In the analysis, events are divided into V_z bins that are 6 cm wide for event-mixing. In order to further improve the description of the background, two events are only mixed if they have similar event multiplicities. These requirements ensure that the two events used in mixing have similar event structure, so the mixed-event invariant mass distribution can better represent the combinatorial background in the same-event invariant mass distribution [211].

In order to reduce statistical uncertainty in the mixed-event, each event is mixed with five (in Au+Au collisions) to twenty other events (in d+Au collisions). To extract the ϕ meson signal, the mixed-event and same-event K^+K^- invariant mass distributions are accumulated and the mixed-event distribution is normalized to the same-event distribution in the region above ϕ meson mass, $1.04 < m_{\rm inv} < 1.06$ GeV/c^2, and subtracted in each p_T and y (rapidity) bin for every collision centrality [211].

Despite the requirements for mixing events described above, a residual background remains over a broad mass region in the subtracted invariant mass distribution. This is due to an imperfect description of the combinatorial background and the fact that the mixed-event cannot account for the real correlated background from decay pairs due to Coulomb interactions, photon conversions ($\gamma \rightarrow e^+e^-$) and particle decays like $K^{0*} \rightarrow K^+\pi^-$, $\rho^0 \rightarrow \pi^+\pi^-$, $K^0_S \rightarrow \pi^+\pi^-$ and $\Lambda \rightarrow p\pi^-$ [209]. For example, when both pions from a K^0_S decay are misidentified as kaons, the real correlation from the decay will remain in the same-event as a broad distribution, but will not be reproduced by the event mixing method.

Due to contamination of electrons/positrons in the selected kaon sample, the K^+K^- invariant mass distribution contains residual background near the threshold from correlated e^+e^- pairs, mainly from photon conversions ($\gamma \rightarrow e^+e^-$). The δ-dip-angle between the photon converted electron and positron is usually quite small. The δ-dip-angle is calculated from

$$\delta - dip - angle = \cos^{-1}(\frac{p_{T1}p_{T2} + p_{z1}p_{z2}}{p_1 p_2}), \tag{5.1}$$

where p_1, p_2, p_{T1}, p_{T2}, p_{z1}, p_{z2} are momentum, transverse and longitudinal momentum components of two tracks. It represents the opening angle of a pair in the p_z-p_T plane. We require the δ-dip-angle to be larger than 0.04 radians. This cut is found to be very effective in removing the photon conversion background.

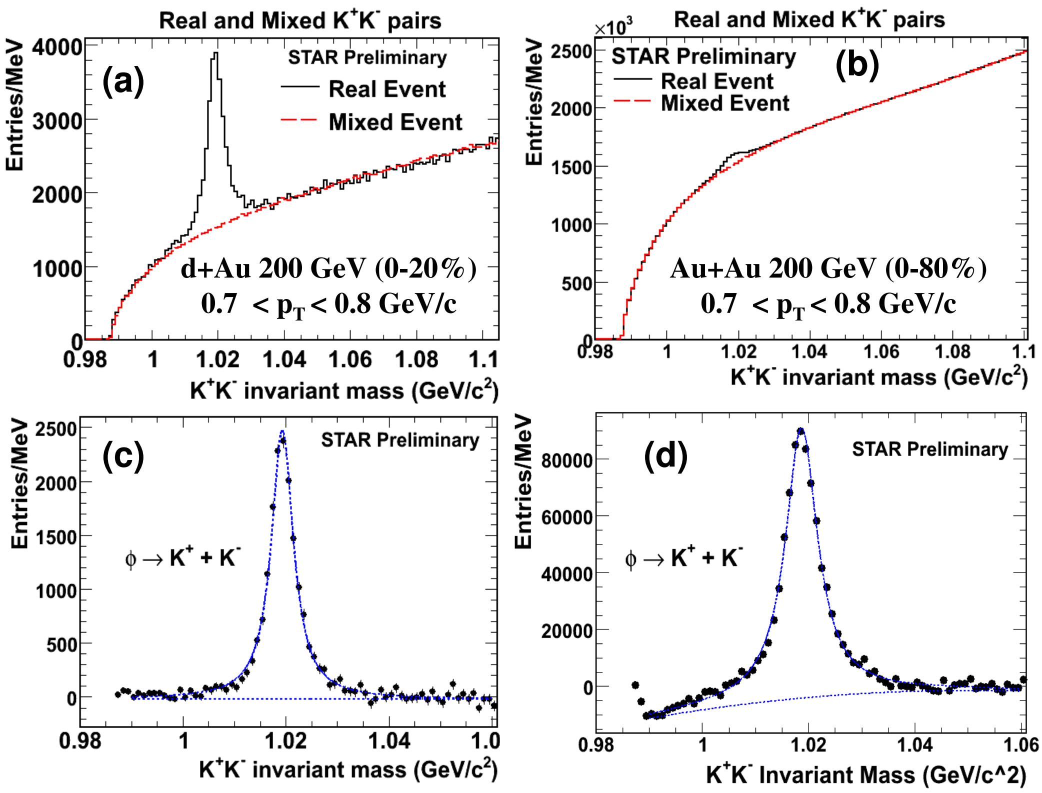

Figure 5.4: Upper panels: same-event (solid line) and mixed-event (dashed line) K^+K^- invariant mass distributions at $0.7 < p_T < 0.8$ GeV/c; (a) d+Au 200 GeV (0-20%), (b) Au+Au 200 GeV (0-80%). Lower panels: the corresponding ϕ meson invariant mass peaks after subtracting the background. Dashed curves show a Breit-Wigner + linear/polynomial background function fit in (c) and (d).

Fig. 5.4 shows the K^+K^- invariant mass distributions in d+Au 200 GeV (0-20%) and Au+Au 200 GeV (0-80%) collisions. Solid lines in the upper panels are same-event pairs while the dashed lines are from mixed-event. The ϕ meson peak is clearly visible for d+Au 200 GeV (0-20%) (Fig. 5.4 (a)) before background subtraction, but not so clear for Au+Au 200 GeV (0-80%) (Fig. 5.4(b)) due to its smaller signal significance. However, after background subtraction, the ϕ meson invariant mass peak can be seen clearly for both data sets. The lower panels in Fig. 5.4 show the mixed-event background subtracted ϕ meson invariant mass distributions. In Fig. 5.4(d) the small bump around $m_{inv} \sim 0.9875$ GeV/c^2 is the residual γ conversion background since in Run 7 Au+Au collisions the SVT and SSD contribute to extra material budget.

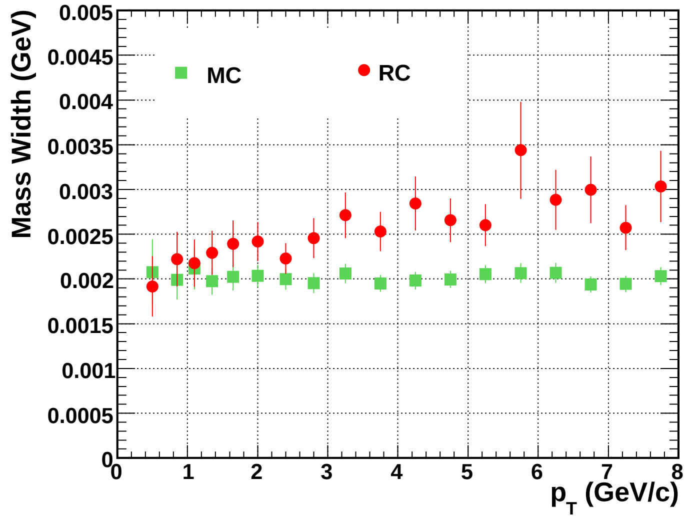

Figure 5.5: Mass resolutions of the reconstructed (RC, σ_{RC}) and standard (from PDG value [220], MC, σ_{std}) ϕ meson invariant mass peaks (fitted with Gaussian) versus ϕ meson transverse momenta.

Raw yields of ϕ mesons are determined by fitting the background subtracted $m_{\rm inv}$ distribution in the appropriate range with a Breit-Wigner function superimposed on a linear (or polynomial) background function

$$\frac{dN}{dm_{inv}} = \frac{A\Gamma}{(m_{inv} - m_0)^2 + \Gamma^2/4} + B(m_{inv}), \tag{5.2}$$

where A is the area under the peak corresponding to the number of ϕ-mesons, Γ is the Full Width at Half Maximum (FWHM) of the peak, m_0 is the resonance mass position. $B(m_{inv})$ denotes a linear ($B(m_{inv}) = p_0 + p_1 m_{inv}$) (Fig. 5.4(c)), or polynomial ($B(m_{inv}) = p_0 + p_1 m_{inv} + p_2 m_{inv}^2$) (Fig. 5.4(d)) residual background function. The parameters (p_0, p_1 and p_2) of $B(m_{inv})$ are free parameters.

Due to limited momentum resolution of the measured particles, it will propagate to the mass measurement. The observed ϕ meson width distributions usually show an apparent FWHM larger than the value from Particle Data Group (PDG) [220], being a convolution with a resolution function due to measurement uncertainties. Previous STAR ϕ meson raw yields were extracted from standard Breit-Weigner function, while

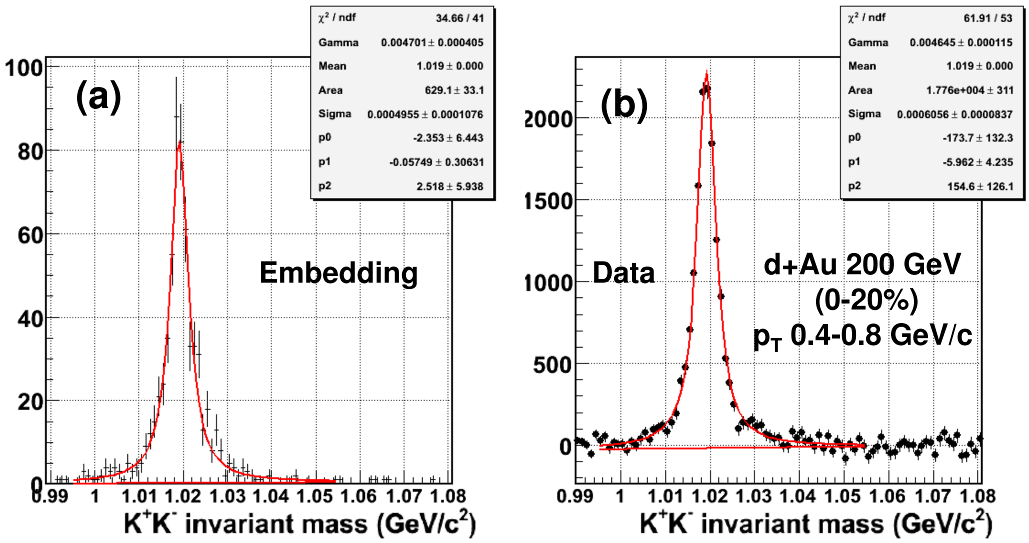

Figure 5.6: $\phi \to K^+K^-$ invariant mass distribution (a: from embedding; b: from data) in d+Au 200 GeV collisions fitted with Gaussian convoluted Breit-Wigner function superimposed on a linear (or polynomial) background function.

PHENIX used Gaussian convoluted Breit-Weigner function due to its relatively poor momentum resolution. The difference between the two kinds of methods is studied. We convolute each point of the Breit-Wigner function with the detector mass resolution of ϕ meson. Detector mass resolution should be extracted from zero width simulation for different p_T bins. Currently, we do not have detector mass resolution from simulation. However, we can approximately extract the mass resolution of detector ($\sigma_{detector}$) from the width of the reconstructed mass peak according to the relation $\sigma_{RC}^2 = \sigma_{std}^2 + \sigma_{detector}^2$. Here σ_{RC} and σ_{std} are the mass resolutions of reconstructed ϕ mesons and the PDG value, respectively.

Fig. 5.5 shows the ϕ meson mass resolutions extracted from fitting the reconstructed (RC, σ_{RC}) and standard (from PDG value, MC, σ_{std}) ϕ meson invariant mass peaks with Gaussian function. From σ_{RC} and σ_{std} we can get the detector mass resolution in different p_T bins. Then we can fit the invariant mass peak with the Gaussian convoluted Breit-Wigner function superimposed on a linear (or polynomial) background function. An example of the fit is shown in Fig. 5.6. It is seen from Fig. 5.6 that the Gaussian convoluted Breit-Wigner function works well.

The ratio between ϕ meson raw yields extracted from Gaussian convoluted Breit-Wigner function and Breit-Wigner function is shown in Fig. 5.7. It can be seen from Fig. 5.7 that the difference between the raw yields extracted from the two methods is

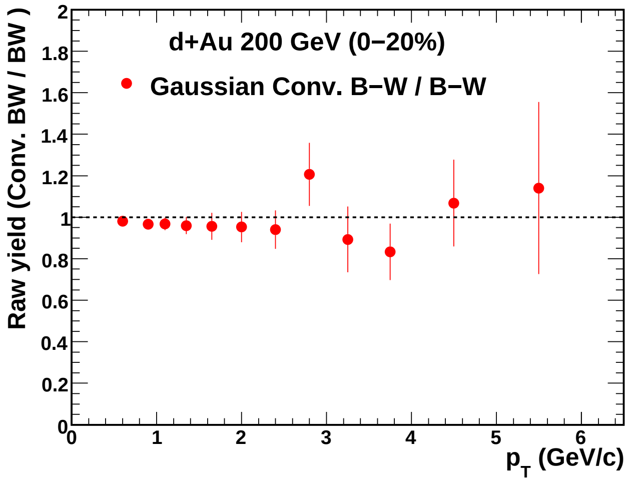

Figure 5.7: The ratios between ϕ meson raw yields extracted from Gaussian convoluted Breit-Wigner function and Breit-Wigner function versus transverse momenta of ϕ mesons.

$\sim$ 5% in d+Au 200 GeV collisions (0-20%).

Table 5.5: List of cuts for selecting good electron candidates.

Primary Track	Yes (dca < 3 cm)
Track Fitting Flag	0 < flag < 1000
Track Number of Fit Points	nHitsFit $\geq$ 20
Track Fit Points to Maximum Points Ratio	nHitsFit/nMax > 0.52
Track Number of dE/dx Points	ndEdx $\geq$ 15
Track Pseudo-Rapidity	$\lvert\eta\rvert < 1.0$
Track Momentum	$0.2 < p < 12.0$ GeV/c
Track Transverse Momentum	$0.2 < p_T < 12.0$ GeV/c
Electron PID by dE/dx	$-2.0 \leq n\sigma_{\rm electron} \leq 3.0$
Pion rejection	$\lvert n\sigma_{\pi}\rvert > 2.0$
Kaon rejection	$\lvert n\sigma_{\rm kaon}\rvert > 2.0$
Proton rejection	$\lvert n\sigma_{\rm proton}\rvert > 2.0$

5.4 $\phi \to e^+e^-$ reconstruction

With less γ conversion background by removing the inner trackers in Run 8 d+Au 200 GeV collisions, we have the first chance to look at the ϕ meson reconstructed from its e^+e^- decay channel [214]. The $\phi \to e^+e^-$ is rare electromagnetic decay with much smaller branching ratio $(2.97 \pm 0.04) \times 10^{-4}$, thus the ϕ meson reconstruction via di-electronic channel is limited by statistics. The $\phi \rightarrow e^+e^-$ reconstruction technology is similar to $\phi \rightarrow K^+K^-$ except that we select electron instead of kaon tracks. In addition, the correlated combinatory background is also different in e^+e^- case.

5.4.1 Electron track selection

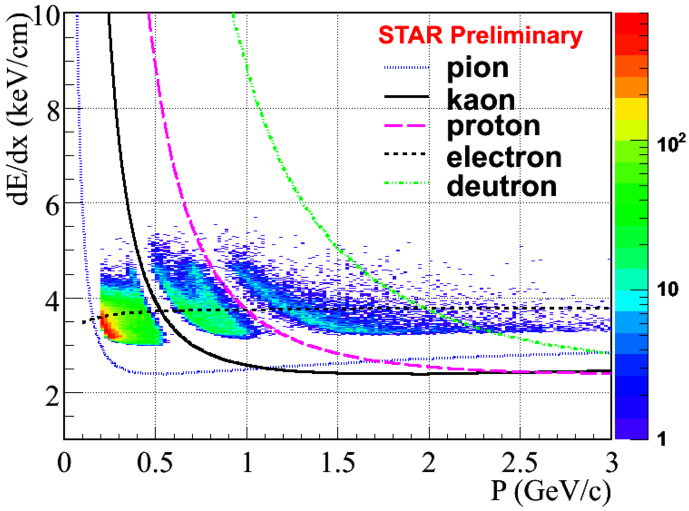

Figure 5.8: $< dE/dx >$ of selected electron candidate in Run 8 d+Au 200 GeV collisions versus its momentum measured from the TPC.

The cuts for electron candidate selection are listed in Table 5.5. Besides the usual track quality cuts used for kaon candidate selection (Table 5.4), some special cuts for electron candidate selection are used. For example, to ensure good measurement of particle ionization energy loss, we require ndEdx $\geq$ 15, where ndEdx is the number of dE/dx points. The lower limits of p and p_T are set to be 0.2 GeV/c for rejecting some of the low-momentum electrons from photon conversions. Since the electron band in the $< dE/dx >$ versus momentum plot (Fig. 5.3) cross with pion, kaon, and proton band in different momentum range, we use the veto cuts which require the selected tracks are 2σ away from the pion/kaon/proton Bichsel curve. Fig. 5.8 shows the $< dE/dx >$ of selected electron candidate in Run 8 d+Au 200 GeV collisions versus its momentum measured from TPC.

5.4.2 Event mixing and signal building

After selecting the electron candidates, the similar signal and background reconstruction technology developed for $\phi \rightarrow K^+K^-$ (section 5.3.2) is used for $\phi \rightarrow e^+e^-$

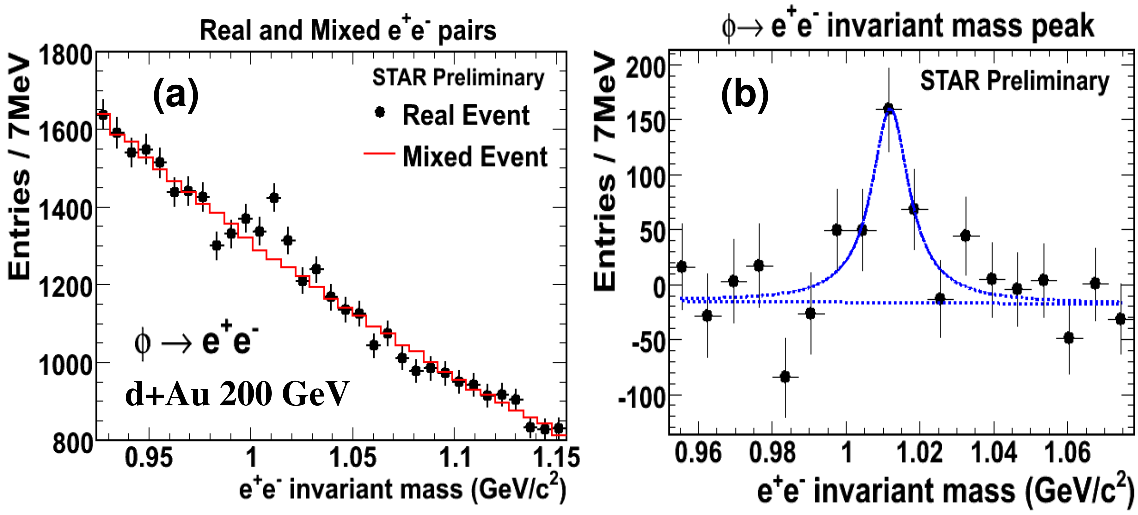

Figure 5.9: (a): Same-event and mixed-event e^+e^- invariant mass distribution in d+Au 200 GeV collisions. (b): The corresponding ϕ meson invariant mass peak after subtracting the background. Dashed curve shows a Breit-Wigner + linear background function fit.

reconstruction.

Fig. 5.9 shows the e^+e^- invariant mass distributions in d+Au 200 GeV collisions. Solid circles in the left panel are same-event pairs while the solid lines are from mixed-event. The ϕ meson peak is a little bit visible (Fig. 5.9(a)) before background subtraction, but not very clear due to its small signal significance. However, after background subtraction, the ϕ meson invariant mass peak can be seen clearly. The right panel in Fig. 5.9 shows the mixed-event background subtracted ϕ meson invariant mass distribution. Raw yields for the ϕ mesons reconstructed from e^+e^- decays are determined by similar method as shown for K^+K^- case, that is, fitting the background subtracted $m_{\rm inv}$ distribution in the appropriate range with a Breit-Wigner function superimposed on a linear (or polynomial) background function.

5.5 Acceptance and tracking efficiency correction

To get corrected ϕ meson yields one needs to simulate the detector acceptance and tracking efficiency. The ϕ meson acceptance and reconstruction efficiency are calculated using an embedding technique, in which simulated tracks are embedded into real events. The number of embedded simulated tracks is 1 ϕ meson for each event in d+Au 200 GeV collisions. The ϕ meson decay and the detector responses are simulated by the GEANT program package [221] and the simulated output signals are embedded into real events

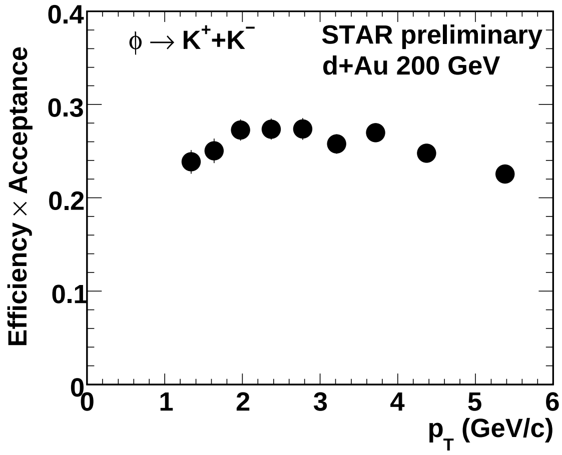

Figure 5.10: Reconstruction efficiency including acceptance of $\phi \rightarrow K^+ + K^-$ as a function of p_T in d+Au 200 GeV collisions.

before being processed by the standard STAR event reconstruction code. Embedded data are then analyzed to calculate tracking efficiencies and detector acceptance by dividing the number of reconstructed ϕ mesons by the number of input ϕ mesons in the desired kinematic regions. Fig. 5.10 shows an example of correction factors (tracking efficiency $\times$ acceptance) for our analysis as a function of ϕ meson p_T for $\phi \rightarrow K^+ + K^-$ reconstruction in d+Au 200 GeV collisions. It can be seen that the overall correction factor for ϕ meson with $p_T > 1$ GeV/c is $\sim 25\%$. The reconstruction efficiency drops at high p_T due to the δ-dip-angle cut.

5.6 Elliptic flow v_2 measurement

In this section we present the method used to measure the anisotropic flow parameter v_2 of ϕ meson [54,211,213]. In Ref. [52], it is shown that the particle emission with respect to the reaction plane angle can be described as Fourier series, that is,

$$E\frac{d^3N}{d^3p} = \frac{1}{2\pi}\frac{d^2N}{p_T dp_T dy}(1 + \sum_{n=1}^{\infty} 2v_n \cos[n(\varphi - \Psi_r)]), \tag{5.3}$$

where Ψ_r is the real reaction plane angle and φ is the particle's azimuthal angle. The coefficient v_2 in the second order term of the expansion is the dominant part and is called the 2nd harmonic anisotropic flow parameter, or elliptic flow.

The real reaction plane is not known, but the event plane, an experimental estimator of the true reaction plane, can be calculated from the azimuthal distribution of primary tracks from TPC. In this analysis the estimated reaction plane angle from the second

Table 5.6: Selection criteria for flow tracks used in the event plane reconstruction

global dca	< 2 cm
Track Hit points	nHits > 15
Track Hit Points to Maximum Points Ratio	nHits/nMax > 0.52
Track Pseudo-Rapidity	$\|\eta\| < 1.0$
Track Transverse Momentum	$0.1 < p_T < 2.0$ GeV/c

order harmonic (Ψ_2) is used. For experiments at RHIC energies—unlike those at lower energies—the reaction plane is assumed to be transverse to the beam axis. As such, since it is not necessary to rotate the flow coordinate system in the polar direction, only the transverse direction is considered. The error introduced by this assumption will go as the square of the polar flow angle, $\theta_{\text{flow}} \sim < p_x > /p_{\text{beam}} \ll 1$, and is negligible. Thus the event plane angle, (Ψ_2), can be calculated by the following equation

$$\Psi_2 = \frac{1}{2}\tan^{-1}(\frac{\sum_i w_i \sin(2\varphi_i)}{\sum_i w_i \cos(2\varphi_i)}), \tag{5.4}$$

where the sums are over all charged particles used for reaction plane determination, w_i and φ_i are the weight and azimuthal angle for the ith particle in a given event, respectively. The selection criteria for the primary tracks used to calculate the event plane is given in Table 5.6. The weights include both p_T-weight and φ-weight. The p_T weight is applied to improve the event plane resolution. It is taken to be the particle's p_T up to 2.0 GeV/c and constant (2.0) above that [52]. The acceptance and efficiency of the detectors in azimuth is corrected by compensating the azimuth to a flat distribution with φ weights. Technically, the φ weights are created for different running time and centralities to deal with the different situations in long period run. It is taken to be the reciprocal of the φ distribution (normalized by the average entries) for all selected tracks. The auto-correlations are eliminated by excluding both kaon tracks used in the ϕ meson invariant mass calculation from the reaction plane angle estimation [210].

There is a finite resolution due to a limited number of particles available in each event and a different event-by-event v_2, which is used for the reaction plane estimation. The estimated reaction plane resolution is used to correct the observed v_2^{obs} to obtain the final estimation of v_2.

The resolution of event plane is calculated through sub-event method [52]. Each event is divided into two sub-events with nearly equal multiplicity randomly. The event plane is reconstructed in each sub-event, denoted as Ψ_2^a and Ψ_2^b. Then the event plane resolution $r = \cos[2(\Psi_2 - \Psi_{\rm rp})]$ can be calculated from Eq.(14) and (11) from [52], which are shown as follows:

$$< \cos[2(\Psi_2 - \Psi_{\rm rp})] >= \frac{\pi}{2\sqrt{2}}\chi_2 \exp(-\chi_2^2/4) \times [I_0(\chi_2^2/4) + I_1(\chi_2^2/4)], \tag{5.5}$$

$$< \cos[2(\Psi_2^a - \Psi_{\rm rp})] >= \sqrt{< \cos[2(\Psi_2^a - \Psi_2^b)] >}, \tag{5.6}$$

where $\chi_2 \equiv v_2/\sigma = (v_2\sqrt{2N}$ for number flow) and I_1 is the first order modified Bessel function. Firstly, we obtain the sub-event resolution $< \cos[2(\Psi_2^a - \Psi_{\rm rp})] >$ from Eq. (5.6). Then using Eq. (5.5) applied on sub-event, we can extract the sub-event χ_2^a. The variable is proportional to $\sqrt{N}$, so the total event χ_2 was obtained by $\chi_2 = \sqrt{2}\chi_2^a$. And after putting this χ_2 into Eq. (5.5), we can calculate the final full event resolution. The physical v_2 is calculated as $v_2 = v_2^{obs}/r$. However, experimentally, what we observe is $< v_2^{obs} >$, the averaged v_2^{obs} over a data sample (particle wise), such as the minimum bias events. Then

$$< v_2 >=< \frac{v_2^{obs}}{r} >\approx (\text{but } \neq)\frac{< v_2^{obs} >}{< r >}. \tag{5.7}$$

This is not quite correct when we just divide the $< v_2^{obs} >$ by the event-wise averaged resolution $< r >$. Practically, we calculate a track-wise averaged resolution by weighting each event with the number of observed particles that used in v_2^{obs} calculation. As shown in Fig. 4.3 of Ref. [222], there is small difference between event-wise averaged and track-wise averaged event plane resolution for peripheral centrality bins. Fig. 5.11 presents the reaction plane resolutions in different centrality bins for Au+Au 200 GeV collisions. The minimum bias resolution (0-80%, centrality -1 in Fig. 5.11) are weighted by ϕ meson raw yields.

v_2^{obs} of ϕ meson is extracted by the invariant mass method. The method was proposed in Ref. [223], which decomposes the anisotropic flow (v_n) of short-lived particle from that of all possible daughter pairs as a function of invariant mass. For extracting the v_2 of ϕ meson, it utilizes the fact that the v_2 of K^+K^- pairs is composed of the v_2 of combinatorial background and the v_2 of ϕ meson. Following the mixed event background subtraction procedure described in section 5.3.2, the number of K^+K^- pairs in each invariant-mass bin are counted, irrespective of the pair azimuth. Then

$$N_{K^+K^-}(m_{\rm inv}) = N_\phi(m_{\rm inv}) + N_B(m_{\rm inv}), \tag{5.8}$$

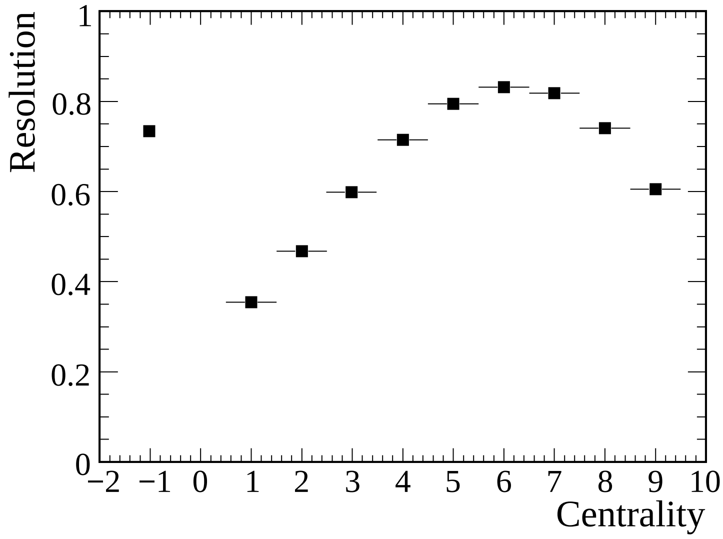

Figure 5.11: Event plane (Ψ_2) resolution as a function of centrality (centralities 1 to 9 are from peripheral (70-80%) to central collisions (0-5%) as defined in Table 5.3) in Run 7 Au+Au 200 GeV collisions. The minimum bias resolution (0-80%, centrality -1 in this plot) are weighted by ϕ meson raw yields.

where N_ϕ and N_B are from ϕ meson signal and the background respectively. Once N_ϕ has been extracted via event-mixing and subsequent fitting of ϕ meson invariant mass distribution with Eq. (5.2) for each p_T bin (see section 5.3.2), N_B can be obtained from Eq. (5.8). It is shown in Fig. 5.12 the ϕ meson invariant mass peaks after subtracting the mixed-event background at different p_T for Run 7 Au+Au 200 GeV collisions (0-80%). The invariant mass peak after background subtraction is prominent and can be well described by the Breit-Wigner + linear/polynomial background function. From the fitting, we can get $N_\phi(m_{\rm inv})$ and $N_B(m_{\rm inv})$.

The same-event v_2 for K^+K^- pairs versus invariant mass can be described by the equation [211]

$$v_2(m_{\rm inv}) = a(m_{\rm inv})v_{2S} + [1 - a(m_{\rm inv})]v_{2B}(m_{\rm inv}), \tag{5.9}$$

where $v_2(m_{\rm inv})$ is the v_2 of same-event K^+K^- pairs, $v_{2S} \equiv v_{2\phi}$ is the v_2 of the ϕ meson, v_{2B} is the effective v_2 of the combinatorial background and $a(m_{\rm inv}) = N_\phi(m_{\rm inv})/N_{K^+K^-}(m_{\rm inv})$ is the ratio of ϕ signal to the sum of background and ϕ signal. The reaction plane angle, Ψ_2, was estimated according to Eq. (5.4). $v_2(m_{\rm inv})$ can then be calculated from the following equation for each $v_2(m_{\rm inv})$ bin,

$$v_2(m_{\rm inv}) =< \cos[2(\varphi_{KK} - \Psi_2)] >, \tag{5.10}$$

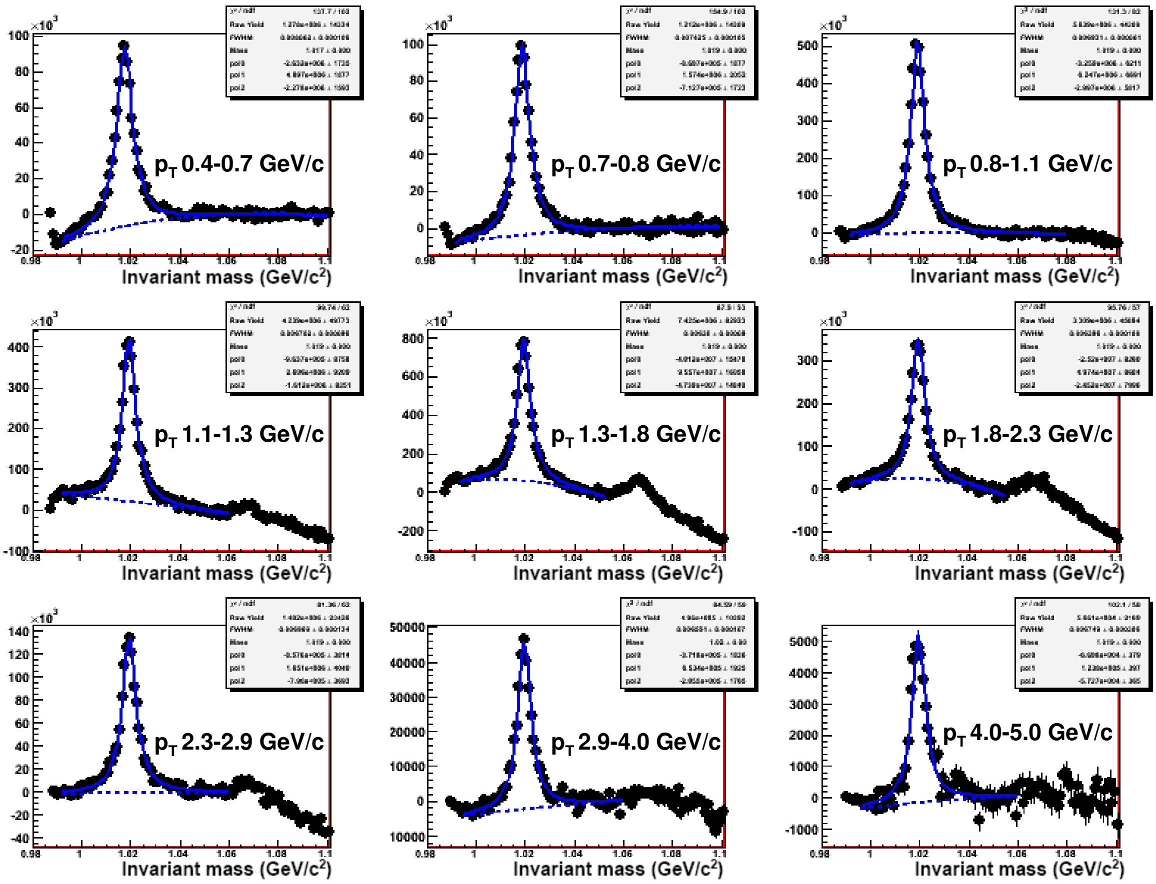

Figure 5.12: ϕ meson invariant mass peaks after subtracting the mixed-event background at different p_T for Run 7 Au+Au 200 GeV collisions (0-80%). Solid curves show a Breit-Wigner + linear/polynomial background function fit.

where φ_{KK} is the azimuthal angle of the K^+K^- pair.

Under the assumption that the background contribution to $v_2(m_{\rm inv})$ (the second part on right side of Eq. (5.9)) is smooth as a function of $m_{\rm inv}$ [223], a polynomial function, $p_0 + p_1 m_{\rm inv} + p_2 m_{\rm inv}^2 + p_3 m_{\rm inv}^3$, can be used to parameterize the background v_{2B} versus $m_{\rm inv}$. v_{2S} was then obtained by fitting $v_2(m_{\rm inv})$ by Eq. (5.9) in each p_T bin, with v_{2S} as a free parameter. Figure 5.13 shows $< \cos[2(\varphi_{KK} - \Psi_2)] >$ (that is, $v_2(m_{\rm inv})$ in Eq. (5.10)) versus $m_{\rm inv}$ at different p_T in Au+Au 200 GeV collisions (0-80%), where the solid curve is the result of fitting by Eq. (5.9). The decrease of $< \cos[2(\varphi_{KK} - \Psi_2)] >$ around ϕ meson invariant peak ($m_{\rm inv}$ = 1.01946 GeV/c^2) is due to relatively small ϕ meson v_2 compared to the v_2 of background K^+K^- pairs in the same p_T range. Besides the v_2 difference between $v_{2\phi}$ and v_{2B}, the signal to background ratio also strongly affects the uncertainty of $v_{2\phi}$ extraction (i.e., the error bar $\sigma(v_{2\phi}) \propto 1/a(m_{\rm inv})$). At the same time, $< \sin[2(\varphi_{KK} - \Psi_2)] >$ vs. $m_{\rm inv}$ is found, as expected, to be consistent with zero

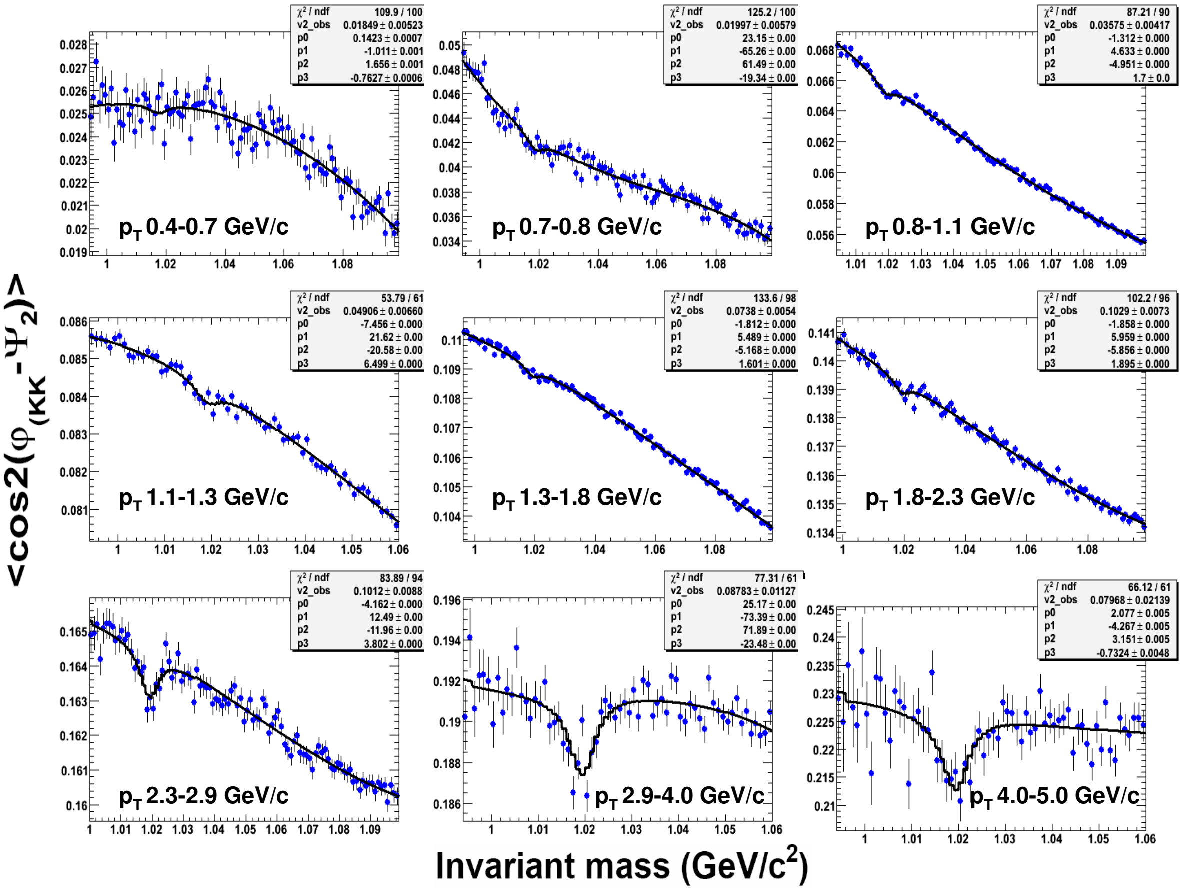

Figure 5.13: $<\cos[2(\varphi_{KK}-\Psi_2)]>$ (solid circles) as a function of $m_{\rm inv}$ of K^+K^- pairs at different p_T in Au+Au 200 GeV collisions (0-80%), where the solid curve is the result of fitting by Eq. (5.9).

due to collisional geometry symmetry [52]. Then the v_{2S} value (i.e. v_2^{obs} in Eq. (5.7)) determined by the fit is corrected for the reaction plane resolution to obtain the final v_2 of ϕ meson. The final v_2 results and related discussions will be presented in the following section 6.3.

Chapter VI Results and implications from ϕ meson production at RHIC

I start this chapter with presenting theoretical insights on particle species dependence of Cronin effect by our transport model calculations [224] in section 6.1. In the followed section, our experimental results on ϕ meson production in year 2008 d+Au 200 GeV collisions at RHIC [212,214,215] will be presented and compared with theoretical expectations. The implications on particle species dependence of Cronin effect will be discussed. Finally, the ϕ meson elliptic flow results in year 2007 Au+Au 200 GeV collisions [213] and their indications will be discussed in section 6.3.

6.1 Particle species dependence of Cronin effect — theoretical insights with transport model — final state hadronic interactions

6.1.1 The AMPT model

Firstly, I briefly introduce the AMPT model which is used for calculations [224]. The AMPT (A Multi-Phase Transport) model [62, 92] is a hybrid model that consists of four main components: the initial conditions, the partonic interactions, conversion from the partonic to the hadronic matter, and the hadronic interactions. The initial conditions, which include the spatial and momentum distributions of hard minijet partons and soft string excitations, are obtained from the HIJING model (version 1.383 for this study) [91]. One uses a Woods-Saxon radial shape for the colliding gold nuclei and introduces a parameterized nuclear shadowing function that depends on the impact parameter of the collision. The ratio of quark structure function is parameterized as the following impact-parameter-dependent but Q^2 (and flavor)-independent form [62]

$$
\begin{aligned}
R_A(x,r) &\equiv \frac{f_a^A(x,Q^2,r)}{Af_a^N(x,Q^2)} \\
&= 1 + 1.19\ln^{1/6} A(x^3 - 1.2x^2 + 0.21x) \\
&\quad -[\alpha_A(r) - \frac{1.08(A^{1/3}-1)\sqrt{x}}{\ln(A+1)}]e^{-x^2/0.01},
\end{aligned}
\tag{6.1}
$$

where x is the light-cone momentum fraction of parton a, and f_a is the parton distribution function. The impact-parameter dependence of the nuclear showing effect is controlled by

$$\alpha_A(r) = 0.133(A^{1/3} - 1)\sqrt{1 - r^2/R_0^2}, \tag{6.2}$$

with r denoting the transverse distance of an interacting nucleon from the center of the nucleus with radius $R_0 = 1.2A^{1/3}$. The structure of deuteron is described by the Hulthen wave function. Scatterings among partons are modeled by the Zhang's parton cascade (ZPC) [225], which at present includes only two-body elastic scatterings with cross sections obtained from the pQCD with screening masses. In the default AMPT model, after partons stop interacting, they recombine with their parent strings, which are produced from initial soft nucleon-nucleon interactions. The resulting strings are converted to hadrons using the Lund string fragmentation model [89, 90]. In case of string melting, the produced hadrons from string fragmentation, are converted instead to their valence quarks and antiquarks. The followed partonic interactions are modeled by ZPC. After the partons freeze out, they are recombined into hadrons through a quark coalescence process. The dynamics of the subsequent hadronic matter is described by a hadronic cascade, which is based on a relativistic transport model (ART) [226]. Final hadronic observables including contributions from the strong decays of resonances are determined when the hadronic matter freezes out.

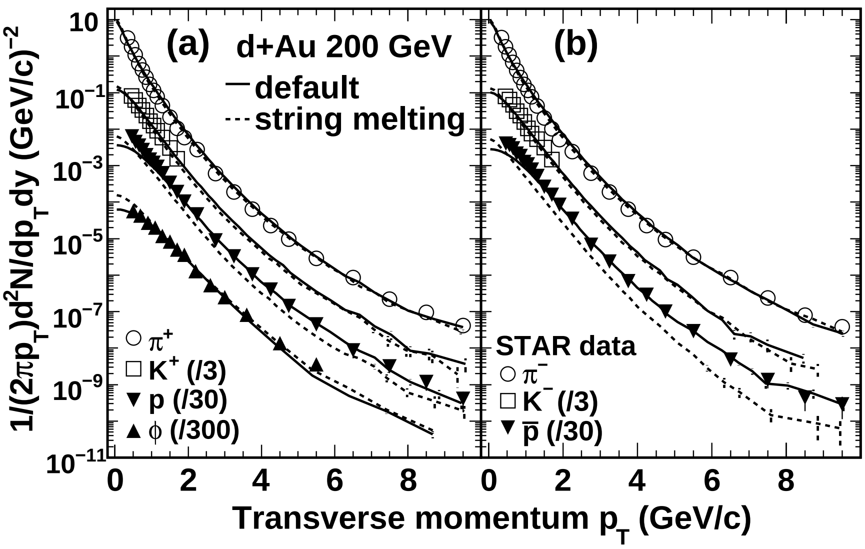

Figure 6.1: Transverse momentum spectra of mid-rapidity ($|y| < 0.5$) pions, kaons, protons and ϕ mesons in "minimum bias" d+Au collisions from default AMPT (solid lines) and string melting AMPT (dashed lines) versus data from STAR Collaboration (statistical error only) [73, 211].

6.1.2 Final state hadronic interactions on particle production in d+Au collisions at RHIC

We learn that Lin and Ko have done a nice study [92] on global properties of deuteron-gold collisions with default AMPT model, which shows good agreement with later experimental data [227,228]. Their study on nuclear effects is up to $p_T = 2$ GeV/c. Here we focus on the intermediate to higher p_T range where the Cronin effect exists. We study the deuteron-gold collisions at $\sqrt{s_{NN}} = 200$ GeV. The string fragmentation parameters are chosen to be the same as in Ref. [92]. The partonic scattering cross section is chosen to be 3 mb. The events are separated into different centrality bins using the number of participant nucleons suffering inelastic collisions. Fig. 6.1 shows the mid-rapidity ($|y|$ <0.5) transverse momentum spectra of pions, kaons, protons and ϕ mesons for "minimum bias" d+Au collisions from default AMPT (solid line) and string melting (dashed line). It is seen that both default and string melting AMPT can reproduce the $\pi^{\pm}$ and $K^{\pm}$ spectra well. For proton and antiproton production, the default version works well for $p_T > 1$ GeV/c, but underestimates the low p_T proton and antiproton yields. The string melting version underestimates the proton and antiproton production in the whole p_T range. For ϕ meson spectrum, the default version works well in the whole p_T range, while the string melting one overestimates the low p_T ϕ meson yields in the "minimum bias" d+Au collisions.

To study the final state effect on the nuclear modification factor R_{CP}, we first calculate the R_{CP} (0-20%/40-100% centrality) of different hadrons without including the final state hadronic interactions and resonance decays in the default AMPT. The R_{CP}, which compares particle yield from central collisions to that of peripheral collisions, is defined as the ratio of particle yields in central collisions over those in peripheral ones scaled by number of inelastic binary collisions $N_{\rm bin}$, that is,

$$R_{CP} = \frac{[dN/(N_{bin}p_T dp_T)]_{\rm central}}{[dN/(N_{bin}p_T dp_T)]_{\rm peripheral}}. \tag{6.3}$$

Here we use the same N_{bin} value as STAR Collaboration at the corresponding collision centrality [73]. One can see in Fig. 6.2(a) that there are only slight differences for the R_{CP} of different particle species. This is because hadrons are produced from string fragmentation in the Lund model, and the fragmentation patterns for different particle species in central collisions and in peripheral collisions are set to be the same. We note that the R_{CP} of proton and Λ would be larger due to the associate production N+N $\rightarrow$ N+Λ+K^+ from initial-state multiple scatterings in the gold beam direction

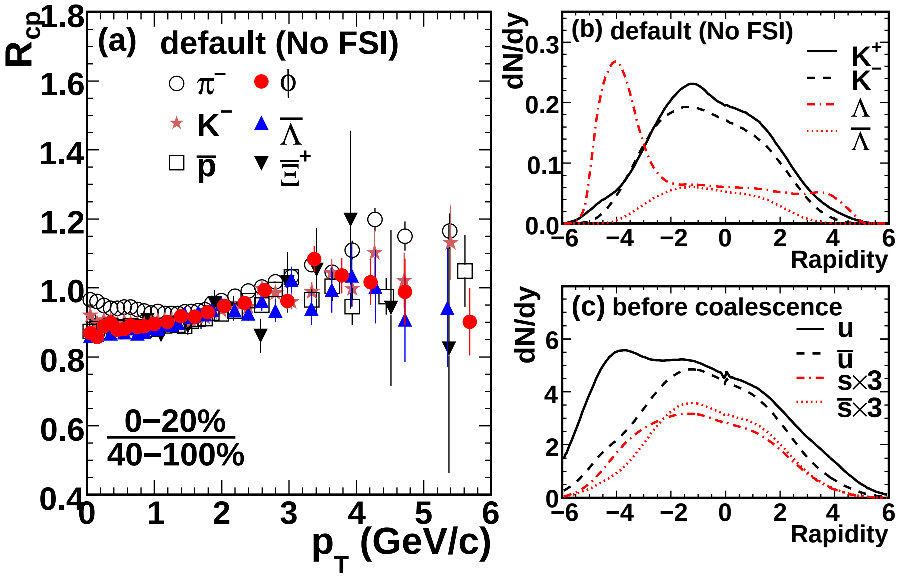

Figure 6.2: (a) R_{CP} for π^-, K^-, $\bar{p}$, ϕ, $\overline{\Lambda}$ and $\overline{\Xi}^+$ in d+Au $\sqrt{s_{NN}}$ = 200 GeV collisions from default AMPT without final state interactions included. (b) Kaon and Λ rapidity distribution in "minimum bias" d+Au collisions from default AMPT without final state interactions included. (c) quark (u, $\bar{u}$, s, and $\bar{s}$) rapidity distribution before coalescence in "minimum bias" d+Au collisions from string melting AMPT.

($y < 0$) at large rapidity, as shown in Fig. 6.2(b) the enhanced production of Λ and K^+ in "minimum bias" d+Au collisions. Some of the particles are scattered into mid-rapidity region. The strange quark enhancement in the large rapidity region (gold beam direction) will cause the corresponding increase of $\bar{s}$ quark at other rapidity regions due to net strangeness conservation. This is shown in Fig. 6.2(c): the quark rapidity distribution before coalescence in "minimum bias" d+Au collisions from the string melting AMPT.

After including the final-state hadronic interactions and strong decays of resonances, the R_{CP} of different particle species will change differently, as they have different masses and scattering cross sections. We show in Fig. 6.3 the comparisons of R_{CP} with and without the final state rescatterings and resonance decays. For π^- and K^-, the R_{CP} decreases after including the final state interactions from intermediate to high p_T. And this suppression increases with p_T. Since most of the produced particles are pions at mid-rapidity, the scatterings are mainly the particle-pion interactions for $p \gg m_0$, where m_0 is the mass of corresponding particles. For $\pi - \pi$ elastic collisions, the resonance peak centers at the position of $\pi - \pi$ center-of-mass energy $\sqrt{s_{\pi\pi}}$ close to ρ meson rest mass. Since most of the outgoing particles which probably scatter with each other

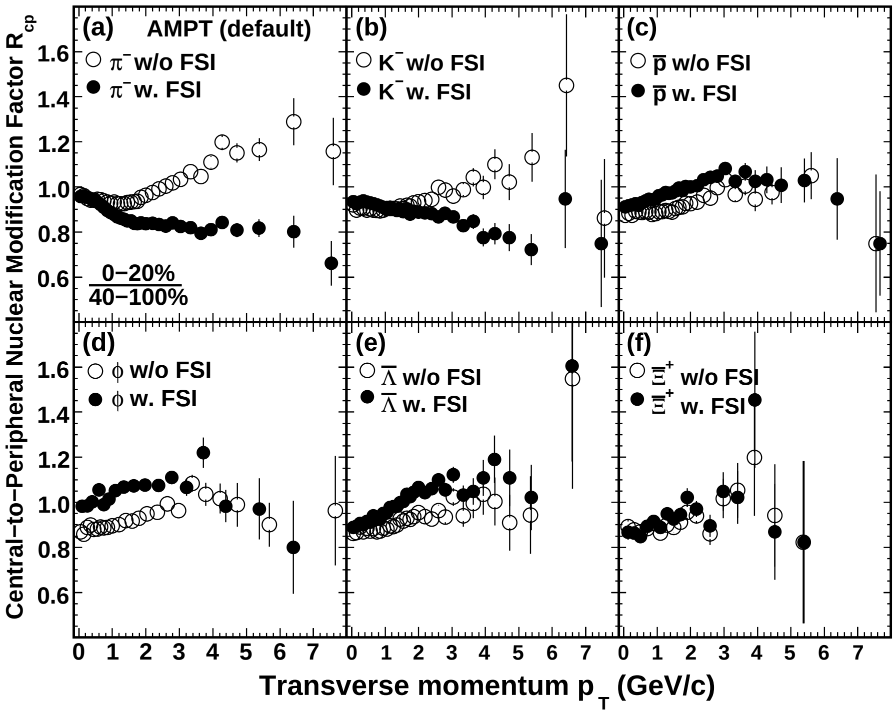

Figure 6.3: Mid-rapidity R_{CP} ($|y| < 0.5$) in d+Au $\sqrt{s_{NN}} = 200$ GeV collisions from default AMPT with (red circles) and without (black circles) final state interactions.

are in the similar directions, the open angle between two scattering particles is small. In our studied p_T and rapidity range, for one particle at low p_T, and another particle with higher energy, the calculated $\sqrt{s_{\pi\pi}}$ is closer to the resonance peak. As a result, this hadronic effect on R_{CP} is enhanced with p_T for pion. Similar argument is also valid for K$-\pi$ scatterings. For heavier particles like antiproton, ϕ meson, $\overline{\Lambda}$, the R_{CP} increases at low p_T according to their corresponding production channels or due to diffusions into mid-rapidity region, but changes slightly for $p_T > 3$ GeV/c. For even heavier particle, like $\overline{\Xi}^+$, there is no obvious change of R_{CP} due to the final state interactions. Here particle mass plays important roles in the hadronic rescatterings. It will determine the space-time configuration of formed hadrons [229].

According to above analysis, the final state hadronic rescatterings will lead to particle mass dependence of R_{CP}. In Fig. 6.4, we compare the data with model calculations. At intermediate p_T, the R_{CP} of heavier particles like antiproton, ϕ meson, $\overline{\Lambda}$, $\overline{\Xi}^+$ will be larger than those of π^- and K^-. The result is qualitatively consistent with experimental data [73], as shown in Fig. 6.4(c). At intermediate p_T, the R_{CP} of antiproton is systematically larger than that of π^-. In Fig. 6.4(d), the ratio $R_{CP}(\bar{p})/R_{CP}(\pi^-)$ from the default AMPT model also agrees very well with experimental data. We note that

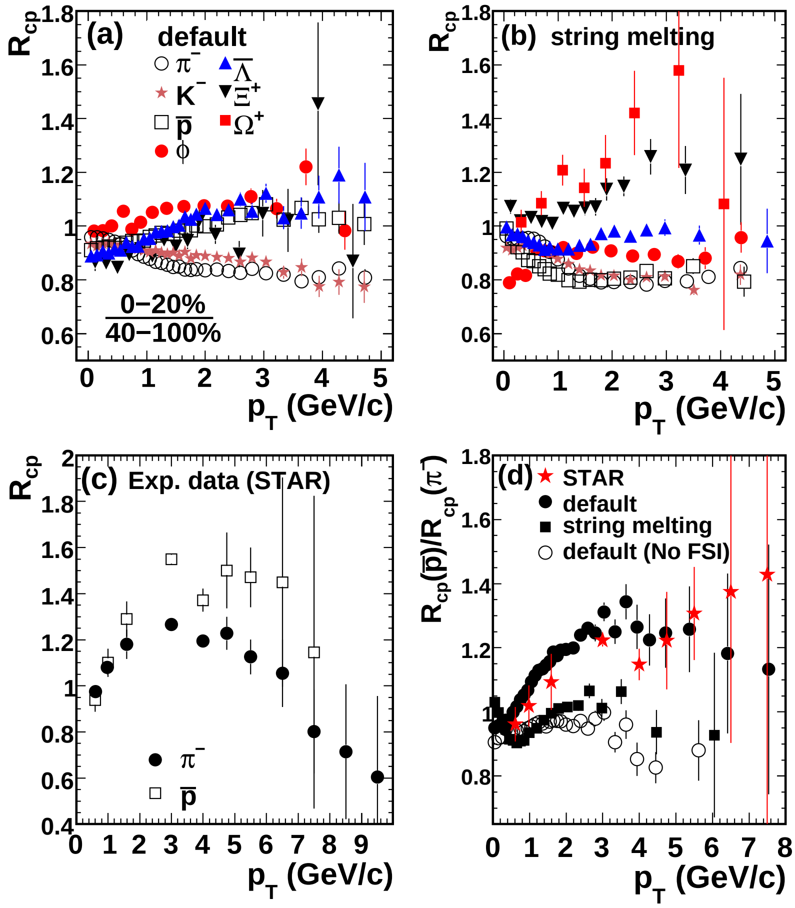

Figure 6.4: Mid-rapidity ($|y| < 0.5$) R_{CP} in d+Au $\sqrt{s_{NN}} = 200$ GeV collisions: (a) default AMPT with final state interactions; (b) string melting AMPT with final state interactions; (c) experimental data of R_{CP} from STAR Collaboration (statistical error only) [73]. (d) The ratios of $R_{CP}(\bar{p})/R_{CP}(\pi^-)$ from STAR Collaboration, from default AMPT, from string melting AMPT, and from default AMPT without final state interactions.

the present calculation without including the possible quark intrinsic p_T broadening at initial state can not reproduce the p_T dependence of R_{CP}. This difference between data and model results may indicate that the initial state effect is important. The year 2008 data of RHIC with higher statistics will provide more precise measurements and test our predictions for other hadron species like ϕ meson, $\overline{\Lambda}$, $\overline{\Xi}^+$, etc.

For comparisons, the R_{CP} from string melting AMPT with quark coalescence is also studied. We have shown in Fig. 6.2(c) that the excess of $\bar{s}$ quark over s quark at mid-rapidity is partly due to associate production from initial multiple interactions. Combining this effect with the coalescence of partons, there are enhancements of corresponding hadrons at intermediate p_T. The R_{CP} values for different particle species that contain different number of $\bar{s}$-quarks are shown in Fig. 6.4(b). Note, multi-strange hadrons are particularly interesting as they suffer much less hadronic interactions [63] compared with non-strange hadrons. Therefore they are more sensitive to early stage dynamics. At intermediate p_T, there is an enhancement of R_{CP} according to the number of $\bar{s}$ quarks, that is, $R_{CP}(\overline{\Lambda}) < R_{CP}(\overline{\Xi}^+) < R_{CP}(\overline{\Omega}^+)$. Note that the values of R_{CP} for strange particles (Λ, Ξ, and Ω) are close to each other (not shown here) at the same transverse momentum region. If one assumes the validity of the coalescence approach, this observation shows that the measured R_{CP} can, to some extend, reflect the density of quarks shortly before the freeze-out. However, from the coalescence calculation the R_{CP} of antiproton is close to that of π^- at intermediate p_T, which is not consistent with experimental data, as shown in Fig. 6.4(d).

In summary, we studied the mechanism of hadron formation and subsequent interactions in d+Au collisions at $\sqrt{s}$ = 200 GeV. In a multiphase transport model with Lund string fragmentation for hadronization and the subsequent hadronic rescatterings included, we find particle mass dependence of central-to-peripheral nuclear modification factor R_{CP}. The AMPT calculation indicates the suppression of low mass particles (pions and kaons) at large p_T during the final-state hadronic rescatterings, thus results in the observed particle species dependence of R_{CP} in d+Au collisions at RHIC. This shows the importance of final state hadronic interactions in d+Au collisions, since none of the initial-state models would predict a species-dependent R_{CP} at present.

However, the calculations can not reproduce the p_T dependence of R_{CP} with only final state interactions, this indicates the initial state effects might be also important. Issues associated with the initial condition such as gluon saturation [230–234], parton intrinsic p_T broadening [75–80] and so on were not addressed here. The future more complete analysis should include these effects. In comparison, if the hadron is formed from quark coalescence, it is difficult to explain antiproton transverse momentum spectra and the particle species dependence of R_{CP} with AMPT model. On the other hand, the strangeness effect plays an important role. In the following section 6.2, we will test the findings here with STAR Run 8 d+Au data.

6.2 ϕ meson production and implications on Cronin effect in d+Au 200 GeV collisions

Our AMPT calculation [224] in above section (Sec. 6.1) shows that final-state hadronic interactions is important to understand the particle species dependence of hadron production in d+Au 200 GeV collisions at RHIC. The default AMPT model with string-fragmentation hadronization and final-state hadronic interactions included describes the observed difference between proton and pion central-to-peripheral nuclear modification factors (R_{CP}) well. As a result of the final-state hadronic rescatterings, the default AMPT model predicts that there is a hadron mass dependence of nuclear modification factors in d+Au collisions for $p_T > 2$ GeV/c, that is $R_{CP}(\pi^-) \sim R_{CP}(K^-) < R_{CP}(\overline{p}) \sim R_{CP}(\phi) \sim R_{CP}(\overline{\Lambda}) \sim R_{CP}(\overline{\Xi}^+)$.

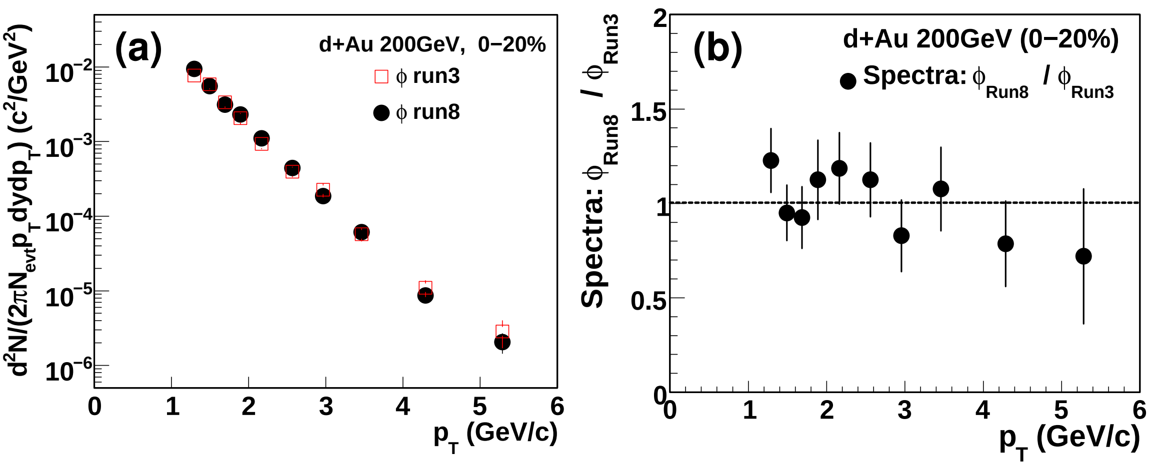

Figure 6.5: (a): ϕ meson transverse momentum distributions for d+Au (0-20%) collisions at 200 GeV from year 2008 (Run 8) data and year 2003 (Run 3) data [211]. (b) The ratios of ϕ meson yields from Run 8 and Run 3 versus transverse momenta.

On the other side, the coalescence model (see section 1.3.3.3) which considers the recombination of soft and shower partons in the final state could also explain different enhancements of high p_T protons and pions due to baryon (3 valence quarks) and meson (2 valence quarks) differences. ϕ meson is a very good probe to distinguish these two mechanisms of hadronization. Because ϕ is a heavy meson with mass close to the baryons $\overline{p}$ and $\overline{\Lambda}$. If ϕ meson at large p_T is from string fragmentation, then the nuclear modification factor of ϕ will be close to those of $\overline{p}$ and $\overline{\Lambda}$, and larger than those of π^- and K^-. If ϕ meson at large p_T is from coalescence of low p_T soft partons and higher

p_T shower partons, then we would expect the nuclear modification factor of ϕ meson to be close to those of π^- and K^-, and smaller than those of $\overline{p}$ and $\overline{\Lambda}$. In this section, we test the two different kinds of theoretical models by ϕ meson measurements in d+Au 200 GeV collisions at STAR.

6.2.1 Invariant transverse momentum spectra

Table 6.1: Invariant yields [$\frac{d^2N}{2\pi p_T dp_T dy}$ (c^2/GeV^2)] in d+Au 0-20% collisions from Run 8 at mid-rapidity ($|y| < 0.5$).

p_T (GeV/c)	Invariant yields (c^2/GeV^2)	p_T (GeV/c)	Invariant yields (c^2/GeV^2)
1.2-1.4	$(9.38 \pm 0.71) \times 10^{-3}$	1.2-1.5	$(7.92 \pm 0.49) \times 10^{-3}$
1.4-0.6	$(5.54 \pm 0.43) \times 10^{-3}$	1.5-1.8	$(4.09 \pm 0.29) \times 10^{-3}$
1.6-1.8	$(3.11 \pm 0.28) \times 10^{-3}$	1.8-2.2	$(1.86 \pm 0.15) \times 10^{-3}$
1.8-2.0	$(2.31 \pm 0.21) \times 10^{-3}$	2.2-2.6	$(7.00 \pm 0.53) \times 10^{-4}$
2.0-2.4	$(1.10 \pm 0.76) \times 10^{-3}$	2.6-3.0	$(2.93 \pm 0.27) \times 10^{-4}$
2.4-2.8	$(4.43 \pm 0.35) \times 10^{-4}$	3.0-3.5	$(1.22 \pm 0.11) \times 10^{-4}$
2.8-3.2	$(1.86 \pm 0.19) \times 10^{-4}$	3.5-4.0	$(4.04 \pm 0.49) \times 10^{-5}$
3.2-4.0	$(6.04 \pm 0.52) \times 10^{-5}$	4.0-5.0	$(8.48 \pm 0.13) \times 10^{-6}$
4.0-5.0	$(8.48 \pm 0.13) \times 10^{-6}$	5.0-6.0	$(2.02 \pm 0.60) \times 10^{-6}$
5.0-6.0	$(2.02 \pm 0.60) \times 10^{-6}$		

ϕ meson differential invariant yields are calculated by correcting the extracted raw yields by tracking efficiency, detector acceptance and the decay branching ratio. The invariant yields $\frac{d^2N}{2\pi p_T dp_T dy}$ are listed in Table 6.1. In Table 6.1, the left two columns and right two columns correspond to two different binning settings for the convenience of later comparisons with other collision systems. The analysis details are presented in Chapter 5. The transverse momentum distribution of ϕ mesons produced in d+Au 0-20% central collisions is plotted in Fig. 6.5(a). The spectra from year 2008 run (Run 8) are shown as solid circles, while the published spectra from year 2003 run (Run 3) [211] are shown as open squares for comparisons. One can see that the spectra from Run 8 are consistent with those from Run 3 for d+Au 0-20% central collisions when $p_T > 1.2$ GeV/c. This can be further justified by looking at the ratios between spectra from Run 8 and those from Run 3. As shown in Fig. 6.5(b), the ratios are consistent with unity within statistical error bar. It is good to see that with a factor of 3 higher statistics and with inner trackers (SSD and SVT) removed in Run 8, the spectra with $p_T > 1.2$ GeV/c are consistent with Run 3 in which the inner trackers were present.

6.2.2 Nuclear modification factor

In relativistic ion collisions, it is found that the produced charged particle multiplicity scales with number of participating nucleons (N_{part}) [235]. Since the measured total charged particle multiplicities are completely dominated by the emission of low p_T (≤ 1.5 GeV/c) particles, one might speculate that the production of low p_T (soft) particles is dominated by N_{part}. On the other hand, the high p_T particles are believed to be produced mainly from the initial QCD hard scattering processes (with large momentum transfer) followed by parton fragmentation. In the absence of parton-medium interaction, the production of high p_T particles should scale with number of binary collisions (N_{bin}). The soft particles are used to study the bulk properties like strangeness enhancement, particle ratio and various fluctuations and correlations, and so on. The high p_T particles can be used as good probes for studying the interaction of partons with the hot dense medium in Au+Au collisions or with the cold nuclear matter in d+Au collisions. A widely used observable for this study is the nuclear modification factor R_{AB} which is the ratio of the spectra in ion (A+B) collision and those in p+p collisions, scaled by the number of binary nucleon-nucleon collisions:

$$R_{\mathrm{AB}}(p_T) = \frac{d^2N_{\mathrm{AB}}/dp_T dy}{d^2\sigma^{\mathrm{pp}}/dp_T dy}; \tag{6.4}$$

where $T_{\mathrm{AB}} = N_{\mathrm{bin}}/\sigma_{pp}^{inel}$ is the nuclear overlap geometry factor, calculated from a Glauber model [58]. In the absence of parton-medium interaction in nuclear-nuclear collision, the R_{AB} should be consistent with unity. Another quantity, so called central-to-peripheral nuclear modification factor R_{CP}, which compares the particle yields in central collision and those in peripheral collision, is defined as

$$R_{CP} = \frac{[dN/(N_{\mathrm{bin}} p_T dp_T)]_{\mathrm{central}}}{[dN/(N_{\mathrm{bin}} p_T dp_T)]_{\mathrm{peripheral}}}. \tag{6.5}$$

To study the possible nuclear modification, we first compare the spectra shapes in different collision systems at $\sqrt{s_{NN}} = 200$ GeV (Au+Au 0-5% central, d+Au 0-20% central and inelastic p+p collisions). The spectra are normalized by number of binary collisions (N_{bin}) and number of participant pairs ($N_{\mathrm{part}}/2$). N_{bin} and $N_{\mathrm{part}}/2$ are determined by Glauber model calculations [58]. The total inelastic cross section for p+p collisions at 200 GeV used in the Glauber model is $\sigma_{NN}^{inel} = 42$ mb. However, STAR only measures p+p non-singly diffractive (NSD) cross section which is $\sigma_{NN}^{inel} = 30.0 \pm 3.5$ mb. So the ratio $\sigma_{NN}^{NSD}/\sigma_{NN}^{inel}$ is used to scale our measured yields in NSD p+p collisions to inelastic p+p collisions. This is reasonable since singly diffractive interactions contribute predominantly to low p_T part, thus its impact on our measured ϕ yield at large p_T is negligible and the only correction needed is the overall normalization of the total cross section.

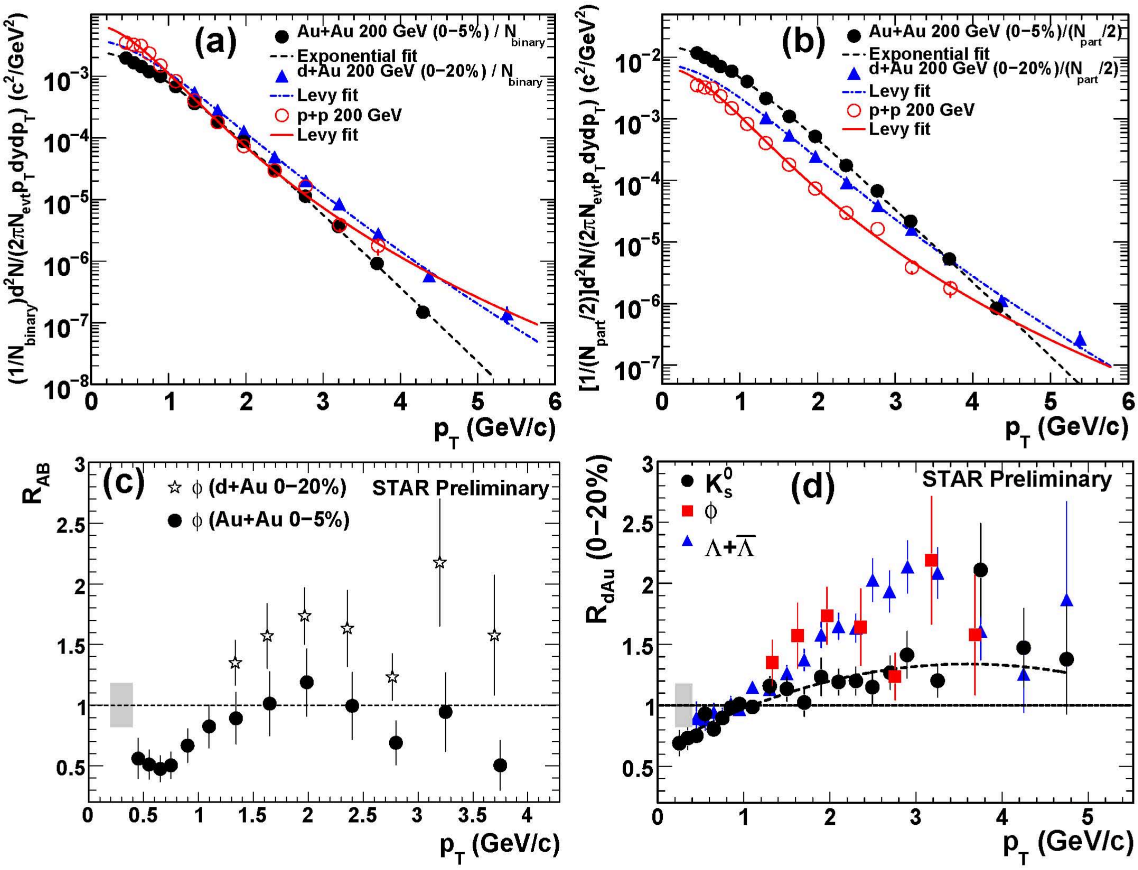

Figure 6.6: Comparison of transverse momentum spectra (mid-rapidity, $|y| < 0.5$) shapes among different reaction systems (Au+Au 200 GeV (0-5%) [211], d+Au 200 GeV (0-20%) and p+p 200 GeV [211] (inelastic)). The spectra are normalized by number of binary collisions ($N_{\rm bin}$) (a) and number of participant pairs (b). (c) ϕ meson nuclear modification factors in d+Au 200 GeV (0-20%) and Au+Au 200 GeV (0-5%) collisions [211]. (d) Particle species dependence of nuclear modification factors in d+Au 200 GeV (0-20%) collisions. STAR preliminary K_S^0 and $\Lambda + \overline{\Lambda}$ data are from Ref. [236]. The dashed lines are plotted for guiding the eyes.

A change in the shape of spectra from p+p to central d+Au and central Au+Au collisions is visible in Fig. 6.6(a). Compared to the p+p spectra at intermediate p_T region, the N_{bin} normalized yield is enhanced in d+Au central collisions (0-20%) at

200 GeV and the enhancement is larger than that in central (0-5%) Au+Au collisions at 200 GeV [211]. By plotting the spectra ratio (R_{AB}) in Fig. 6.6(c), one can see this difference clearly. This may suggest different effects of cold nuclear matter (d+Au collisions) and hot-medium (Au+Au collisions) on intermediate p_T ϕ meson production. From the extrapolation of p+p spectra to higher p_T, one can see in d+Au collisions, there is enhanced hadron production at intermediate p_T and $R_{dAu} \sim 1$ at large p_T, while in Au+Au collisions hadrons at large p_T are suppressed (Fig. 6.6(a)). One may argue that the final state hadronic rescatterings will increase dramatically with the increasing particle multiplicity in the final state, this may destroy the high p_T particles thus leads to the suppression in Au+Au central collisions. The advantage of ϕ meson is its presumably small hadronic cross sections with other non-strange particles, therefore the hadronic rescattering effect should be smaller than other particles like π and K mesons. It is also seen that the spectra in different collision systems can be described by different fitting functions [211]. In Au+Au central (0-5%) collisions, the spectra can be fitted with exponential function, that is,

$$\frac{d^2N}{2\pi p_T dp_T dy} = \frac{dN/dy}{2\pi T_{exp}(T_{exp}+m_0)} e^{-(\sqrt{p_T^2+m_0^2}-m_0)/T_{exp}}, \tag{6.6}$$

where the slope parameter T, and yield dN/dy, are free parameters. While in p+p and d+Au collisions, ϕ meson spectra can be better fitted with Levy function with the following form:

$$\frac{d^2N}{2\pi p_T dp_T dy} = \frac{dN/dy(n-1)(n-2)}{2\pi n T_{Levy}(nT_{Levy}+m_0(n-2))}(1+\frac{\sqrt{p_T^2+m_0^2}-m_0}{nT_{Levy}})^{-n}, \tag{6.7}$$

where the index n, the slope parameter T, and yield dN/dy, are free parameters. In fact, the exponential function (Eq. (6.6)) is the limit of the Levy function (Eq. (6.7)) as n approaches infinity, i.e. $T_{exp} = T_{Levy}(n \rightarrow \propto)$.

By scaling the spectra with number of participant nucleon pairs ($N_{part}/2$), one can clearly see the significant enhancement of low p_T ϕ meson yields in Au+Au collisions compared to those in p+p collisions. This indicates that the hot environment created by central Au+Au collisions favors the production of soft ϕ mesons [211].

The particle species dependence of nuclear modification factor R_{dAu} is shown in Fig. 6.6(d). One can see that R_{dAu} of $\Lambda+\overline{\Lambda}$ are larger than that of K_S^0. And ϕ meson seems to follow the trend of $\Lambda+\overline{\Lambda}$. It is shown in Fig. 6.7 the ratios between nuclear modification factor R_{dAu} of ϕ meson and those of K_S^0 and $\Lambda+\overline{\Lambda}$ in d+Au 200 GeV (0-20%) collisions. One can see from Fig. 6.7 that the ratios have no apparent p_T dependence

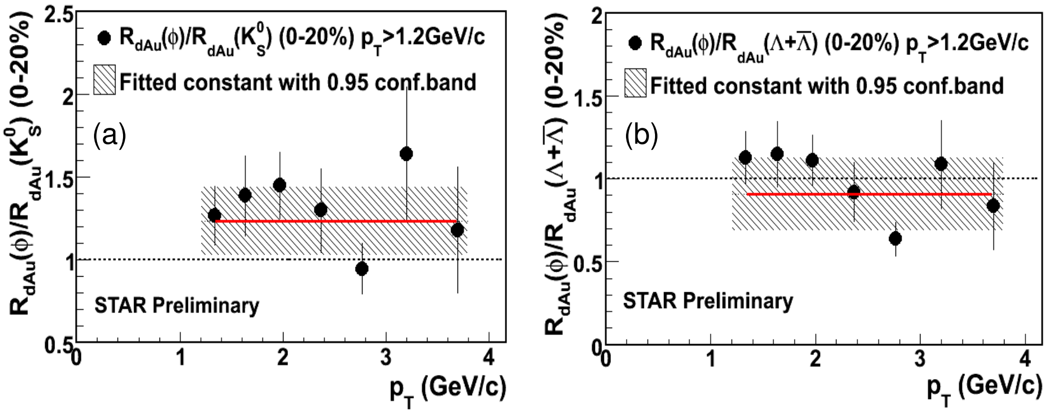

Figure 6.7: (a) The ratio between nuclear modification factor R_{dAu} of ϕ meson and that of K^0_S versus transverse momentum in d+Au 200 GeV (0-20%) collisions. The solid line is a constant fit to the ratios. The band corresponds to 95% confidence intervals of the constant fit. (b) Similar to (a), but for $R_{\mathrm{dAu}}(\phi)/R_{\mathrm{dAu}}(\Lambda+\bar{\Lambda})$. STAR preliminary K^0_S and $\Lambda+\overline{\Lambda}$ data are from Ref. [236].

for $1.2 < p_T < 4$ GeV/c. By a constant fit on the points within this p_T interval, we get the ratio $R_{\mathrm{dAu}}(\phi)/R_{\mathrm{dAu}}(K^0_S)$ to be 1.23 ± 0.08. This shows a larger enhancement of ϕ meson than that of K^0_S in this p_T region. Similarly, from the constant fit, the ratio $R_{\mathrm{dAu}}(\phi)/R_{\mathrm{dAu}}(\Lambda+\overline{\Lambda})$ is 0.91±0.06, which indicates a slightly smaller enhancement of ϕ meson than that of $\Lambda+\overline{\Lambda}$. The mass of ϕ meson is a little smaller than that of Λ ($\overline{\Lambda}$), while larger than that of K^0_S. This shows a likely particle mass dependence other than the baryon-meson difference of enhanced hadron productions in d+Au collisions. It is consistent with our AMPT calculation (default, hadronization from Lund string fragmentation) which indicates that the final state hadronic rescatterings and resonance decays are the origins of this particle mass dependence. On the other hand, we would expect baryon-meson difference from the quark coalescence model [81]. Besides the physical argument that the energy density in d+Au collisions may not be so high to allow for the "free" quarks to recombine, our experimental data do not favor the expectation of baryon-meson difference either.

Besides R_{dAu}, it is also plotted in Fig. 6.8 the p_T dependence of central-to-peripheral nuclear modification factors R_{CP} of ϕ meson, π^- and antiprotons in d+Au 200 GeV collisions. π^- and antiprotons are from STAR published results in Ref. [73]. Currently, the peripheral centrality (40-100%) in Run 8 d+Au collisions is not finalized yet. Run 3 (40-100%) ϕ meson spectra [211] are used as our reference. From Fig. 6.8 one can see the antiproton R_{CP} is larger than that of π^- at intermediate-large p_T. ϕ meson seems to follow the trend of antiproton for $p_T > 2$ GeV/c. Again, this supports the mass dependence of the enhanced hadron production at intermediate-large p_T which is qualitatively consistent with our AMPT calculations with hadronization from string fragmentation and final state hadronic rescatterings included.

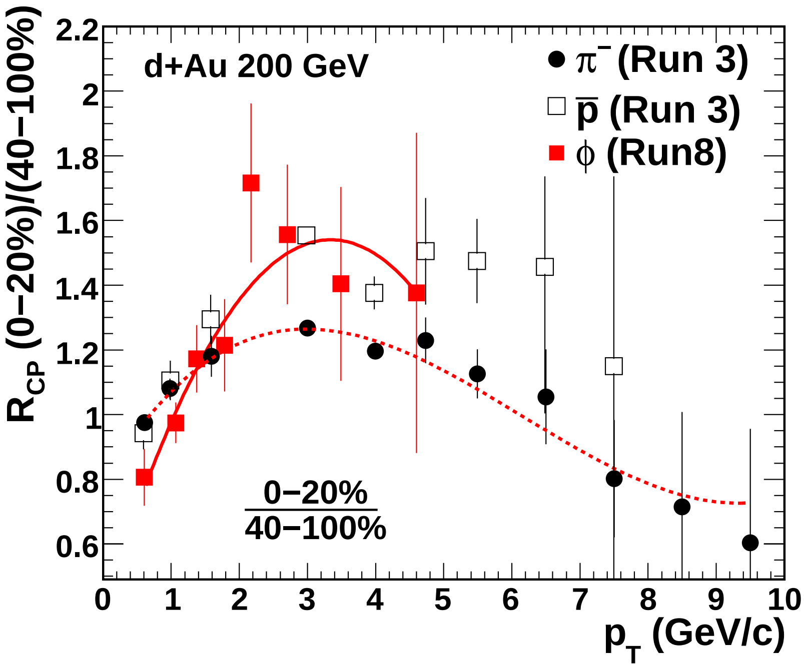

Figure 6.8: Central-to-peripheral nuclear modification factors $R_{\mathrm{CP}}(0-20\%/40-100\%)$ in d+Au 200 GeV collisions at mid-rapidity ($|y| < 0.5$). R_{CP} of π^- and antiprotons are from STAR Run 3 results [73]. The lines are for guiding eyes only.

6.2.3 Pseudo-rapidity asymmetry

Besides previous discussed hadronzation mechanisms and final state hadronic rescatterings, particle productions in d+Au collisions are also affected by different aspects in initial state: the initial parton distribution function, nuclear modification of the parton distributions inside a nucleus (nuclear shadowing effect), initial multiple scatterings, parton energy loss in cold nuclear matter, and so on. Models based on the color glass condensate [69, 233, 234], HIJING [238], multiphase transport (AMPT) [92] and parton coalescence [239] predict specific pseudorapidity (η) and particle species dependence of produced particle yields. The particle species dependence will shed light on the different hadronization mechanisms and final state hadronic interactions, while the particle production at forward and backward rapidities will help to constrain nuclear parton distribution function by enlarging our dynamic reach to small x region, here x is the fraction of momentum carried by the parton. A comparative study of particle production at forward and backward rapidity can be carried out using a ratio called the pseudo-rapidity asymmetry (η_{asym}), which is defined as

$$\eta_{\text{asym}}(p_T) = \frac{dN/d\eta^{\text{Back}}(p_T)}{dN/d\eta^{\text{Foward}}(p_T)}, \tag{6.8}$$

where $dN/d\eta^{\text{Foward}}$ and $dN/d\eta^{\text{Back}}$ are forward (deuteron beam direction, $\eta > 0$) and backward (gold beam direction $\eta < 0$) particle yields in unit pseudo-rapidity, respectively. η_{asym} may provide unique information for determining the relative contributions of various physics processes. By taking the ratio of particle yields in the same measurements, some systematical errors will be canceled out.

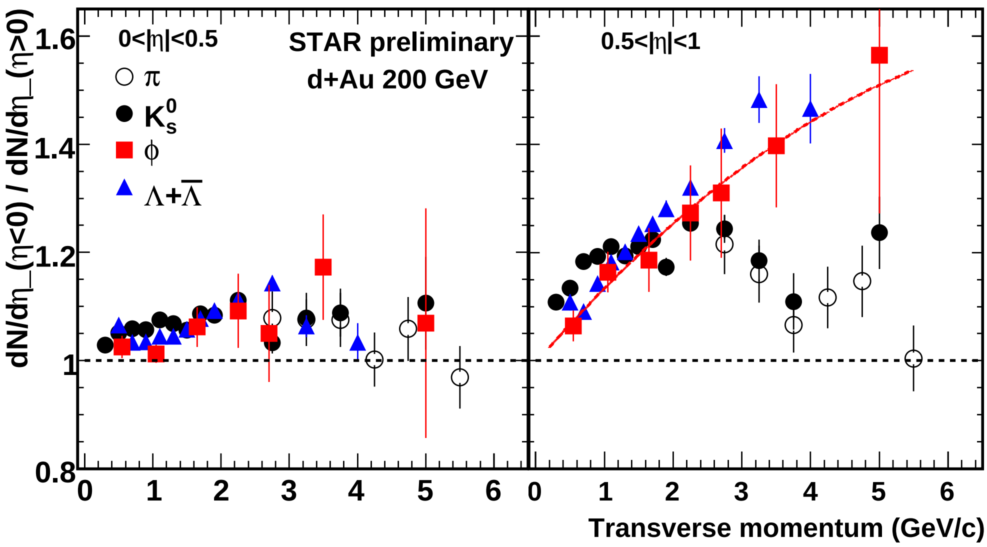

Figure 6.9: Pseudo-rapidity asymmetry (η_{asym}) of identified hadrons for $0 < |\eta| < 0.5$ (left panel) and $0.5 < |\eta| < 1$ (right panel) in d+Au 200 GeV collisions. $\pi^+ + \pi^-$ points are from STAR data of Run 3 in "minimum bias" d+Au collisions [237]. K_S^0 and $\Lambda + \overline{\Lambda}$ are STAR preliminary measurements in Run 8 [236]. Note that the centrality in Run 8 data set is not finalized yet (may not be "minimum bias"). For K_S^0, ϕ and $\Lambda + \overline{\Lambda}$, the error bars are statistical errors only.

Fig. 6.9 shows STAR measurements on pseudo-rapidity asymmetries of identified particles ($\pi^+ + \pi^-$, ϕ, K_S^0 and $\Lambda + \overline{\Lambda}$) in d+Au collisions at 200 GeV. $\pi^+ + \pi^-$ points are from STAR Run 3 data in "minimum bias" d+Au collisions [237]. K_S^0 and $\Lambda + \overline{\Lambda}$ data are from STAR preliminary measurements in Run 8 [236]. Note that the centrality determination in Run 8 d+Au collisions is not finalized yet (may not be "minimum bias" with 0-100%), it may be biased to central collisions. Although we do not know the centrality (0-X%) of Run 8 data set, however, one can compare the particle species dependence of the $\eta_{\rm asym}$. One can see from Fig. 6.9 that the $\eta_{\rm asym}$ increases with the η gap between forward and backward pseudo-rapidities, that is, $\eta_{\rm asym}$ of $0.5 < |\eta| < 1$ is larger than that of $0 < |\eta| < 0.5$. In the right panel of Fig. 6.9, one can clearly see a particle species dependence of $\eta_{\rm asym}$. The asymmetry of $\Lambda + \overline{\Lambda}$ is larger than that of K^0_S for $p_T > 3$ GeV/c. The $\eta_{\rm asym}$ of ϕ meson follows the trend of $\Lambda+\overline{\Lambda}$. At intermediate p_T, the data suggest a likely mass dependent $\eta_{\rm asym}$ other than a baryon-meson dependent one which is expected from the simple quark coalescence model [239]. This shows the similar likely mass dependence as observed for the nuclear modification factors.

To understand this mass dependence, we performed the AMPT calculations including different hadronization mechanisms: string fragmentation and parton coalescence. To study the effect of final-state hadronic interactions, we switch on/off the hadronic rescatterings and resonance decays after the formation of hadrons. The calculated $\eta_{\rm asym}$ for different hadrons are plotted in Fig. 6.10. It is shown in Figs. 6.10(a) ($0 < |\eta| < 0.5$) and 6.10(b) ($0.5 < |\eta| < 1$) the $\eta_{\rm asym}$ from default AMPT calculation with string fragmentation hadronization and subsequent hadronic interactions included. One can see that default AMPT can reproduce qualitatively the properties of measured $\eta_{\rm asym}$, for example, the larger $\eta_{\rm asym}$ with increased η gaps, and the mass-dependent $\eta_{\rm asym}$ at intermediate p_T. The quantitative comparisons with theoretical model will be performed once the centrality selection in Run 8 d+Au collisions is finalized.

In order to understand the effect of hadronic interactions in the final state, the default AMPT calculation in minimum bias d+Au 200 GeV collisions is also performed without including the hadronic rescatterings and resonance decays. The calculated $\eta_{\rm asym}$ ($0.5 < |\eta| < 1$) is shown in Fig. 6.10(c). One can see from Fig. 6.10(c) that there is no particle species dependence for $p_T > 1$ GeV/c in the absence of final state hadronic interactions. By comparing Figs. 6.10(b) and 6.10(c), one can see that the mass dependence is originated from the suppression of $\eta_{\rm asym}$ of $\pi^+ + \pi^-$ and $K^+ + K^-$ at large p_T. From the discussions in section 6.1.2, the transverse momentum of pions and kaons at large p_T are much easier to be changed by hadronic rescatterings. With higher particle multiplicity in backward pseudo-rapidity (gold beam direction), there will be more chances for the large-p_T pions and kaons to be suppressed at backward pseudo-rapidity via hadronic rescatterings.

For comparison, it is presented in Fig. 6.10(d) the results from another hadroniza-

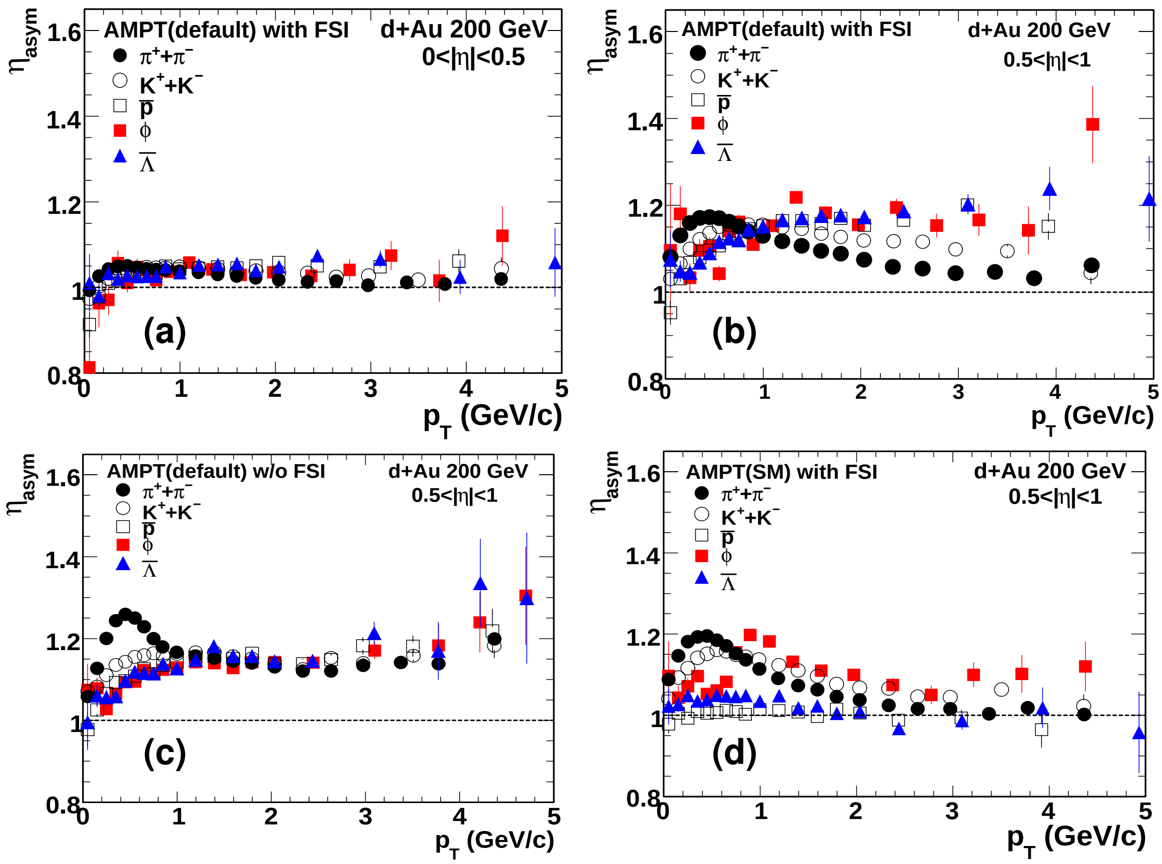

Figure 6.10: Pseudo-rapidity asymmetry (η_{asym}) in minimum bias d+Au 200 GeV collisions from AMPT model: (a) default AMPT with final-state hadronic interactions for $0 < |\eta| < 0.5$; (b) similar as (a), but for $0.5 < |\eta| < 1$; (c) default AMPT without final-state hadronic interactions for $0.5 < |\eta| < 1$; (d) string melting AMPT with final-state hadronic interactions.

tion mechanism (recombination of partons from string melting) in AMPT model. One can see that there is no strong particle species dependence of η_{asym} at intermediate p_T. This calculation is not consistent with our data.

In summary, we have studied the transverse momentum, centrality and pseudo-rapidity dependence of ϕ meson production in d+Au collisions at $\sqrt{s_{NN}} = 200$ GeV. Enhanced production of intermediate-p_T ϕ meson — with respect to binary collision scaling — have been observed in d+Au 200 GeV (0-20%) central collisions at mid-rapidity ($|y| < 0.5$). The ϕ meson yields are observed to be higher in the gold beam direction (backward pseudo-rapidity) than the deuteron beam direction (forward pseudo-rapidity) of the collisions. Ratios of ϕ-meson yields in backward pseudo-rapidity to those in forward pseudo-rapidity increase with ϕ-meson transverse momentum for p_T below 5 GeV/c. Compared to the enhancements of other identified hadrons K_S^0 and

$\Lambda + \overline{\Lambda}$, both nuclear modification factors and the pseudo-rapidity asymmetries seem to show the similar particle mass dependence. This is consistent with our transport model (AMPT) calculation which employs the string model with soft and coherent interactions for hadronization and includes the final-state hadronic rescatterings and resonance decays. The AMPT calculation indicates the suppressions of low mass particles (pions and kaons) at large p_T during the final-state hadronic rescatterings, which leads to the likely particle mass dependence of Cronin effect at RHIC energy ($\sqrt{s_{NN}} = 200$ GeV).

6.3 ϕ meson elliptic flow v_2 in Run 7 Au+Au 200 GeV collisions

It is discussed in section 1.3.4.3 that ϕ meson v_2 would provide important constrain on present various models. We can test these models by taking advantage of Run 7 data with a factor of ~ 5 higher statistics and provide insights into the real underlying physical process.

6.3.1 Centrality dependence

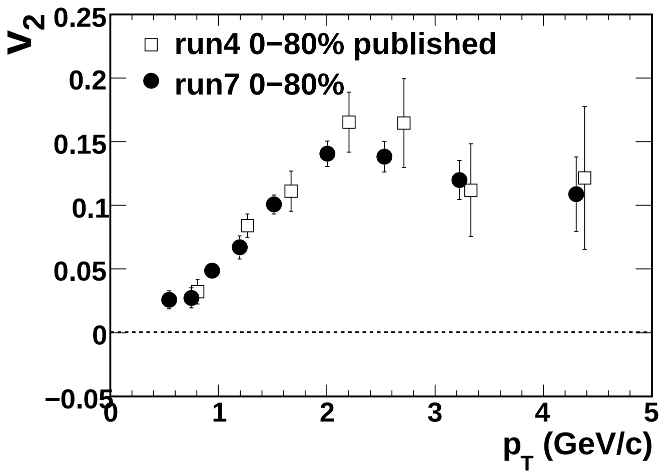

Figure 6.11: v_2 from Run 7 Au+Au 200 GeV collisions (0-80%) compared with that from Run 4 ones [54].

At first, a consistency check is performed by comparing with previous Run 4 published v_2 results [54]. It is seen from Fig. 6.11 that the measured ϕ meson v_2 in Run 7 Au+Au 200 GeV (0-80%) collisions is consistent with Run 4 published results with improved statistical uncertainties.

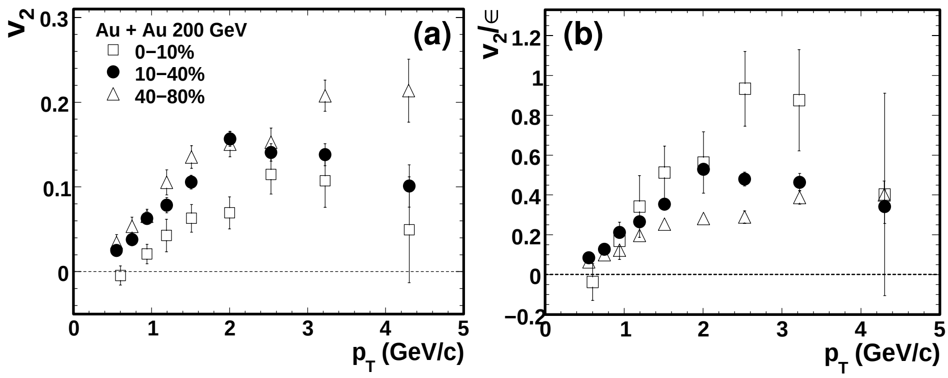

Figure 6.12: The ϕ-meson elliptic flow $v_2(p_T)$ (a) and $\varepsilon_{\rm part}$ scaled $v_2(p_T)$ (b) as a function of centrality.

The v_2 of the ϕ mesons from 3 centralities bins are shown in Fig. 6.12. The v_2 is extracted from the invariant mass method. 0-10% centrality corresponds to central collision where the initial geometric anisotropy is relatively smaller than that in peripheral collisions (40%-80%). We note that the initial geometry of the QCD matter is determined by the overlap region of two colliding nuclei. Generally, the two nuclei collide at finite impact parameter rather than head-on. In this case the initial geometry is not a disk, but is an "almond shaped" ellipse. (The short and long axes of the initial ellipse in transverse plane are taken as the x and y axes respectively.) The spatial anisotropy can be quantified by estimating the eccentricity ε of the initial source,

$$\varepsilon = \frac{< y^2 - x^2 >}{< y^2 + x^2 >} \tag{6.9}$$

Extracting the mean eccentricity $< \varepsilon >$ of the initial source for a given centrality interval is helpful for understanding the event-by-event anisotropy in the final state momentum distribution. One can see from Fig. 6.12(a) that the v_2 in mid-central (10-40%) and peripheral (40-80%) collisions is larger than that in central (0-10%) collisions. This is expected since in central collisions, the initial space anisotropy is smaller than that in peripheral collisions. To remove the effect of initial geometry, the v_2 is scaled by its initial geometry anisotropy from the participant nucleons (quantified as $\varepsilon_{\rm part}$). The $\varepsilon_{\rm part}$ scaled v_2 shows that the flow strength is larger in central Au+Au collisions compared to peripheral collisions. This is contradict to ideal hydrodynamic calculation in an equilibrium scenario, where little sensitivity to the collision centrality is expected. So the data suggest that in peripheral collisions the viscous effect from QGP (if there is) and final state hadronic dissipation should be taken into account and/or early-time local thermalization hypothesis should be re-evaluated.

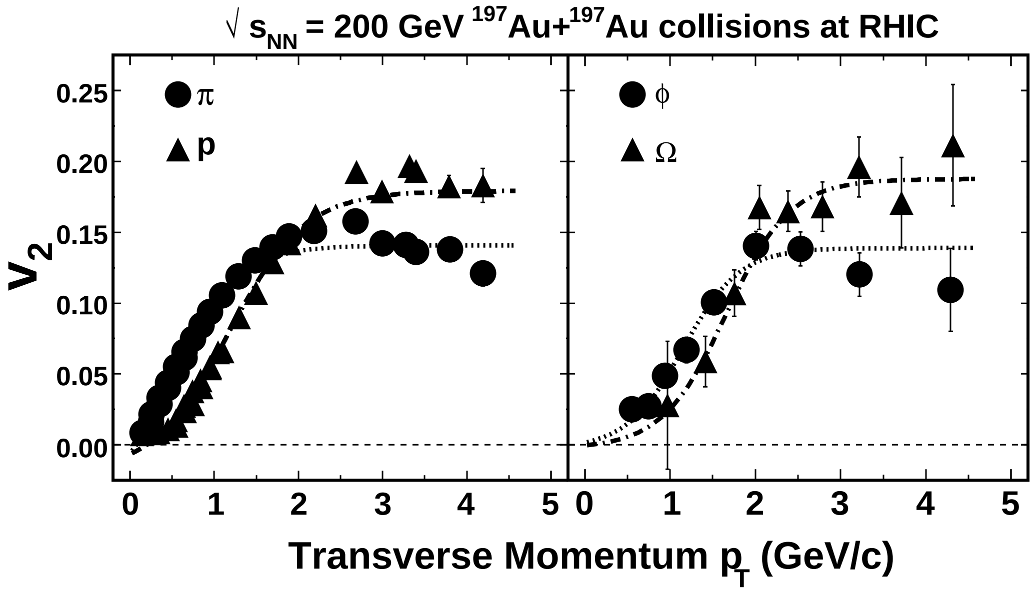

Figure 6.13: (a) The v_2 as a function of p_T for pions (circles) and protons (triangles) from STAR and PHENIX experiments (open symbols) [240] in “minimum bias” Au+Au collisions at $\sqrt{s_{NN}} = 200$ GeV. The “minimum bias” events are 0-80% for STAR and 0-92% for PHENIX. The bars show only statistical errors, and the errors are smaller than symbols for pions and protons. The dotted and dash dotted lines represent parameterizations inspired by number-of-quark scaling ideas from Ref. [57] for $n_q = 2$ and $n_q = 3$, respectively. (b) The same plot as (a) for ϕ meson (circles) and Ω (triangles). The Ω data are from Ref. [213].

6.3.2 Number-of-quark scaling for multi-strange hadrons

Fig. 6.13 shows the comparisons of v_2 as a function of p_T between (a) non-strange and (b) multi-strange hadrons in “minimum bias” Au+Au collisions at $\sqrt{s_{NN}} = 200$ GeV. The results of v_2 for pions and protons from the PHENIX experiment is also plotted in Fig. 6.13(a) for comparisons [240]. The v_2 of pions and protons are in good agreement between STAR and PHENIX in spite of the small difference of definitions of minimum bias events. The PHENIX v_2 is measured from event plane calculated from BBC hits with the pseudo-rapidity coverage $3 < |\eta| < 3.9$. STAR v_2 is measured from FTPC event plane with $2.5 < |\eta| < 4$. A large η gap between the measured particles at mid-rapidity and the particles used for event plane determination reduces the influence of possible non-flow contributions, especially those from dijets. The v_2 of ϕ and Ω are measured from event plane determined by TPC tracks with $|\eta| < 1$. For $1.5 < p_T < 5$ GeV/c, the non-flow contribution from STAR TPC event plane is about 10-15% for identified particles (pions, K_0^S, protons and Λ) [241] and with little p_T and particle species dependence. So the estimated non-flow contribution for ϕ and Ω is $\sim$10-15% for $1.5 < p_T < 5$ GeV/c. v_2 of ϕ and Ω above $p_T = 2$ GeV/c shows the same separation of mesons and baryons as that for pion and proton. We note that it is estimated that there are $\sim$ 10-15% non-flow contribution for ϕ and Ω measured from TPC event plane. Thus the "real" v_2 of ϕ and Ω may be 10-15% less for $1.5 < p_T < 5$ GeV/c. The dotted and dash dotted lines represent parameterizations inspired by number-of-quark scaling ideas from Ref. [57] for $n_q = 2$ and $n_q = 3$, respectively. It shows that the number-of-quark scaling works similarly well for multi-strange hadrons with only s valence quarks as for the hadrons (protons and pions) constituted by u and d valence quarks. Therefore the results provide evidence for u, d, and s quarks collectivity at RHIC within the framework of constituent quark coalescence model [242].

6.3.3 $m_T - m_0$ scaling and viscous hydrodynamics

Figure 6.14 shows the comparison of v_2 for π, K_S^0, proton, Λ [241] and ϕ in 10-40% Au+Au collisions at $\sqrt{s_{NN}} = 200$ GeV. The v_2 of all hadrons are measured from TPC event plane. From previous discussions, the non-flow effect has little PID dependence. Thus we can compare the relative magnitude of v_2 for different hadrons. In Fig. 6.14(a), the v_2 is plotted as a function of p_T. One can see that for $p_T > 2.5$ GeV/c, ϕ meson v_2 is systematically lower than those of pions and K_0^S, although they are all mesons. It is shown in Fig. 6.14(c) that the n_q scaling is a rough scaling. For $p_T/n_q > 1.5$ GeV/c, there seems to be 2 groups, π and K_S^0 versus Λ and ϕ. This is hard to understand within the framework of constituent quark coalescence model. It is expected that if the scaling breaks, then there would be meson-baryon dependent deviation. However, in our data, n_q scaled v_2 of ϕ meson follows that of Λ. If the hard process contributes to the produced hadrons in this p_T region, it is also difficult to understand the relatively smaller ϕ meson v_2. Since the strange quark production is suppressed in the fragmentation process due to its relatively larger mass than light quarks (u and d) [243], as a result the hard process contribution to the production of ϕ meson will be relatively smaller compared to non-strange particles, larger ϕ v_2 is expected due to relatively small v_2 of hard process. This expectation contradicts our observation.

If we plot the v_2 versus $(m_T - m_0)/n_q$ suggested by PHENIX collaboration [240], then there is a universal scaling for $(m_T - m_0)/n_q < 1$ GeV/c^2 for all particles. Approaching larger $(m_T - m_0)/n_q$, the scaling starts to break. The recently developed viscous hydrodynamic calculation by K. Dusling *et al.* [51] by considering species de-

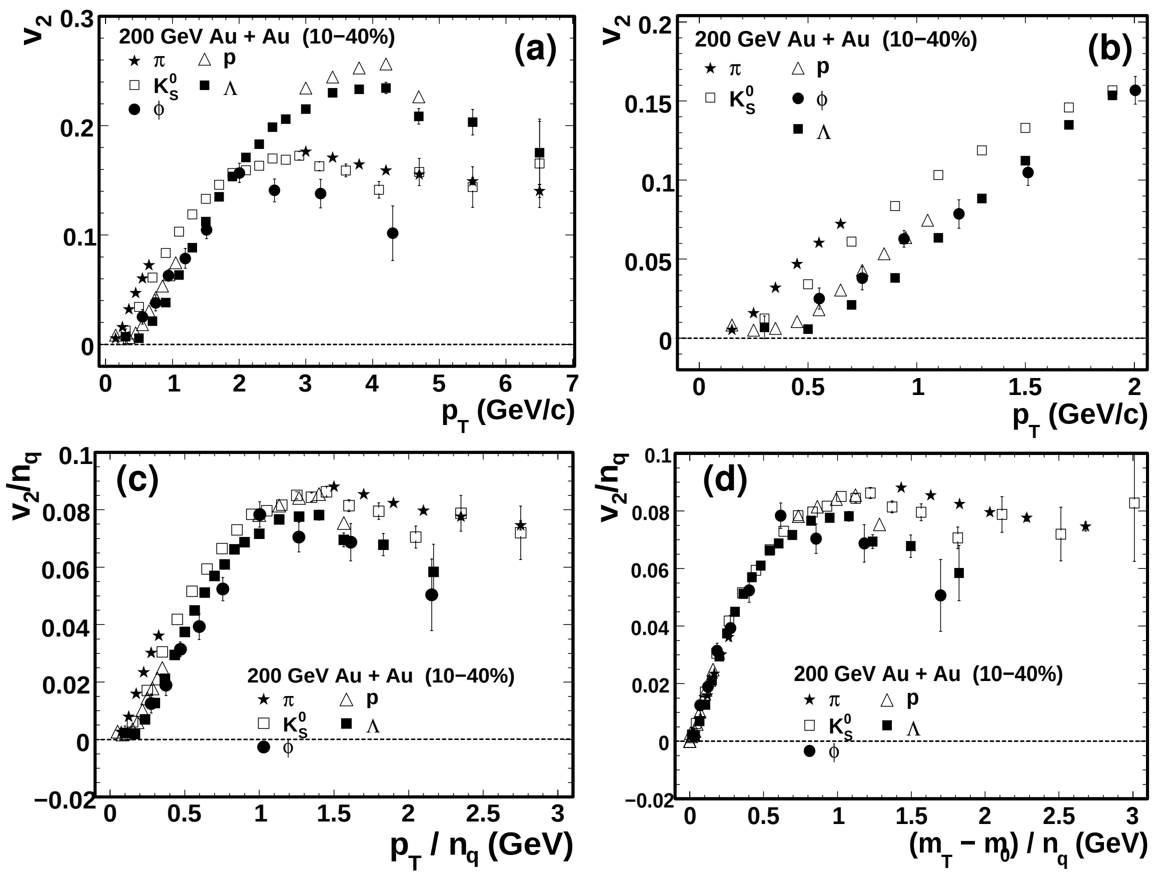

Figure 6.14: (a) The v_2 as a function of p_T for π, K_S^0, protons, Λ [241], and ϕ in Au+Au 10-40% collisions at $\sqrt{s_{NN}} = 200$ GeV measured from TPC event plane. The bars show only statistical errors. (b) The same plot as (a), but for low p_T points. (c) v_2/n_q versus p_T/n_q for identified hadrons. (d) v_2/n_q versus $(m_T - m_0)/n_q$ for identified hadrons.

pendent relaxation time may qualitatively help to understand this scaling breaking. In this calculation, the baryons and mesons in the $p_T = 2 - 3$ GeV/c region are produced in the complex transition region where the energy density decreases from 1.2 GeV/fm^3 to 0.5 GeV/fm^3. In this range, the temperature decreases by only $\triangle T \simeq 20$ MeV. However, the hydrodynamic simulations evolve this complicated region for a significant period of time, $\tau \simeq 4fm \leftrightarrow 6.5fm$, and the hadronic currents are built up over this time period [51]. The ϕ meson is presumed to have small hadronic cross sections, so it will have a longer relaxation time, equivalently, it will decouple from the hydrodynamic evolution earlier, thus a smaller v_2 is expected. This seems to be qualitatively consistent with present data. An quantitative understanding of the $m_T - m_0$ scaling and its breaking require detailed mechanism at the hadronization stage and the inclusion of dissipative effect from later stage hadronic interactions.

6.3.4 Violation of mass ordering?

Figure 6.14 (b) shows the comparison of v_2 for pion, K_0^S, proton [241], ϕ meson and Λ below p_T = 2 GeV/c in 10-40% Au+Au collisions at $\sqrt{s_{NN}}$ = 200 GeV. The mass ordering of $v_2(\pi) > v_2(K_0^S) > v_2(\mathrm{p}) > v_2(\Lambda)$, due to the effect of radial flow, can be clearly seen. In contrast, the v_2 of ϕ meson is consistent with that of proton and even larger below $p_T \sim 0.7$ GeV/c, though the mass of ϕ meson is ~9% heavier than that of proton. This observation is qualitatively consistent with what Hirano *et al.* calculated by their ideal hydrodynamic model with hadron cascade afterburner in Ref. [104]. The violation of mass ordering pattern of ϕ meson v_2 arises from both the dissipative effects in the later hadronic stage and the relatively small hadronic cross section of ϕ mesons.

In summary, we presented the measured ϕ meson elliptic flow v_2 in year 2007 Au+Au collisions at $\sqrt{s_{NN}}$ = 200 GeV. The eccentricity scaled ϕ meson v_2 shows stronger flow strength in more central collisions. The number of quark scaling has been evidenced with ϕ and Ω at intermediate p_T ($2.5 < p_T < 5$ GeV/c). Within the framework of valence quark coalescence model, this is thought to be a strong evidence of the development of partonic collectivity at the early stage, thus indicates the QGP formation at RHIC. However, the number-of-quark scaled v_2 versus p_T/n_q or $(m_T - m_0)/n_q$ for ϕ meson is systematically smaller than those of pions and kaons, and follows the trend of scaled v_2 of Λ for $2.5 < p_T < 5$ GeV/c. This challenges the simple quark coalescence explanation of number-of-quark scaling. From recently developed viscous hydrodynamic model [51] which employs species dependent relaxation time, the relatively smaller ϕ meson v_2/n_q versus $(m_T - m_0)/n_q$ may be qualitatively understood by its longer relaxation time and thus early decoupling from hydrodynamic evolution due to its presumably small hadronic cross section. The v_2 of ϕ mesons below $p_T = 1$ GeV/c seems to be consistent with that of proton, and even larger than that below $p_T = 0.7$ GeV/c. This observation contradicts the prediction of the mass ordering of v_2 from ideal hydrodynamic models, where heavier hadrons have smaller v_2 for a given p_T. This result supports the picture that the dynamics at late hadronic stage is described well by hadron cascade models and the ϕ has small hadronic cross section. Extending the low p_T reach will be crucial to see the violation of mass ordering more clearly and could be possible by using Barrel Time-Of-Flight installed in 2010 RHIC run at STAR.

Chapter VII Summary and outlook

7.1 New exponential law for $\beta^{\pm}$-decay half-lives of nuclei far from β-stable line

Precise input of $\beta^{\pm}$ decay half-lives of nuclei far from the β stable line is a prerequisite for understanding astrophysical nucleosynthesis process. At present, most of the unstable neutron-rich heavy nuclei can not be synthesized in the terrestrial laboratory and one has to rely on theoretical extrapolations for their β-decay properties. The accuracy of sophisticated microscopic model calculation on β-decay matrix element is limited by the uncertainty of the description of nuclear many-body problem. For the nucleus far from β-stable line, its β decay occurs between the ground state of parent nucleus to multiple excited energy levels of daughter nucleus, which is different from the β-decay of the nucleus close to β-stable line, that is, the transition from the ground state of parent nucleus to individual energy levels of daughter nucleus. Thus, the β-decay half-life of the nucleus far from stability is expected to manifest statistical behavior.

We have systematically investigated the experimental data of $\beta^{\pm}$-decay half-lives for both light nuclei and heavy nuclei far from β-stable line. A new exponential law is found between the half-life of $\beta^{\pm}$-decay and the nucleon number (Z, N) for proton-rich or neutron-rich nucleus. This new law implies an exponential dependence of nuclear $\beta^{\pm}$-decay half-lives on the maximum kinetic energy E_{m} of the electron or positron emitted in the $\beta^{\pm}$-decay process. It may approximately reflect the statistical properties of multi-energy-level decay behavior for the nucleus far from β-stable line, that is, from the ground state of parent nucleus to many excited energy levels of daughter nucleus. This is superior to the traditional Sargent law, a fifth power law between $\beta^{\pm}$-decay half-life and E_{m}, which can be approximately derived from Fermi theory of β-transition from single energy level of parent nucleus to that of daughter nucleus.

Based on the new exponential law and including reasonable nuclear structure effects, new formulae are proposed to describe the $\beta^{\pm}$-decay half-lives of nuclei far from β-stable line. Experimental half-lives are well reproduced by the simple formulae. The agreement with experimental data is comparable or even slightly better than the best microscopic model calculations for 735 nuclei ranging from $A = 9 - 238$ and with half-lives spanning 6 orders of magnitude (10^{-3}–10^{3} s). This shows that the formula have a firm basis in physics. It can be used to predict the $\beta^{\pm}$-decay half-lives of the nuclei far from the β-stable line.

Interesting nuclear structure effects on β-decay half-lives manifest beyond the "mean" behavior part of the simple formula (after systematical analysis, the part of nuclear structure effects is also included in our formula). For example, it is noticed that the even-odd effects on the β^+-decay half-lives of the first and second forbidden β^+ decays are much less apparent than those of the allowed β^+-transitions. This is a new phenomenon which demonstrates that the allowed β^+-transitions are more sensitive to nuclear even-odd effects than the forbidden β^+-transitions. It is also found that the shell or subshell effects strongly affect β^--decay half-lives even for nuclei far from β-stable line. The additional correlation between the major shell or subshell closures and β^--decay half-lives is obtained according to systematic investigation. This correlation provides the feasibility of obtaining information of the major shell or subshell closures of the nuclei far from the β-stable line according to the exponential law.

Besides the above study on nuclei far from stability, the half-life of allowed orbital electron-capture (EC) transition of the nucleus close to β-stable line is also systematically investigated. We have found the hindrance of angular momentum of parent and daughter nuclei on half-life of allowed orbital electron-capture (EC) transition. The hindrance of angular momentum is related to the overlap between multi-particle wave functions of parent and daughter nuclei. A new parameterized formula including the effect of angular momentum hindrance is proposed to calculate the half-life of allowed EC transition of nuclei close to β-stable line. Experimental half-lives of allowed EC transitions of nuclei close to β-stable line are well reproduced by this formula. In addition, the formula is also proved to be valid for calculating allowed EC-decay half-lives of U and transuranic nuclei. It is useful to experimental physicists for designing experiments to identify the synthesized long-lived superheavy nuclei approaching the superheavy stable island according to their decay properties and analyzing experimental data.

7.2 α decay and spontaneous fission half-lives of heavy and superheavy nuclei

α decay and spontaneous fission are the main decay modes of superheavy nuclei. Synthesis and identification of superheavy nucleus require precise prediction on its half-lives of decays from ground-states to ground-states, from isomeric-states to ground-states, and from isomeric-states to isomeric-states. Due to extra angular momentum hindrance factor, the isomeric state of superheavy nucleus may have a longer half-life than that of corresponding ground state, which is observed experimentally. Although observed, theoretical studies on α-decays from isomers are rare.

In this part, we have generalized the effective liquid drop model to describe the half-lives of α-transitions from ground-states to ground-states, from isomeric-states to ground-states, and from isomeric-states to isomeric-states by including the centrifugal potential barrier. Firstly, we test the model by calculating the half-lives of α-transitions occurring between the ground states of even-even heavy and superheavy nuclei. Theoretical half-lives agree with experimental ones, within a factor of $2-3$. Then we extend this model to calculate the favored α-decay half-lives of isomeric-states near proton shell Z=82. Good agreement is achieved between the experimental data and theoretical ones without any adjustment on the model parameters. Finally we generalize this model to calculate the α-decays of isomers in superheavy region by taking into account the effect of centrifugal potential barrier for the unfavored α decays. The agreement between calculated half-lives of isomers and experimental data is acceptable for superheavy region. In a word, we show that α-decay half-lives of both ground-states and isomeric-states can be calculated in a unified theoretical framework by the effective liquid drop model with centrifugal potential barrier included.

In addition, spontaneous fission half-lives of heavy and superheavy odd-mass nuclei are also systematically investigated. Available experimental data of spontaneous fission half-lives of odd-A nuclei with $Z = 92-110$ are well reproduced by an improved formula, with the average deviation from experimental data about one order of magnitude. In addition, a new exponential relation is found between the spontaneous fission half-lives along the long lifetime line and maximum Q values of the fission processes for odd-A nuclei with $Z = 92 - 106$. This relation may indicate the tunnelling property of spontaneous fission. An interesting result is that the experimental spontaneous fission half-lives are apparently larger than the anticipant values from the above exponential relation for nuclei with $Z \geqslant 108$. This may be caused by enhanced shell effects for the nuclei approaching $Z = 114$. Systematical calculation of fission barrier is performed for odd-A heavy and superheavy nuclei by the macroscopic-microscopic (MM) model. The analyses of experimental spontaneous fission half-life and the corresponding calculated fission barrier suggest that both the height and shape of the barrier determine the spontaneous fission half-life. The apparent increase of the height of the fission barrier and the double-humped shape of the barrier for nuclei close to $Z = 114$ make the spontaneous fission half-lives much longer than the expected values from the exponential relation, which means enhanced stability against spontaneous fission for odd-A nuclei approaching $Z = 114$. We suggest the experimental physicists to measure the spontaneous fission half-lives of $Z = 114$ isotopes to get more information of possible shell effect at $Z = 114$.

7.3 Final-state hadronic interactions on Cronin effect in d+Au 200 GeV collisions at RHIC — theoretical insights and preliminary experimental results

To address the long-outstanding problem of the origin of Cronin effect which was discovered more than 30 year ago, especially, its particle species dependence, both new theoretical insights and the corresponding preliminary experimental measurements are presented.

In theoretical side, we have studied the mechanism of hadron formation and subsequent hadronic interactions in d+Au collisions at center of mass energy per nucleon-nucleon pair $\sqrt{s_{NN}} = 200$ GeV. In a multiphase transport model (AMPT) with Lund string fragmentation for hadronization and the subsequent hadronic rescatterings and resonance decays included, we find particle mass dependence of central-to-peripheral nuclear modification factor R_{CP}. The AMPT calculation indicates the suppressions of low mass particles (pions and kaons) at large p_T during the final-state hadronic rescatterings, thus results in the observed particle species dependence of R_{CP} in d+Au collisions at RHIC. Recently measured difference between R_{CP} of antiproton and that of pion at mid-rapidity in year 2003 d+Au collisions at RHIC can be understood in terms of this final-state hadronic rescatterings. This shows for the first time the importance of final state hadronic interactions in d+Au collisions, since none of the initial-state models would predict a species-dependent Cronin effect at present.

Our above theoretical findings are further tested with STAR year 2008 d+Au data. We have studied the transverse momentum, centrality and pseudo-rapidity dependence of ϕ meson production in d+Au collisions at $\sqrt{s_{NN}} = 200$ GeV. Enhanced production of intemediate-p_T ϕ meson — with respect to binary collision scaling — have been observed in d+Au 200 GeV (0-20%) central collisions at mid-rapidity ($|y| < 0.5$). The ϕ meson yield is observed to be higher in the gold beam direction (backward pseudo-rapidity) than the deuteron beam direction (forward pseudo-rapidity) of the collision. Ratios of ϕ-meson yields in backward pseudo-rapidity to those in forward pseudo-rapidity increase with ϕ-meson transverse momentum for p_T below 5 GeV/c. Compared to the enhancements of other identified hadrons K_S^0 and $\Lambda + \overline{\Lambda}$, both nuclear modification factors and the pseudo-rapidity asymmetry likely show particle mass dependence. This preliminary result is consistent with our transport model (AMPT) calculation which employs the string model with soft and coherent interactions for hadronization and includes the final state hadronic rescatterings and resonance decays. This calculation suggests that final state hadronic interaction contributes to particle species dependence of Cronin effect at RHIC for the first time.

7.4 ϕ meson elliptic flow in Au+Au 200 GeV at RHIC — partonic collectivity and possible violation of mass ordering

ϕ meson is a golden probe to study the QGP formation and evolution in the early stage and its transport properties like viscosity since it is little affected by the late stage hadronic rescatterings due to its presumably small hadronic interaction cross section. We presented the preliminary measurement of ϕ meson elliptic flow v_2 in year 2007 Au+Au collisions at $\sqrt{s_{NN}} = 200$ GeV. The eccentricity scaled ϕ meson v_2 shows stronger flow strength in more central collisions. The number of quark scaling has been evidenced with ϕ ($s\bar{s}$) and Ω (sss) at intermediate p_T ($2.5 < p_T < 5$ GeV/c). Within the framework of valence quark coalescence model, this is thought to be a strong evidence of the development of partonic collectivity at the early stage, thus indicate the QGP formation at RHIC. However, the number-of-quark scaled v_2 versus p_T/n_q or $(m_T - m_0)/n_q$ for ϕ meson is systematically smaller than those of pions and kaons, and follows the trend of scaled v_2 of Λ for $2.5 < p_T < 5$ GeV/c. This challenges the simple quark coalescence explanation of number-of-quark scaling. From recently developed viscous hydrodynamic model [51] which employs species dependent relaxation time, the relatively smaller ϕ meson v_2/n_q versus $(m_T - m_0)/n_q$ may be qualitatively understood by its longer relaxation time and thus early decoupling from hydrodynamic evolution due to its presumably small hadronic cross section. The v_2 of ϕ mesons below $p_T = 1$

GeV/c seems to be consistent with that of proton, and even larger than that below $p_T = 0.7$ GeV/c. This observation contradicts the prediction of the mass ordering of v_2 from ideal hydrodynamic models, where heavier hadrons have smaller v_2 for a given p_T. This result supports the picture that the dynamics at late hadronic stage is described well by hadron cascade models and the ϕ has small hadronic cross section. Extending the low p_T reach will be crucial to see the violation of mass ordering more clearly and could be possible by using Barrel Time-Of-Flight installed in 2010 RHIC run at STAR.

7.5 Outlook

To get a decisive conclusion on the likely particle mass dependent enhancement for understanding the origin of Cronin effect in d+Au collisions, one needs a better p+p baseline measurement with higher statistics. This measurement is feasible with RHIC year 2009 p+p data. With better understandings of the hadronization mechanisms and subsequent hadronic rescatterings in d+Au collisions, we can further address the question of initial conditions of nuclei with relativistic energy. In this work we only focused on the final state hadronization mechanisms and subsequent hadronic interactions. The effect of initial conditions such as gluon saturation, parton multiple scatterings and so on will be addressed in our later theoretical and experimental investigations.

Taking the advantage that ϕ may suffer less hadronic interactions in the final state, we will address the questions on local thermalization and QGP viscosity with our current data. To compare our data with viscous hydrodynamic plus hadron cascade model calculation, we have a good chance to extract the QGP viscosity. Now the work is ongoing.

With ~72% (in year 2009 run) and subsequent full (in year 2010 run) coverage of barrel time-of-flight (TOF) system in STAR, the electron identification is greatly enhanced. It is shown in our TOF calibrations in Run 9 and Run 10 that the barrel TOF system has excellent stability and timing resolution. Taking the advantage of large acceptance of STAR detector and a factor of 10 faster data taking capability than before, it is feasible for a direct measurement of di-lepton thermal radiation from QGP. In addition, the measurements of vector mesons ρ, ω and ϕ through electromagnetic decay channels can shed light on whether chiral symmetry that breaks in QCD vacuum is restored in the QGP, and furthermore indicate the origin of mass in nature. Our first $\phi \to e^+e^-$ measurement in STAR d+Au 2008 run is a good start toward this exciting direction.

References

[1] E. Fermi, Z. Phys. **88**, 161 (1934).

[2] E. J. Konopinski and M. E. Rose, in Alpha-, Beta-, and Gamma-Ray Spectroscopy, edited by K. Siegbahn (North Holland, Amsterdam, 1965), Vol. II.

[3] T. D. Lee and C. N. Yang, Phys. Rev. **104**, 254 (1956).

[4] C. S. Wu, E. Ambler, R. W. Hayward, D. D. Hoppes and R. P. Hudson, Phys. Rev. **105**, 1413 (1957).

[5] R. P. Feynman and M. Gell-mann, Phys. Rev. **109**, 193 (1958).

[6] E. C. G. Sudarshan and R. E. Marshak, Phys. Rev. **109**, 1860 (1958).

[7] S. Weinberg, Phys. Rev. Lett. **19**, 1264 (1967).

[8] A. Salam, in Elementary Particle Physics, (Almquist and Wiksels, Stockholm, 1968), Edited by N. Svartholm, p. 367.

[9] S. L. Glashow, Nucl. Phys. **22**, 579 (1961).

[10] G. Arnison *et al.*, Phys. Lett. B **122**, 103 (1983).

[11] M. Banner *et al.*, Phys. Lett. B **122**, 476 (1983).

[12] P. Bagnaia *et al.*, Phys. Lett. B **129**, 130 (1983).

[13] Jameel-Un Nabi and H. V. Klapdor-Kleingrothaus, Atomic Data and Nuclear Data Tables **88**, 237 (2004).

[14] B. W. Sargent, Proc. Roy. Soc. A **139**, 659 (1933).

[15] K-L Kratz and G. Herrmann, Z. Physik **263**, 435 (1973).

[16] B. Pfeiffer, K.-L. Kratz and P. Möller, Prog. Nucl. Energy **41**, 39 (2002).

[17] K. Takahashi and M. Yamada, Prog. Theor. Phys. **41**, 1470 (1969).

[18] Overview of Research Opportunities with Radioactive Nuclear Beam[M]. ISL Steering Committee, USA, 1995.

[19] H. Masui and Y. K. Ho, Phys. Rev. C **65**, 054305 (2002).

[20] T. Suzuki, H. Geissel, O. Bochkarev *et al.*, Phys. Rev. Lett. **75**, 3241 (1995).

[21] I. Tanihata, J. Phys. G **22**, 157 (1996).

[22] Z. Ren, G. Xu, B. Chen *et al.*, Phys. Lett. B **351**, 11 (1995).

[23] T. Minamisono, T. Ohtsubo, I. Minami *et al.*, Phys. Rev. Lett. **69**, 2058 (1992).

[24] X. Z. Cai, H. Y. Zhang, W. Q. Shen, Z. Z. Ren *et al.*, Phys. Rev. C **65**, 024610 (2002).

[25] Q. Zhi and Z. Ren, Phys. Lett. B **638**, 166 (2006).

[26] G. T. Seaborg, Nobel lecture (1951). http://www.osti.gov/accomplishments/documents/fullText/ACC0048.pdf

[27] S. Hofmann and G. Münzenberg, Rev. Mod. Phys. **72**, 733 (2000).

[28] Yu. Ts. Oganessian, V. K. Utyonkov, and S. N. Dmitriev *et al.*, Phys. Rev. C **72**, 034611 (2005).

[29] Yu. Ts. Oganessian, V. K. Utyonkov, Yu. V. Lobanov *et al.*, Phys. Rev. C **74**, 044602 (2006).

[30] Yu. Ts. Oganessian *et al.*, Phys. Rev. Lett. **104**, 142502 (2010).

[31] K. Morita *et al.*, J. Phys. Soc. Jpn. **73**, 2593 (2004).

[32] Z. G. Gan, Z. Qin, H. M. Fan *et al.*, Eur. Phys. J. A **10**, 21 (2001).

[33] Z. G. Gan *et al.*, Eur. Phys. J. A **20**, 385 (2004).

[34] N. Bohr and J. A. Wheeler, Phys. Rev. **56**, 426 (1939).

[35] M. G. Mayer, Phys. Rev. **75**, 1969 (1949).

[36] O. Haxel, J. H. Jensen, and H. E. Suess, Phys. Rev. **75**, 1766 (1949).

[37] H. Fritzsch and M. Gell-Mann, arXiv: hep-ph/0208010v1 (2002).

[38] D. Gross and F. Wilczek, Phys. Rev. Lett. **30**, 1343 (1973); H. Politzer, Phys. Rev. Lett. **30**, 1346 (1973).

[39] S. Bethke, arXiv:0908.1135 [hep-ph] (2009).

[40] H. Satz, Nucl. Phys. A **661**, 104c-118c (1999).

[41] J. L. Ping, F. Wang, and T. Goldman, Phys. Rev. C **62**, 054007 (2000).

[42] H. R. Pang, J. L. Ping, F. Wang, and T. Goldman, Phys. Rev. C **65**, 014003 (2001).

[43] F. Karsch, E. Laermann, and A. Peikert, Phys. Lett. B, **478**, 447 (2000).

[44] S. Hands, arXiv:physics/0105022v1 [physics.ed-ph] (2001).

[45] BRAHMS Collaboration, I. G. Bearden *et al.*, Phys. Rev. Lett., **93**, 102301 (2004).

[46] J. D. Bjorken, Phys. Rev. D **27**, 140 (1983).

[47] PHENIX Collaboration, S. S. Adler *et al.*, arXiv: nucl-ex/0409015 (2004).

[48] L. McLerran, arXiv:hep-ph/0104285v2 (2001).

[49] H. Zong, and W. Sun, Phys. Rev. D **78**, 054001 (2008).

[50] H. Zong, L. Chang, F. Hou, W. Sun, and Y. Liu, Phys. Rev. C **71**, 015205 (2005).

[51] K. Dusling, G. Moore, D. Teaney, arXiv:0909.0754 (2009).

[52] A. M. Poskanzer and S. A. Voloshin, Phys. Rev. C **58**, 1671 (1998).

[53] S. A. Voloshin, A. M. Poskanzer, R. Snellings, arXiv:0809.2949v2 [nucl-ex] (2008).

[54] STAR collaboration, B. I. Abelev *et al.*, Phys. Rev. Lett. **99**, 112301 (2007).

[55] P. Huovinen, P. F. Kolb, U. Heinz, P. V. Ruuskanen, and S. A. Voloshin, Phys. Lett. B **503**, 58 (2001).

[56] STAR Collaboration, C. Adler *et al.*, Phys. Rev. Lett. **87**, 182301 (2001).

[57] X. Dong *et al.*, Phys. Lett. B **597**, 328 (2004).

[58] STAR collaboration, B. I. Abelev *et al.*, Phys. Rev. C **79**, 034909 (2009).

[59] J. Adams *et al.*, Phys. Rev. Lett. **91**, 072304 (2003).

[60] C. Blume, arXiv:nucl-ex/0609022v1 (2006).

[61] F. Cooper, G. Frye, Phys. Rev. D **10**, 186 (1974).

[62] Z. Lin, C. M. Ko, B. Li, B. Zhang, and S. Pal, Phys. Rev. C **72**, 064901 (2005), and references therein.

[63] H. van Hecke, H. Sorge, and N. Xu, Phys. Rev. Lett. **81**, 5764 (1998).

[64] M. Gyulassy, X. N. Wang, Nucl. Phys. B **420**, 583 (1994); X. N. Wang, M. Gyulassy, M. Plumer, Phys. Rev. D **51**, 3436 (1995).

[65] R. Baier, *et al.*, Nucl. Phys. B **484**, 265 (1997); R. Baier, *et al.*, Phys. Rev. C **58**, 1706 (1998).

[66] B. G. Zhakharov, JETP Lett. **63**, 952 (1996).

[67] M. Gyulassy, P. Lévai, I. Vitev, Nucl. Phys. B **594**, 371 (2001); M. Gyulassy, P. Lévai, I. Vitev, Phys. Rev. Lett. **85**, 5535 (2000).

[68] U. Wiedemann, Nucl. Phys. B **588**, 303 (2000).

[69] D. Kharzeev *et al.*, Phys. Lett. B **561**, 93 (2003); J. Jalilian-Marian *et al.*, Phys. Lett. B **577**, 54 (2003); D. Kharzeev *et al.*, Phys. Rev. D **68**, 094013 (2003); R. Baier *et al.*, Phys. Rev. D **68**, 054009 (2003); J. L. Albacete *et al.*, Phys. Rev. Lett. **92**, 082001 (2004).

[70] J. W. Cronin, H. J. Frisch, and M. J. Shochet, *et al.*, Phys. Rev. D **11**, 3105 (1975).

[71] D. Antreasyan, J. W. Cronin, and H. J. Frisch, *et al.*, Phys. Rev. D **19**, 764 (1979).

[72] P. B. Straub *et al.*, Phys. Rev. Lett. **68**, 452 (1992).

[73] STAR Collaboration, J. Adams, *et al.*, Phys. Lett. B **616**, 8 (2005); STAR Collaboration, J. Adams, *et al.*, Phys. Lett. B **637**, 161 (2006).

[74] PHENIX Collaboration, S. S. Adler, *et al.*, Phys. Rev. C **74**, 024904 (2006).

[75] B. Z. Kopeliovich, J. Nemchik, A. Schafer, and A. V. Tarasov, Phys. Rev. Lett. **88**, 232303 (2002).

[76] M. Lev and B. Petersson, Z. Phys. C **21**, 155 (1983).

[77] A. Accardi and M. Gyulassy, Phys. Lett. B **586**, 244 (2004).

[78] G. Papp, P. Lévai, and G. Fai, Phys. Rev. C **61**, 021902(R) (1999).

[79] I. Vitev and M. Gyulassy, Phys. Rev. Lett. **89**, 252301 (2002).

[80] X. N. Wang, Phys. Rev. C **61**, 064910 (2000).

[81] R. C. Hwa and C. B. Yang, Phys. Rev. Lett. **93**, 082302 (2004); R. C. Hwa and C. B. Yang, Phys. Rev. C **70**, 037901 (2004).

[82] A. Shor, Phys. Rev. Lett. **54**, 1122 (1985).

[83] K. Haglin, Nucl. Phys. A **584**, 719 (1995).

[84] W. Smith and K. L. Haglin, Phys. Rev. C **57**, 1449 (1998).

[85] L. Alvarez-Ruso and V. Koch, Phys. Rev. C **65**, 054901 (2002).

[86] T. Ishikawa *et al.*, Phys. Lett. B **608**, 215 (2005).

[87] H. J. Behrend *et al.*, Phys. Lett. B **56**, 408 (1975).

[88] A. Sibirtsev, H.-W. Hammer, U.-G. Meissner, and A. W. Thomas, Eur. Phys. J. A **29**, 209 (2006).

[89] B. Andersson, G. Gustafson, B. Söderberg, Z. Phys. C **20**, 317 (1983).

[90] B. Andersson, G. Gustafson, G. Ingelman, T. Sjöstrand and X. Artru, Phys. Rep. **97**, 31 (1983).

[91] X. N. Wang and M. Gyulassy, Phys. Rev. D **44**, 3501 (1991).

[92] Z. Lin and C. M. Ko, Phys. Rev. C **68**, 054904 (2003).

[93] STAR Collarboration, J. Adams *et al.*, Phys. Rev. Lett., **92**, 052302 (2004).

[94] PHENIX Collarboration, S. S. Adler *et al.*, Phys. Rev. Lett., **91**, 182301 (2003).

[95] STAR Collarboration, J. Adams *et al.*, Phys. Rev. Lett., **95**, 122301 (2005).

[96] STAR Collarboration, B. I. Abelev *et al.*, Phys. Rev. Lett., **99**, 112301 (2007).

[97] J.-Y. Ollitrault, Phys. Rev. **D** 46, 229 (1992)

[98] D. Teaney, J. Lauret, and E. V. Shuryak, Phys. Rev. Lett. **86**, 4783 (2001).

[99] P. Huovinen, P. F. Kolb, U. W. Heinz, P. V. Ruuskanen, and S. A. Voloshin, Phys. Lett. B **503**, 58 (2001).

[100] STAR collaboration, B. I. Abelev *et al.*, Phys. Rev. C **77**, 054901 (2008).

[101] T. Hirano and M. Gyulassy, Nucl. Phys. A **769**, 71 (2006).

[102] H. Song and U. W. Heinz, Phys. Lett. B **658**, 279 (2008).

[103] M. Luzum and P. Romatschke, Phys. Rev. C**78**, 034915 (2008).

[104] T. Hirano, U. Heinz, D. Kharzeev, R. Lacey, and Y. Nara, Phys. Rev. C **77**, 044909 (2008).

[105] M. Bleicher and H. Stoecker, Phys. Lett. B **526**, 309 (2002).

[106] X. Zhang and Z. Ren, Phys. Rev. C **73**, 014305 (2006).

[107] X. Zhang, Z. Ren and Q. Zhi, Commun. Theo. Phys. **48**, 1072 (2007).

[108] X. Zhang, Z. Ren, Q. Zhi and Q. Zheng, J. Phys. G **34**, 2611 (2007).

[109] R. D. Evans, in the Atomic Nucleus, (McGraw-Hill, New York, 1955), p. 559.

[110] O. Tarasov and D. Bazin, Nucl. Phys. A **746**, 411 (2004).

[111] XiTing Lu, DongXing Jiang and YanLin Ye, in Nuclear Physics (Atomic Energy Press, Beijing, 2000), p. 153.

[112] G. Audi, O. Bersillon, J. Blachot and A. H. Wapstra, Nucl. Phys. A **729**, 3 (2003).

[113] M. B. Smith *et al.*, Eur. Phys. J. A **5**, 43 (1999).

[114] S. Grévy, J. C. Angélique and P. Baumann *et al.*, Phys. Lett. B **594**, 252 (2004).

[115] F. Montes, A. Estrade and P. T. Hosmer *et al.*, Phys. Rev. C **73**, 035801 (2006).

[116] G. Audi, A. H. Wapstra and C. Thibault, Nucl. Phys. A **729**, 337 (2003).

[117] C. M. H. Smith, in a Textbook of Nuclear Physics, (Pergamon, Oxford, 1965), p. 437.

[118] T. H. R. Skyrme, Prog. Nucl. Phys. **1**, 115 (1950).

[119] M. A. Preston, in Physics of the Nucleus, (Addison-Wesley, Reading, Mass., 1962), p. 407.

[120] V. E. Viola and G. T. Seaborg, J. Inorg. Nucl. Chem. **28**, 741 (1966).

[121] T. Dong and Z. Ren, Eur. Phy. J. A **26**, 69 (2005).

[122] Z. Ren, C. Xu and Z. Wang, Phys. Rev. C **70**, 034304 (2004).

[123] P. Möller, J. R. Nix and K. Kratz, Atomic Data and Nuclear Data Tables **66**, 131 (1997).

[124] P. Kienle, T. Faestermann, J. Friese *et al.*, Progress in Particle and Nuclear Physics **46**, 73 (2001).

[125] X. Zhang and Z. Ren, J. Phys. G **31**, 959 (2005).

[126] Nuclear structure and decay data by NNDC, Brookhaven National Laboratory. http://www.nndc.bnl.gov/nudat2/indx_dec.jsp

[127] D. Lunney, J. M. Pearson and C. Thibault, Rev. Mod. Phys. **75**, 1021 (2003).

[128] R. W. Ibbotson, T. Glasmacher and B. A. Brown *et al.*, Phys. Rev. Lett. **80**, 2081 (1998).

[129] J. Fridmann, I. Wiedenhöver and A. Gade *et al.*, Nature **435**, 922 (2005).

[130] J. M. Blatt and V. F. Weisskopf, Theoretical Nuclear Physics (John Wiley & Sons, New York, 1952), p. 690.

[131] A. de-Shalit and I. Talmi, Nuclear Shell Theory (Academic Press, New York and London, 1963), p. 58.

[132] B. A. Brown and B. H. Wildenthal, Nucl. Phys. A **474**, 290 (1987).

[133] W. Bambynek, H. Behrens, M. H. Chen, B. Crasemann, M. L. Fitzpatrick, K. W. D. Ledingham, H. Genz, M. Mutterer, and R. L. Intemann, Rev. Mod. Phys. **49**, 77 (1977).

[134] P. Möller, B. Pfeiffer, and K.-L. Kratz, Phys. Rev. C **67**, 055802 (2003).

[135] Z.-C. Gao, Y. Sun, and Y.-S. Chen, Phys. Rev. C **74**, 054303 (2006).

[136] P. Vogel and M. R. Zirnbauer, Phys. Rev. Lett. **57**, 3148 (1986).

[137] S. E. Koonin, Nature **354**, 468 (1991).

[138] W. C. Haxton and C. Johnson, Phys. Rev. Lett. **65**, 1325 (1990).

[139] K. Langanke and G. Martínez-Pinedo, Nucl. Phys. A **673**, 481 (2000).

[140] P. Sarriguren, R. Álvarez-Rodríguez and E. M. Guerra, Eur. Phys. J. A **24**, 193 (2005).

[141] A. Faessler and F. Šimkovic, J. Phys. G **24**, 2139 (1998).

[142] G. Pantis, F. Šimkovic, J. D. Vergados and A. Faessler, Phys. Rev. C **53**, 695 (1996).

[143] I. Talmi, Phys. Rev. **91**, 122 (1953).

[144] P. Meunier, Nucl. Phys. B (Proc. Suppl.) **66**, 207 (1998).

[145] M. Bhattacharya, A. García, M. M. Hindi, E. B. Norman, C. E. Ortiz, N. I. Kaloskamis, C. N. Davids, O. Civitarese, and J. Suhonen, Phys. Rev. C **58**, 1247 (1998).

[146] Data from LBNL Isotopic Project. http://ie.lbl.gov/toi/

[147] J. Dvorak, W. Brüchle, and M. Chelnokov *et al.*, Phys. Rev. Lett. **97**, 242501 (2006).

[148] G. Gamow, Z. Phys. **51**, 204 (1928).

[149] B. Buck, A. C. Merchant and S. M. Perez, At. Data Nucl. Data Tables **54**, 53 (1993).

[150] B. Buck, A. C. Merchant and S. M. Perez, Phys. Rev. Lett. **72**, 1326 (1994).

[151] A. Săndulescu *et al.*, Rep. Prog. Phys. **55**, 1423 (1992).

[152] K. Varga, R. G. Lovas and R. J. Liotta, Phys. Rev. Lett. **69**, 37 (1992)

[153] C. Detraz, Nucl. Phys. A **654**, 12c (1999).

[154] H. J. Mang, Annu. Rev. Nucl. Sci. **14**, 1 (1964).

[155] P. E. Hodgeson and E. Betak, Phys. Rep. **374**, 1 (2001).

[156] Z. Ren and H. Toki, Nucl. Phys. A **689**, 691, (2001).

[157] C. Xu and Z. Ren, Phys. Rev. C **69**, 024614 (2004).

[158] D. N. Poenaru *et al.*, At. Data Nucl. Data Tables **34**, 423 (1986).

[159] S. Hofmann, F. P. Heßberger, D. Ackermann, S. Antalic, P. Cagarda, S. Ćwiok, B. Kindler, J. Kojouharova, B. Lommel, R. Mann, G. Münzenberg, A. G. Popeko, S. Saro, H. J. Schött and A. V. Yeremin, Eur. Phys. J. A **10**, 5 (2001).

[160] F. R. Xu, E. G. Zhao, R. Wyss, and P. M. Walker, Phys. Rev. Lett. **92**, 252501 (2004).

[161] M. Gonçalves and S. B. Duarte, Phys. Rev. C **48**, 2409 (1993).

[162] S. B. Duarte, O. A. P. Tavares, F. Guzmán and A. Dimarco, At. Data Nucl. Data Tables **80**, 235 (2002).

[163] O. A. P. Tavares, S. B. Duarte, O. Rodríguez, F. Guzmán, M. Gonçalves and F. García, J. Phys. G **24**, 1757 (1998).

[164] X. Zhang and Z. Ren, High Energy Phys. & Nucl. Phys. **30**, No. 1, 47 (2006). (Chinese)

[165] M. Gaudin, J. Phys. **35**, 885 (1974).

[166] Yu. A. Lazarev, Yu. V. Lobanov, Yu. Ts. Oganessian, V. K. Utyonkov, F. Sh. Abdullin, G. V. Buklanov, B. N. Gikal, S. Iliev, A. N. Mezentsev, A. N. Polyakov, I. M. Sedykh, I. V. Shirokovsky, V. G. Subbotin, A. M. Sukhov, Yu. S. Tsyganov, V. E. Zhuchko, R. W. Lougheed, K. J. Moody, J. F. Wild, E. K. Hulet and J. H. McQuaid, Phys. Rev. Lett. **73**, 624 (1994).

[167] A. Türler A, Ch. E. Düllmann, H. W. Gäggeler *et al.*, Eur. Phys. J. A **17**, 505 (2003).

[168] S. B. Duarte, O. A. P. Tavares, M. Gonçalves, O. Rodríguez, F. Guzmán, T. N. Barbosa, F. García and A. Dimarco, J. Phys. G **30**, 1487 (2004).

[169] R. B. Firestond and V. S. Shirley, Table of Isotopes, Vol. 2, 8th ed., Wiley, New York (1996).

[170] C. Xu and Z. Ren, Commun. Theor. Phys. **42**, 745 (2004).

[171] C. Mazzocchi *et al.*, Phys. Lett. B **532**, 29 (2002).

[172] T. Papenbrock and G. F. Bertsch, Phys. Rev. Lett. **80**, 4141 (1998).

[173] C. G. Gallagher, and J. O. Rasmussen, J. Inorg. Nucl. Chem. **3**, 333 (1957).

[174] R. Vandenbosch and J. R. Huizenga, Nuclear Fission (Academic, New York, 1973).

[175] Z. Ren, Nucl. Phys. Rev. **22**, No. 2, 153 (2005).

[176] W. J. Swiatecki, Phys. Rev. **100**, 937 (1955).

[177] C. Xu and Z. Ren, Int. J. Mod. Phys. E **15**, 1569 (2006).

[178] D. S. Delion, R. J. Liotta and R. Wyss, Phys. Rev. Lett. **96**, 072501 (2006).

[179] C. Xu and Z. Ren, Phys. Rev. C **71**, 014309 (2005).

[180] Z. Ren and C. Xu, Nucl. Phys. A **759**, 64 (2005).

[181] M. G. Itkis, Yu. Ts. Oganessian, and V. I. Zagrebaev, Phys. Rev. C **65**, 044602 (2002).

[182] J. L. Egido and L. M. Robledo, Phys. Rev. Lett. **85**, 1198 (2000).

[183] S. Bjørnholm and J. E. Lynn, Rev. Mod. Phys. **52**, 725 (1980).

[184] S. G. Nilsson, Chin Fu Tsang, A. Sobiczewski *et al.*, Nucl. Phys. A **131**, 1 (1969).

[185] M. G. Itkis, J. Äystö, S. Beghini *et al.*, Nucl. Phys. A **734**, 136 (2004).

[186] K. E. Gregorich, J. M. Gates, Ch. E. Düllmann *et al.*, Phys. Rev. C **74**, 044611 (2006).

[187] N. E. Holden and D. C. Hoffman, Pure Appl. Chem. **72**, 1525 (2000).

[188] Y. L. Zhao, I. Nishinaka, Y. Nagame *et al.*, Phys. Rev. Lett. **82**, 3408 (1999).

[189] Q. Zhi and Z. Ren, Nucl. Phys. A **794**, 10 (2007).

[190] P. Möller, J. R. Nix, W. D. Myers, and W. J. Swiatecki, Atomic Data and Nuclear Data Tables **59**, 185 (1995).

[191] V. M. Strutinsky, Nucl. Phys. A **122**, 1 (1968).

[192] A. Franz, Nucl. Instrum. Meth. A **566**, 54 (2006).

[193] K. H. Ackermann *et al.*, Nucl. Instrum. Meth. A **499**, 624 (2003).

[194] F. Simon *et al.*, "The Forward GEM Tracker of STAR at RHIC", (2008).

[195] A. Shabetai, Eur. Phys. J. C **49**, 169 (2007).

[196] J. Kapitan, "Open charm measurement with HFT at STAR", (2008).

[197] M. Beddo *et al.*, Nucl. Instrum. Meth. A **499**, 725 (2003).

[198] C. E. Allgower *et al.*, Nucl. Instrum. Meth. A **499**, 740 (2003).

[199] M. Shao *et al.*, Nucl. Instrum. Meth. A **558**, 419 (2006).

[200] X. Dong, AIP Conf. Proc., **865**, 332 (2006).

[201] W. J. Llope, Nucl. Instrum. Meth. B **241**, 306 (2005).

[202] M. Anderson *et al.*, Nucl. Instrum. Meth. A **499**, 659 (2003).

[203] Z. Tang, Ph.D. Thesis, University of Science and Technology of China (2009). http://drupal.star.bnl.gov/STAR/system/files/Tang_Zebo.pdf

[204] S. Eidelman *et al.*, Phys. Lett. B **592**, 1 (2004).

[205] Z. Xu *et al.*, arXiv: nucl-ex/0411001 (2004).

[206] Y. Xu *et al.*, arXiv: 0807.4303 (2008).

[207] M. Shao *et al.*, Meas. Sci. Technol. **20**, 025102 (2009).

[208] STAR-TOF software documentation.
http://drupal.star.bnl.gov/STAR/system/files/TOFSoftware.2.pdf

[209] E. Yamamoto, Ph.D. Thesis, University of California - Los Angeles (2001).
http://drupal.star.bnl.gov/STAR/files/startheses/2001/yamamoto_eugene.pdf.

[210] J. Ma, Ph.D. Thesis, University of California - Los Angeles (2006).
URL http://drupal.star.bnl.gov/STAR/files/startheses/2006/ma_jingguo.pdf.

[211] STAR Collaboration, B. I. Abelev *et al.*, Phys. Rev. C **79**, 064903 (2009).

[212] X. Zhang for the STAR Collaboration, AIP Conference Proceedings **1182**, 783 (2009).

[213] S. Shi for the STAR Collaboration, Nucl. Phys. A **830**, 187c (2009).

[214] X. Zhang for the STAR Collaboration, "ϕ meson measurements via e^+e^- decays in d+Au collisions at $\sqrt{s}$ = 200 GeV in STAR" (poster), Quark Matter 2009, Knoxville, Tennessee.

[215] X. Zhang for the STAR Collaboration, "ϕ meson production and cold nuclear matter effect in d + Au collisions at $\sqrt{s}$ = 200 GeV in STAR", APS 2010 April meeting, Washington, DC.

[216] Run 8 d+Au centrality selection.
http://www.star.bnl.gov/protected/lfspectra/cjena/run8_dAu200GeV/dAu_centrality /documentation/centrality_run8_dAu200GeV.html

[217] Run 7 Au+Au centrality selection.
http://www.star.bnl.gov/protected/lfspectra/atimmins/AuAu200GeV/Centrality/page.html

[218] D. L'Hote, Nucl. Instrum. Meth. A **337**, 544 (1994).

[219] D. Drijard, H. G. Fischer, and T. Nakada, Nucl. Instr. Meth. A **225**, 367 (1984).

[220] Particle Data Group. http://pdg.lbl.gov/

[221] F. Carminati *et al.*, GEANT 3.21: Detector Description 38 and Simulation Tool, CERN Program Library Long Writeup W5013 (1993).

[222] X. Dong, Ph.D. Thesis, University of Science and Technology of China (2005).
http://drupal.star.bnl.gov/STAR/files/startheses/2005/dong_xin.pdf.

[223] N. Borghini and J. Y. Ollitrault, Phys. Rev. C **70**, 064905 (2004).

[224] X. Zhang, J. Chen, Z. Ren, N. Xu, Z. Xu, Q. Zheng, and X. Zhu, arXiv: 1001.4734[nucl-th].

[225] B. Zhang, Comput. Phys. Commun. **109**, 193 (1998).

[226] B. A. Li and C. M. Ko, Phys. Rev. C **52**, 2037 (1995).

[227] STAR Collaboration, J. Adams, *et al.*, Phys. Rev. C **70**, 064907 (2004).

[228] STAR Collaboration, B. I. Abelev, *et al.*, Phys. Rev. C **76**, 064904 (2007).

[229] K. Gallmeister, and T. Falter, Phys. Lett. B **630**, 40 (2005).

[230] L. V. Gribov, E. M. Levin, M. G. Ryskin, Phys. Rept. **100**, 1 (1983).

[231] A. H. Mueller and J. Qiu, Nucl. Phys. B **268**, 427 (1986).

[232] L. McLerran and R. Venugopalan, Phys. Rev. D **49**, 2233 (1994); L. McLerran and R. Venugopalan, Phys. Rev. D **49**, 3352 (1994).

[233] D. Kharzeev, Nucl. Phys. A **730**, 448 (2004).

[234] J. Jalilian-Marian *et al.*, Phys. Lett. B **577**, 54 (2003); J. L. Albacete *et al.*, Phys. Rev. Lett. **92**, 082001 (2004); D. Kharzeev *et al.*, Phys. Rev. D **68**, 094013 (2003); R. Baier *et al.*, Phys. Rev. D **68**, 054009 (2003).

[235] PHOBOS collaboration, B. B. Back *et al.*, Phys. Rev. C **70**, 021902(R) (2004).

[236] X. Zhu for the STAR Collaboration, Nucl. Phys. A **830**, 845c (2009).

[237] STAR collaboration, B. I. Abelev *et al.*, Phys. Rev. C **76**, 054903 (2007).

[238] X. N. Wang, Phys. Lett. B **565**, 116 (2003).

[239] R. C. Hwa, C. B. Yang, and R. J. Fries, Phys. Rev. C **71**, 024902 (2005).

[240] PHENIX Collaboration, A. Adare *et al.*, Phys. Rev. Lett. **98**, 162301 (2007).

[241] N. Li, "Study of the Number of Quark Scaling of v_2 at High Transverse Momentum", APS April Meeting 2010, Washington, DC.
http://meetings.aps.org/link/BAPS.2010.APR.Y14.5

[242] J. H. Chen, J. Fu, H. Z. Huang, and Y. G. Ma, J. Phys. G **36**, 064016 (2009).

[243] R. C. Hwa and C. B. Yang, arXiv:nucl-th/0602024v3 (2007).

List of Publications & Presentations

Refereed Journal

- *α-decay half-lives of ground and isomeric states calculated in a unified theoretical framework*
  Xiaoping Zhang and Zhongzhou Ren, J. of Phys. G, **31**, 959 (2005).

- *New exponential law of β^+-decay half-lives of nuclei far from β-stable line*
  Xiaoping Zhang and Zhongzhou Ren, Phys. Rev. C, **73**, 014305 (2006).

- *Theoretical study on the alpha decay half-life of superheavy elements with the effective liquid drop model*
  Xiaoping Zhang and Zhongzhou Ren, High Energy Physics & Nuclear Physics, **30**, No. 1, 47 (2006). (Chinese)

- *Systematics of β^--decay half-lives of nuclei far from β-stable line*
  Xiaoping Zhang, Zhongzhou Ren, Qijun Zhi and Qiang Zheng, J. Phys. G, **34**, 2611 (2007).

- *Simple formula of β^+-decay half-lives of nuclei far from β-stable line*
  Xiaoping Zhang, Zhongzhou Ren and Qijun Zhi, Commun. Theo. Phys., **48**, 1072 (2007).

- *Loschmidt echo near a dynamical phase transition in a Bose-Einstein condensate*
  Qiang Zheng, Wen-ge Wang, Xiaoping Zhang and Zhongzhou Ren, Phys. Lett. A, **372**, 5139 (2008).

- *Exact solutions and coherence structures of generalized Breor-Kaup equations*
  Qiang Zheng, Xiaoping Zhang and Zhongzhou Ren, Commun. Theor. Phys., **50**, 1283 (2008).

- *Control of entanglement sudden death by Kerr medium*
  Qiang Zheng, Xiaoping Zhang and Zhongzhou Ren, Chin. Phys. B, **17**, 3553 (2008).

- *Ground state properties of superheavy nuclei in macroscopic-microscopic model*
  Qijun Zhi, Zhongzhou Ren, Xiaoping Zhang and Qiang Zheng, Commun. Theo. Phys., **50**, 707 (2008).

- *Alpha-decay energies and half-lives for possibly synthesized superheavy elements*
  Qijun Zhi, Zhongzhou Ren, Xiaoping Zhang, Xiaohong Zhou, Zaiguo Gan, Zhi Qin and Hushan Xu, Chin. Phys. C, **32**, No. 1, 40 (2008).

- *Decay of Loschmidt echo in a Bose-Einstein condensate at a dynamical phase transition*
  Qiang Zheng, Wen-ge Wang, Pinquan Qin, Ping Wang, Xiaoping Zhang and Zhongzhou Ren, Phys. Rev. E, **80**, 016214 (2009).

- *Entanglement dynamics of a Heisenberg chain with Dzyaloshinskii-Moriya interaction*
  Qiang Zheng, Xiaoping Zhang, Qijun Zhi and Zhongzhou Ren, Chin. Phys. B, **18**, 3210 (2009).

- *Progress of studies on nuclei around "Island of Inversion"*
  Qijun Zhi and Xiaoping Zhang, Nucl. Phys. Rev., **26**, 275 (2009). (Chinese)

- *Systematical law of β^+-decay half-lives of nuclei far from β-stable line*
  Xiaoping Zhang, Zhongzhou Ren, Qijun Zhi and Qiang Zheng, Chin. Phys. C (in press).

- *Relatively-long time decay of Loschmidt echo of a Bose-Einstein Condensate in a double-well potential*
  Qiang Zheng, Wen-ge Wang, Xiaoping Zhang and Zhongzhou Ren, Eur. Phys. J. D (in press).

- *Entanglement sudden death induced by Dzyaloshinskii-Moriya interaction and its controlling*
  Qiang Zheng, Ping Sun, Xiaoping Zhang and Zhongzhou Ren, Chin. Phys. C (in press).

Proceedings

- *ϕ meson production and cold nuclear matter effect in d+Au collisions at $\sqrt{s} = 200$ GeV in STAR*
  Xiaoping Zhang (for the STAR Collaboration), proceedings of 10^{th} Conference on the Intersections of Particle and Nuclear Physics, AIP Conference Proceedings, Volume **1182**, p. 783-786 (2009).

Papers to be submitted

- *Effect of final state interactions on particle production in d+Au collisions at RHIC*
  Xiaoping Zhang, Jinhui Chen, Zhongzhou Ren, N. Xu, Zhangbu Xu, Qiang Zheng and Xianglei Zhu, arXiv: `1001.4734[nucl-th]`.

- *Measurement of elliptic flow for multistrange hadrons in Au+Au collisions at $\sqrt{s_{NN}} = 200$ GeV*
  STAR collaboration, primary authors: Xiaoping Zhang, ShuSu Shi, Nu Xu, Na Li, Hiroshi Masui and Jie Zhao, in preparation for Phys. Rev. Lett.

- *Analytical formula for half-lives of allowed orbital electron-capture transition*
  Xiaoping Zhang, Zhongzhou Ren, Qijun Zhi and Qiang Zheng, to be submitted.

- *Magnetic moments of odd-odd and near-spherical 2^+-states of even-even nuclei with two valence nucleons in same shell-model orbit*
  Xiaoping Zhang, Zhongzhou Ren, Qijun Zhi and Qiang Zheng, to be submitted.

- *Nuclear spontaneous fission approaching Z=114*
  Xiaoping Zhang, Zhongzhou Ren, Qijun Zhi and Qiang Zheng, to be submitted.

- *Systematics of (n,γ) reaction cross section*
  Xiaoping Zhang, Zhongzhou Ren, Guangwu Li, Qijun Zhi and Qiang Zheng, to be submitted.

Papers in STAR Collaboration

- *Longitudinal double-spin asymmetry and cross section for inclusive neutral pion production at midrapidity in polarized proton collisions at $\sqrt{s} = 200$ GeV*
  B. I. Abelev et al. (STAR Collaboration), Phys. Rev. D **80**, 111108 (2009).
- *Longitudinal Spin Transfer to Λ and $\bar{\Lambda}$ Hyperons in Polarized Proton-Proton Collisions at $\sqrt{s} = 200$ GeV*
  B. I. Abelev et al. (STAR Collaboration), Phys. Rev. D **80**, 111102, (2009).
- *Azimuthal Charged-Particle Correlations and Possible Local Strong Parity Violation*
  B. I. Abelev et al. (STAR Collaboration), Phys. Rev. Lett. **103**, 251601 (2009).
- *Long range rapidity correlations and jet production in high energy nuclear collisions*
  B. I. Abelev et al. (STAR Collaboration), Phys. Rev. C **80**, 064192 (2009).
- *Neutral Pion Production in Au+Au Collisions at $\sqrt{s_{NN}}$ = 200 GeV*
  B. I. Abelev et al. (STAR Collaboration), Phys. Rev. C **80**, 044905 (2009).
- *Center of mass energy and system-size dependence of photon production at forward rapidity at RHIC*
  B. I. Abelev et al. (STAR Collaboration), Nucl. Phys. A **832**, 134 (2009).
- *Growth of Long Range Forward-Backward Multiplicity Correlations with Centrality in Au+Au Collisions at $\sqrt{s_{NN}}$ = 200 GeV*
  B. I. Abelev et al. (STAR Collaboration), Phys. Rev. Lett. **103**, 172301 (2009).
- *J/ψ production at high transverse momentum in p+p and Cu+Cu collisions at $\sqrt{s_{NN}}$ = 200 GeV*
  B. I. Abelev et al. (STAR Collaboration), Phys. Rev. C **80**, 041902 (2009).
- *Pion interferometry in Au+Au and Cu+Cu collisions at $\sqrt{s} = 62.4$ and 200 GeV*
  B. I. Abelev et al. (STAR Collaboration), Phys. Rev. C **80**, 024905 (2009).
- *k/π Fluctuations at Relativistic Energies*
  B. I. Abelev et al. (STAR Collaboration), Phys. Rev. Lett. **103**, 092301 (2009).
- *Measurement of D^* mesons in jets from p+p collisions at $\sqrt{s} = 200$ GeV*
  B. I. Abelev et al. (STAR Collaboration), Phys. Rev. D **79**, 112006 (2009).
- *System size dependence of associated yields in hadron-triggered jets*
  B. I. Abelev et al. (STAR Collaboration), Phys. Lett. B **683**, 123 (2010).
- *Identified particle production, azimuthal anisotropy, and interferometry measurements in Au+Au collisions at $\sqrt{s_{NN}} = 9.2$ GeV*
  B. I. Abelev et al. (STAR Collaboration), Phys. Rev. C **81**, 024911 (2010).
- *Observation of an Antimatter Hypernucleus*
  B. I. Abelev et al. (STAR Collaboration), Science **328**, 58 (2010).

Presentations (not including talks in Chinese)

- *ϕ meson measurements via e^+e^- decays in d+Au collisions at $\sqrt{s} = 200$ GeV in*

STAR (poster)
Quark Matter 2009, Knoxville, Tennessee, March 30^{th} to April 4^{th}, 2009

- *ϕ meson production and cold nuclear matter effect in d + Au collisions at* $\sqrt{s} = 200$ *GeV in STAR*
  CIPANP 2009: 10^{th} Conference on the Intersections of Particle and Nuclear Physics, San Diego, CA, USA, May 26-31, 2009

- *ϕ meson production and cold nuclear matter effect in d + Au collisions at* $\sqrt{s} = 200$ *GeV in STAR*
  APS 2010 April meeting, Washington, DC, Feb. 13-17, 2010

Acknowledgements

First, I feel strongly thankful to my advisor, Prof. Zhongzhou Ren. He has guided me into exciting science research since my undergraduate study. He gave me a very good start on the theoretical and experimental study of low energy nuclear physics and continued to supervise and support me in the last seven years. His enormous physics knowledge, theoretical intuition and serious attitude on science give me a deep impression. He also gave me a lot of help on life and sent me to Lawrence Berkeley National Lab for experimental research on the relativistic heavy ion collisions. I greatly appreciate Dr. Hans Georg Ritter and my co-advisor, Dr. Nu Xu, for offering me the opportunity to work at RNC group in LBNL and STAR collaboration, the wonderful place for relativistic heavy-ion physics research. I am very impressed by Nu's profound insight of physics, enthusiasm on the research and serious attitude on science. I benefit a lot from his guidance and lots of fruitful discussions with him.

I would like to thank Prof. Guoxing Ju, Dr. Guangwu Li, Zhangbu Xu and Aihong Tang, for many guidances on physics and data analysis details. Many thanks to my cooperators, Qiang Zheng, Qijun Zhi, Jinhui Chen, Xianglei Zhu, Shusu Shi, Na Li, Chitrasen Jena, and Hiroshi Masui etc. for fruitful and enjoyable discussions. Special thanks to Zebo Tang, Xin Dong, Jinhui Chen, Shusu Shi and Lijuan Ruan for tremendous help and discussions on details of physical analysis and TOF calibrations in STAR.

I would like to thank the STAR light flavor spectra and bulk correlation physics working group especially the convenors for enlightening discussions and constructive suggestions. Thank all other hundreds of STAR collaborators for providing beautiful detector performance and data.

Members of the physics department at Nanjing University and RNC group at LBNL have provided me with an excellent research and study environment and tremendous amount of support. They are, for example, Fei Tai, Dinghan Chen, Zaijun Wang, Chang Xu, Xiaotao He, Baiping Gu, Yingchen Mao, Wenjun Guo, Changying Cai, Fei Li, Weixing Shu, Hailu Luo, Yanqing Guo, Tiekuang Dong, Jianguo Jiang, Yang Xiang, Ying Fan, Zheyong Fan, Yuqing Chen, Gang Chen, Yanyun Chu, Shuang Cheng, Jinjuan Zhang, Dongdong Ni, Xiangming Sun, Qinghua Xu, Yifei Zhang, Xinghua Shi, Xiaofeng Luo and so on. I benefit a lot from their visions and values in both academic and daily life throughout my Ph.D. study. I would like to thank all of them for their kind help.

I would like to thank all my friends for the joyful time we had together at Nanjing, Berkeley and Brookhaven National Lab. Thanks Feiyue Shi for great help on my life in Nanjing. Thanks Shengli Huang for many help on my living at BNL. Thanks other friends at BNL for making the life colorful there. For example, Yichun Xu, Jin Fu, Hao Qiu, Yi Zhou, Xuan Li, Jiayun Chen, Bingchu huang, Jie Zhao, Liang Xue and so on.

Finally, I express my deep gratitude to my family. I'll never forget tens of years of continuing self-giving sacrifices from my parents. I'll never forget continuous support, encouragement and understanding from my love, Yi Xu.